

Measurement and Modeling of Snow Physical Properties

by

DO HYUK KANG

Department of Civil and Environmental Engineering

Duke University

Date:

Approved:

Ana P. Barros, Supervisor

Gary A. Ybarra

Miguel A. Medina

Martin A. Brooke

Andrei Khlystov

Dissertation submitted in partial fulfillment of
the requirements for the degree of Doctor of Philosophy in the Department of
Civil and Environmental Engineering in the Graduate School of
Duke University

2010

ABSTRACT

Measurement and Modeling of Snow Physical Properties

by

DO HYUK KANG

Department of Civil and Environmental Engineering

Duke University

Date:

Approved:

Ana P. Barros, Supervisor

Gary A. Ybarra

Miguel A. Medina

Martin A. Brooke

Andrei Khlystov

An abstract of a Dissertation submitted in partial fulfillment of
the requirements for the degree of Doctor of Philosophy in the Department of
Civil and Environmental Engineering in the Graduate School
of Duke University

2010

Copyright by
DO HYUK KANG
2010

Abstract

The overall objective of this thesis is to characterize the space-time variability of snowpack physical properties at high spatial and temporal resolution for downscaling of remote-sensing products of snow cover, snow depth and snow water equivalent. The hypothesis is that the temporal evolution of the sub grid-scale statistical structure of relative permittivity fields and other snow properties can be related to the temporal evolution of the areal averages obtained from remote-sensing, thus enabling downscaling of snow water equivalent and snow depth even in the absence of ground-based measurements. For this purpose, research was conducted on ground-based measurements of subgrid-scale properties, and on the development and evaluation of a microwave simulation system consisting of coupled snow hydrology and radiative transfer models.

First, an L-band transmitter (TX)-receiver (RX) wireless sensor to monitor snow accumulation and snow wetness was designed, fabricated, and tested under laboratory conditions. The sensor was designed to operate at 39 discrete frequencies (39 channels) in the 1.00–1.76-GHz frequency range (0.02-GHz increments). Full-system testing of the first-generation system was conducted using commercial attenuators up to 20.0 dB to test the prototypes against design specifications. It was determined that performance was nearly optimal in the 1–1.2-GHz range. Next, snow layers of varying snow wetness were physically modeled under controlled laboratory conditions. This was achieved by adding varying amounts of water to a layer of fixed porosity foam inside a rectangular

tank placed above the transmitter. The attenuation and relative phase shift of the RF signal propagating through the experimental “snowpack” and through the laboratory “atmosphere” were subsequently analyzed as a function of volumetric water content equivalent to snow wetness. Under the space and geometry limitations of the laboratory setup, the data show that the single-frequency measurements exhibit high sensitivity for wetness values up to 24%, whereas multifrequency retrieval is necessary for higher liquid water contents. Measurements from a field deployment during snowfall in January 2009 are also presented. The results suggest that there is potential for using the RF sensor to measure cumulative snowfall for short-duration events.

Second, a land-surface hydrology model (*LSHM*) [Devonec 2002] with one-layer snowpack physics was coupled to a microwave emission model (*MEMLS*, [Wiesmann 1999], [Matzler 1999]) including an atmospheric attenuation correction algorithm. The objective is to develop a parsimonious and autonomous framework for monitoring snow water equivalent in remote regions where ancillary data and ground-based observations for model calibration and, or data assimilation are lacking. Two case-studies were conducted to evaluate the coupled hydrology-emission model in forward mode: 1) the intercomparison of a multi-year simulation of snowpack radio-brightness behavior at Valdai, Russia, against Scanning Multi-channel Microwave Radiometer (*SMMR*) observations at three frequencies (18, 21, and 37 GHz, V and H polarizations) for a six year period, 1978-1983; and 2) an intercomparison against Special Sensor Microwave Imager (*SSM/I*) and Advanced Microwave Scanning Radiometer-EOS (*AMSR-E*) during

February 2003 in Colorado as part of *CLPX* (Cold Land Processes Field Experiment). The results show that the model captures well the radiative behavior of the snowpack, especially for vertical polarization in the winter accumulation season January-March for all years of simulation and all cases. Large biases for the Valdai case study were identified for intermittent snowpack conditions at the beginning of the cold season (e.g. fall) which can be explained by uncertainty in fractional snow cover and spatial variability of skin liquid water content at the large spatial scale of *SMMR* products. Nevertheless, the modeling system uncertainty range remains below the known biases of *SMMR* products as compared to *SSM/I* [Derksen 2003]. Using meteorological data from NASA *CLPX* [Cline 2003], the simulated brightness temperatures agree well with *SSM/I* and *AMSR-E* during February, 2003. Overall, the coupled *LSHM-MEMLS* forward model also performs well at smaller scales and where more ancillary data are available, and its performance is consistent with that of more complex snow models. This research suggests there is therefore potential of this modeling framework model that does not require calibration for useful physically-based estimation of snow water equivalent from remote sensing observations over large areas at multiple spatial resolutions.

Third, the snow hydrology model was modified to include a multi-layer transient representation of the evolution of snowpack properties with time. The coupled multi-layer snow hydrology and emission model was implemented and tested independently for two very different climatic and physiographic regions (Valdai and

CLPX2002-2003) for both wet and dry snow regimes over multiple years with good results both in terms of capturing the evolution of snowpack physical properties, and the radiometric signature consistent with SMMR, SSM/I and AMSR-E observations at 18-19, 22-23, and 36-37 GHz V and H polarizations. These applications show transferability of the modeling system, and its potential utility in large-scale retrieval over large areas with limited if any ground-based observations to constrain the model or for data-assimilation. Despite overall good skill as demonstrated by relatively low errors, one weakness was identified with respect to the simulation of the emission behavior of the snowpack, especially for horizontal polarization induced by liquid water in the snowpack, when ice layers (ice lenses) form due to freezing of liquid water either due to daytime melting, or due to rain-on-snow events. Furthermore, it was established that a more accurate estimation of snow density especially in the case of wet snow regimes would be important to improve skill for vertical polarization. Consequently, a multi-layer snow hydrology model (MLSHM) that can capture the events and snowpack gradients in water content and structure through accumulation, ripening and melting phases was developed and coupled to MEMLS. Significant differences between the simulations using the single and multilayer model formulations were found in the ripening and melting phases when wet snow regimes are more frequent. These differences result from differences in snow density, with the single-layer formulation exhibiting higher density (shallower snow depths) and faster melting rates. Whereas there are no significant changes in the microwave brightness temperatures in the vertical

polarization from single to multilayer simulations, there is dramatic improvement in the results for horizontal polarization in Valdai, but not in the case of the more complex snow regimes in CLPX. Further work is required to improve parameterizations of snow density and snow structure including evolution of grain size distribution.

Overall error statistics and detailed analysis of physical behavior show that the coupled MLSHM-MEMLS is apt to be used in data-assimilation in snow retrieval.

Dedication

First of all, I would like to show my great gratitude to my advisor, Dr. Ana P. Barros. She provided me with the opportunity to study at Duke University, spent time with me and my research and guided me in the right direction. I also thank NASA, which supported in part my research financially through an Earth System Science Fellowship. I also would like to thank my thesis committee members for their valuable comments and suggestions. Their advice was very important to me.

Prabhakar Sheresta, Julien Brun, Xiaoming Sun, Jing Tao, and Dr. Olivier Prat have been with me all the time. I give special thanks to Dr. Olivier Prat, who was in charge of the field activities in Oklahoma and the Great Smoky Mountains. My friends in other disciplines, Sungshin Kim in Biomedical Engineering, Hyoseok Park in Atmospheric Science and Dr. Sule Ozev in Electrical Engineering continuously gave me feedback and encouragement.

Finally, I would like to express my deep gratitude to my parents. Without them and their support, I would have not been able to study here and finish my Ph.D. They always believed in my potential to be a great scholar, and a caring person for others. Furthermore, I entrust my special love to my wife, Yoonjin Cho and my son, Ethaniel Dongkun Kang.

In closing, God was always a source of peace in whom I found courage and strength.

Table of Contents

Abstract.....	iv
List of Figures	xiv
List of Tables	xix
List of Symbols	xxiii
CHAPTER 1: Introduction.....	1
1.1. Overview of the Problem and Research Objectives.....	1
1.2. Background and Current Research	2
1.3Microwave signature of dry snow.....	5
1.4. Microwave signature of wet snow	8
1.5. Science Questions and Thesis Outline	11
CHAPTER 2: Full-System Testing in Laboratory Conditions of an L-band Snow Sensor System for In Situ Monitoring of Snow Water Content	13
2.1. Introduction	14
2.2. Design of Sensor System.....	21
2.2.1Design and Laboratory Physical Model	21
2.2.2 Reliability Test of System Design and Fabrication.....	29
2.3. Methods on Data Collection and Processing	32
2.4. Results of System Testing	37
2.4.1Laboratory Conditions	37
2.4.2Field Measurements During Snowfall	48

2.5. Conclusions.....	54
CHAPTER 3: An evaluation of a coupled snow hydrology and microwave emission model for data-sparse regions	56
3.1. Introduction	57
3.2. Model Description	63
3.2.1 Land Surface Hydrology Model (LSHM).....	64
3.2.2 Microwave Emission Model of Layered Snowpack (<i>MEMLS</i>)	72
3.2.3 Atmospheric Correction of Microwave Radiation.....	77
3.3. Data	79
3.3.1. Scanning Multichannel Microwave Radiometer (<i>SMMR</i>).....	79
3.3.2. Special Sensor Microwave Imager (<i>SSM/I</i>)	80
3.3.3. Advanced Microwave Scanning Radar-EOS (<i>AMSR-E</i>)	80
3.3.4.....Project for the Intercomparison of Land-Surface Parameterization Schemes (<i>PILPS</i>).....	81
3.3.5. Cold Land Processes Experiment (<i>CLPX</i>)	81
3.3.6. ERA 40 (ECMWF Re-Analysis 40)	84
3.4. Results and Discussions	90
3.4.1. Comparison Statistics	90
3.4.2. Presence of Water.....	98
3.4.3. Seasonal Responses of Snowpack Radiation	102
3.4.4. Diurnal Cycle of Snowpack Radiation.....	104
3.5. Comprehensive Simulation of CLPX Conclusion	109
3.6. Conclusion	118

CHAPTER 4: Characterization of microwave signatures of snowpack using Multi-layer Snow Hydrology Model	120
4.1. Introduction	121
4.2. Model Description	125
4.2.1. LSHM-MEMLS	125
4.2.2. Microwave Emission Model of Layered Snowpack (<i>MEMLS</i>)	132
4.2.3. Coupled MLSHM-MEMLS Modeling.....	135
4.3. Data	136
4.3.1. Satellite Data	136
4.3.2. Reanalysis Data	141
4.3.3. Forcing Data for Valdai and CLPX 2002.....	141
4.3.4. Ground Truth Data from CLPX 2002	142
4.4. Results and Discussion: Valdai	143
4.4.1. Snow Physics	143
4.4.2. Microwave Behavior.....	147
4.5. Results and Discussion: CLPX 2002-2003	164
4.5.1. Snow Physics	164
4.5.2. Microwave Signature	175
4.6. Conclusion	190
CHAPTER 5: Concluding Remarks.....	192
5.1. Overview	192
5.2. Summary of Findings and Contributions.....	193

5.2.2 Modeling	195
5.3. Recommendations for Further Research	199
Appendix A: Uncertainties of Phase Measurements	202
Appendix B: Lobe Diagram of RF sensor	203
References	204
Biography	214

List of Figures

- Figure 2-1 – a) Illustration of field-scale measurement concept – infer snowpack dielectric properties based on amplitude and phase differences between RF continuous waves traveling through the snowpack (Red signal) from RF node to the receiver tower, subsequently, the received signals communicate with other receivers to synthesize all RF signals through the snowpack (yellow arrows). Network geometry can be derived from high-resolution up to 10 meters Digital Elevation Maps (DEM) and GPS (Global Positioning System) coordinates..... 19
- Figure 2-2 - Block diagram of the transmitter system fabricated by Vadum , Inc. for Duke University. Red and blue circles mark the internal and external antennas, respectively. 23
- Figure 2-3– Physical model of the snowpack in the laboratory. R10, R30 and R60 refer to the porosity of the Regicell foam layers. A single layer foam is placed inside the plexiglass tank (53 ×53×50 cm³) shown above before pouring water.. 25
- Figure 2-4 Dielectric properties of dry Regicell foam of different porosities (R10, R30 and R60). The dielectric properties were measured in the laboratory using an HP-Agilent 85070. a) real part of permittivity (ϵ'); b) loss tangent ($\tan \delta = \epsilon'/\epsilon''$). (Note: HP Agilent 85070 has intrinsic measurement errors at higher frequencies.) 28
- Figure 2-5 – Examples of voltage difference between the external and internal antenna with and without the 20 dB attenuators for two TX-RX systems: a) T1; b) T3. The results were obtained by conducting thirty replicate sequences of measurements for each system. 31
- Figure 2-6 - Raw data and corresponding histogram for dry Regicell (R10) conditions (a) raw, b) histogram) and in the presence of 12 % of volumetric water content (c) raw, d) histogram), at 1.02 GHz. The (x,y) indices in the right-hand panel are (0.0296 Volt,2351) and (0.0163 Volt,2229) respectively for dry and wet Regicell conditions. The lower potential energy from the internal antenna when water is present is reflected in the lower index value. 34
- Figure 2-7– Algorithm to extract attenuation and phase difference between the signal from dry Regicell 10 (Fig. 2-6a) and the signal when Regicell is moist with 12 % VWC (Fig. 2-6c) at 1.02 GHz, respectively: (a) and (b) FFT; (c) and (d) are magnitude and phase angle of multiplication of (a) and conjugate of (b). Finally,

(e) is calculated by summing all 30 replicates (d). The final value of the relative phase-shift is determined by a moving-window algorithm to identify the most stable value within ± 0.5 rad in the interval [0,10MHz].	36
Figure 2-8– Laboratory results expressed in terms of ΔA using T1 and Regicell 10 as a function of volumetric water content (VWC). (a) 1GHz, b) 1.02 GHz, c) 1.04 GHz).....	40
Figure 2-9 - Laboratory results expressed in terms of A_r using T1 and Regicell 10 as a function of volumetric water content (VWC). (a) 1GHz, b) 1.02 GHz, c) 1.04 GHz	41
Figure 2-10– Schematic setup for wave propagation calculation using transmission coefficient [Hallikainen et al. 1986]and F_{riis} factor (a) and Calculated power at the receiver (b).	43
Figure 2-11– Unwrapepd phase shift measurements using TY1 and Regicell 10 as a function of volumetric water content (VWC). (a) 1GHz, b) 1.02 GHz, c) 1.04 GHz).....	47
Figure 2-12- Snowfall intensity on January, 19 2009 storm in North Carolina. Two distinct episodes of snowfall can be identified corresponding to significantly different intensity rates. There was intermittent rainfall at the beginning of the storm and in-between snowfall episodes. Blue circles in the top panel indicate measurement times on January 20, 2009, respectively from left to right: 2:20, 3:50, 5:50, 10:50, 11:40 AM and 12:30 and 1:30 PM.	49
Figure 2-13– Intercomparison of measurements using T1 under laboratory and under field conditions (Jan. 19 th 2009) at 1GHz for both attenuation cases ΔA (a) lab, b) field) and A_r (c) lab, d) field). Since initial conditions are very different, only the changes in attenuation difference between initial and final conditions (~ 3dB) can be compared.	52
Figure 2-14- Field measurements of amplitudes at various frequencies using T1 during the snow storm of January 19-20, 2009. (a) 1.02 GHz, b) 1.04 GHz, c) 1.06 GHz, d) 1.08 GHz).....	53
Figure 3-1 Schematic view of grid resolutions of ERA40 (2.5 °) and SMMR (0.25 °) located in Valdai, Russia	61

Figure 3-2 Small Regional Study Area for CLPX 2002 including our application site, the Fraser MSA, (meso cell study area) [http://nsidc.org/data/docs/daac/nsidc0173_clpx_ISA_corner_met/http://nsidc.org/data/clpx/clpx_pits.html]. The GBMR-7 (Ground Based Passive Microwave Radiometer-7) is located in the Local Scale Observation Station, LSOS in Fraser MSA above).....	62
Figure 3-3 Schematic view of model flow chart for simulated and apparent brightness temperature at radiometer, T_{sim} , T_{app} , and T_{appm}	63
Figure 3-4 Schematic view of LSHM including state variables and their processes [Devonec 2002].	70
Figure 3-5 Snow Density [kg/m ³] and Compaction Rate [1/sec].	71
Figure 3-6 Multilayered Snowpack System with incident radiation from sky with an angle θ_n [modified from Wiesmann and Mätzler 1999] including optical depth, before the satellite microwave receiver. (b)-incoming and outgoing microwave propagation variables of snow layers in MEMLS	76
Figure 3-7 LSHM-MEMLS simulations of snow physical properties compared with GBMR snowpit observations: a) SWE, b) snow depth, and c) snow density.	83
Figure 3-8 Vertical liquid water, L in mm and Precipitable water, V in mm in Valdai Russia extracted from ECMWF ERA 40.....	86
Figure 3-9 SMMR (red circle), compared with T_{app} and T_{appm} (blue dot) at 18 GHz (H and V Upper and lower panels, respectively).....	87
Figure 3-10 SMMR (red circle), compared with T_{app} and T_{appm} (blue dot) at 21 GHz (H and V Upper and lower panels, respectively).....	88
Figure 3-11 SMMR (red circle), compared with T_{app} and T_{appm} (blue dot) at 37 GHz (H and V Upper and lower panels, respectively).....	89
Figure 3-12 Comparison between MEMLS-LSHM (Blue circle) and T_{appm} (Red Dot) from Ascending path at 11:00 LST (Area inside dashed blue circle indicates overestimation during early accumulation and late melting).....	96

Figure 3-13 Comparison between *MEMLS-LSHM* (Blue circle) and T_{appm} (Red Dot) from Descending path at 23:00 LST (Area inside black dashed circle indicates overestimation during early accumulation and late melting)..... 97

Figure 3-14 Radiation properties and corresponding physical properties of snowpack during 1982 to 1983 snow year (red dot square: Domain for liquid water assessment, Yellow square, triangle, and circle: accumulation, peak and melting, respectively, green parallelogram and diamond: wet and dry snow case for diurnal cycle study). Note: the dotted horizontal line in *LWC* is the maximum *LWC* specified for the Valdai simulation. 100

Figure 3-15 (a): Sensitivity of permittivity to *LWC* within the red square from Fig. 3-14, (b): imaginary part of permittivity and (c): absorption coefficient during the same time. 101

Figure 3-16 Temporal evolution of radiation properties with snow density in the *dry snow* regime on February 3rd to 4th in 1982. 107

Figure 3-17 Comparison of radiation properties with snow density in the *wet snow* regime on December 5th to 7th in 1981. 108

Figure 3-18 Snow temperature simulation compared with snow pit measurement in Feb and Mar. 2003 during CLPX located only in Fraser, MSA..... 112

Figure 3-19 Inter-Comparison among *SSM/I* (blue filled circle), *MEMLS-LSHM* (red star) at 37.0, 22.2, and 19.35 GHz H/V (22.2 H is not available)..... 113

Figure 3-20 Inter-Comparison among *AMSR-E* (blue filled circle), *MEMLS-LSHM* (red star) at 36.5, 23.8, and 18.7 GHz H/V. 114

Figure 3-21 Snow emissivity at 37 GHz V versus snow density (a), and versus snow wetness, *LWC* (b) [kg/kg]. 116

Figure 3-22 Increase of brightness temperature induced by snow wetness at 37-V GHz *SSM/I* (blue filled circle), T_b (red star), and rainfall (solid line) during February, 2003 117

Figure 4-1 Schematic view of snow layers containing snow temperature, snow water equivalent, snow depth, snow density, and liquid water content at each snow layer. 126

Figure 4-2 Schematic view of the incoming and outgoing microwave propagation variables of snow layers in MEMLS	133
Figure 4-3 Schematic view of model flow chart for simulated and apparent brightness temperature at radiometer, T_{sim} , T_{app} , and T_{appm} using the simulation of multi-layer snowpack.....	136
Figure 4-4 Schematic view of grid resolutions of ERA40 (2.5 °) and SMMR (0.25 °) located in Valdai, Russia.....	138
Figure 4-5 Small Regional Study Area for CLPX 2002 including our application site, Fraser MSA, also corresponding to GBMR-7 site and Local Scale Observation Site (LSOS), in the lower right corner. (L:LSOS, S: St. Louis Creek, F: Fool Creek, A: Alpine) Sources: [http://nsidc.org/data/docs/daac/nsidc0173_clpx_ISA_corner_met/ and http://nsidc.org/data/clpx/clpx_pits.html]. GBMR-7 is located in the Local Scale Observation Station, LSOS, in Fraser, MSA.	140
Figure 4-6 LSHM-MEMLS simulations in Valdai, Russia using PILPS of snow physical properties compared with ground assimilated observation only in SWE: a) SWE, b) snow depth, and c) snow density.....	145
Figure 4-7 Number of snow layers in LSHM-MEMLS corresponding to with SWE simulation in Valdai, Russia.....	146
Figure 4-8 SMMR (red circle), compared with <i>multi-layer</i> (blue dot) at 37 GHz (H and V polarizations, upper and lower panels, respectively).....	149
Figure 4-9 SMMR (red circle), compared with <i>multi-layer</i> (blue dot) at 21 GHz (H and V polarizations, upper and lower panels, respectively).	150
Figure 4-10 SMMR (red circle), compared with <i>multi-layer</i> (blue dot) at 18 GHz (H and V polarizations, upper and lower panels, respectively).....	151
Figure 4-11 - Radiation properties and corresponding physical properties of snowpack during 1982 to 1983 snow year, and the Circle: melting point, A ¹ to A ³ : Accumulation to peak, respectively. Note: LWC has the maximum LWC of 0.05 [kg/kg] assigned in this Valdai case. A ¹ : Feb. 5 th , A ² : Mar. 15 th , A ³ : Mar. 23 rd , and Yellow Ellipse: March 21 st	157

Figure 4-12 Snow temperature and density with the vertical snow depth with respect to A ¹ , A ² , and A ³ from Figure 4-11	158
Figure 4-13 Horizontal brightness temperatures at 37 GHz H on March 21 st 1983 corresponding to the yellow circle from Figure 4-11	160
Figure 4-14 D_n and $1-s_n$ on March 21 st 1983 by decomposing T_b at 37-H GHz.	161
Figure 4-15 Summation of internal reflectivity and transmissivity on March 21 st , 1983.....	162
Figure 4-16 Horizontal brightness temperature of multi-layer simulation at 37 GHz H superposed with the rainfall occurred during the entire day on March 21 st , 1983.....	163
Figure 4-17 <i>LSHM-MEMLS</i> simulations of CLPX conditions using RUC40 forcing compared with GBMR snowpit observations: a) SWE, b) snow depth, and c) snow density(C^1 , C^2 and C^3 are 12/19/2002, 2/21/2003, and 3/16/2003, respectively, the red circle in (a) is on April 9 th to 10 th 2003).....	165
Figure 4-18 Number of snow layers in <i>LSHM-MEMLS</i> corresponding to with SWE simulation in CLPX.	166
Figure 4-19 Snow temperature and density with the vertical snow depth with respect to GBMR C^1 , C^2 , and C^3 in Figure 4-17. Dates are 12/19/2002, 2/21/2003, and 3/16/2003, respectively.....	171
Figure 4-20 Snow temperature and density with the vertical snow depth with respect to GBMR D^1 , D^2 , and D^3 only in Feb/2003 in Figure 4-17. Dates are 3 rd , 9 th , and 21 st of February 2003, respectively	172
Figure 4-21 Snow temperature distribution compared with the snow pit data in Fraser, (a): Alpine (b): Fool Creek, (c): St. Louis Creek	173
Figure 4-22 Vertical profiles of snow temperature and density in diurnal cycles 9:00, 12:00 and 15:00 on Feb. 20 th 2003 in Fraser MSA.	174
Figure 4-23 Temporal evolution of the difference in Brightness temperature between 37-H and 18-H GHz from single and multi-layer simulations and simulated Snow Water Equivalent.....	178

Figure 4-24 Temporal evolution of the difference in brightness temperature between 18-H and 37-H GHz for AMSRE-E and SSM/I and simulated Snow Water Equivalent.	179
Figure 4-25 Scatter plot of AMSR-E, SSM/I, and multi-layer simulations of brightness temperature differences at 37-H GHz versus SWE. (rectangle: accumulation, circle: peak, and hexagon: melting phases).....	180
Figure 4-26 Comparison of brightness temperatures between multi-layer model and SSM/I at 19.35, 22.2, and 37.0GHz H/V.	185
Figure A-1 Box-plot for phase extraction from RF signals with respect to water content at 1.08 GHz.....	202
Figure B-1 Simulated Antenna Pattern provided by Vadum, Inc.	203

List of Tables

Table 2-1 Attenuation Slope [$0 < \text{VWC} < 24\%$] and [$0 < \text{LWE} < 22 \text{ mm}$]	46
Table 3-1- Coefficients β_f and ϕ_f for optical depth τ_f [Mätzler 1992]	86
Table 3-2 Locally estimated parameters β_f and ϕ_f ($\tau_{f,i} - \zeta_f L_i = \beta_f + \phi_f V_i$), using two years of SMMR and LSHM-MEMLS data at Valdai while ζ_f was maintained as per Matzler (1996) for ascending paths.....	93
Table 3-3 Locally estimated parameters β_f and ϕ_f ($\tau_{f,i} - \zeta_f L_i = \beta_f + \phi_f V_i$), using two years of SMMR and LSHM-MEMLS data at Valdai while ζ_f was maintained as per Matzler (1996) for descending paths.	93
Table 3-4 Differences in error statistics for ascending paths due to local estimation of atmospheric correction parameters (T_{appm}) as compared to general values (T_{app}). [Derksen and Walker 2003] reported Bias of -5.4 at 19-V GHz and 1.0 at 37-V GHz between SMMR and SSM/I for ascending paths.	94
Table 3-5 Differences in error statistics for descending paths due to local estimation of atmospheric correction parameters (T_{appm}) as compared to general values (T_{app}). [Derksen and Walker 2003] reported Bias of -8.85 at 19-V GHz and 4.59 at 37-V GHz between SMMR and SSM/I for ascending paths.	95
Table 4-1 Locally estimated parameters β_f and ϕ_f ($\tau_{f,i} - \zeta_f L_i = \beta_f + \phi_f V_i$), using two years of.....	152
Table 4-2- Locally estimated parameters β_f and ϕ_f ($\tau_{f,i} - \zeta_f L_i = \beta_f + \phi_f V_i$), using two years of SMMR and LSHM-MEMLS data at Valdai while ζ_f was maintained as per [Mätzler 1996] for descending paths.	153
Table 4-3 Differences in error statistics between T_{appm} and SMMR observations for ascending paths (11:00 AM LST).	154
Table 4-4 Differences in error statistics between T_{appm} and SMMR observations for descending paths (11:00 PM LST).....	155
Table 4-5 Comparison of simulated radiation properties between 36.5-V and 23.8-V GHz. Time is 20:00 UTC, 13:00 LST, 3/20/2003.	183

Table 4-6 Model error statistics [Multilayer(single layer)] intercomparison using the correlation length, p_{ec} based on the classification by Mätzler (1996) for the Fraser MSA during CLPX: SSM/I, AMSR-E and Wójcik et al. [2008, W08]. Single-layer simulation results are from Chapter 3 (Kang and Barros 2010^b)..... 184

Table 4-7 Model error statistics [Multilayer(single layer)] intercomparison using the correlation length, p_{ec} =constant=0.06mm, for the Fraser MSA during CLPX: SSM/I, AMSR-E and Wójcik et al. [2008, W08]. Single-layer simulation results are from Chapter 3 (Kang and Barros 2010^b)..... 187

List of Symbols

LSHM (input and output)

ρ_a : air pressure [Pa]

Q_{sn} : amount of heat used to melt the snowpack [J]

Δh_{sm} : amount of snowmelt [m]

ρ_w : density of water [kg/m³]

ε_{am} : emissivity of ambient atmosphere

ε_s : emissivity of snowpack/ground surface

F_{si} : incoming solar radiation [W/m²]

F_{lo} : outgoing long wave radiation from the ground surface [W/m²]

C_{sn}^* : snow depth coefficient

Φ_{sn} : snowmelt outflux [m/s]

σ : Stefan-Boltzmann's constant ($5.67 \times 10^{-8} \text{ W / m}^2 \text{ K}^4$)

E_{sk}^{snow} : temporal change of snow depth [m]

a_g : reflectance composite of bare soil, snow, and vegetated fractions

c^* : heat capacity of snow [J/kg K]

c_i : heat capacity of ice [J/kg K]

C_p : heat capacity of air at the constant pressure [J/kg K]

c_s : heat capacity of the soil [J/kg K]

C_{sn} : fraction of snow covered area

C_v : fraction of vegetation cover

F_{li} : incoming long wave radiation from cloud and aerosols [W/m²]

FR : net solar radiation [W/m²]

F_s : net solar radiation [W/m²]

G_h : ground heat flux [W/m²]

h_0 : snow water equivalent [m]

h_d : soil depth [m]
 h_{sn} : snow water equivalent of one layer LSHM simulation [m]
 K_H : aerodynamic transfer coefficients for heat
 K_L : aerodynamic transfer coefficients for vapor
 L_h : latent heat flux [W/m²]
 L_v : latent heat of vaporization from liquid water to vapor [J/kg]
 LWC : liquid water content
 S_h : sensible heat flux [W/m²]
 T_o : snow temperature [K]
 T_o : snowpack temperature of one layer LSHM simulation [K]
 T_1 : temperature measured in the reference height [K]
 T_{air} : air temperature [K]
 T_d : soil temperature [K]
 T_e : equivalent temperature for melting [K]
 T_i : melting temperature [K]
 U_1 : horizontal wind speed [m/s]
 xP_r : accumulated snow from rain-on-snow [m]
 bk^k : snow density (k = 1 to n) [kg/m³]
 h_{sd}^k : snow depth of one layer LSHM simulation (k = 1 to n) [m]
 h_{sn}^k : snow water equivalent of one layer LSHM simulation (k = 1 to n) [m]

MEMLS (input)

ϵ_k (k=a, b, and c): Debye snow mixture terms
 γ_a : absorption coefficient [1/m]
 γ_c : combination effect from scattering and absorption coefficient [1/m]
 ϵ : effective permittivity of wet snow

ϵ_i'' : imaginary part of permittivity of ice
 n'' : imaginary part of refractive index of internal snowpack
 s_j : interface reflectance between j and j+1 layers
 ϵ_a' : real part of permittivity of air
 ϵ_d' : real part of permittivity of dry snow
 ϵ_i' : real part of permittivity of ice
 γ_b : scattering coefficient [1/m]
 e : emissivity of internal snowpack
 e_{back} : emissivity of internal snowpack backwardly calculated from T_s and T_b
 f : frequency used for a passive microwave radiometer
 h_{sd} : snow depth at each snowpack layer [m]
 K^2 : the squared field factor
 LWC : liquid water content at each snowpack layer [kg/kg]
 p_{cc} : snow grain size correlation length [m]
 r : reflectivity of internal snowpack
 t : transmissivity of internal snowpack
 T_b : brightness temperature [K]
 T_s : snow temperature at each snowpack layer [K]
 T_{sim} : simulated brightness temperature just after the snowpack surface [K]
 T_{sky} : sky downwelling radiation [K]
 ρ_s : snow density at each snowpack layer [kg/m³]
 M_1 to M_4 : n by n matrices containing r , t and e
 E , F : the n vectors with brightness temperatures at the boundaries including T_{sky} and T_{soil}

Atmospheric Correction (input and output)

τ : atmospheric optical depth [neper]
 e : atmospheric emissivity

e_s : snowpack surface emissivity generated from MEMLS routine []

L : vertical liquid water [mm]

r : atmospheric reflectivity

t_a : atmospheric transmissivity

T_{app} : Apparent brightness temperature approximated at radiometer [K]

T_{appm} : Apparent brightness temperature locally approximated at radiometer [K]

T_{sim} : simulated brightness temperature before atmospheric correction [K]

V : precipitable water [mm]

β_f : intercept of linear fit on optical depth with V and L [neper]

ϕ_f : coefficient of V in linear fit on optical depth with V and L [neper/mm]

ζ_f : coefficient of L in linear fit on optical depth with V and L [neper/mm]

Other

μ : the cosine of the incidence angle

$C3$, $C4$, $C5$ and $C6$ are constants for compaction rate equation.

SSA : Specific Surface Area

ΔT : difference between emissions of vertical and horizontal polarization

κ_a : absorption coefficient of atmosphere [dB/m]

κ_e : extinction coefficient of atmosphere [dB/m]

CHAPTER 1:

Introduction

1.1. Overview of the Problem and Research Objectives

One third of the continental area in the northern hemisphere is seasonally covered with snow. The western U.S., countries along the Andes Mountains, north east India along the Himalayas and even the arid countries in central Asia depend on mountain snowmelt for freshwater resources. Currently, changes in the distribution of snow cover also provide an essential indicator of climate change at the global scale. In this context, the National Research Council's Decadal Survey (2007) recommended that Snow and Cold Land Processes (SCLP) are a high priority to climate change science. Specifically, a satellite mission including active and passive microwave sensors was proposed in order to collect data necessary to conduct the research. The SCLP mission will be coordinated with other satellite launches to measure soil moisture and freeze-thaw conditions for weather and water cycle processes (SMAP) as well as sea ice monitoring. Due to the heterogeneous distribution of snow cover, and its complex structural behavior linked to solar energy forcing, many challenges must be addressed in the remote-sensing of snow properties.

The objective of this thesis is to characterize the space-time variability of snowpack physical properties at high spatial and temporal resolution for downscaling of remote-sensing products of snow cover, snow depth and snow water equivalent. The hypothesis is that the temporal evolution of the sub grid-scale statistical structure of

relative permittivity fields and other snow properties can be related to the temporal evolution of the areal averages obtained from remote-sensing, thus enabling downscaling of snow water equivalent and snow depth even in the absence of ground-based measurements.

1.2. Background and Current Research

In the 1950 and 60's, Cumming (1956) identified the relationship between real part of the snow permittivity and the snow density at about 10.0 GHz. Based on the Debye mixing theory, the real part of the snow permittivity was formulated in terms of snow density. This was also confirmed with experimental datasets near 10.0 GHz in laboratory conditions. At the same time, the so-called Hokkaido group studied the radiometric behavior of the snowpack in the microwave range [Yoshida et al. 1956], and made contributions to the morphological characterization of snow crystals by classifying snow flakes with respect to its shape and orientation of falling snow [Magono and Lee 1966]. Based on these early foundations on radiation and physical properties of snow, the US Army Corps of Engineers (1956) comprehensively summarized snowpack characteristics with respect to physics and radiation properties, and to this day the report "Snow Hydrology" and series of technical reports produced by the Cold Regions Research and Engineering Laboratory (CRREL) are widely considered a many bases of snow hydrology science.

During the 1970's, the research on satellite remote sensing emerged after the launch of the lunar rocket in 1969. The passive microwave radiometer, SMMR (Scanning

Multi-channel Microwave Radiometer) was deployed in the DMSP (Defense Meteorological Satellite Program) satellite, Nimbus-7. In 1985, Hallikainen and Jolma (1992) introduced a retrieval algorithm for snow physical properties from the remote sensing data from SMMR observation. Before the practical application of SMMR data, Shanda and Matzler (1981) thoroughly investigated the optimal frequency and polarization to assess the various states of the snowpack such as in winter and spring conditions. They also considered the geometry of the electromagnetic wave propagations with respect to incidence angle of the radiometer and surface roughness of the snowpack. Due to these contributions, radiative transfer became an essential component both for the design concept of radiometer and forward modeling of microwave brightness temperatures above the snowpack in microwave observing system simulation.

The 1980's was the peak of the snow permittivity research in Finland, Austria, and some U.S. groups. Ambach and Denoth (1980) determined an empirical equation for the relationship between the relative dielectric constant (ϵ'), i.e. the real part of dielectric constant) of snow, snow density (ρ_s) in g/cm³ and the liquid water content (LWC) in vol % in the range from 1 MHz to 2 GHz :

$$LWC = 4.69(\epsilon' - 1.22\rho_s) \quad (1-1)$$

Tiuri *et al.* (1984) studied the dielectric properties of snow at different stages of metamorphosis with frequency ranges at 1.9 GHz, 5.6 GHz, and 12.6 GHz. The real part

of the relative dielectric constant (ϵ'_d , Eq. 2) was found to depend almost solely on the density regardless of snow age and condition (i.e. coarse old snow, aged snow, new fine grained snow, undisturbed snow, and man-made snow):

$$\epsilon'_d = 1 + 1.7 \rho_d + 0.7 \rho_d^2 \quad (1-2)$$

where ρ_d is the relative density of dry snow (compared to water). Hallikainen et al. (1982) derived a relationship for dry snow in the 4-18 GHz range:

$$\epsilon'_d = 1 + 1.91 \rho_d \quad (1-3)$$

Frolov and Macheret (1999) modeled experimental data on dielectric properties of dry and wet snow at high frequencies (1 MHz to 10 GHz). They showed a possibility of approximations of dielectric data as the functions of dry snow density and water content using the Looyenga's mixture formula with error of about 2 %. The relationship between snow dielectric constant (ϵ'_d) and density (ρ_d) has been investigated by many others including Tiuri *et al.* (1984), Achammer and Denoth (1994), Denoth (1994), Kovacs *et al.* (1993), Looyenga's formula (1965), Lichtenecker's formula (Chelidze *et al.* 1977), Schneebeli *et al.* (1998), and Mätzler (1996).

Expressing the dielectric constant ϵ'_s of wet snow as: $\epsilon'_s = \epsilon'_d + \Delta\epsilon'_s$, where ϵ'_d is dielectric constant of dry snow, and $\Delta\epsilon'_s$ is incremental dielectric constant due to water volumetric content, Frolov and Macheret (1999) used Looyenga's mixture formula to determine the incremental dielectric constant ($\Delta\epsilon'_s$) and plotted previous estimates of it.

Mätzler (1996) investigated the effects of snow metamorphism and grain size and morphology on the ice volume fraction of snow ($VF = \rho_s/\rho_i$) at about 1 GHz, and found non-linear behavior showing that the shape is less and less spherical with increasing snow density up to a critical volume fraction of 1/3, and subsequently decreases with increasing VF (not shown). Sweeny and Colbeck (U.S. Army Cold Regions Research and Engineering Laboratory 1974) investigated the parameters affecting the complex dielectric constant of wet snow and retrieved a data base from which other instrumentation can be calibrated at 6 GHz. They proposed a formula for the complex dielectric constant of snow water mixture (ϵ_m^*) and wet snow that is a function of the complex dielectric constant of water, the LWC (liquid water content), and two factors related to grain shape and metamorphic state of the snow-pack, both of which are determined empirically.

In addition to the general literature review, the following sections focus on work related to the sensitivity of dry snow permittivity with respect to microwave frequency, and the parameterization of wet snow permittivity to retrieve liquid water content and snow metamorphosis effects.

1.3. Microwave signature of dry snow

Dry snow is composed of air and ice. To calculate the dry snow permittivity, an appropriate mixture theory is necessary. Cumming (1954) used the Polder and van Santen (1946) mixture theory to compare his observed data with the theoretical dry

snow dielectric permittivity. The dry snow density is only dependent upon the real part of the dry snow permittivity because the density of ice (ρ_i) is 0.917 g/cm³, and the real part of ice permittivity (ϵ_i) is about 3.17.

$$\frac{\epsilon_d' - 1}{3\epsilon_d'} = \frac{\rho_i}{\rho_s} \cdot \frac{\epsilon_i - 1}{\epsilon_i + 2\epsilon_d'} \quad (1-4)$$

The range of the snow density is from 0 to 0.5 or 0.916 which is the ice density. Snow temperature is below 0 ° C. The grain size of snow varies from 0.5 to 1.5 mm (Nyfors 1983). Matzler (1996) generalized the effective permittivity of dry snow considering snow metamorphism such as fresh, old, wind-pressed, depth hoar, and refrozen crusts and also compared the existing snow dielectric data against the snow dielectric equation with the complex mixture theory of Polder and van Santen (1946).

Sihvola and Kong (1989) generalized the equation for effective snow permittivity for homogeneous and isotropic ellipsoid permittivity ϵ_s , and the ice volume fraction per total snowpack volume v :

$$\epsilon_{eff} = 1 + \frac{v(\epsilon_i - 1) \sum_{i=1}^3 \frac{\epsilon_a}{\epsilon_a + A_i(\epsilon_i - 1)}}{3 - v(\epsilon_i - 1) \sum_{i=1}^3 \frac{A_i}{\epsilon_a + A_i(\epsilon_i - 1)}} \quad (1-5)$$

where ϵ_a is the apparent permittivity and A_i is the depolarization factor of the ellipsoids due to the surrounding water inclusions with snow particles. ϵ_a and A_i are followed by the relationships by:

$$A_1 + A_2 + A_3 = 1 \quad (1-6)$$

$$\varepsilon_a = 1 + a(\varepsilon_{eff} - 1) \quad (1-7)$$

The parameter a is determined by the effective medium equation (Polder and van Santen 1946):

$$a = 1 - A_i \quad (1-8)$$

For the dry snow effective permittivity, the Equation (1-5) agrees well with the Polder and van Santen Equation for dry snow even though it requires the iterative solution.

The depolarization factor A_i is determined by (Hippel 1954) based on the shapes such as oblate and prolate:

$$A = \left\{ \frac{X}{2(1-X^2)} \left[\frac{\arccos(X)}{\sqrt{1-X^2}} - X \right] \right\}; \quad \text{for oblate} \quad (1-9)$$

$$A = \left\{ \frac{1}{2(1-X^2)} \left[1 - \frac{X^2}{2\sqrt{1-X^2}} - \ln \frac{1+\sqrt{1-X^2}}{1-\sqrt{1-X^2}} \right] \right\}; \quad \text{for prolate} \quad (1-10)$$

The axial ratio (X) is defined by the ratio between minor axis and major axis. Matzler (1996) also explained the relationship between the ice volume fraction v and the depolarization factor A_i in terms of snow metamorphism.

There is a clear increase of the depolarization factor with increasing the ice volume fraction of the dry snow from 0 to 0.33, which indicates the presence of freshly fallen snow crystals such as needles, plates, stars and their fragments. With time, destructive metamorphism affects the snow crystals producing rounded snow particles which correspond to ice volume fractions from 0.25 to 0.3 sampled from the bottom of snowpacks, the so called depth hoar. In the presence of depth hoar, Matzler (1996)

reported that the axial ratio (X) is slightly reduced from 1 to 0.65. At this volume fraction ($v=0.33$), the reversal of the depolarization factors happens due to the rounded shapes of snow grains. The critical volume fraction ($v=0.33$) also accounts for constructive and melt metamorphism effects such as sintering which creates the large scales snow grains. Therefore, the depolarization factor (A_i) can be assumed to be $1/3$ regardless of the different crystal shapes.

Frolov and Macheret (1999) summarized the behavior of dry snow permittivity and also they applied the Looyenga (1965) mixture theory instead of Polder and van Santen (1946) used by previous researchers:

$$\varepsilon_d' = \left[\frac{\rho_d}{\rho_i} \cdot (\varepsilon_i'^{1/3} - 1) + 1 \right]^3 \quad (1-11)$$

Because ε_i' (the real part of ice permittivity) is constant ($\varepsilon_i'=3.17$) and ρ_i (the density of ice) is 0.917 g/cm^3 , the real part of dry snow permittivity ε_d' is a function of the dry snow density ρ_d . If the real part of dry snow permittivity is measured, the dry snow density can be estimated.

1.4. Microwave signature of wet snow

Wet snow is composed of air, ice, and water. The characteristic of the wet snow permittivity is more complex than that of the dry snow permittivity. Due to the high permittivity of the water, the wet snow permittivity is usually a complex number, and the attenuation values are higher than those of dry snow.

The permittivity and attenuation of wet snow samples were measured and interpolated the relationship between the snow wetness and the attenuation at two frequencies (4 and 12 GHz) (Linlor 1980). Linlor established the complex permittivity of wet snow and attenuation due to snowpack. Then, he compared them with the empirical equations using snow physical properties such as snow density, wetness and the snow depth.

$$\varepsilon_s' = (1 + \phi / 12 \cdot d_s \nu)^2 \quad (1-12)$$

$$\varepsilon_s'' = \varepsilon_s' \tan \delta \quad (1-13)$$

$$\tan^2 \delta + 1 = \left[\left(\frac{A_p}{1.286 \nu (\varepsilon_s')^{1/2}} \right)^2 + 1 \right]^2 \quad (1-14)$$

$$\tan \delta = \left[1.0994 / \nu (\varepsilon_s')^{1/2} \right] \cdot A_p \quad \text{if} \quad \tan \delta \ll 1 \quad (1-15)$$

Equations 1-16~1-18 show the theoretical equations for the complex permittivity of snow (ε_s' , ε_s'' , and $\tan \delta$) and the attenuation (A_p in dB/cm) which are functions of the phase change (ϕ), d_s (snow depth in cm), and the frequency (ν) in GHz. Also, Linlor (1980) provided the empirical equations using the wet snow samples:

$$A_p = W [0.045(\nu - 4) + 0.066(1 + d)] \quad (1-16)$$

$$\varepsilon_s' = 1 + 2\rho_s + bW^{3/2} \quad (1-17)$$

$$b = 5.87 \times 10^{-2} - 3.10 \times 10^{-4}(\nu - 4)^2 \quad (1-18)$$

where W is the volumetric wetness in snow and d is the snow particle diameter in mm.

To explain the relationship between the wetness and the snow permittivity of the wet snow, the incremental dielectrics changes in permittivity as a function of wetness of the wet snow need to be considered:

$$\Delta\epsilon'_s = \epsilon'_s - \epsilon'_d \quad (1-19)$$

Snow research in the 1990's was highly influenced by climate change research needs. Climate change concerns with glaciers and ice sheets accelerated cryospheric research not only limited to scientific endeavor, but stimulated by public interest in monitoring the endangered earth environment. To meet these needs, NASA JPL (Jet Propulsion Laboratory) and Goddard Research Center continued to conduct global scale snow retrieval projects [Chang et al. 1987 and many others]. Global-scale observations of snow and ice since 1978 when the first passive microwave radiometer, SMMR (Scanning Multi-channel Microwave Radiometer) was deployed on the Nimbus-7 satellite provide a unique historical record to investigate the climate change.

In the late 90's, groups in Switzerland, Finland and the U.S. made efforts to develop forward simulators to estimate the microwave radiation from the snowpack in given snowpack layers. The Microwave Emission Model for Multi-layered Snowpack (MEMLS, Matzler and Wiesmann 1999), the Helsinki University of Technology (HUT, Hallikainen 1997), and the Dense Media Radiative Transfer (DMRT, Tsang et al. 2000) are passive microwave simulation models which consider radiation behaviors of layered snowpack such as emissivity, transmissivity, and reflectivity. These models are benefitted from the theoretical and experimental contributions from earlier permittivity

studies. On the other hand, from the hydrological point of view, snow hydrology models has been capable of simulating the mass and energy balance of snow-covered regions available since the 1960's [Anderson 1964]. The first Anderson's snow hydrology model was initiated to address the needs of water resources in the dry western U.S. for quantitative monitoring of mountain snowmelt. Since then a variety of watershed scale hydrology models [Anderson 1973, 1976, Morris 1982, Kondo and Yamazaki 1990] has been developed to meet water resources needs. Pomeroy (2007) introduced wind redistribution effects and the interactions between snow cover and the atmospheric boundary layer. However, coupling of hydrological models with forward Radiative Transfer models is an emerging research area [Andreadis et al. 2008]. From the perspective of snowpack measurements, CLPX (Cold Land Process Field Experiment, 2002) in early 2000's was a major interdisciplinary research effort [Cline et al. 2003], which for the first time established concurrent data bases of satellite and ground based observations of the snowpack including metamorphosis effects.

1.5. Science Questions and Thesis Outline

The overarching goal of this research is develop improved models and tools to overcome current limitations in snow research. In particular, better integration of measurements and models are needed to meet the current challenges of quantitative assessment of the physical properties of snowpack using remote sensing data. Also, full coupling of forward radiation model with a snow hydrology has not been yet conducted for continuous long-term simulations. This will be addressed in this thesis. The three

major research thrusts of this work are as follows: 1) Systematic ground-based measurement of snow physical properties; 2) Microwave remote sensing of snowpack, and 3) Modeling of physical properties and radiation behavior of snowpack. The research was divided into three major tasks corresponding to thesis Chapters: 1) Laboratory system testing of a new RF sensor for noninvasive snow measurements (Chapter 2), 2) Single-layer simulations of snow physics and radiative transfer (Chapter 3), and 3) Multi-layer simulations of snow physics and radiative transfer (Chapter 4). Tasks (2) and (3) are implemented by coupling forward radiative transfer (MEMLS) and snow hydrology models. The description of each task in the corresponding chapter is self-contained. The material in Chapter is published in IEEE Transactions on Geoscience and Remote Sensing [Kang and Barros 2010]. Chapters 3 and 4 are also planned for the submissions to the same journal. Chapter 5 presents concluding remarks and discussion of further research directions.

CHAPTER 2:
**Full-System Testing in Laboratory Conditions of an L-band Snow Sensor
System for In Situ Monitoring of Snow Water Content**

2.1. Introduction

About one billion of the world's population relies on snowmelt water as water resources from drinking water to food production, ecosystem services, and industrial use [Barnett et al. 2005]. In the western US, more than 50 to 80 % of water resources are generated during the spring melting season and subsequently stored behind dams for a broad range of water uses during the dry season [Stewart et al. 2004]. Whereas snow covered area is an important property of the snowpack especially for the surface energy balance, snow water equivalent is the quantity of interest for water resources management.

The spatial and temporal distribution of snow depth, snowpack internal structure, snow wetness (liquid water content of snow by volume), and snow water equivalent (SWE, the equivalent depth of liquid water per unit area if the snowpack melted completely) are highly heterogeneous and widely variable [Sturm and Benson 2004]. This is due to complex thermodynamics, mixed-phase physics and land-atmosphere interactions at the snow-air interface including radiative forcing, wind redistribution, and precipitation input. For instance, SWE can change on the order of 100 to 300% within small distances (100's m) due to changes in landform, land-cover, wind exposure and terrain aspect [Luce et al. 1998]. Traditional measurements that involve coring, digging, or extracting snow samples are destructive in nature and thus modify snowpack structure. In addition, hand-held devices or measurement methods that require a human operator face many challenges for sampling in remote regions, or

are too labor intensive for sampling at the high-resolution (10- 100 m) necessary to characterize the space-time variability of the snowpack [Denoth 1994]. SNOTEL stations (SNOWpack TELemetry) provide the most rigorous ground-based measurements of snow water equivalent based on the weight of accumulated snow (snow pillow) as a function of time [<http://www.wcc.nrcs.usda.gov/snow>], but they are expensive to install and maintain. There is therefore great need for an automated, reliable ground-based snow sensor that can be used in remote harsh environments for long periods of time.

Whereas the great opportunity afforded by satellite based observations is that they provide field estimates globally at the nominal scale of the measurement (e.g. usually 25 km for post-processed products using combinations of snow reflectivity from MODIS, the Moderate-Resolution-Imaging-Spectroradiometer and SWE estimates from AMSR-E, the Advanced Microwave Scanning Radiometer-Earth Observing System), SWE errors on the order of 50% and higher are common due to sub-grid scale variability (snow water equivalent, snow grain-size distribution, fingering effects and ice layers, wind redistribution, among others) within the satellite sensor footprint, which is difficult to assess in operational retrieval algorithms in the absence of ground-truth ([Kelly et al. 2003], [Foster et al. 2005]). Recently, a number of studies have been pursued in the application of ground penetrating radar ([Granlund et al. 2009], [Lundberg et al. 2000]. [Lundberg et al. 2000b]). In either the case of passive or active sensing, snow wetness is especially critical as small changes in volumetric liquid water content can lead to large errors in SWE estimates ([Denoth 1994], [Kelly et al. 2003],

[Lundberg et al. 2000b]). A distributed system of ground-based autonomous sensors operating at high spatial resolution should provide valuable information to characterize the sub-grid scale variability of the properties of seasonal snowpacks as a function of time, which then could be integrated into retrieval algorithms.

The dielectric properties of snow and ice as expressed by the complex permittivity at frequency f [$\epsilon(f) = \epsilon'(f) + j \epsilon''(f)$] exhibit strong sensitivity to liquid water content, and consequentially research toward developing measuring capability of snow density and snow wetness using active and passive microwave sensors ranging from 500 MHz to 100 GHz has been undertaken for over more than fifty years ([Cumming 1952], [Looyenga 1965], [Foster et al. 2005], [Kendra et al. 1994], [Meissner and Wentz 2004], [Rotschky et al. 2006], [Koskinen et al. 2010]). In the case of dry snow, the focus of most studies has been on documenting the relationship between the real part of the permittivity and snow density ([Denoth 1994], [Lounge et al. 1997], [Hallikainen et al. 1982], [Ambach and Denoth 1980], [Mätzler 1996]) For the case of wet snow, studies focused on the sensitivity of the imaginary part of the permittivity to snow wetness ([Denoth et al. 1984], [Tiuri et al. 1984]), as well as the difference between the real part of the permittivity in wet and dry snow conditions as a function of snow wetness ([Ambach and Denoth 1980], [Kuroiwa, 1954], [Sweeny and Colbeck 1974], [Tiuri et al. 1984], [Hallikainen et al. 1986]). Field studies and laboratory experiments suggest that the relationship between the real part of the permittivity and snow density is independent of frequency, and this is also the case for the relationship between the

imaginary part of permittivity and snow wetness [Tiuri et al. 1984]. These theoretical and experimental studies on snow permittivity established the physical parameterizations that relate snow wetness and snow physical properties to the dielectric behavior of snow that are widely used in microwave simulators such as the MEMLS (Microwave Emission Model of Layered Snowpack, [Wiesmann and Mätzler 1999], [Mätzler and Wiesmann 1999]), and HUT (Helsinki University of Technology, [Pulliainen et al. 1999]). The practical implication for snow measurement is that if the permittivity can be estimated, and snow depth can be measured or estimated, then snow wetness and snow density can be estimated, and consequently SWE can be estimated. SWE is of critical interest to operational Hydrology (rain-on-snow events, flooding) and Water Resources (snowmelt runoff, climate).

Furthermore, previous research showed that the highest sensitivity to liquid water content takes place around 1 GHz because the real part of the permittivity of water is very large as compared to ice, and there is a difference of four orders of magnitude in the imaginary parts at 0°C respectively for water and ice [[Denoth et al. 1984], [Meissner and Wentz 2004]: $\epsilon_w = 86.9 - j9.1$ and $\epsilon_i = 3.15 - j0.001$]. This is the basis for the design of hand-held snow wetness and snow density probes consisting of transmission type electromagnetic resonators operating near 1 GHz, which were successfully demonstrated for relatively dry snow conditions (snow wetness $\leq 5\%$) [Tiuri et al. 1984], [Kendra et al. 1994]. One shortcoming of these sensors for high density sampling in remote regions is that they require a human operator and, or a support

station (i.e. only in-situ measurements), the sampling volume is limited to a 6-cm long cylinder around the prongs, the measurement is somewhat intrusive due to preferential compaction at the points of probe insertion, and the range of snow wetness under which they can operate is narrow. Here, we present system testing and feasibility/reliability results of the first-generation prototype of an L-band sensor system that aims to improve on previous sensors operating near 1 GHz via nonintrusive placement and nondestructive measurement integrated over the snowpack, by extending the range of sensitivity to snow wetness and by relying on wireless technology to achieve sensor autonomy (Fig. 2-1). The ultimate goal is to develop a measurement strategy to deploy low-maintenance high-spatial resolution networks of L-band WRF (wireless radio-frequency) sensors in remote (mountainous) regions, which currently presents a daunting observational challenge.

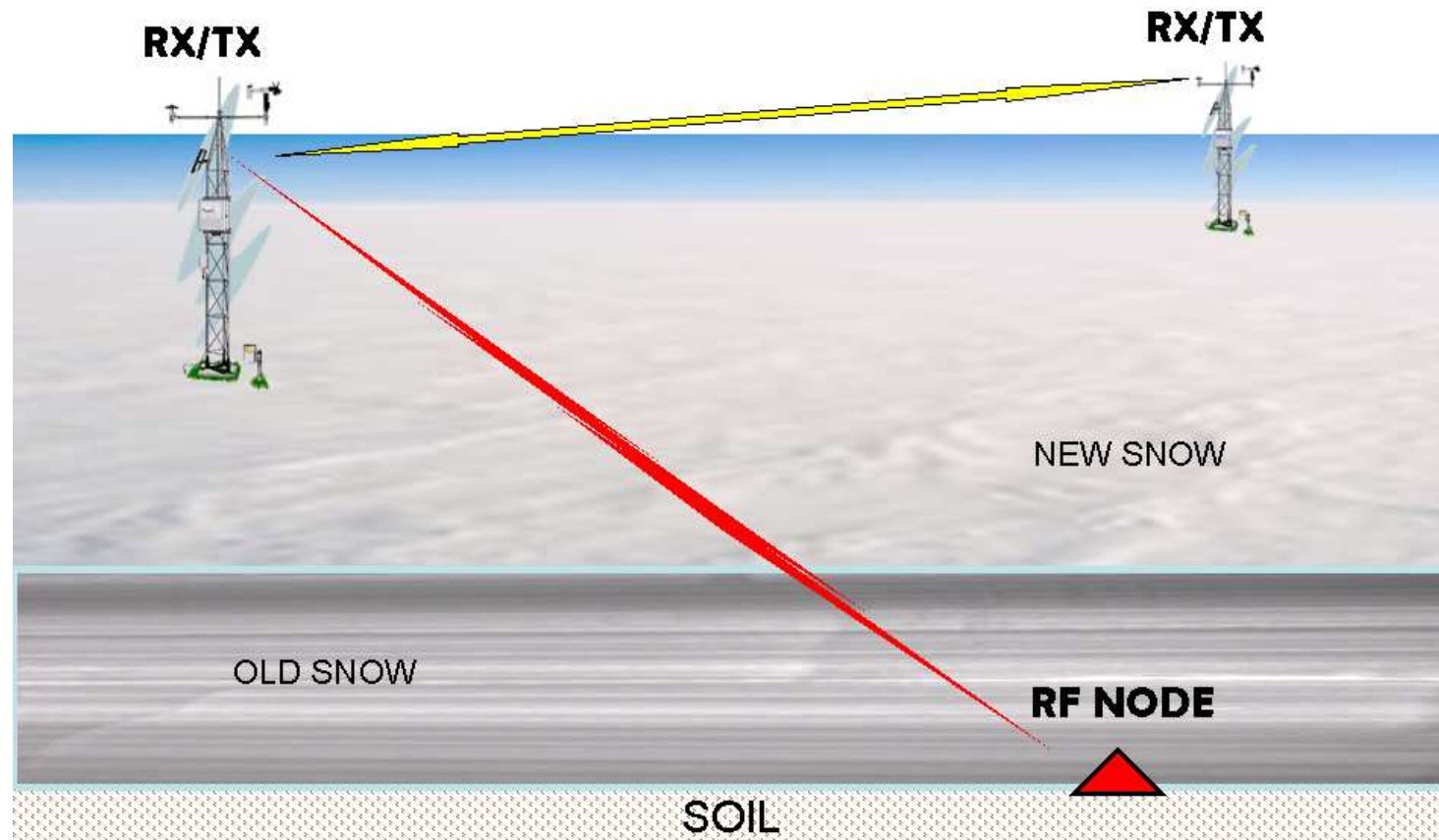


Figure 2-1 – a) Illustration of field-scale measurement concept – infer snowpack dielectric properties based on amplitude and phase differences between RF continuous waves traveling through the snowpack (Red signal) from RF node to the receiver tower, subsequently, the received signals communicate with other receivers to synthesize all RF signals through the snowpack (yellow arrows). Network geometry can be derived from high-resolution up to 10 meters Digital Elevation Maps (DEM) and GPS (Global Positioning System) coordinates.

The basic make-up of the sensor system consists of one transmitter operating in the 1.00 to 1.76 GHz frequency range, and a central pod equipped with a receiver, the Vector Signal Analyzer (VSA). The VSA collects raw data to determine frequency-dependent attenuation and phase-shift information between radio signals that propagate through air and through the snowpack (Fig. 2-1). The sensors are equipped with an internal clock that wakes up the transmitter at user specified intervals to obtain a user-specified number of samples. The snow wetness retrieval algorithm relies on the differences in amplitude and phase shift between the transmitted signal as it propagates through the air on the one hand, and as it propagates separately through the snowpack first and next through the air until it reaches the receiver. By using multiple channels, more than one independent measurement is collected for the same snow conditions, hence providing the retrieval algorithm with additional constraints for realistic snow conditions when density and characteristic grain size can change dramatically in short periods of time such as after a snowstorm [Schneebeli and Johnson 1998].

The specific objective of this manuscript is to present the conceptual design and system-testing in laboratory conditions to characterize the sensor's sensitivity response to snow wetness, as well as to develop the sensor's signal capture and processing algorithms. Section 2-2 describes in detail the new sensor design and laboratory setup, including results of system testing using commercial attenuators. Section 2-3 presents the retrieval algorithms to estimate frequency-dependent attenuation and phase shift from the raw RF signals. Experiments conducted using a simulated snowpack with

varying volumetric water content as well as results from deployment during a snowfall event are described in Section 2-4. Finally, a summary and analysis of the results are presented in Section 2-5.

2.2. Design of Sensor System

2.2.1. Design and Laboratory Physical Model

The current architecture of the WRF (Wireless Radio-Frequency) TX-RX sensor system relies on two basic elements: a dual antenna transmitter and a single-antenna receiver system. The sensors were fabricated using commercially available components from National Instruments (NI), smaller off-the-shelf parts from various vendors, and a special-order resonator from Vadum, Inc under contract with Duke University. The receiver system includes a Dedicated Data Channel receiver (DDC), and a central unit PXI chassis loaded with an RF pre-amplifier (NI 5690), a controller (NI 8196), a down-converter (NI 5600), and a vector signal analyzer (VSA, NI 5620). The sensor is designed to transmit CW (continuous wave) RF signals in the 1.00 -1.76 GHz range at 0.02 GHz intervals, corresponding to 39 independent channels, using a two-antenna broadcast system. The signal from the transmitter is directed for propagation in free air via an external antenna above the snowpack, and a second antenna directs the signal for propagation through the snowpack. Sensor operations are controlled by NI LabView™ software. The DDC receives data directly from the transmitter, and triggers the VSA to retrieve the RF CW data, including frequency and the identification of the antenna source. A detailed description of the transmitter system is provided by the block

diagram in Fig. 2-2. For each measurement, and at each frequency, a switch inside the microprocessor in the transmitter alternately directs the RF signal to the external (*e*) and internal (*i*) antennas during 1.5 ms according to a specified pattern (*e-i-e-i-i*). Because the RF signal at the receiver has high energy levels near 1 GHz, it needs to be modulated (converted from GHz to MHz) and sampled (digitized) in the Vector Signal Analyzer using the same center frequency f_c (4.0 MHz) and the same sampling frequency f_s (64.0 MHz) for all channels.

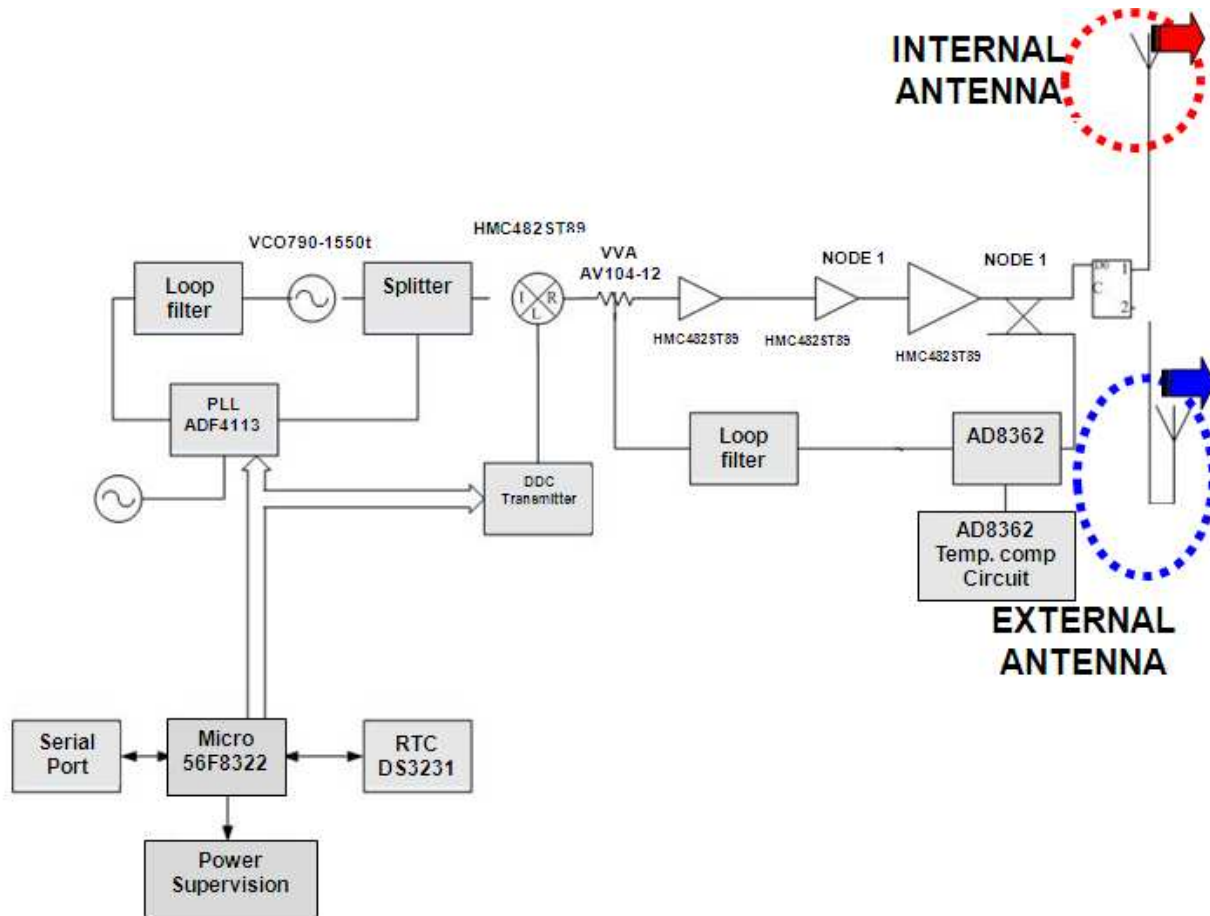


Figure 2-2 - Block diagram of the transmitter system fabricated by Vadum , Inc. for Duke University. Red and blue circles mark the internal and external antennas, respectively.

A physical model of the snowpack was built in the laboratory according to the measurement concept presented in Fig. 2-3. The internal transmitter antenna and two 12 V battery packs are stored inside a rugged box (orange box) along with the transmitter itself, and the external antenna was stored separately (yellow box) hanging above the experimental snowpack. The rugged impermeable boxes provide sensor packaging necessary to prevent the sensors operating in the natural environment from direct contact with water, wind, and dust. The performance of the batteries was tested for long durations to investigate whether there was an impact on the stability of signal power, and it was determined that this is not an issue in the current implementation of the design for periods as long as 9-months. This is sufficient to monitor seasonal snow accumulations on an annual basis, but it is still far from reaching the desirable multi-year capability.

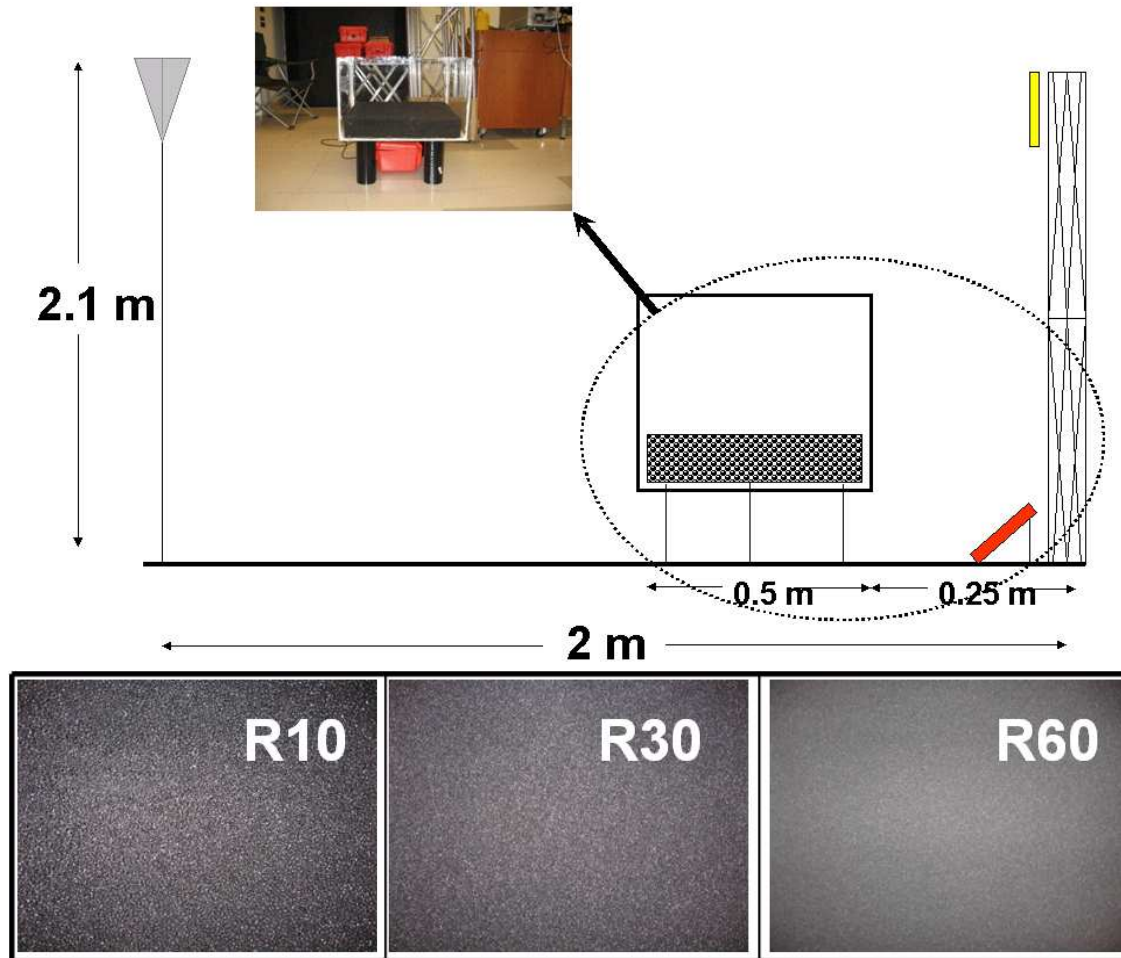


Figure 2-3– Physical model of the snowpack in the laboratory. R10, R30 and R60 refer to the porosity of the Regicell foam layers. A single layer foam is placed inside the plexiglass tank ($53 \times 53 \times 50 \text{ cm}^3$) shown above before pouring water.

At present, five replicates (T1, T2, T3, T4 and T5) of the sensor system were hand fabricated and tested independently. As mentioned previously, the snow wetness measurement principle relies on the relationship between the difference in the characteristics of the RF signal (amplitude and phase) propagating through air and through the snowpack as a function of frequency. In the laboratory, Regicell foam (a non-polar polymer) is used instead of dry snow structure which is composed of ice and air. Specifically, the snowpack is simulated by layers of foam of varying porosity (88%, 42 % and 7 % respectively for Regicell 10, 30 and 60 where the numerical index is the number of bubbles per inch³). To determine the background effect of Regicell itself on laboratory permittivity study, direct measurement of Regicell permittivity was conducted using HP Agilent permittivity probe (Agilent 850702). The probe was placed against a sample of foam and thirty independent measurements at randomly selected locations were made for each frequency. The average dielectric properties of the three different types of Regicell foam used in the laboratory experiments as a function of frequency are presented in Fig. 2-4: the real part of the dielectric constant (ϵ_{foam}') in Fig. 2-4a, and the loss tangent ($\tan \delta = \epsilon_{\text{foam}}'/\epsilon_{\text{foam}}''$) in Fig. 2-4b. The typical permittivity of plastic materials is from 2 to 5. Here, the expected permittivity of dry Regicell and air (permittivity near 1.0) should be between 1 and 2 near 1 GHz, and it should vary with frequency (dielectric dispersion) reflecting changes in dielectric relaxation mechanisms besides measurement errors [Blythe and Bloor 2005]. The real part of the dielectric constant (ϵ') varies between 1.28 and 1.64 at 1 GHz depending on foam density, and it

varies slowly up to 1.4 GHz. The loss tangent varies slowly between 0.4 and 0.6 in the 1-1.4 GHz range. The magnitude of the real part of the Regicell dielectric constant as a function of frequency $\epsilon_{\text{foam}}'(f)$ is of the same order of magnitude of the imaginary part, and 1-2 orders of magnitude lower than the real part of dry snow. Thus the foam layers act as a passive dielectric host to suspend different volumes of water (liquid water content) that represent varying snow wetness (liquid water content by volume). The rectangular area of the Plexiglas tank is 0.52×0.54 (0.2808) m². For R10, with porosity of 88%, 1.0 liter (0.001 m³) of water corresponds to approximately 4% of wetness (i.e. volumetric water content by volume, VWC = 4%). The experiments were conducted for wetness values up to 72% with stepwise increments of 2% (0.5 l of water). Even though the snow wetness range typically does not exceed 30 %, the aim of this experiment is to evaluate the RF responses against the water content up to the maximum value which can be retained the foam. This maximum outlier of snow wetness can be used to evaluate the case studies of liquid water effects on snow such as rain on snow, melting snowpack and maritime snow whose wetness usually much higher than continental snow. Each measurement condition was repeated a minimum of 30 and a maximum of 300 times for the lower frequency channels.

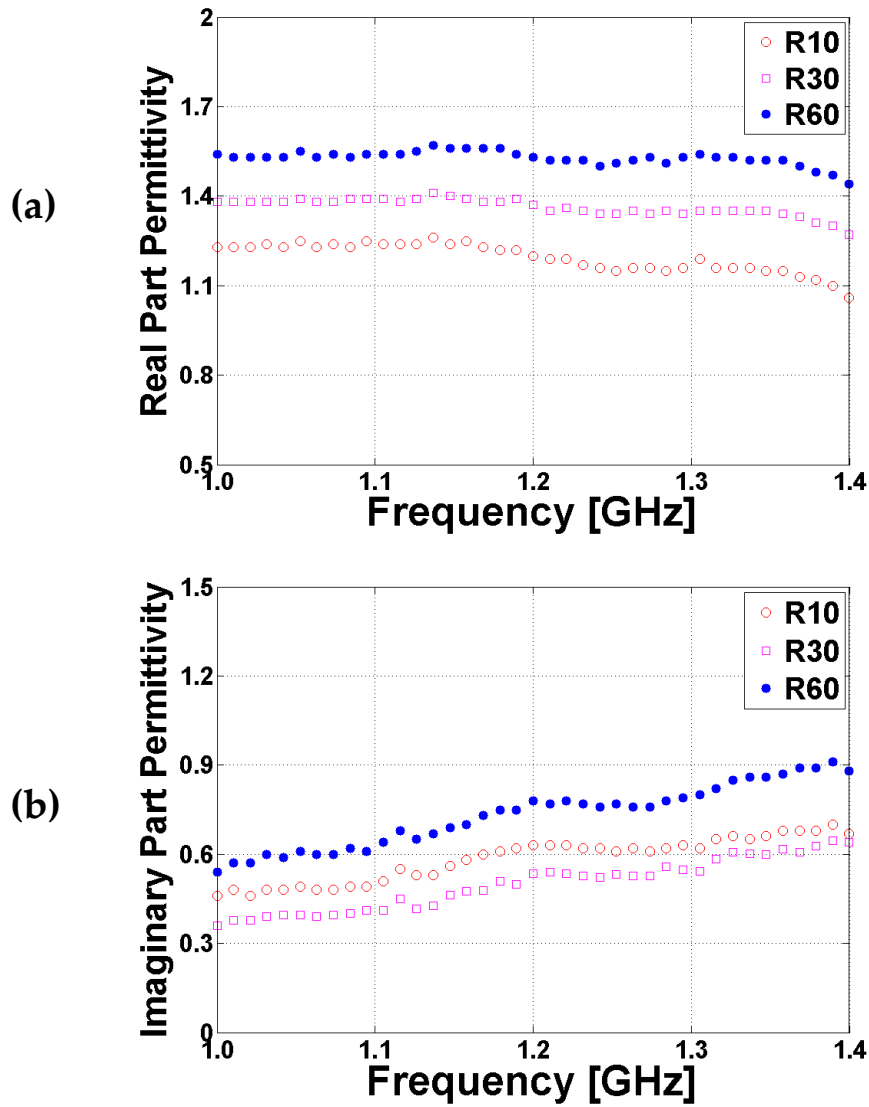


Figure 2-4 Dielectric properties of dry Regicell foam of different porosities (R10, R30 and R60). The dielectric properties were measured in the laboratory using an HP-Agilent 85070. a) real part of permittivity (ϵ'); b) loss tangent ($\tan \delta = \epsilon''/\epsilon'$). (Note: HP Agilent 85070 has intrinsic measurement errors at higher frequencies.)

2.2.2. Reliability Test of System Design and Fabrication

For system testing and to evaluate sensor-to-sensor performance variability due to fabrication (each sensor was hand fabricated), amplitude differences between the signal received from the internal and external antennas for each sensor were analyzed using 20 dB electric RFCW (RF Continuous Wave) attenuators to simulate the effect of an attenuating medium of known dielectric behavior. Following [Linlor 1980], the attenuation Δ (dB/cm) for frequencies $f \geq 4$ GHz is given by $[\Delta = W [0.045(f-4) + 0.066]$, where W is the snow wetness in percent, and assuming that for lower frequencies $\Delta \sim \text{const} = 0.066$ dB/cm, the 20 dB attenuation corresponds roughly to a layer of 1-1.50 m snow depth with 20-24% volumetric water content at 1 GHz. For practical reasons, the electric attenuators were connected to the external antenna. The objectives of this test were two-fold: 1) to characterize the frequency dependent behavior of each sensor; and 2) to characterize the degree of asymmetry in the transmission via the two antennas. Recall that the external antenna is connected to the TX by a cable, whereas the internal antenna is lodged in the same compartment with the battery pack and the TX. Thus, if the power attenuation Δ between the signal from the external and the internal antennas is larger than 20 dB, that is indicative of asymmetry in system losses: if $|\Delta| < -20$ dB, more power is lost in the propagation through the external antenna than through the internal antenna. If this asymmetry were to vary unpredictably with frequency, this would pose a problem in that it would be difficult to separate signal attenuation due to

frequency dependence in response to the presence of water from artificial frequency-dependent attenuation generated by the hardware, independently of the medium. The attenuation curves as a function of frequency are shown for 30 measurement sequences for all 39 channels and for T1 and T3 in Fig. 2-5. The measurements are remarkably similar from one sequence to another with little variations up to 1.4 GHz. For frequencies above 1.4 GHz, the attenuation magnitude for all sensors is excessively high doubling the 20 dB loss imposed by the attenuators. Therefore, the higher frequency channels ($f > 1.4$ GHz) are not expected to be useful for snow wetness and SWE retrieval, at least in the current hardware configuration. The performance of T1 up to 1.12 GHz (first 7 channels) is stable with an asymmetry of 5 dB, and we will rely on measurements from sensor T1 to illustrate system-testing results for the remainder of the manuscript. For the case of field testing or laboratory experiments using our replicates, this is not important as the system losses were characterized for each sensor separately, and therefore the necessary corrections are known, and further calibration is not required. Nevertheless, mass production of such sensors is required to achieve the numbers needed to achieve high spatial and temporal sampling. The different behavior among all five sensors T1-T5 illustrates the importance of standardization and quality control during fabrication for mass production to assure sensor reliability when operating under laboratory, and even more so under field conditions.

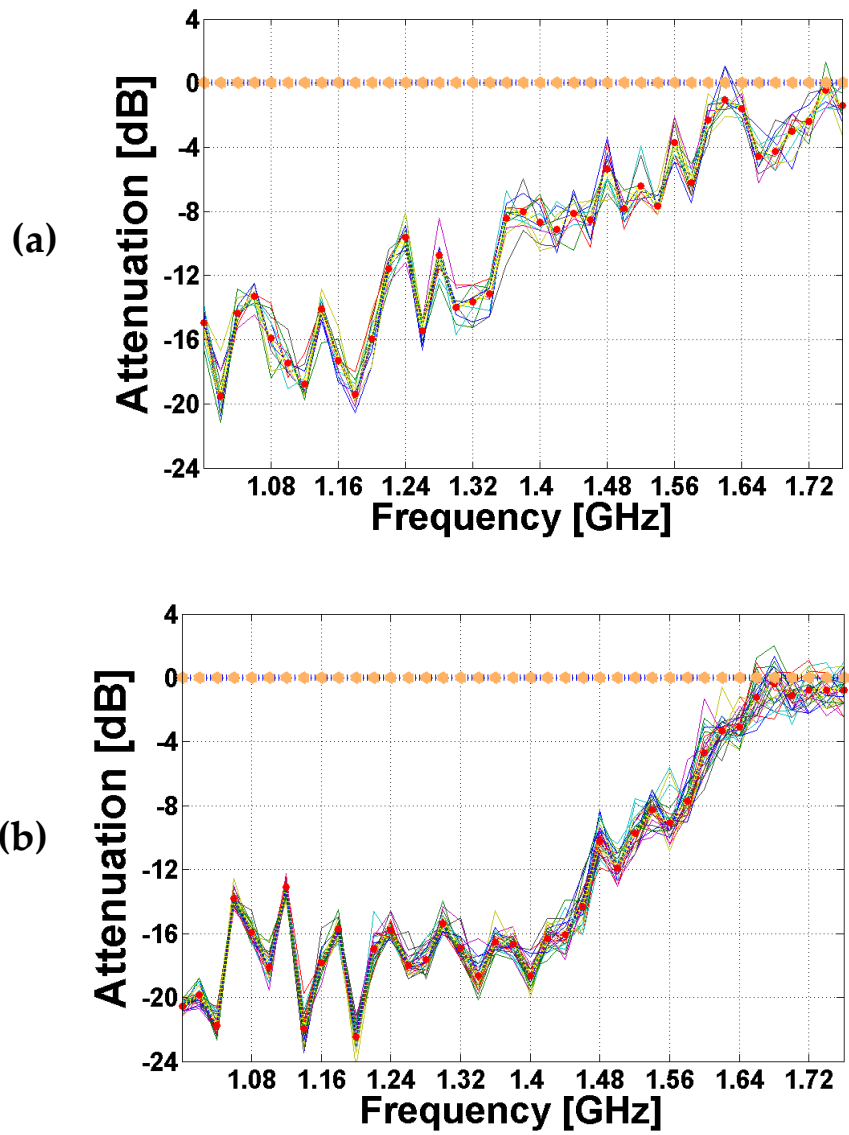


Figure 2-5 – Examples of voltage difference between the external and internal antenna with and without the 20 dB attenuators for two TX-RX systems: a) T1; b) T3. The results were obtained by conducting thirty replicate sequences of measurements for each system.

2.3. Methods on Data Collection and Processing

As outlined earlier, the measurement objective is to monitor the attenuation and relative phase shift between the RF signal that propagates through the snowpack and through the atmosphere as a function of frequency. Subsequently, the ratios of the amplitude of the two waves at the receiver can be used to determine complex permittivity and conductivity of the simulated snowpack ([Sweeny and Colbeck 1974], [Hallikainen et al. 1986]). Subsequently, the volumetric liquid water content (snow wetness) and snow density can be estimated from these measurements ([Ambach and Denoth 1980], [Kuroiwa, 1954], [Tiuri et al. 1984], [Hallikainen et al. 1986], and [Lundberg et al. 2000b]). Alternatively, direct relationships between the detected attenuation and phase shift from sensor calibration can be used to infer liquid water content.

The measurement protocol consists of collecting a minimum of 30 samples at each measurement time. The RF attenuation at each frequency is calculated by the amplitude difference (in Volts) between the signal transmitted by the external antenna that propagates through air alone (V_a) and the signal transmitted by the internal antenna that is directed to propagate through the simulated snowpack (V_s). The left two panels of Fig. 2-6 show an example of T1 data in the time domain for two distinct conditions: Fig. 2-6a – RF signal from both external and internal antennas propagating through a 10 cm thick dry layer (VWC= 0%) of R10 foam; Fig. 2-6c – RF signal from the lower antenna is directed to an R10 layer with the same geometry as Fig 2-6a. after

adding liquid water corresponding to 12% wetness (VWC=12%). The amplitude attenuation (amplitude change) due to the medium (R10 layer + water) above the internal antenna is calculated from the difference between the magnitude of the amplitudes marked with the arrows in both plots. In order to determine the amplitude change, the histogram of each packet of raw data is calculated to obtain the indices of the smaller and larger peaks. Due to the presence of water, the X index of the Vs peak corresponding to a lower potential energy class in the histogram is lower than that of Vd (68 and 87 respectively) as expected.

For determining the relative phase shift, the external and internal antenna signals are multiplied in the frequency domain as follows: (1) take Vd and N samples of Vs and calculate their Fourier Transforms (FT); (2) multiply the FT of Vd by each of the conjugates of the N Vs samples and add them together to obtain the overall summation; and (3) extract the angle of the signal corresponding to the final product summation. Conceptually, the relative phase angle should be constant for all frequencies because for each packet the frequency modulated signals are centered at 4 MHz, and the only source of asymmetry is the propagation through the simulated snow layer. In practice, however, the phase angle varies with the sampling frequency due to noise.

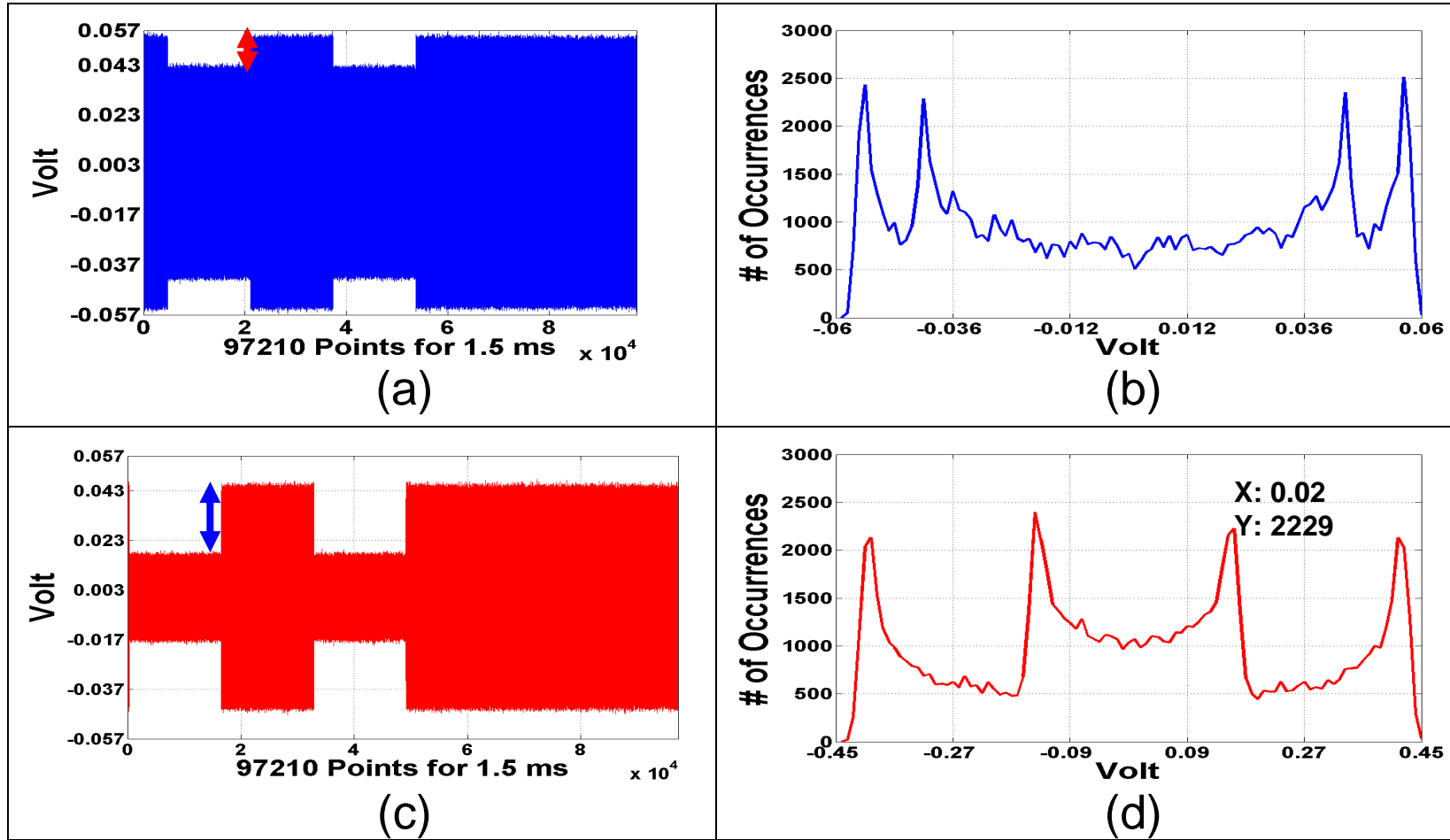


Figure 2-6 - Raw data and corresponding histogram for dry Regicell (R10) conditions (a) raw, b) histogram) and in the presence of 12 % of volumetric water content (c) raw, d) histogram), at 1.02 GHz. The (x,y) indices in the right-hand panel are (0.0296 Volt,2351) and (0.0163 Volt,2229) respectively for dry and wet Regicell conditions. The lower potential energy from the internal antenna when water is present is reflected in the lower index value.

The algorithm is illustrated in Figure 2-7 for the two signals V_d and V_s shown in Fig. 2-6 for R10 and VWC=12% at 1.02 GHz. The frequency range (-32MHz, 32MHz) is determined by half of the sampling frequency, 64.0 MHz. In the first step, the Fast Fourier Transforms (FFTs) of both signals are calculated, and the FFT of V_d (Fig. 2-7a) is multiplied by the conjugate of the FFT of V_s (Fig. 2-7b). Figures 2-7c and 7d show respectively the magnitude and phase angle of the summation product. In the frequency domain, the dotted blue square in Fig. 2-7d indicates the region (0-10 MHz) used to estimate the mean phase angle. In theory, the convolution of two signals with the same center frequency should yield a constant phase angle along all frequency ranges. Nevertheless, note the presence of noise throughout, even at lower frequencies. To reduce noise, the FFT products for several samples can be summed. Figure 2-7e shows much improved results when $N=30$ samples were used corresponding to an average angle close to 2.0 rad. Higher number of samples should lead to even better results. However, ultimately, a balance needs to be struck between system requirements, specifically increased power usage as the number of samples increases, and the number of samples required for substantial noise reduction.

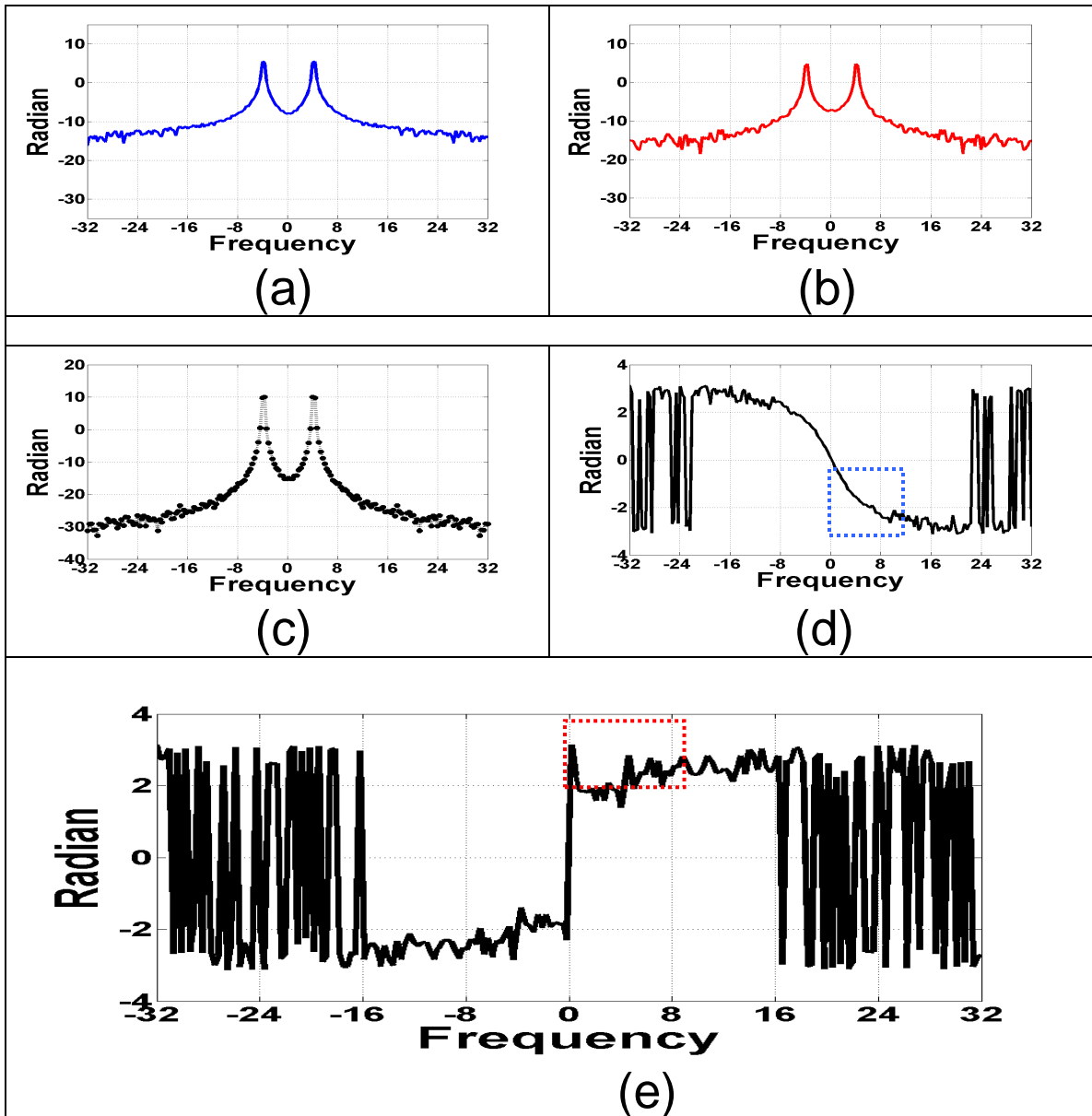


Figure 2-7– Algorithm to extract attenuation and phase difference between the signal from dry Regicell 10 (Fig. 2-6a) and the signal when Regicell is moist with 12 % VWC (Fig. 2-6c) at 1.02 GHz, respectively: (a) and (b) FFT; (c) and (d) are magnitude and phase angle of multiplication of (a) and conjugate of (b). Finally, (e) is calculated by summing all 30 replicates (d). The final value of the relative phase-shift is determined by a moving-window algorithm to identify the most stable value within ± 0.5 rad in the interval [0,10MHz].

2.4. Results of System Testing

2.4.1. Laboratory Conditions

As described earlier, the Regicell foam layers were impregnated with various amounts of water corresponding to a range of volumetric water content (VWC) varying between 0 and 72% with increments of 2%. This range of VWC permits testing for conditions similar to rain-on-snow events and during the melting phase of the snowpack. Care was taken to avoid the total reflection of the RF waves in the sensor setup by maintaining the angle between the RF wave direction of propagation and the horizontal water level above the critical angle. For each VWC condition, thirty distinct measurements were made at each time. The batteries were always fully charged during the observation period. There are two potential ways to analyze the amplitude data, which are relevant for different operating conditions. In a laboratory setting, where the environmental conditions are maintained fixed, the amplitude attenuation ratio ΔA between dry and wet conditions as a function of VWC can be estimated as follows: $\Delta A(\text{VWC}) = 20 \times \log_{10} [V_s(\text{VWC})/V_d]$. In field conditions, where the state of the atmosphere can vary widely, it is important to account for changes in the relative amplitude attenuation A_r of the signals emitted by the external and internal antennas at the same time t : $A_r(\text{VWC}, t) = 20 \times \log_{10} [V_s(\text{VWC}, t)/V_a(t)]$. Another potential source of variability besides weather is that of the geometry and physical lay-out of the environment which can have important implications for non-random multi-path propagation that can affect the interpretation and attribution of changes in the observed

signal. This can be addressed by collecting data prior to snow accumulation to characterize the background environment.

Results of ΔA and A_r from T1 measurements under laboratory conditions are presented in Figs. 2-8 and 9 for three selected frequencies (1.0, 1.02, and 1.04 GHz). The overall oscillatory pattern of the attenuation as a function of wetness is consistent with the expected behavior of propagation through layered media ([Linlor 1980], [Hallikainen et al. 1986]) due to multiple reflections (air, water, and foam interfaces). This phenomenon is illustrated in Figure 2-10 for the propagation of a planar electromagnetic wave through a layer of water of semi-infinite extent between two layers of air. The transmitted power R_{TX} is attenuated to P_{RX} at the receiver according to the following Equation:

$$P_{RX} = R_{TX} \cdot \Gamma_{eff} \cdot \eta \quad (2-1)$$

where the transmission coefficient Γ_{eff} is a function of permittivity, and η is the Friis factor for free space attenuation: $\eta = \left(\frac{f 4\pi d}{c} \right)^{-1}$. Γ_{eff} is determined by using the impedances of air and water and the propagation constant depends on the complex permittivity and conductance [Inan and Inan 2000] where f is the frequency in Hz, c is the speed of light in m/s, and d is the thickness of the water layer. Γ_{eff} also exhibits oscillatory behavior. Due to the geometry of the laboratory set-up, with the largest dimension of the tank (53 cm) larger than the wavelength of the lower frequency (30 cm), the cutoff resonance frequency is 0.57 GHz for the dominant longitudinal mode

[Dixon 2005], and therefore some frequency-dependent behavior should be expected (e.g. compare Figs. 2-8 and 9). Such cavity resonance effects could be small for the typical snowpack under field conditions due to the lack of reflective boundaries, although heterogeneities such as ice layers may pose a problem. Note that at 1 GHz, the question of penetration depth δ (e-folding attenuation depth, [Griffiths 1999]) is not an issue for the laboratory set-up nor for typical snowpack conditions [Sturm et al. 1995]:

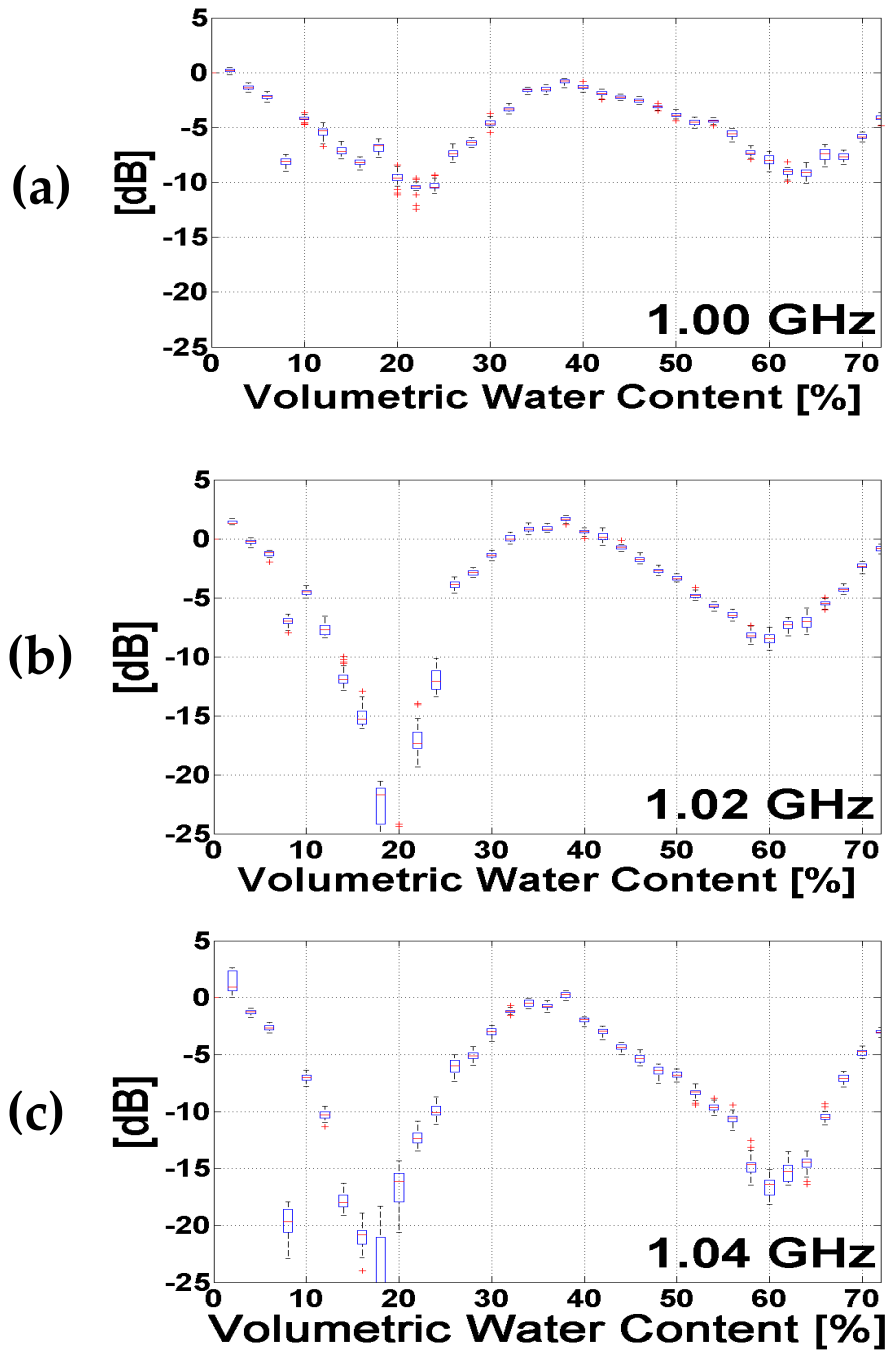


Figure 2-8– Laboratory results expressed in terms of ΔA using T1 and Regicell 10 as a function of volumetric water content (VWC). (a) 1GHz, b) 1.02 GHz, c) 1.04 GHz)

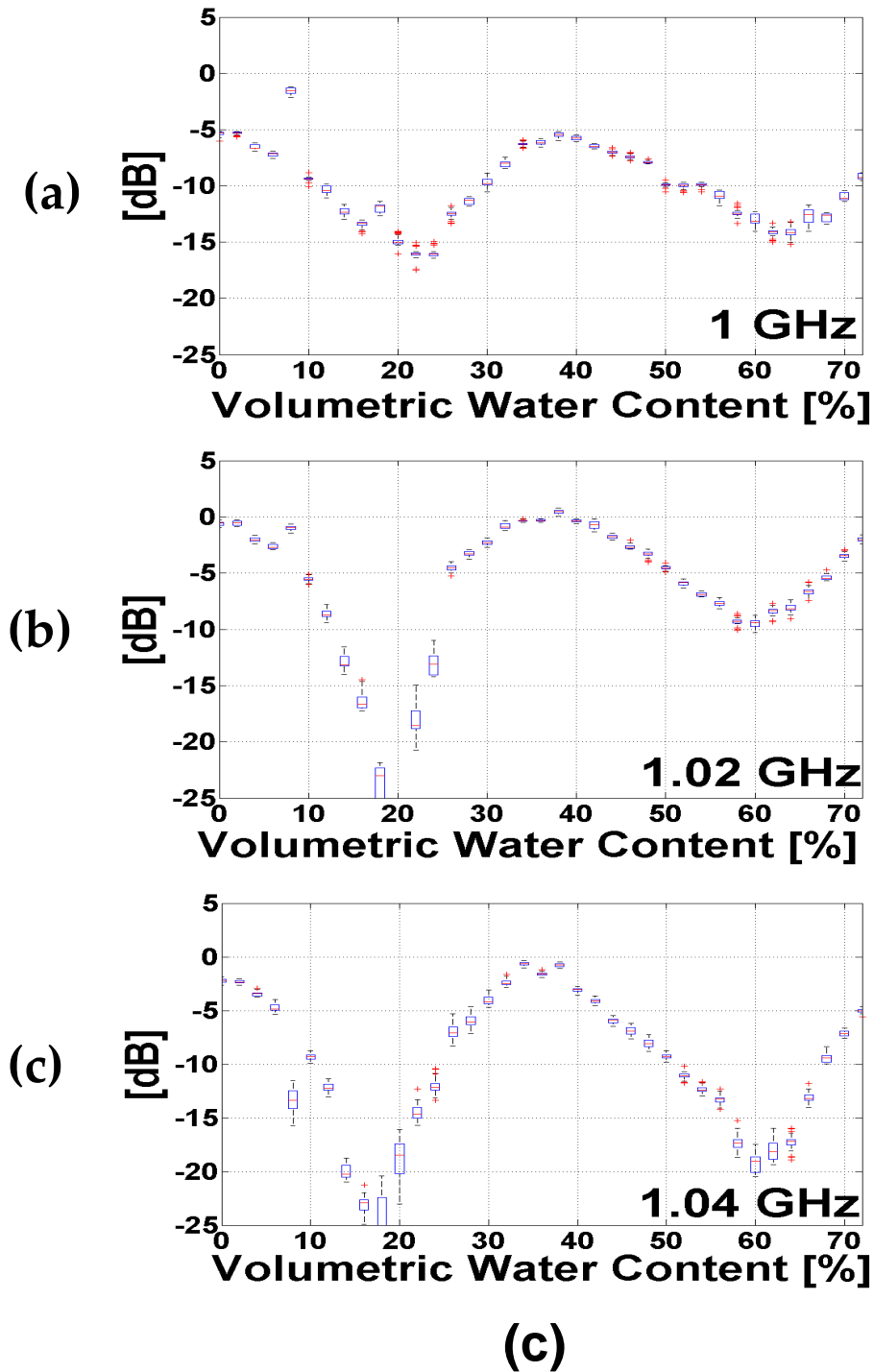
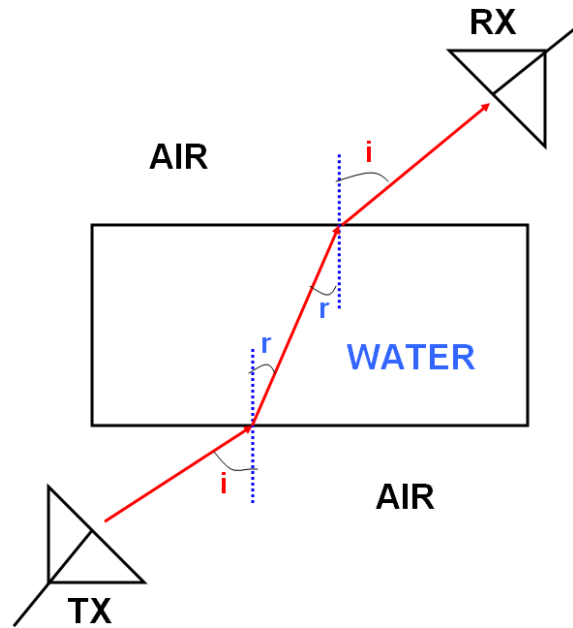


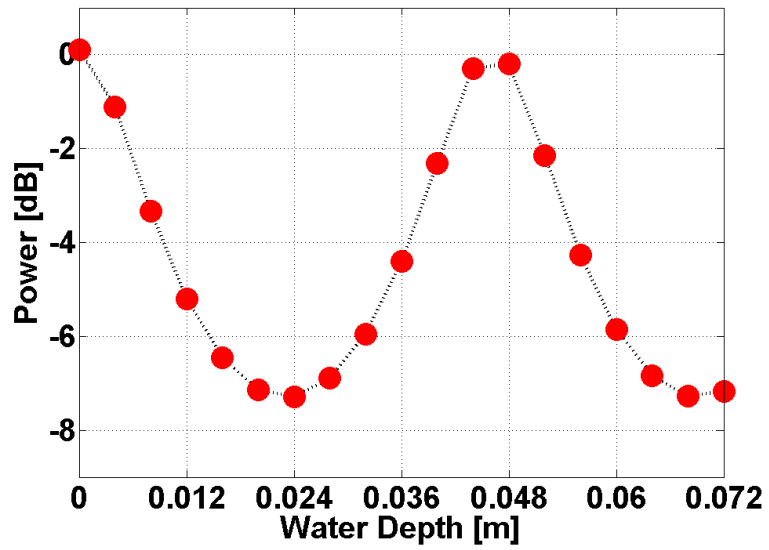
Figure 2-9 - Laboratory results expressed in terms of Ar using T1 and Regicell 10 as a function of volumetric water content (VWC). (a) 1GHz, b) 1.02 GHz, c) 1.04 GHz

$$\delta = \left(\omega \sqrt{\frac{\mu \varepsilon'}{2} \left(\sqrt{1 + \left(\frac{\varepsilon''}{\varepsilon'} \right)^2} - 1 \right)} \right)^{-1} \quad (2-2)$$

where ω is the angular velocity as $2 \pi f$ [1/sec], ε' is the real part of permittivity, ε'' is the imaginary part of permittivity, and μ is the electric permeability as $4 \pi 10^{-7}$ [H/m]. The magnitude of penetration depth varies from tenths of centimeters for wet snow (~28 cm in the laboratory tests) to meters for very dry snow conditions [Schanada and Mätzler 1981] whose setup and amplitude responses are illustrated in Figure 2-10 (a) and (b).



(a)



(b)

Figure 2-10– Schematic setup for wave propagation calculation using transmission coefficient [Hallikainen et al. 1986] and F_{riis} factor (a) and Calculated power at the receiver (b).

Figures 2-8 and 9 show an unambiguous relationship between attenuation for both ΔA and A_r and wetness up to 24% VWC, which represents a substantial improvement for sensitivity to liquid water content as compared to previous sensors (e.g. 5%, [Tiuri et al. 1984], [Kendra et al. 1994]) including ground penetrating radar experiments ([Granlund et al. 2009], [Lundberg et al. 2000], [Lundberg et al. 2000b]). Also, since [Gubler and Hiller 1984], specifically, frequency modulated continuous wave radar (FMCW) has been used and applied to many field campaigns [Marshall and Koh 2008] [Bradford et al. 2009]. At volumetric water content of 6-8 % depending on frequency, the attenuation loss is significantly larger (smaller) than preceding and posterior values. This results from the formation of water clusters, filets and veins that form due to the microstructure of the Regicell foam. Similar behavior associated with clustering and heterogeneities of wet snow at the micro-scale was reported earlier by [Ambach and Denoth 1980] and [Colbeck 1979]. Table 2-1 summarizes the attenuation slope for the three frequencies shown in Figs. 2-8 and 9, suggesting that it should be possible to use the data directly to monitor the temporal evolution of the water content of standing water lenses, ice or snow up to an accumulation of 30-40 cm of fresh snow. For VWC > 24%, there is ambiguity due to the oscillatory nature of the transmission coefficient (i.e. the same attenuation is measured for different values of liquid water content). To address this challenge, one may rely on time-tracking algorithms that monitor the attenuation as a function of time to be compared against meteorological

data for interpretation and, or rely on multi-frequency composites to reduce ambiguity as proposed by [Tiuri et al. 1978] and [Tiuri et al. 1984].

The relative phase shift information (Fig.2-11) can be used along with amplitude response to determine the complex permittivity using complex transmission coefficients [Hallikainen et al. 1986]. Although the graphs suggest a linear relationship over a limited range of VWC, there is significantly less independent phase-shift information as compared to amplitude attenuation even at 1 GHz, and this gets worse with increasing frequency. Nevertheless, this information could provide a valuable additional constraint in retrieval to reduce ambiguity both in the case of very shallow snow accumulation, and in the case of resonance effects.

Table 2-1 Attenuation Slope [0< VWC< 24%] and [0<LWE< 22 mm]

ΔA	Frequency	Slope	Slope [dB/ %VWC]	R ²
	[GHz]	[dB/ mm LWE]		
	1.00	-0.501	-0.442	0.86
	1.02	-1.964	-1.675	0.80
1.04	-0.845	-0.875	0.71	
A_r	Frequency	Slope	Slope [dB/ %VWC]	R ²
	[GHz]	[dB/ mm LWE]		
	1.00	-0.506	-0.438	0.80
	1.02	-1.917	-1.716	0.77
1.04	-1.001	-0.738	0.88	

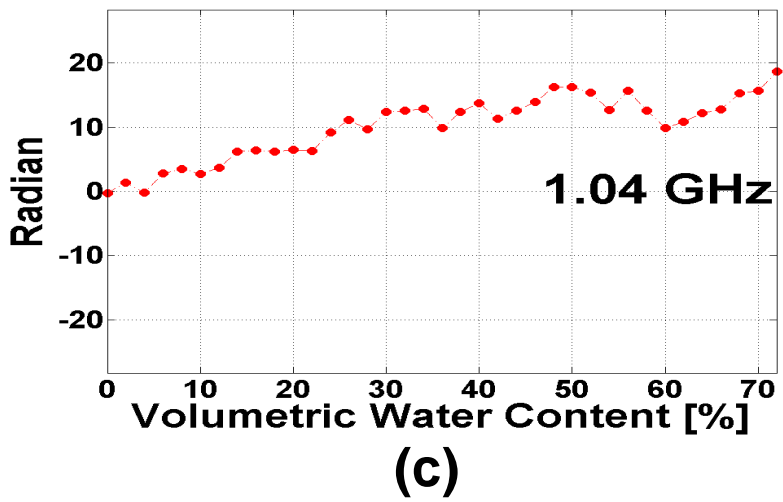
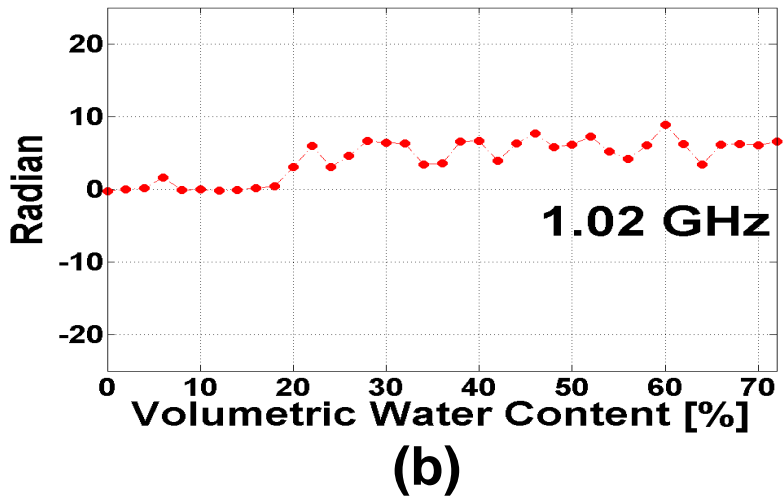
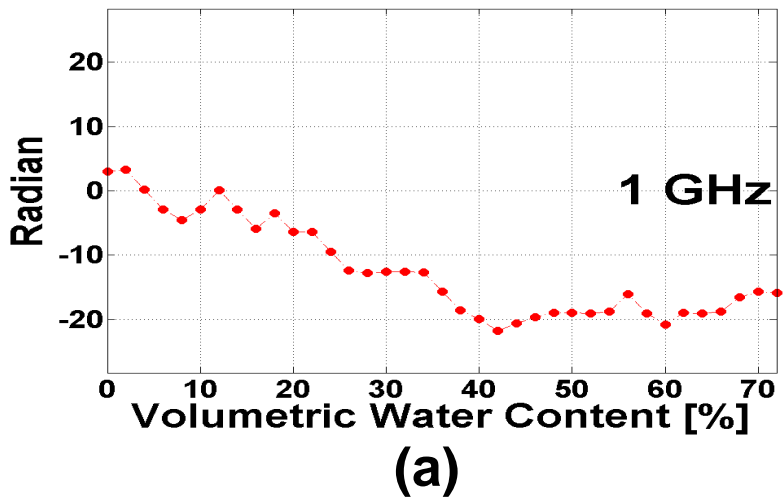


Figure 2-11– Unwrapped phase shift measurements using TY1 and Regicell 10 as a function of volumetric water content (VWC). (a) 1GHz, b) 1.02 GHz, c) 1.04 GHz)

2.4.2. Field Measurements During Snowfall

On January 19-20, a major snowfall crossed North Carolina producing roughly 6 cm of snow accumulation at the Raleigh-Durham International Airport (RDU, Fig.2-12). During the first hours of the snowfall, before midnight on January 19, the precipitation was in the form of rain. After midnight, on January 20, there were two distinct episodes of snowfall – identified as (1) and (2) in Fig. 2-12: the first episode took place during early morning hours, and the second episode by the end of the morning on January 20th. The sensors were placed outside of the engineering building buried in a flat area, with the RX and TX located roughly 4 m apart from each other. Measurements were made throughout the night and morning including during snowfall. The set-up was not the same as one envisions for operational conditions (Fig.2-1) in terms of being able to make automatic measurements at pre-specified intervals. Instead, each sequence of 30 measurements was prompted manually when snowfall conditions allowed (e.g. calm winds).

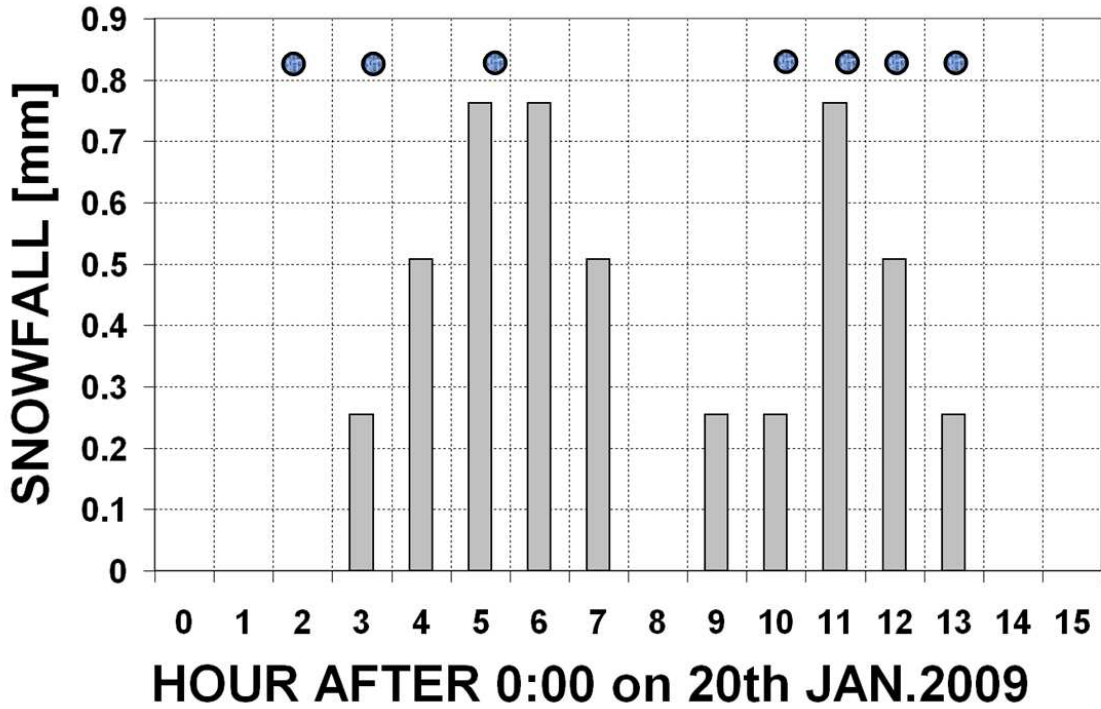


Figure 2-12- Snowfall intensity on January, 19 2009 storm in North Carolina. Two distinct episodes of snowfall can be identified corresponding to significantly different intensity rates. There was intermittent rainfall at the beginning of the storm and in-between snowfall episodes. Blue circles in the top panel indicate measurement times on January 20, 2009, respectively from left to right: 2:20, 3:50, 5:50, 10:50, 11:40 AM and 12:30 and 1:30 PM.

Figure 2-13 shows an inter-comparison of field measurements at 1 GHz against laboratory measurements at the same frequency. Field measurements at other frequencies are shown in Fig. 2-14. Note that the observations are expressed in terms of SWE (mm) instead of snow wetness (%). SWE and snow depth are the two standard measurements of snow reported in the meteorological and hydrological records. It is not possible to measure snow wetness in field conditions using standard hydrometeorological data collection procedures and technology [Derksen et al. 2009]. During the snowfall event at Duke, SWE was obtained from melting completely samples of the accumulated snow layer and from records at the Raleigh-Durham Airport (RDU). Because the total snow accumulation was very small, and the snow was very wet with intermittent rainfall both at the beginning and during the snowstorm (in-between snow episodes, Fig.2-12) the difference between the magnitude of SWE and snow wetness by volume should be very small also [Sturm et al. 1995]. Therefore, we compare attenuation under field conditions during the snowfall event with the results obtained in the laboratory. We rely on the RDU measurements as an indicator of snowfall accumulation (x-axis in Figs. 2-13 and 14). Based on site-based measurements of bulk snow density (150.0 kg/m^3) and SWE (6 mm) at the end of the second episode, the upper limit of the uncertainty could be on the order of $\pm 1 \text{ mm}$ or higher (i.e. $\sim 15\text{-}20\%$) during the snow event, and $< 0.5 \text{ mm}$ ($< 10\%$) for the overall accumulation at the end of the snow event.

There is close agreement between ΔA and A_r evolution at 1 GHz between the beginning of snowfall and the end of the snow event, and the corresponding gain in liquid water equivalent in the field and in the laboratory as shown in Fig. 2-13. Similar results can also be inferred by applying the attenuation slopes reported in Table 2-1 to the return loss reported in Fig. 2-13 and 14 for the appropriate frequencies. At the two lowest frequencies, 1 and 1.02 GHz, the measurements are sensitive to snowfall conditions in the atmosphere, and it is possible to clearly distinguish the first from the second snowfall events with stronger response in the second snow event) as the return difference between external and internal antennas is expected to decrease with the density of the atmospheric medium, that is snowfall intensity. The changes between the last two measurements are attributed to the rapid changes in environmental conditions (wind speed and air temperature and relative humidity, Fig. 2-13) during the second snow episode. Finally, whereas these field observations demonstrate the potential utility of the proposed sensor under realistic environmental conditions, there is the need for comprehensive testing under a wide range of snow accumulation conditions and for long periods of time including effects of snow metamorphosis.

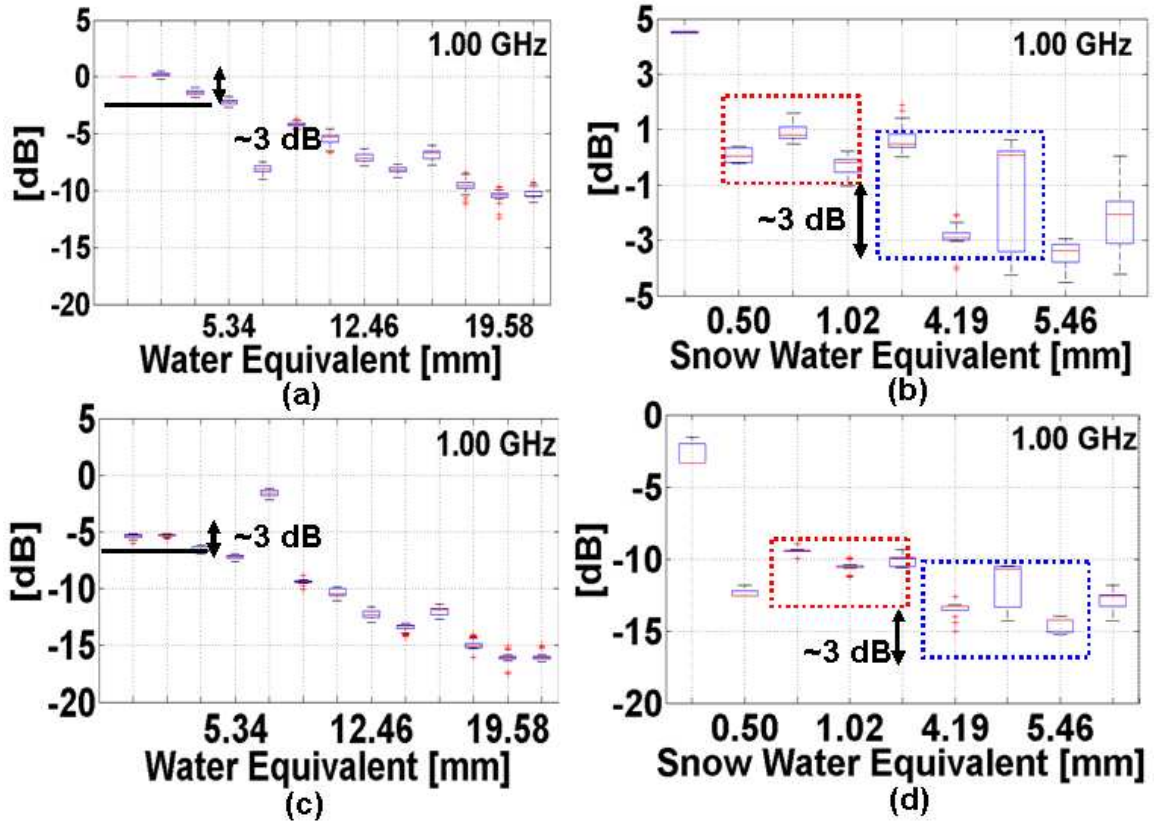


Figure 2-13– Intercomparison of measurements using T1 under laboratory and under field conditions (Jan. 19th 2009) at 1GHz for both attenuation cases ΔA (a) lab, b) field) and A_r (c) lab, d) field). Since initial conditions are very different, only the changes in attenuation difference between initial and final conditions (~ 3 dB) can be compared.

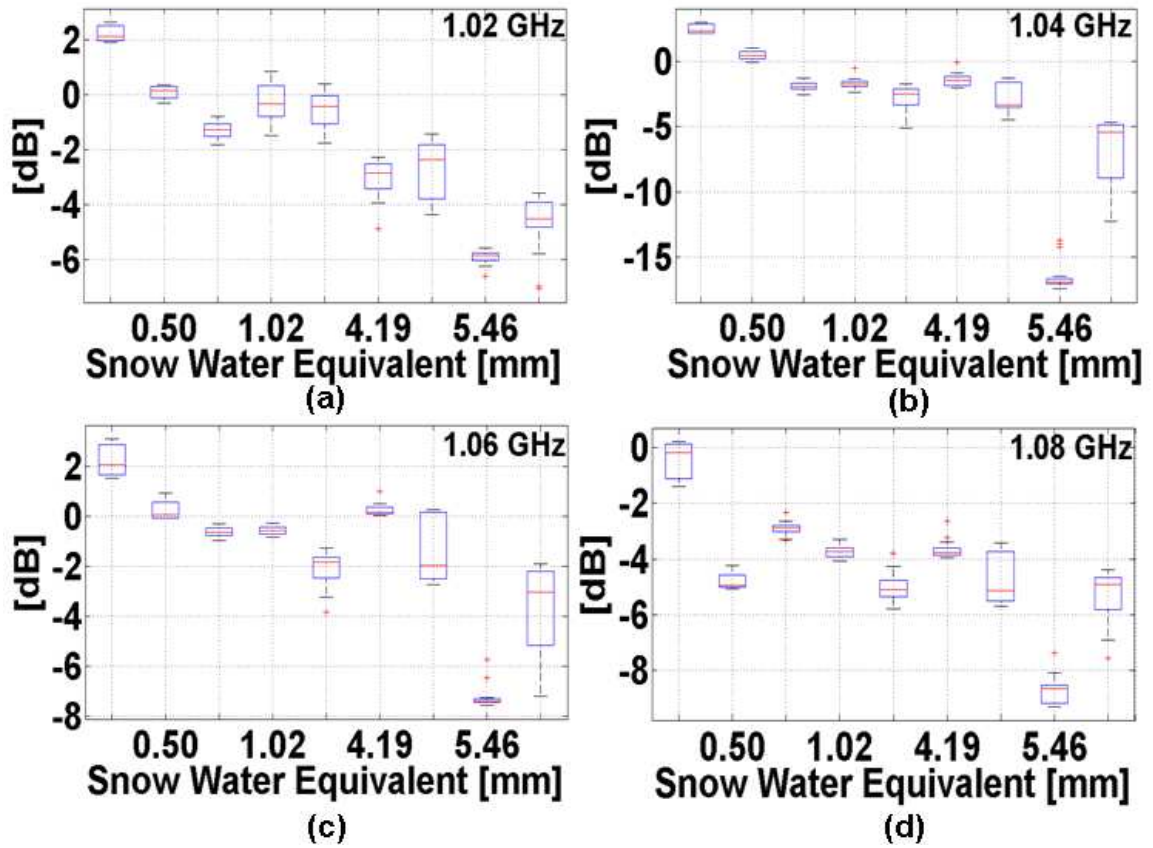


Figure 2-14- Field measurements of amplitudes at various frequencies using T1 during the snow storm of January 19-20, 2009. (a) 1.02 GHz, b) 1.04 GHz, c) 1.06 GHz, d) 1.08 GHz)

2.5. Conclusions

A new L-band TX-RX wireless system of sensors to monitor snow accumulation, snow wetness and snow water equivalent was designed, fabricated, and tested under laboratory conditions. The sensor was developed in the context of a broader effort aimed at designing new low-cost, small-size sensors (motes) for measuring and monitoring snowpack properties in remote mountainous regions. The L-band sensor can be deployed in remote and rugged terrain to operate in the framework of dense, self-organizing, wireless networks to monitor snow permittivity which can be related to wetness and snow density directly, which in turn can subsequently be used to estimate SWE over large areas with a given snow depth. Under the space and geometry limitations of the laboratory set-up, the data show that the sensors perform well for snow wetness measured in terms of liquid water content at least up to 24%. It is expected that this upper bound would be increased by using multi-frequency composites to unravel the ambiguity of oscillatory patterns at higher VWC values [e.g. 30]. Results from deployment of the sensors during a snowfall in January 2009 also suggest that the sensors exhibit sensitivity to variations in real snow content that could be used as snow/ice gauges in operational networks. This implies that the L band sensor can be applied into intelligent road-weather sensing networks along major highways, and in urban settings even with considering operational limits. Nevertheless, further work must continue with regard to developing a retrieval algorithm that could be used to estimate the dielectric properties of the snowpack using amplitude and relative phase

shift from the RF signals under heterogeneous and transient field conditions (evolving grain size, density, layering, varying depth, and snow chemistry). Robust validation under field conditions and for long periods of time at several locations, at least one snow season is also required.

CHAPTER 3:
**An evaluation of a coupled snow hydrology and microwave emission
model for data-sparse regions**

3.1. Introduction

Snowfall, snow accumulation and snow cover extent vary with weather and climate regime, continental vs. marine environments, land-cover and land-use, and landform and elevation. Where present, snow cover controls the terrestrial energy budget in the cold season, and snowmelt available for infiltration and runoff in the warm season governs the water budget of large regions [NRC 2007]. Approaches to monitor snow accumulation include in-situ measurements, passive/active remote sensing, and operational systems combining snow hydrology, snow microphysics, radiative transfer and data-assimilation that integrate models and observations. Ground-based, in-situ snowpack observations have relied traditionally on direct physical measurements from snow pit, snow pillows, and snow cores [Pomeroy and Gray 1995]. Recently, new instrumentation has been introduced to monitor snow cover and snow water content indirectly without disturbing the snowpack such as TDR (time domain reflectometry, [Lundberg 1997], ground penetrating radar ([Granlund et al. 2009], [Lundberg et al. 2000a and 2000b]), and active L-band sensors [Kang and Barros 2010^a]. Whereas the integration of TDR and L-band sensors into wireless networks anticipates the possibility of ground-based sensing at high spatial resolution, satellite-based remote sensing is necessary in order to cover large continental areas and for the long-time scales needed for climate research and for water resources applications.

Satellite-based passive remote sensors particularly apt for the retrieval of snow states are the Scanning Multi-channel Microwave Radiometer (*SMMR*, 1979-1987),

the Special Sensor Microwave Imager (SSM/I, 1987-present), and more recently the AMSR-E (Advanced Microwave Scanning Radiometer-EOS) operating at frequencies centered in the 18-19, 21-22 and 36-37 GHz ranges. Snow cover, snow depth, snow wetness estimated (retrieved) from SMMR, SSM/I and AMSR-E observations have been widely used to characterize northern hemisphere snow cover [Foster et al. 1997, Armstrong and Brodzik 2001, Kelly et al. 2003, Markus et al 2006, among many others]. Generally, retrieval algorithms can be divided in two major classes: 1) empirical algorithms (e.g Chang et al . 1987); and 2) physically-based algorithms, or microwave emission simulators, that consist of radiative transfer models coupled to an optimal estimation algorithm to derive snow states from observed brightness temperatures at specific frequencies (e.g. Kummerow et al. 2001). Prominent radiative transfer models for snow retrievals include the Helsinki University of Technology Radiative Transfer Model (HUT) [Hallikainen et al. 1997, Lemmetyinen et al. 2010], the Dense Media Radiative Transfer model (DMRT) [Tsang et al. 2000]; and the microwave emission model for multi-layer snowpack (MEMLS) [Wiesmann and Mätzler 1999, Mätzler and Wiesman 1999]. These models have been evaluated against field observations either independently [e.g. Tedesco et al. 2008] or integrated with various snow hydrology models operating at the field scale [e.g. Durand et al. 2008, Andreadis et al. 2008, Wójcik et al. 2008 among others] in the context of dedicated field campaigns such as CLPX [Cold Land Process Field Experiment, Cline et al. 2003].

Building on previous work, the goal of the research presented here is to establish a modeling framework for simulating snow water equivalent and snow microwave emissions transferable across remote cold regions where ancillary data and ground-based observations are lacking, and thus where model or algorithm calibration, and independent evaluation of data assimilation systems are not viable. Operationally, such framework can either be used as a prediction system or to support physically-based retrieval algorithms. For this purpose, we rely on a coupled snow hydrology-emission modeling system that links an existing hydrology model, the Land Surface Hydrology Model (LSHM) [Devonec and Barros 2002] to MEMLS. The coupled model is evaluated in two stages. In this chapter, the coupled LSHM-MEMLS retains the single-layer snow hydrology parameterization described by Devonec and Barros [2002]. In the next chapter, the single-layer snow hydrology model is adapted to a multi-layer formulation. Two case-studies for very different climatic and physiographic regions were conducted to evaluate the coupled single-layer hydrology-emission model: 1) an intercomparison of a multi-year simulation of snowpack microwave behavior at Valdai, Russia, against Scanning Multi-channel Microwave Radiometer (SMMR) observations at three frequencies (18, 21, and 37 GHz, H and V polarizations) for a six year period, 1978-1983 (Fig. 3-1); and 2) an inter-comparison against SSM/I (Special Sensor Microwave Imager, 19.35, 22.235, and 37.0 GHz H and V polarizations) and AMSR-E (Advanced Microwave Scanning Radiometer-EOS, 18.7, 23.8, and 36.5 GHz H and V polarizations) in Colorado during the 2002-2003 snow season as part of CLPX (Cold Land Processes Field

Experiment, Fig. 3-2). The motivation to select the Valdai case-study was two-fold: i) previously the snow hydrology in the LSHM was successfully evaluated for a 16-year simulation from 1966 to 1983 using PILPS [Project for the Intercomparison of Land Surface Schemes] data sets and without calibration [Devonec and Barros 2002], and ii) Valdai can be viewed as typical of remote sites where limited ground-based ancillary data are available to force and constrain the hydrology model (LSHM). The CLPX case-study provides a means to evaluate the skill of the coupled LSHM-MEMLS model against a comprehensive data-base of ground observations at meso- and point scales.

The chapter is organized as follows. The coupled LSHM-MEMLS modeling system is described in Section 3-2. Section 3-3 presents an overview of all data sets including satellite observations, initial conditions and forcing data for the surface hydrology model, and data used for the atmospheric attenuation correction algorithm used in Valdai. The results for each case-study are analyzed in detail and discussed in Section 3-4 for Valdai and in Section 3-5 for CLPX. Section 3-6 summarizes the research and provides an overview of major results and conclusions.

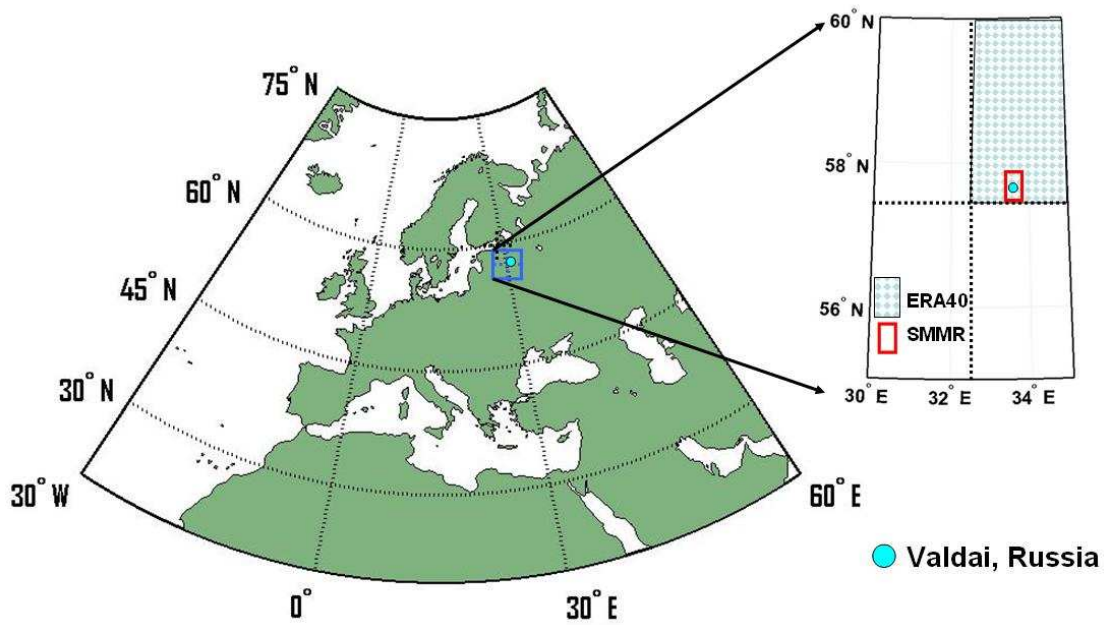


Figure 3-1 Schematic view of grid resolutions of *ERA40* (2.5 °) and *SMMR* (0.25 °) located in Valdai, Russia

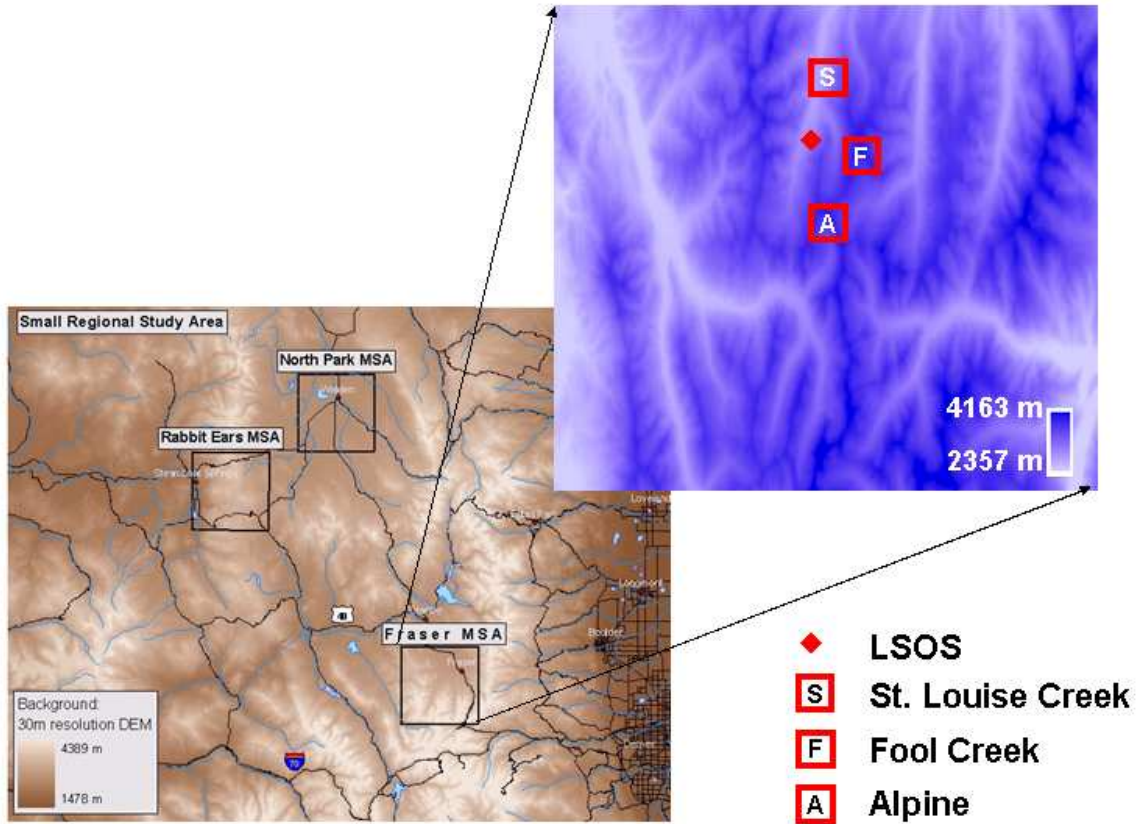


Figure 3-2 Small Regional Study Area for CLPX 2002 including our application site, the Fraser MSA, (meso cell study area) [http://nsidc.org/data/docs/daac/nsidc0173_clpx_ISA_corner_met/ http://nsidc.org/data/clpx/clpx_pits.html]. The GBMR-7 (Ground Based Passive Microwave Radiometer-7) is located in the Local Scale Observation Station, LSOS in Fraser MSA above).

3.2. Model Description

A flow chart showing the LSHM-MEMLS structure is shown in Fig. 3-3. The *LSHM* simulates snowpack liquid water content (*LWC* in percent), snow depth, h_{sd} (m), snow density, ρ_s (kg/m³), snow temperature T_s (K), and the correlation length, p_{cc} (m) that is used to represent the snow grain size distribution effects that modulate snowpack volume scattering in MEMLS. To include the atmospheric effects on the microwave emission from the snowpack, the optical depth, τ of the atmosphere is parameterized based on atmospheric moisture (water vapor and liquid water) profiles. A detailed description of the models is provided next.

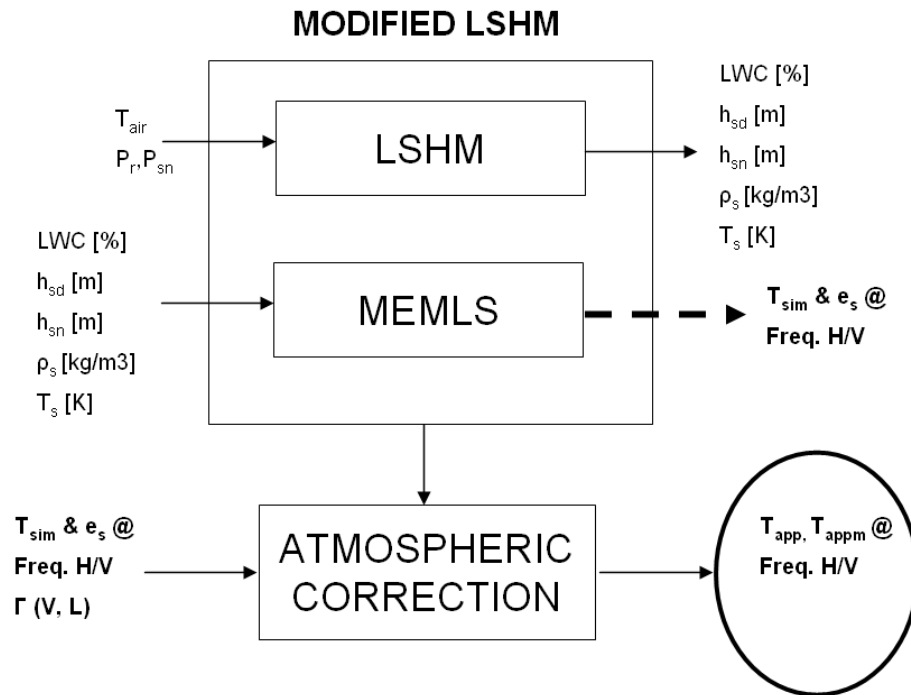


Figure 3-3 Schematic view of model flow chart for simulated and apparent brightness temperature at radiometer, T_{sim} , T_{app} , and T_{appm}

3.2.1. Land Surface Hydrology Model (LSHM)

The model domain of the 1-D LSHM is composed of atmospheric boundary layer, ground-surface (bare soil, snowpack and canopy), and soil column (Figure 3-4). The description of LSHM presented here follows closely [Devonec and Barros 2002].

The simplified single layer heat transfer change between the atmospheric boundary and the snowpack is governed by the surface energy equation:

$$c^* h_0 \frac{\partial T_0}{\partial t} = FR + S_h + L_h + G_h \quad (3-1)$$

Where c^* is the heat capacity of snow [J/kg K], h_0 is the snow water equivalent [m], T_0 is the snowpack temperature, FR is the net radiation flux [W/m²], S_h is the sensible heat flux [W/m²], L_h is the latent heat flux [W/m²], and G_h (Equation 3-3) is the soil heat flux [W/m²]. When soil surface temperature data are available, they are used to specify initial conditions. Otherwise, T_0 is set to $(T_{air} - 2.0)$, and the deep soil temperature is set to climatology. The heat capacity of mixed soil and snow cover, c^* is corrected in the presence of snow as follows:

$$c^* = c_i C_{sn} + c_s (1 - C_{sn}) \quad (3-2)$$

where C_{sn} is the fraction of snow covered area, c_i is the heat capacity of ice and c_s is the heat capacity of the soil. The top soil temperature is, $T_s = T_0$, is diagnosed from Equation (3-1). The bottom boundary condition is open. For the deep soil temperature, the heat diffused from adjacent snow layers plays a dominant role as is:

$$c_s h_d \frac{\partial T_d}{\partial t} = -G_h = k_s \frac{\partial T_d}{\partial z} \quad (3-3)$$

h_d is the soil depth [m], T_d is the soil temperature, and k_s is the heat conductivity of soil [W/(m K)].

The net radiation flux is composed of the net solar radiation, F_s , the incoming long wave radiation, F_{li} from cloud and aerosols, and the outgoing long wave radiation, F_{lo} from the ground surface. The sign convention is positive for incoming solar radiation and negative for the outgoing radiation.

$$FR = F_s + F_{li} + F_{lo} \quad (3-4)$$

F_s is determined by the sum of incoming short wave radiation, F_{si} subtracted by outgoing short wave radiation reflected from the ground surface by albedo, a_g .

$$F_s = F_{si} - a_g F_{si} \quad (3-5)$$

The albedo, a_g is a composite of the albedo of bare soil, snow, and vegetated fractions.

$$a_g = C_{sn} a_{sn} + (1 - C_{sn} - C_v) a_0 + C_v a_v \quad (3-6)$$

Where C_v is the fraction of vegetation cover. The net long wave radiation is calculated by Stefan-Boltzmann's law:

$$F_l = F_{li} - F_{lo} = \sigma(\varepsilon_{atm} T_a^4 - \varepsilon_s T_0^4) \quad (3-7)$$

Where ε_s and ε_{atm} are emissivity of snowpack/ground surface and ambient atmosphere, respectively. σ is the Stefan-Boltzmann's constant, ($5.67 \times 10^{-8} \text{ W} / \text{m}^2 \text{ K}^4$).

The sensible heat flux, S_h , and the latent heat flux, L_h , are parameterized by:

$$S_h = C_p \rho_a K_H |U_1| (T_1 - T_0) \quad (3-8)$$

$$L_h = L_v^* \rho_a K_L |U_1| (q_1 - q_{sat}) \quad (3-9)$$

Where subscript 1 indicates variables measured or simulated at the reference height (e.g. 10 m). C_p is the heat capacity of air at the constant pressure, L_v is the latent heat of vaporization from liquid water to vapor, ρ_a is the air pressure, U_1 is the horizontal wind speed, T_1 is the air temperature, and K_H and K_L are the aerodynamic transfer coefficients for heat and vapor, respectively. Based on energy balance equations, the snow hydrology model updates T_0 which applies to the top soil layer and the overlying snowpack with depth h_{sn} . Melting is initiated when T_0 exceeds the melting temperature, T_i ($T_i = 273.15$ K), and the heat flux, $Q_{sn} = C_{sn} c_i h_{sn} (T_0 - T_i)$ is used to melt the snowpack. Here, the melting processes are divided in superficial and deep melting. The criterion is set based on the equilibrium temperature, T_e .

$$T_e = T_0 + C_{sn}^* \left[(T_d - T_0) + \frac{c_i}{c} (T_0 - T_i) \right] \quad (3-10)$$

with

$$C_{sn}^* = C_{sn} \cdot \min \left\{ 1, \frac{h_{sn}}{h_0} \right\} \quad (3-11)$$

Where C_{sn}^* is the areal fraction covered by snow. Superficial melting occurs

when $T_e < T_i$, and the melt from the upper snowpack layer refreezes in the deep snowpack. Deep snowmelt occurs when $T_e > T_i$ and, affects the entire snowpack leading to a change in snow depth:

$$\Delta h_{sm} = \min \left\{ h_{sn}, \frac{c_i h_{sn} (T_0 - T_i)}{L_m \rho_w} \right\} \quad (3-12)$$

The temporal change of the snow depth, h_{sn} including snowmelt, snowfall, and snow sublimation, E_{sk}^{snow} is expressed as follows,

$$\frac{dh_{sn}}{dt} = \frac{1}{\rho_w} (P_{sn} + xP_r + E_{sk}^{snow}) - \Phi_{sn} \quad (3-13)$$

Where xP_r is the accumulated snow from rain-on-snow events, and Φ_{sn} is the snowmelt outflux outside the snowpack defined by:

$$\Phi_{sn} = \rho_w \frac{dh_{sm}}{dt} \quad (3-14)$$

During rain on snow events, the cold content of the snowpack, $Q_{cc} = C_{sn} c_i h_{sn} (T_0 - T_i)$, is compared with heat content of rainfall, $Q_r = C_{sn} c_w P_r (T_a - T_i)$. When the $Q_{cc} > Q_r$, the rain is fully frozen in the snowpack. The heat released due to freezing process of rainfall is used to update the snowpack temperature, T_0 .

The liquid water content, LWC is the amount of liquid water which can be retained in the snowpack. The maximum LWC is the liquid water retention capacity. Above the retention capacity, water content is released and can infiltrate or runoff. The

snow depth, h_{sn} is calculated based on the snow density which is initially set at 30.0 kg/m³ for fresh fallen snow, unless there are location specific observations. After changing the snow water equivalent due to the snowmelt, sublimation, rain on snow, and snowfall, the snow depth is decreased by the compaction ratio, CR [1/sec], which controls snow depth and consequently snow density. CR is parameterized with metamorphosis and overburden effects following [Jordan 1991]:

$$CR = \left. \frac{1}{\Delta z} \frac{d\Delta z}{dt} \right|_{metamorphosis} + \left. \frac{1}{\Delta z} \frac{d\Delta z}{dt} \right|_{overburden} \quad (3-15)$$

$$\left. \frac{1}{\Delta z} \frac{d\Delta z}{dt} \right|_{metamorphosis} = -2.778 \times 10^{-6} \times C3 \times C4 \times e^{-0.04(273.15-T)} \quad (3-16)$$

Where $C3=C4=1$ if $\gamma_l = 0$ and $\gamma_i \leq 150.0$ kg/m³

$$C3 = \exp^{[-0.046(\gamma_i - 150)]} \quad \text{if } \gamma_l > 150.0 \text{ kg/m}^3$$

$$C4 = 2.0 \quad \text{if } \gamma_l > 0.0$$

$$\left. \frac{1}{\Delta z} \frac{\partial \Delta z}{\partial t} \right|_{overburden} = \frac{-P_s}{\eta_0} e^{-c5 \cdot 0.04(273.15-T)} \cdot e^{-c6 \rho_s} \quad (3-17)$$

and η_0 = the viscosity coefficient at $T = 273.15$ K [N s/m²]

$$C5 = 0.08 \text{K}^{-1}$$

$$C6 = 0.21 \text{m}^3/\text{kg}$$

$$P_s = \text{Pressure due to snowpack weight [N/m}^2]$$

Where γ_i is the ice bulk density, γ_l is the liquid bulk density within a snowpack.

The condition 'C3=C4=1' is designated for dry snow which implies the compaction due to metamorphosis is slower than for wet snow. However, if γ_l is larger than 150.0 kg/m³ when the melting occurs, snowpack metamorphosis slows down again. The overburden compaction rate is based on the pressure of the snowpack due to weight for unit area [P_s]. By multiplying the current snowpack depth by the compaction rate, a new snowpack depth is determined. Figure 3-5 shows the compaction rate [1/sec] versus the snow water equivalent [m] in Valdai, Russia during 1978 to 1983. The compaction rate increases when h_{sn} starts to increase in December. On the other hand, although h_{sn} decreases during May and June, the compaction rate remains very high for very dense old snow. It is noted that in CLPX, the case of the only overburden compaction effect is used.

Snow microphysical effects typically associated with snow grain size are parameterized as proposed by [Wiesmann and Mätzler 1998, Mätzler 2002] in terms of the correlation length $p_{cc'}$ that is dependent on snowpack density and snow temperature to infer an effective grain size corresponding to a statistical distribution of the distances among snow grains according to the snowpack physical and thermodynamical states.

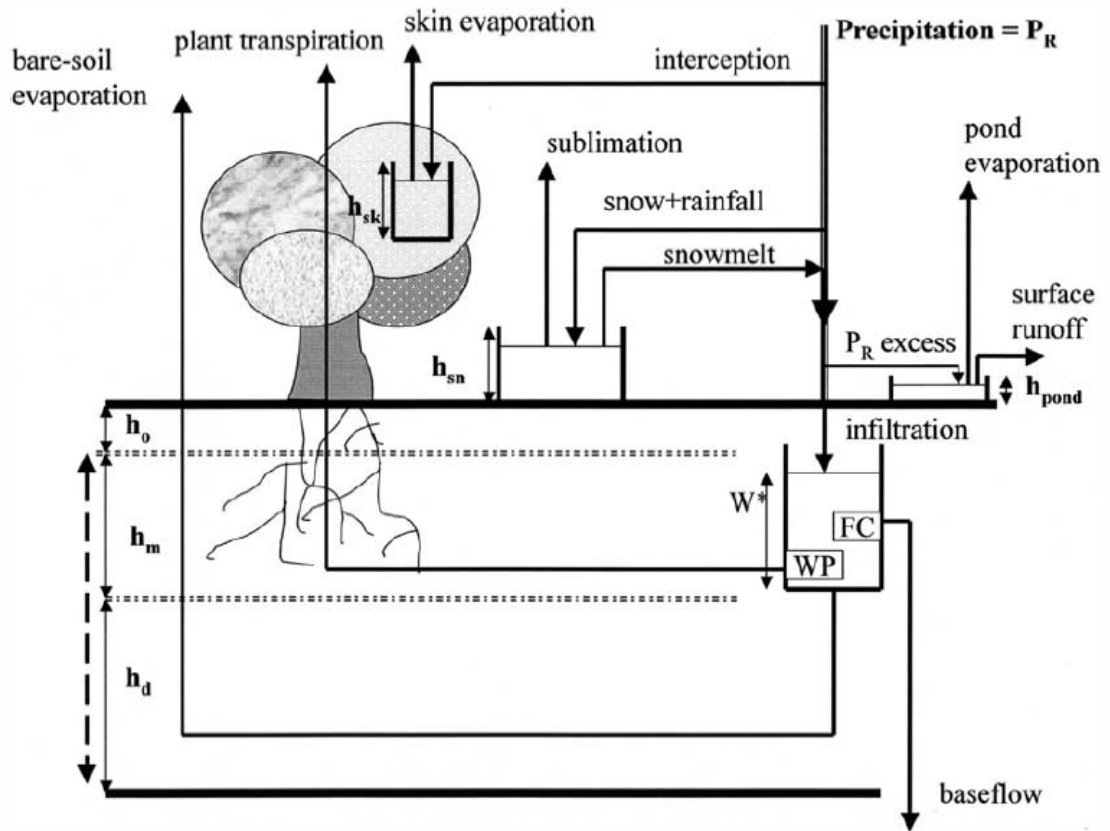


Figure 3-4 Schematic view of LSHM including state variables and their processes [Devonec 2002].

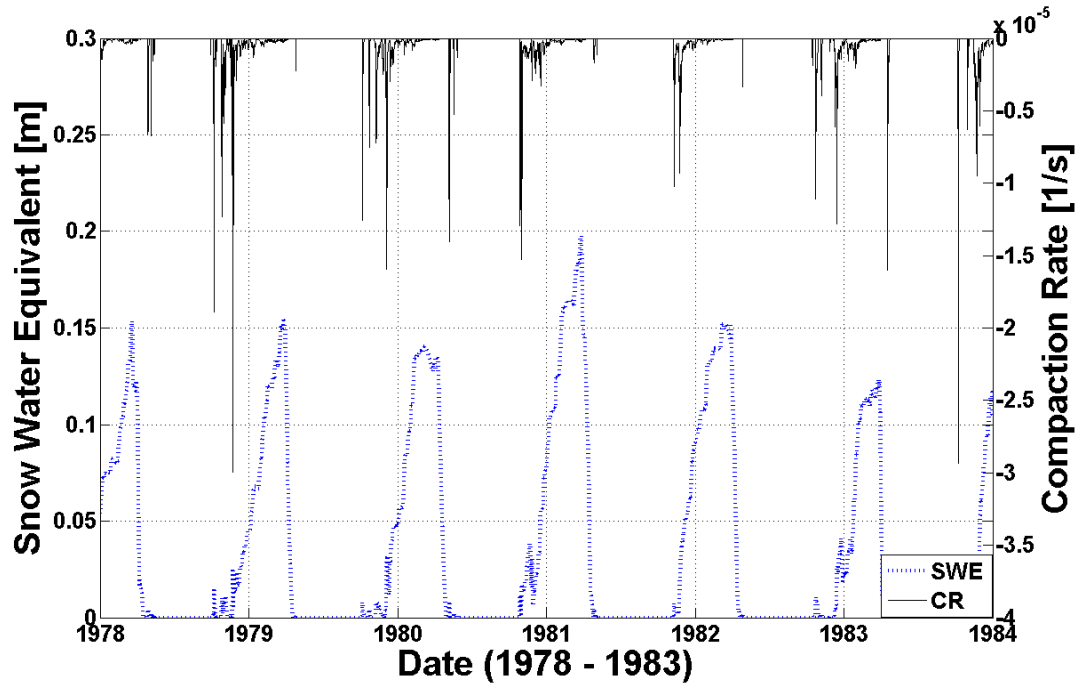


Figure 3-5 Snow Density [kg/m³] and Compaction Rate [1/sec].

3.2.2. Microwave Emission Model of Layered Snowpack (MEMLS)

Whereas the default snowpack in MEMLS consists of n horizontal stacks, the snow hydrology model in this manuscript considers a single-layer snowpack, and then MEMLS was adapted to this formulation. A multilayer implementation of the LSHM-MEMLS framework is presented Part Chapter 4. The description of MEMLS presented next follows closely [Wiesmann and Mätzler 1999; Mätzler and Wiesmann 1999].

Considering planar boundaries between air-snow and snow-soil, the multilayer snowpack at frequency, f , polarization, p , and incidence angle, θ is characterized by the snowpack brightness temperature T_b , the ground-snow interface reflectivity s_0 , the ground temperature T_o , the interface reflectivity s_j on top of layer j , the thickness d_j , temperature T_j , internal reflectivity r_j , emissivity e_j , and transmissivity t_j , of each layer, the sky downwelling radiation, represented by the brightness temperature T_{sky} in Fig. 3-6a. Considering a single layer, $j=1$. The outgoing radiation from one layer to a layer above and below, respectively the atmosphere above and the soil beneath (Fig. 3-6b):

$$A_j = r_j B_j + t_j + e_j T_j \quad (3-18)$$

$$D_j = t_j B_j + r_j C_j + e_j T_j \quad (3-19)$$

With incoming radiation from soil and atmosphere to the snowpack, respectively:

$$B_j = s_{j-1} A_j + (1 - s_{j-1}) D_{j-1} \quad (3-20)$$

$$C_j = (1 - s_j) A_{j+1} + s_j D_j \quad (3-21)$$

Adapting the MEMLS multi-layer simulation, the brightness temperature, T_b of the bulk layer is B_{j+1} ($B_{j+1} = s_j A_{j+1} + (1 - s_j) D_j$), A_{j+1} is the T_{sky} and s_j is the interface reflectivity between snow surface and atmosphere. When $j=1$, the number of unknown variables are A_1 , B_1 , C_1 , and D_1 . Given four equations, D_1 is determined by:

$$D_1 = \frac{\left[t_1 s_0 \frac{r_1 (1 - s_0) T_0 + t_1 (1 - s_1) T_{sky} + e_1 T_1}{1 - r_1 s_0} + t_1 (1 - s_0) T_0 + r_1 (1 - s_1) T_{sky} + e_1 T_1 \right]}{\left[1 - r_1 s_1 - \frac{s_0 s_1 t_1^2}{1 - r_1 s_0} \right]} \quad (3-22)$$

After determining D_1 , the outgoing brightness temperature from the snow surface is given by B_2 which is T_b :

$$T_b = B_2 = s_1 T_{sky} + (1 - s_1) D_1 \quad (3-23)$$

The current version of MEMLS (MEMLS3) only accounts for the second term of the internal contribution to the outgoing radiation (C. Mätzler, pers. communication). Because the snow surface is not a specular reflector, $s_1 T_{sky}$ becomes diffused, which cannot be determined by a single reflectivity, s_1 . Therefore, T_b represents only outgoing radiation from the internal snowpack.

The interior reflectivity, transmissivity, and emissivity, r , t , and e , respectively, are determined by absorption, γ_a and scattering, γ_b coefficients within snowpack.

$$r = \frac{r_0 (1 - t_0^2)}{(1 - r_0^2 t_0^2)} \quad (3-24)$$

$$t = \frac{t_0(1 - r_0^2)}{(1 - r_0^2 t_0^2)} \quad (3-25)$$

$$e = 1 - r - t \quad (3-26)$$

where $r_0 = \gamma'_b(\gamma'_a + \gamma'_b + \gamma)^{-1}$, $\gamma = \sqrt{\gamma'_a(\gamma'_a + 2\gamma'_b)}$, $\gamma'_a = \gamma_a(1 + 4\gamma_c(\gamma_a + 2\gamma_c)^{-1})$, and $\gamma'_b = \gamma_b + 4\gamma_c^2(\gamma_a + 2\gamma_c)^{-1}$.

For simplicity, the derivation of γ_c as a combination of γ_a and γ_b is not presented here. In order to determine the main radiative parameters γ_a and γ_b , the following snow physical properties are necessary at a given frequency f , polarization p , and incidence angle θ : density ρ_j , temperature T_j , liquid water content LWC_j , correlation length p_{ej} , vertical position z_j or thickness d_j for each layer ($j=1, \dots, n$), which are provided to MEMLS by the LSHM. The dielectric properties of the snow layer for dry and wet snow conditions are described by:

$$\varepsilon'_d = 1 + 1.5995\rho_s + 1.861\rho_s^3 \quad 0 < \rho < 0.4 \text{ g/cm}^3 \quad (3-27)$$

$$\varepsilon'_d = (\varepsilon'_0 + (\varepsilon'_i - \varepsilon'_0) \cdot f)^3 \quad \rho > 0.4 \text{ g/cm}^3 \quad (3-28)$$

Where ε'_0 is the real part permittivity of air (1.0), ε'_i is that of ice (3.215 at $T < 0^\circ \text{C}$), and f is the ice volume fraction to the total volume. The imaginary part of the dry snow permittivity is given by:

$$\varepsilon''_d = f \sqrt{\varepsilon'_d} K^2 \varepsilon''_i \quad (3-29)$$

Where K^2 is the squared field factor and ε''_i is the imaginary part of permittivity

of ice.

In terms of the wet snow permittivity, [Lundberg 2000a] proposed an effective permittivity of wet snow, ϵ , that is linearly related to the volumetric snow wetness LWC.

$$\epsilon = \epsilon_a + \epsilon_b + \epsilon_c + \epsilon_d \quad (3-30)$$

ϵ_d is the permittivity of dry snow, and ϵ_k ($k=a, b$, and c) are Debye snow mixture terms which are not presented here. Finally, the absorption and scattering coefficients are determined by:

$$\gamma_a = \frac{4\pi n''}{\lambda} \quad (3-31)$$

$$\gamma_b = \left(9.2 \frac{P_{ec}}{1mm} - 1.23 \frac{\rho_s}{1g/cm^3} + 0.54 \right)^{2.5} \left(\frac{f}{50GHz} \right)^{2.5} \quad (3-32)$$

or

$$\gamma_b = \left(3.16 \frac{P_{ec}}{1mm} + 295 \left[\frac{P_{ec}}{1mm} \right]^{2.5} \right) \cdot \left(\frac{f}{50GHz} \right)^{2.5} \quad (3-33)$$

The scattering coefficient γ_b can be selected between Equation 3-32 and 3-33 depending on field data availability and grain size. Here, it is also noted that the correlation length is introduced to replace the actual grain size. Based on the statistical distribution of the inter-relationship between two particles, the correlation length, p_{ec} is determined.

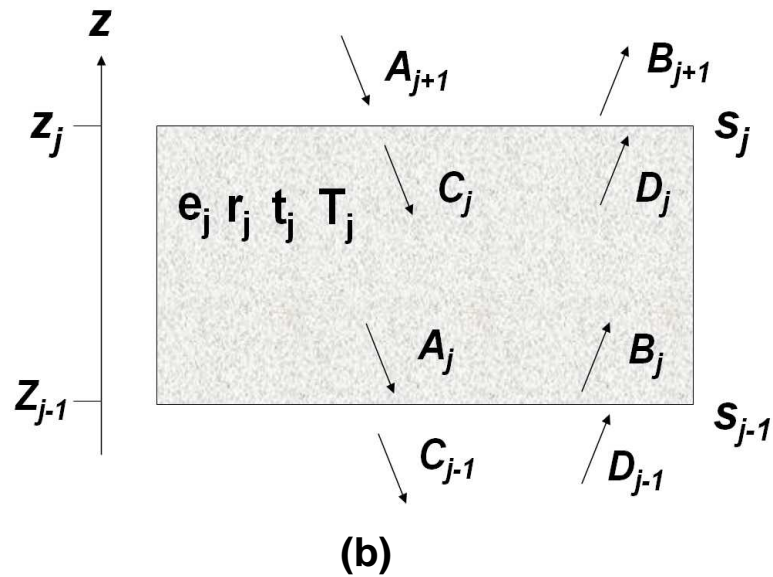
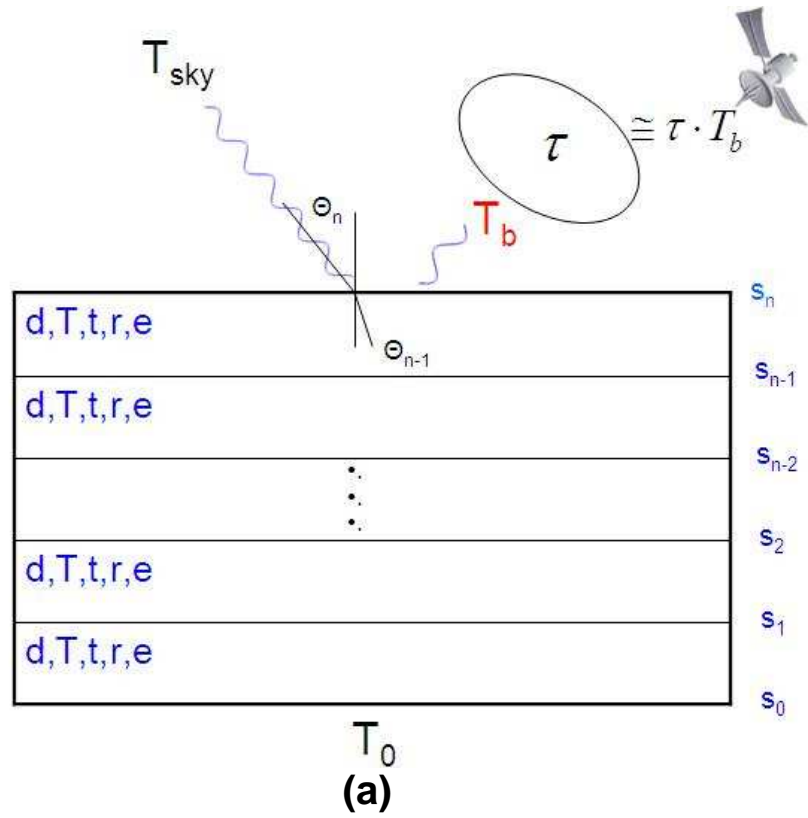


Figure 3-6 Multilayered Snowpack System with incident radiation from sky with an angle θ_n [modified from Wiesmann and Mätzler 1999] including optical depth, τ before the satellite microwave receiver. (b)-incoming and outgoing microwave propagation variables of snow layers in MEMLS .

3.2.3. Atmospheric Correction of Microwave Radiation

Atmospheric correction was not applied to SMMR brightness temperature products available to the public. Therefore, in order to compare LSHM-MEMLS simulated brightness temperatures to SMM observations, it is necessary to apply the correction to the SMMR products, or else apply an atmospheric correction to the model simulations to estimate the apparent brightness temperatures at the SMMR antenna. The latter was the approach selected here. For this purpose, the parameterization of atmospheric effects proposed by [Aschbacher1990] and [Choudhury 1992] was adopted here. Assuming that the earth surface is an emitting medium whereas the atmosphere is a semitransparent medium, the radiative transfer equation for the apparent brightness temperature, T_{app} [K] at radiometer at a frequency, f , polarization p , and zenith angle θ , and the orbit height H [m] of a satellite-borne microwave radiometer is given by:

$$T_{app} \cong e_s T_s t_a + \alpha_{up} T_s (1 - t_a) + \alpha_{dn} T_s (1 - t_a)(1 - e_s) t_a + 2.7 t_a^2 (1 - e_s) \quad (3-34)$$

where e_s is the surface emissivity, α_{up} is the upwelling radiation coefficient, α_{dn} is the downwelling radiation coefficient, T_s is the surface temperature [K], and t_a is the transmissivity of the atmosphere. It is also assumed that the Raleigh-Jeans approximation can be used, and thus the brightness temperature at the earth surface ($z=0$) can be expressed by earth's emissivity e_s times effective surface temperature T_s [K]. The atmosphere is assumed to be non-scattering with a homogeneous extinction

coefficient, k_e , and physical temperature T [K]. Reflection of non-diffuse radiation at the earth surface is determined by $(1 - e_s)$. T_{cos} [K] is used to characterize the contribution of outside the earth's atmosphere to the radiometer. α_{up} and α_{dn} are the "atmospheric profile factors" for the upwelling and downwelling emission, respectively. Following [Aschbacher 1990]:

$$\alpha_{up} = -0.073t_a^2 + 0.101t_a + 0.918 \quad (3-35)$$

$$\alpha_{dn} = -0.035t_a^2 + 0.014t_a + 0.967 \quad (3-36)$$

The atmospheric transmission coefficient (t) can be expressed in terms of the optical depth, τ at the microwave frequency and cosine of incidence angle of the radiometer, μ (for SMMR $\mu = 0.643$) as: $t = \exp(-\tau/\mu)$

Water constituents such as vertical liquid water, L and precipitable water V are the main factors to scatter/absorb the radiation in the atmospheric correction because the dielectric permittivity of water is much higher than other gaseous constituents. Therefore, a parameterization for the optical depth at time i and for frequency f as a function of L and V at the same time proposed first by [Westwater 1990] was adopted here:

$$\tau_{f,i} = \beta_f + \phi_f V_i + \zeta_f L_i \quad (3-37)$$

[Choudhury 1992] estimated the frequency dependent β_f , ϕ_f and ζ_f by fitting Eq. (3-37) against observations of optical depth and atmospheric moisture profiles. [Mätzler 1992] presented a more comprehensive summary of the parameters to describe the

relationship between τ and V and L using ground-truth observations at the same frequencies of *SMMR* for different regions. Here, the values of β and χ at 19 and 37 GHz, for the 'North Sea and Arctic Ocean at sea level' were selected because Valdai Russia is adjacent to the North Sea. The single-layer LSHM-MEMLS results including atmospheric correction at 18, 21 and 37 GHz, H and V polarizations, will be discussed in Section 4 where model results are compared against *SMMR* observations. No atmospheric correction was applied in the case of CLPX because the SSM/I and AMSR-E satellite products are already corrected.

3.3. Data

3.3.1. Scanning Multichannel Microwave Radiometer (*SMMR*)

The *SMMR* was operational aboard NASA's Nimbus-7 satellites from 26 October 1978 to 20 August 1987 [Gloersen 1977]. This polar orbit passive microwave radiometer has a fixed incidence angle of 50.2°. The *SMMR* data is transmitted twice a day corresponding to ascending and descending paths. *SMMR* is a multi-channel radiometer with 10 channels and 5 frequencies of both vertical and horizontal polarizations (6.6, 10.69, 18, 21, and 37 GHz) Significant efforts have been made to retrieving the physical properties of snow using *SMMR* data. Typically, the difference between 37 GHz and 21 or 18 GHz brightness temperatures to take advantage of the sensitivity of microwave behavior at 37 GHz as a function of the snow grain size ([Foster 1997]). The geographic context of Valdai, Russia is presented in Fig. 3-1. Also marked are the spatial resolution of *SMMR* and the European Center Reanalysis Dataset (*ERA-40*). As illustrated, the

resolution of SMMR is 0.25° while ERA-40's grid is 2.5° . Within the coarser domain of ERA-40, Valdai is located in 33.25° E and 57.90° N in the lower left corner. This discrepancy in spatial scales is indicative of uncertainty in atmospheric correction which will be addressed later.

3.3.2. Special Sensor Microwave Imager (SSM/I)

The Special Sensor Microwave Imager (SSM/I) is carried by Defense Meteorological Satellite Program (DMSP) satellites. This passive microwave radiometer operates with seven channels, four frequencies, and orthogonal polarizations at 19.35, 22.2, 37.7, and 85.5 GHz. Within the Large Regional Study Area (LRSA) of CLPX, SSM/I brightness temperature data between October of 2002 and June of 2003 were obtained from the National Snow and Ice Data Center (NSIDC). Figure 3-2 shows the Large Regional Study Area (LRSA) including the Fraser MSA (Meso-cell Study Area) for which detailed simulations were carried out in this study. For the comparison between simulated and observed brightness temperatures for the SSM/I data at 19.35, 22.2, and 37.7 GHz H/V frequencies were are selected. SSM/I data resources and detailed description are publicly available at (<http://nsidc.org/data/nsidc-0032.html>).

3.3.3. Advanced Microwave Scanning Radar-EOS (AMSR-E)

The Advanced Microwave Scanning Radar-EOS (AMSR-E) is carried by NASA's Earth Observing System (EOS) Aqua satellite since May 4th, 2002. AMSR-E is a passive microwave radiometer operating with 6.9, 10.65, 18.7, 23.8, 36.5, and 89.0 GHz H/V. AMSR-E data were also downloaded for CLPX at 25 km resolution. Data and metadata

are available at (<https://nsidc.org/data/nsidc-0301.html>).

3.3.4. Project for the Intercomparison of Land-Surface Parameterization Schemes (*PILPS*)

Motivated by an intercomparison study of land surface hydrology models [Henderson-Seller 1993], the *PILPS* phase2d data for Valdai, Russia was used by [Devonec 2002] to evaluate the snow hydrology. The Valdai research station is located within a grassland watershed in a forested region south of St. Petersburg (57.68N, 33.18E). *PILPS* provides 18 years hourly hydrological and meteorological datasets consisting of soil moisture, streamflow, snow water equivalent, and evaporation in the region. Various spatial measurements of hydrological and meteorological data such as air temperature, precipitation (rain and snow), wind, incoming solar radiation and etc. are averaged to create time series at the catchment scale. The Valdai datasets allow us to simulate brightness temperatures using *LSHM-MEMLS* which can be compared with *SMMR* data from 1978 to 1983.

3.3.5. Cold Land Processes Experiment (*CLPX*)

A detailed description of *CLPX* is provided by the National Snow and Ice Data Center (NSIDC) *CLPX* website (<http://nsidc.org/data/clpx/>). Interdisciplinary research on cold region hydrology from modeling to field measurements was conducted from 2002 to 2003 spring season. The emphasis of *CLPX* was placed on process-oriented understanding, land-surface models, and microwave remote sensing. In order to characterize a variety of topographical and ecological responses induced by snow

hydrological processes, eastern parts of the Rocky Mountains of the western United States were selected for the CLPX for two Intense Observing Periods (IOPs) during which intense ground, airborne and space-borne observations were collected: mid-winter, 2002, when conditions are generally frozen and dry, and early spring, 2003, a transitional period when both frozen and thawed, and dry and wet conditions were widespread. The spatial scale of the project is from 1 ha to 160,000 km² from west of Denver to south-western Wyoming. Also, hourly data sets from RUC40 short-range operational numerical weather forecasts (Rapid Update Cycle at 40 km resolution) were prepared for the Fraser, MSA (http://nsidc.org/data/docs/daac/nsidc0211_clpx_ruc40/). Hydrometeorological towers were also available at the various sites marked in Fig.3-2, which can be used for point-scale simulations. Specifically, a tower was available at the location where a ground-based radiometer (GBMR-7) was operating in the LSOS (Local Scale Observation Site) within the Fraser MSA, which we will also use for model evaluation here since it was used previously by others [Andreadis et al. 2008, Durand et al. 2008, and Tedesco et al. 2006]. Snow density of fresh fallen snow for CLPX was set at 100 kg/m³. Figures 3-7a-c show there is good agreement between the temporal evolution of snow water equivalent, snow depth and snow density simulated by the LSHM with single-layer snow hydrology for the Fraser MSA using RUC40 forcing. GBMR-7 pit measurements are shown for reference.

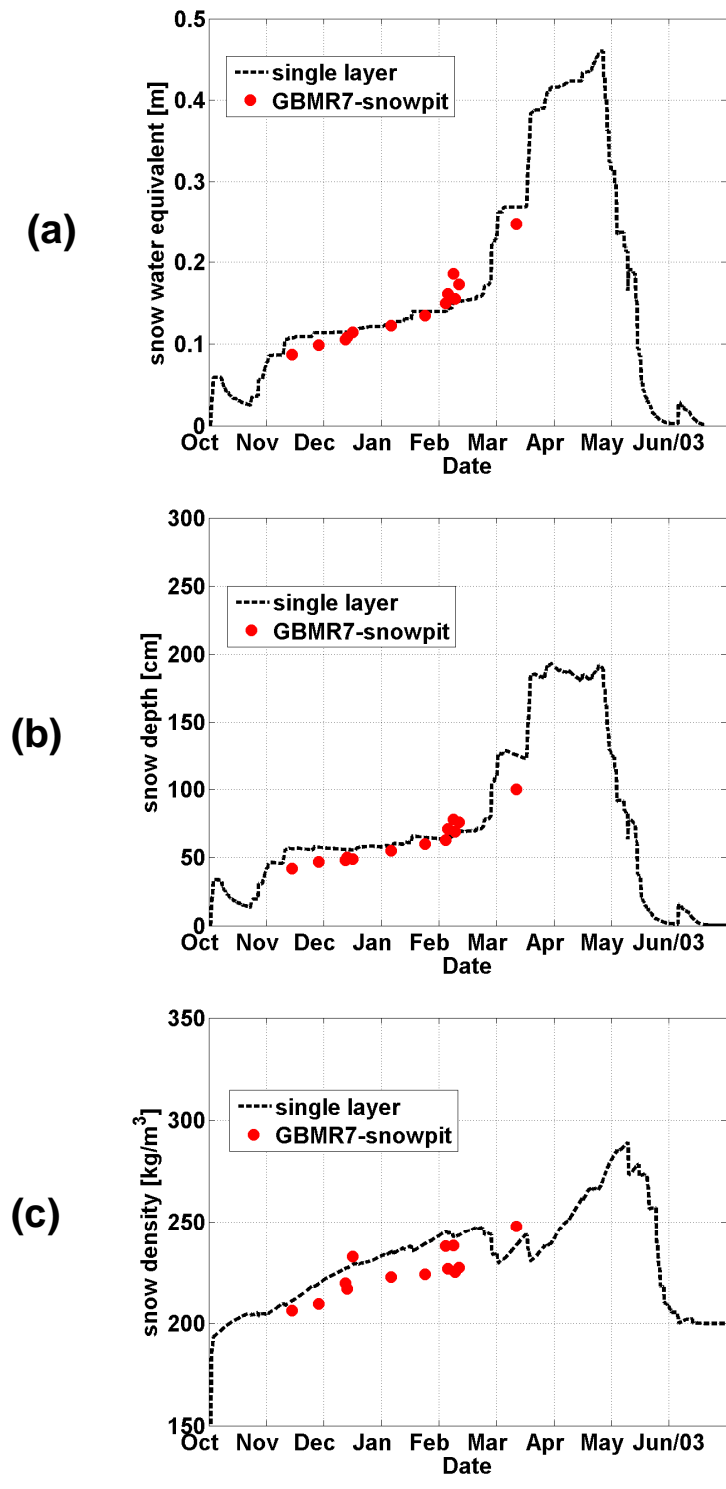


Figure 3-7 LSHM-MEMLS simulations of snow physical properties compared with GBMR snowpit observations: a) SWE, b) snow depth, and c) snow density.

3.3.6. ERA 40 (ECMWF Re-Analysis 40)

In order to account for the atmospheric attenuation due to the absorption and scattering of radiation between the snowpack and the satellite borne radiometer, vertical profiles of liquid water content (L), and precipitable water (V) were extracted from ERA-40 ECMWF (European Centre for Medium-Range Weather Forecasts) Reanalysis data set at 00:00 and 12:00 UTC and were subsequently interpolated to the times of SMMR overpasses at Valdai. Note that besides the time difference between overpass time and ERA-40 moisture profiles, there is a substantial difference among the spatial scale of the Valdai case-study (effectively one location), the spatial resolution of SMMR ($0.25^\circ \times 0.25^\circ$) brightness temperature fields, and the spatial resolution of ERA-40 products ($2.5^\circ \times 2.5^\circ$), which adds uncertainty to the estimation of atmospheric correction effects due to the large spatial and temporal variability of atmospheric moisture. Nevertheless, this is the best available data for this purpose at the specific time and location of interest. A detailed description of ECMWF ERA-40 is provided by [Uppala et al. 2005]. The vertical liquid water (L) and the precipitable water (V) for the grid element that contains Valdai, Russia are shown in Figure 3-8 from 1978 to 1983. As expected, both L and V peak during the summer season (June, July and August) and decrease during the winter time in this region. Therefore, atmospheric attenuation effects will be more important during fall and spring seasons.

A location-specific calibration of the optical depth parameterization was also conducted using two years of data to solve the inverse problem of estimating the

optical depth that lead to the best simulation of observed brightness temperatures at each frequency and polarization. The coefficients of precipitable water V and vertical liquid water L in the parameterization of optical depth, τ were calibrated by comparing *SMMR* data and *LSHM-MEMLS* simulation of brightness temperatures using the following relationship:

$$\tau_{f,i} - \zeta_f L_i = \beta_f + \phi_f V_i \quad (3-38)$$

D_f was maintained from [Westwater et al. 1990] and the optimal $\tau_{f,i}$ was calculated by determining the value that would result in a perfect match of *SMMR* and *LSHM-MEMLS* at each time of overpass i during the calibration period. Vertical profiles of moisture from ERA 40 at 12:00 and 00:00 UTC were interpolated to the overpass time and then integrated to determine the column values of L_i and V_i . Finally, β_f and ϕ_f were determined from the best fit line of $(\tau_{f,i} - \zeta_f L_i)$ and V_i for each frequency over the two-year period 1982-1983 for ascending and descending paths separately (Tables 3-2, 3-3). The coefficient of precipitable water, ϕ_f increased especially for the vertical polarization which implies that liquid water V in this region affects optical depth more strongly than in the cases studied by [Westwater et al. 1990]. Further calibration distinguishing snow accumulation from snow melting phases could also be conducted in order to further improve the effectiveness of the atmospheric correction.

Table 3-1- Coefficients β_i and ϕ_i for optical depth τ_i [Mätzler 1992]

Frequency	Parameters
21.0 GHz	$\beta = 0.018$ neper, $\phi = 0.0046$ neper/mm, $\zeta = 0.0819$ neper/mm
35.0 GHz	$\beta = 0.039$ neper, $\phi = 0.0018$ neper/mm, $\zeta = 0.1867$ neper/mm

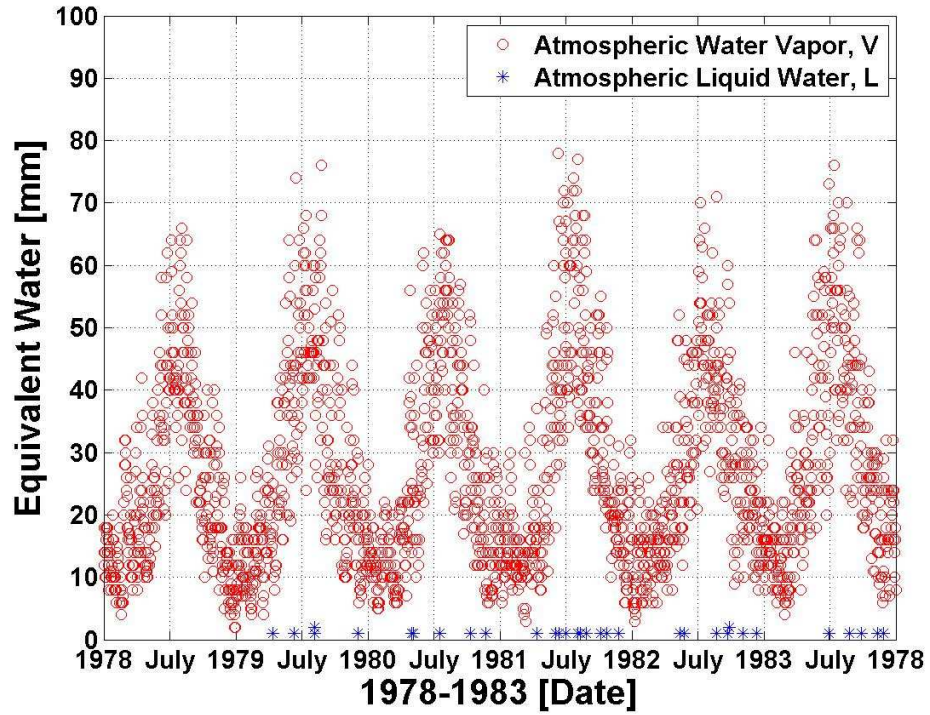


Figure 3-8 Vertical liquid water, L in mm and Precipitable water, V in mm in Valdai Russia extracted from ECMWF ERA 40.

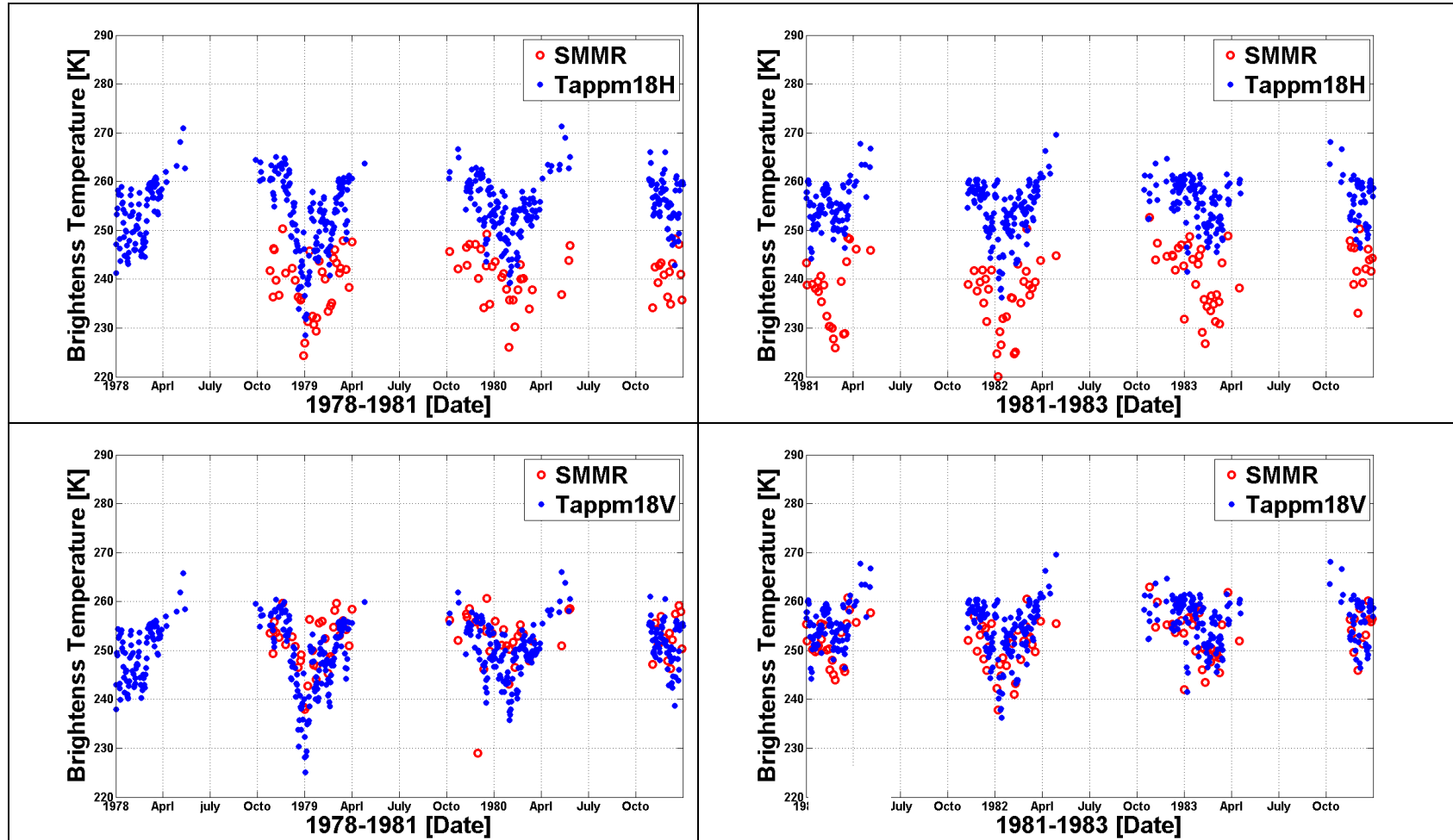


Figure 3-9 SMMR (red circle), compared with T_{app} and T_{appm} (blue dot) at 18 GHz (H and V Upper and lower panels, respectively).

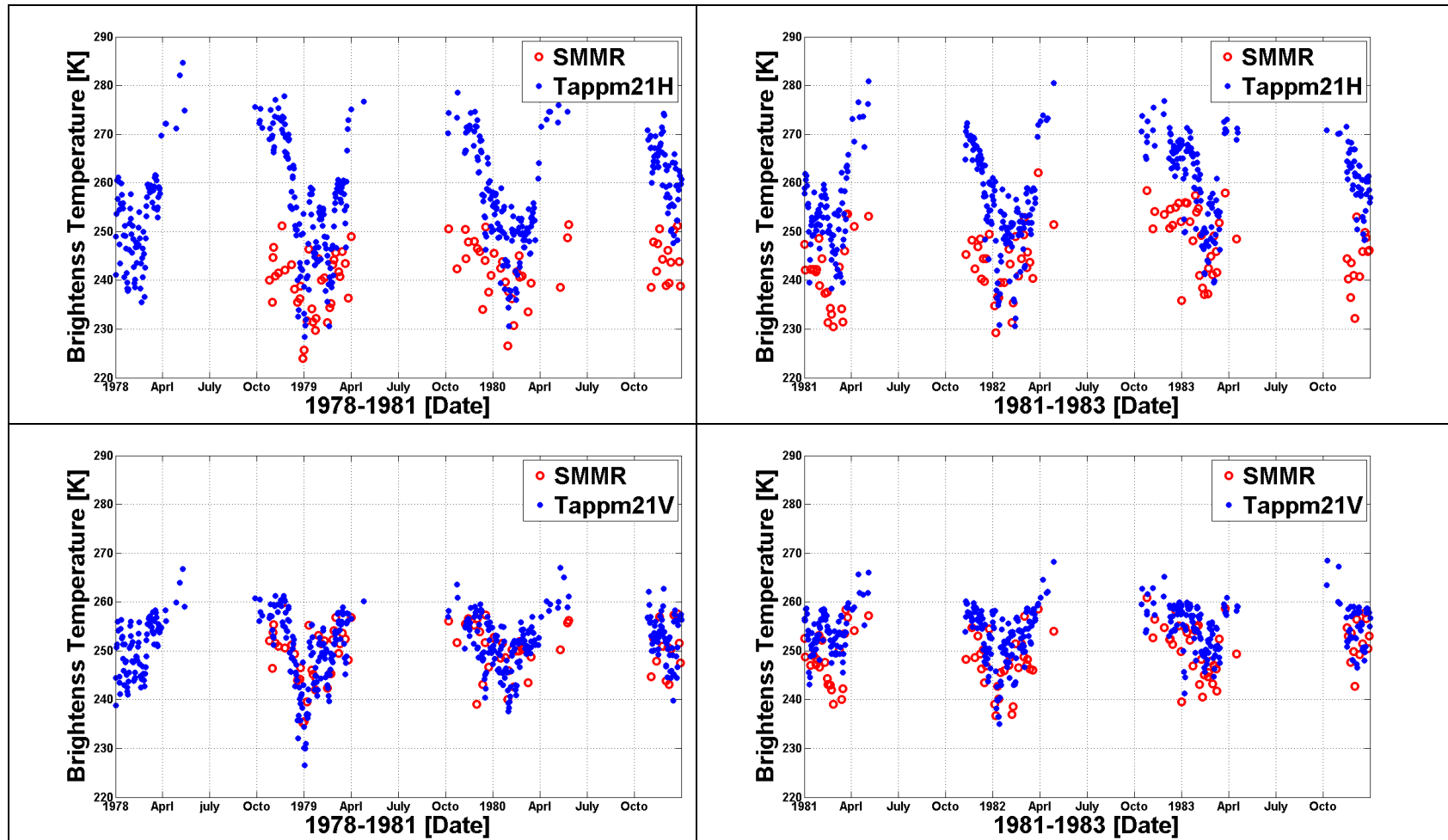


Figure 3-10 SMMR (red circle), compared with T_{app} and T_{appm} (blue dot) at 21 GHz (H and V Upper and lower panels, respectively).

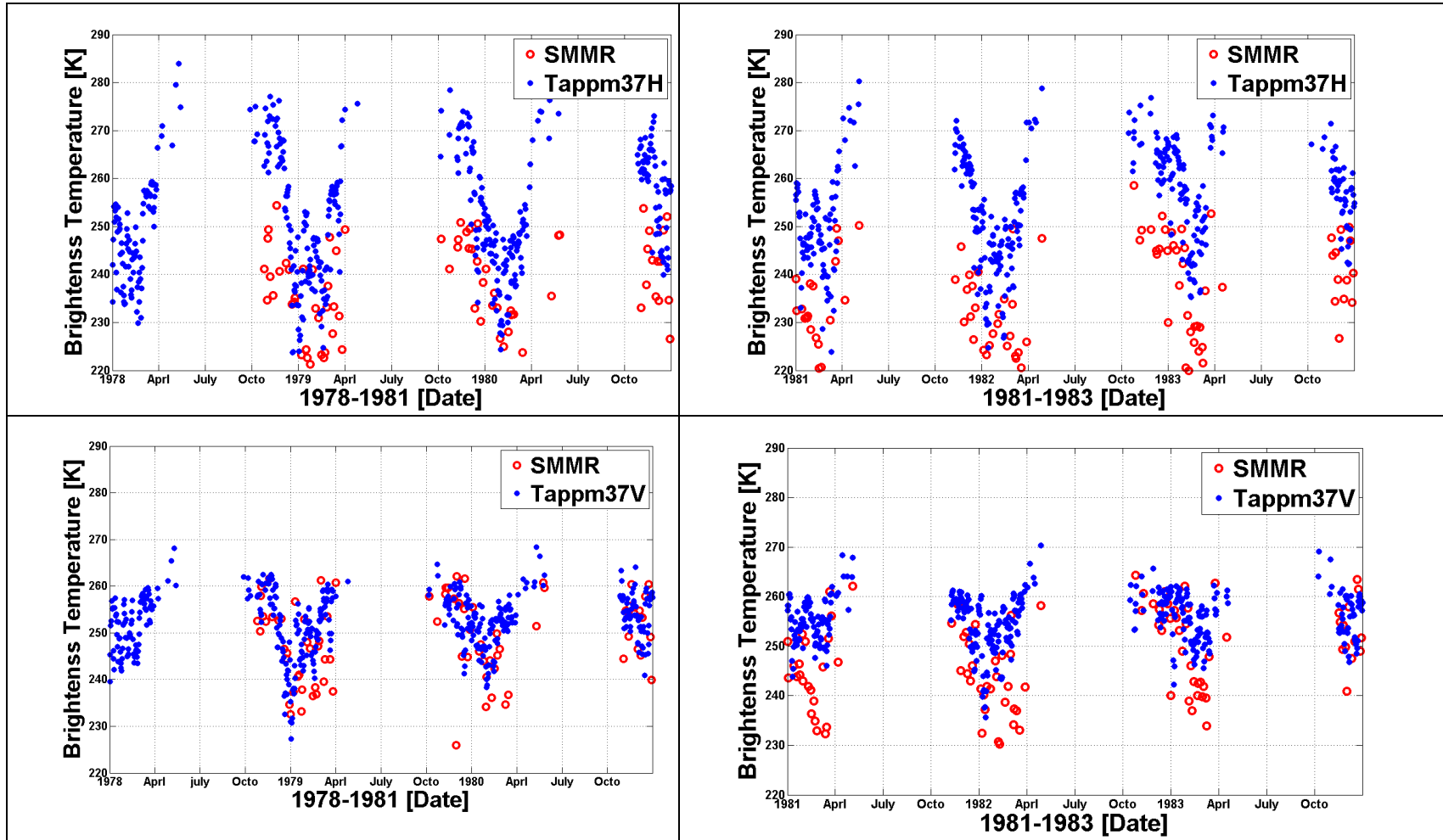


Figure 3-11 SMMR (red circle), compared with T_{app} and T_{appm} (blue dot) at 37 GHz (H and V Upper and lower panels, respectively).

3.4. Results and Discussions

3.4.1. Comparison Statistics

The hourly LSHM-MEMLS brightness temperatures corrected locally for atmospheric effects T_{appm} at 19, 21 and 37 GHz are shown in Figures 3-9, 10 and 11 from 1978 to 1983 by combining ascending (11:00 LST) and descending (23:00 LST) SMMR paths at Val dai. In the remainder of the manuscript T_b refers to simulated brightness temperature without atmospheric correction, T_{app} refers to T_b after applying the general atmospheric correction from the literature (Aschbacher 1990, Section 3.2.3), and T_{appm} refers to T_b after applying the locally calibrated atmospheric correction (Section 3.3.6). For quantitative evaluation, the Mean Absolute Error (MAE), Root Mean Squared Error (RMSE) and Bias (BIAS) were calculated for all results by comparing the simulated value y (LSHM-MEMLS T_b , T_{app} and T_{appm}) against the corresponding SMMR observation \hat{y} at the same frequency and polarization:

$$MAE = \frac{\sum |y - \hat{y}|}{n} \quad (3-39)$$

$$RMSE = \sqrt{\frac{\sum (y - \hat{y})^2}{n}} \quad (3-40)$$

$$BIAS = \frac{y - \hat{y}}{n} \quad (3-41)$$

Previously, [Derksen and Walker 2003] reported negative SMMR bias of -8.85 K

and -5.4 K with respect to the Special Sensor Microwave/Imager (*SSM/I*) at 19-V GHz in descending and ascending paths respectively, and positive bias of 4.59 K and 1.0 K at 37-V GHz, ascending and ascending paths respectively. These values provide a baseline for the inherent uncertainties in the *SMMR* observations, in that simulated brightness temperatures would be expected to exhibit similar or better error characteristics. Tables 3-2 and 3-3 show the coefficients for the atmospheric correction with respect to ascending and descending paths. Tables 3-4 and 3-5 show that for 18, 21 and 37 GHz the Bias estimates of *LSHM-MEMLS* versus *SMMR* are consistent with the data presented by [Derksen, 2003] at 37 GHz, and are much lower at 18 GHz. The local estimates of the optical depth parameterization lead to significantly improved estimates especially as measured by BIAS, and MAE and RMSE also improved for all for all frequencies (18, 21 and 37 GHz) especially in the vertical polarization (Tables 3-4 and 5, respectively for ascending and descending satellite orbits). Even though this polarization difference will be discussed in Chapter 4 in more detail, the single-layer simulates the vertical polarization better than the horizontal polarization. This is because the internal structure of the snowpack is averaged in the single-layer approach, and thus the effects of layer-to-layer heterogeneities that are important for horizontal polarization are not captured. Volume scattering effects dominate in the case of vertical polarization, and therefore if the single layer describes average snowpack properties well then errors should be smaller. Figures 3-12 and 3-13 show separately the relative distribution of *LSHM-MEMLS* T_b , T_{appm} and *SMMR* observations for ascending and descending paths,

respectively. As expected, at the higher range of brightness temperatures, the simulated brightness temperatures overestimate the observations for both ascending (Fig. 3-12) and descending (Fig. 3-13) paths. This corresponds to warmer periods during the winter season, when there might be transient superficial melt and subsequent formation of ice lenses not simulated by the simple layer microphysics [Rees et al. 2010]. In the lower range of brightness temperatures, there is good agreement between simulated values and *SMMR* observations.

Note that overall these error statistics are consistent with results from like-minded applications in the literature using ground-based observations to specify snowpack physical and radiative properties without coupling to a snow hydrology model [e.g. Tedesco et al. 2005, Lemmetyinen et al. 2010]. That is, the results presented here are based on predicted snowpack physical properties, in end-to-end Observing System Simulation (OSS) mode.

Table 3-2 Locally estimated parameters β_f and ϕ_f ($\tau_{f,i} - \zeta_f L_i = \beta_f + \phi_f V_i$), using two years of SMMR and LSHM-MEMLS data at Valdai while ζ_f was maintained as per Matzler (1996) for ascending paths.

Frequency	Parameters
21.0 GHz H	$\beta=0.9685$ neper, $\phi= 0.0043$ neper/mm, $\zeta= 0.0819$ neper/mm
21.0 GHz V	$\beta= 1.1861$ neper, $\phi= 0.0113$ neper/mm, $\zeta= 0.0819$ neper/mm
37.0 GHz H	$\beta= 0.7857$ neper, $\phi= 0.0171$ neper/mm, $\zeta= 0.1867$ neper/mm
37.0 GHz V	$\beta= 1.1594$ neper, $\phi= 0.0449$ neper/mm, $\zeta = 0.1867$ neper/mm

Table 3-3 Locally estimated parameters β_f and ϕ_f ($\tau_{f,i} - \zeta_f L_i = \beta_f + \phi_f V_i$), using two years of SMMR and LSHM-MEMLS data at Valdai while ζ_f was maintained as per Matzler (1996) for descending paths.

Frequency	Parameters
21.0 GHz H	$\beta=0.9997$ neper, $\phi = 0.0024$ neper/mm, $\zeta = 0.0819$ neper/mm
21.0 GHz V	$\beta= 0.9430$ neper, $\phi = 0.0474$ neper/mm, $\zeta = 0.0819$ neper/mm
37.0 GHz H	$\beta= 0.6478$ neper, $\phi = 0.0251$ neper/mm, $\zeta = 0.1867$ neper/mm
37.0 GHz V	$\beta= 0.8036$ neper, $\phi= 0.0448$ neper/mm, $\zeta = 0.1867$ neper/mm

Table 3-4 Differences in error statistics for ascending paths due to local estimation of atmospheric correction parameters (T_{appm}) as compared to general values (T_{app}). [Derksen and Walker 2003] reported Bias of -5.4 at 19-V GHz and 1.0 at 37-V GHz between SMMR and SSM/I for ascending paths.

		H			V		
		T_{sim}	T_{app}	T_{appm}	T_{sim}	T_{app}	T_{appm}
18 GHz	<i>Bias</i>	16.31	16.55	10.83	11.30	10.46	-1.13
	<i>ME</i>	16.60	16.73	11.20	11.94	11.19	4.86
	<i>RMSE</i>	18.58	18.50	12.50	13.44	12.66	6.27
21 GHz	<i>Bias</i>	13.36	13.76	7.56	13.35	12.60	-0.29
	<i>ME</i>	14.15	14.36	8.73	13.71	13.01	4.74
	<i>RMSE</i>	16.21	16.24	10.28	15.25	14.52	6.10
37 GHz	<i>Bias</i>	13.44	14.55	13.59	8.18	8.24	-1.40
	<i>ME</i>	14.59	15.36	14.07	10.55	10.28	6.73
	<i>RMSE</i>	16.77	17.33	16.40	12.65	12.34	8.45

Table 3-5 Differences in error statistics for descending paths due to local estimation of atmospheric correction parameters (T_{appm}) as compared to general values (T_{app}). [Derksen and Walker 2003] reported Bias of -8.85 at 19-V GHz and 4.59 at 37-V GHz between SMMR and SSM/I for ascending paths.

		H			V		
		T_{sim}	T_{app}	T_{appm}	T_{sim}	T_{app}	T_{appm}
18 GHz	<i>Bias</i>	18.27	18.60	15.23	12.68	11.95	-2.06
	<i>ME</i>	18.66	18.89	15.40	13.38	12.68	5.30
	<i>RMSE</i>	21.28	21.32	17.18	15.30	14.55	6.90
21 GHz	<i>Bias</i>	13.76	14.15	10.27	14.67	14.01	1.97
	<i>ME</i>	14.81	14.98	10.96	15.13	14.48	5.49
	<i>RMSE</i>	17.95	17.84	13.17	17.00	16.30	6.94
37 GHz	<i>Bias</i>	16.68	17.90	19.25	10.97	11.11	4.53
	<i>ME</i>	18.00	18.81	19.44	13.47	13.27	7.98
	<i>RMSE</i>	20.87	21.44	21.79	16.21	15.88	10.28

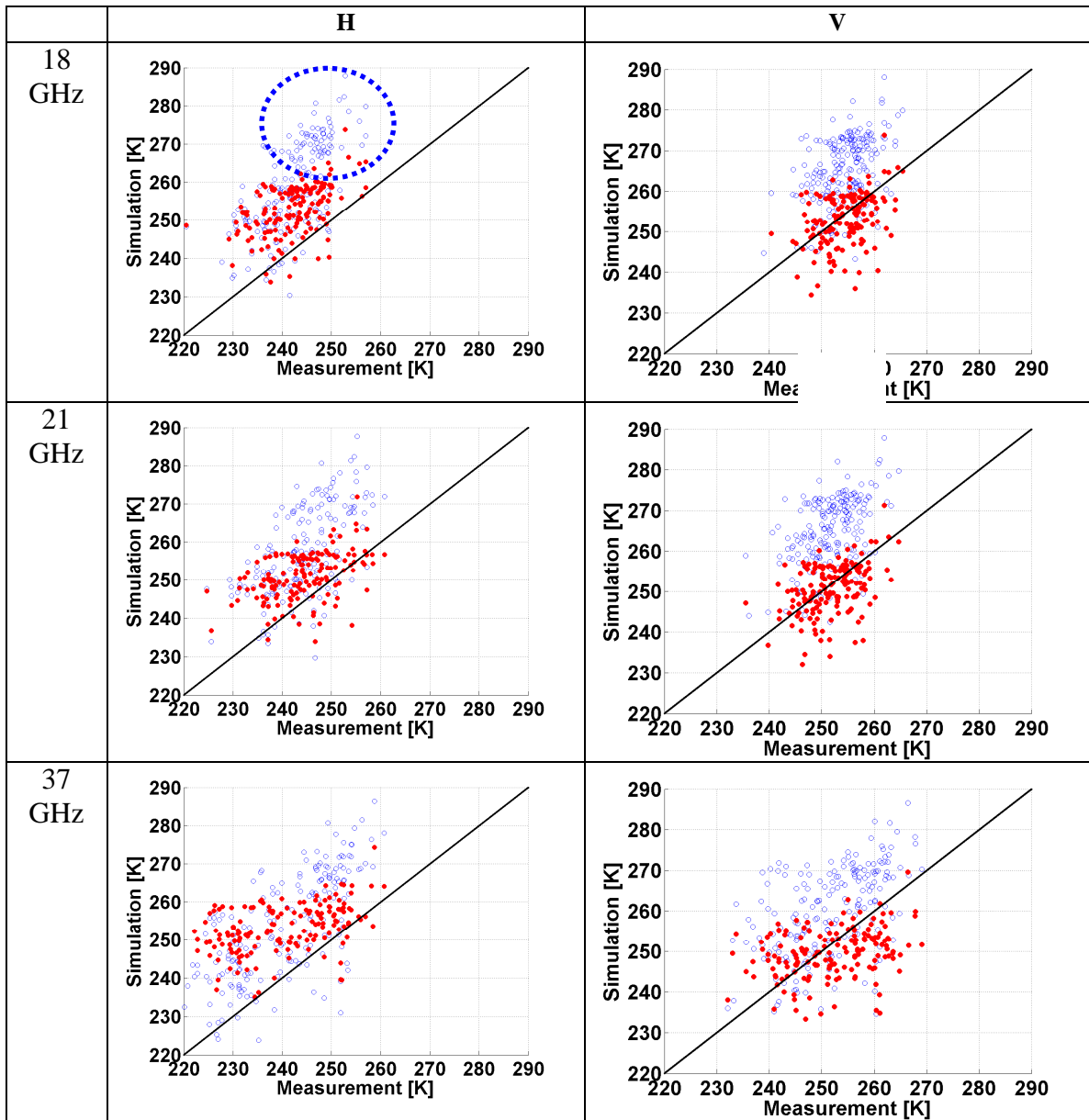


Figure 3-12 Comparison between MEMLS-LSHM (Blue circle) and T_{appm} (Red Dot) from Ascending path at 11:00 LST (Area inside dashed blue circle indicates overestimation during early accumulation and late melting).

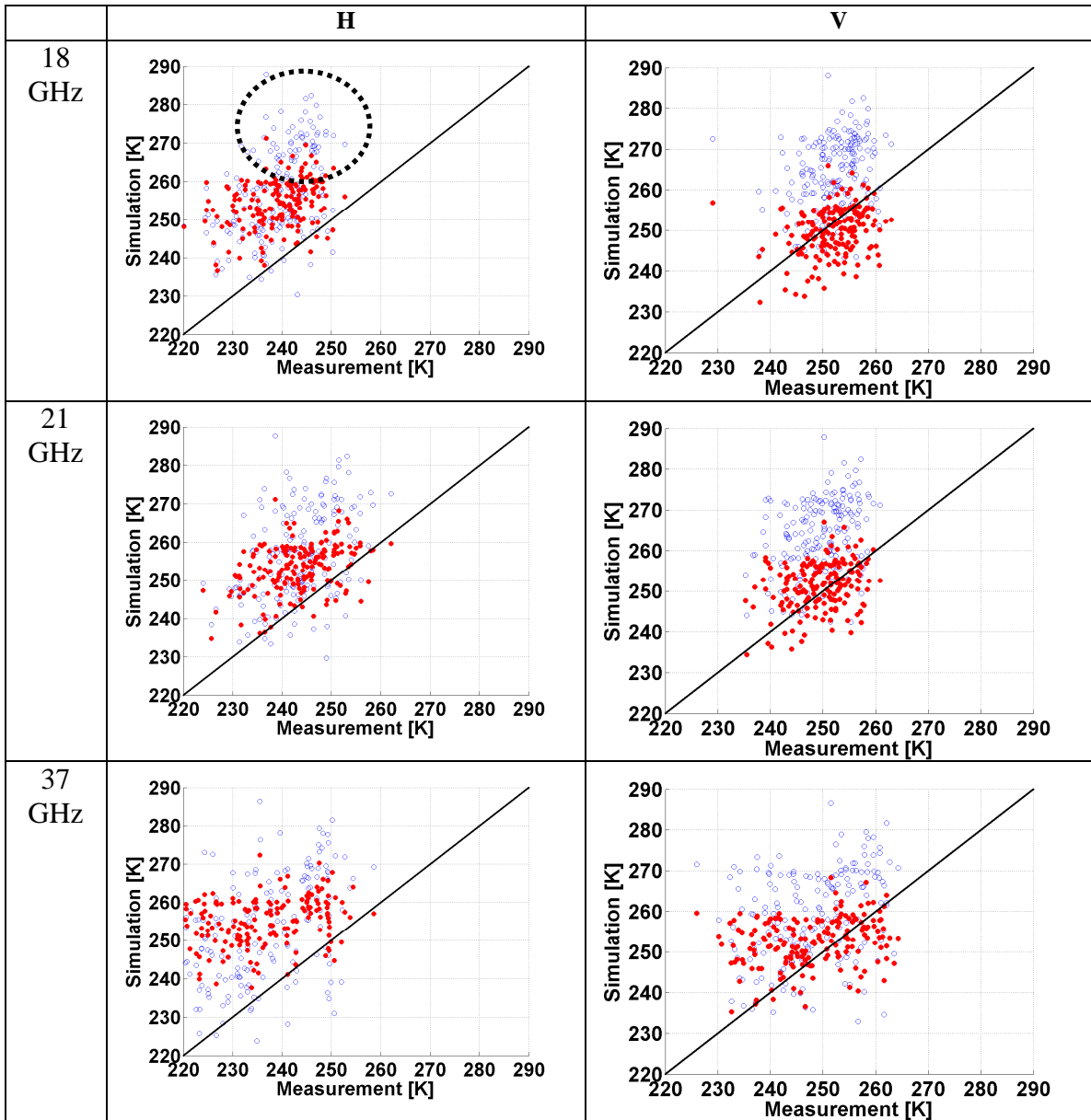


Figure 3-13 Comparison between *MEMLS-LSHM* (Blue circle) and T_{appm} (Red Dot) from Descending path at 23:00 LST (Area inside black dashed circle indicates overestimation during early accumulation and late melting).

3.4.2. Presence of Water

Figure 3-14 shows T_{app} , $SMMR$, and T_{appm} during the 1982 to 1983 snow season at 37-V GHz as well as LSHM SWE (h_{sn}) and LWC in different y-axis. The brightness temperatures decrease throughout the accumulation season as SWE and snow depth increase, and then increase again during the melting season. The LSHM handles rain-on-snow events such as those in March (Fig.3-14) by increasing the liquid water content (LWC) and warming the snowpack due to latent heat release of rainwater as it freezes. The maximum amount of rainfall that remains in liquid form is fixed to a threshold in the model, the maximum liquid water retention capacity. The value of this threshold is somewhat arbitrary in that many different physical properties of the snowpack related to its local history, and which cannot be captured in the simulation, can have an impact (layering structure, porosity, impurities, etc). On the other hand, the microwave behavior of the snowpack is significantly attenuated by the presence of liquid water because the permittivity of the water is much higher than ice. To illustrate the influence of liquid water content on snowpack microwave brightness temperature, the LWC sensitivity was analyzed in detail during the period between November 14th, 1981 and December 11th, 1982 (red box in Fig.3-14). In Figure 3-15-(a), the LWC simulated by LSHM was multiplied by factors of 10 and 15 for input to MEMLS. Note the systematic impact on the simulated brightness temperatures in Figure 3-15. This decrease of brightness temperature is consistent with the literature, specifically the relationship between snow wetness (here, LWC) and the attenuation of brightness temperature

[Schanda 1981]. The decrease of brightness temperature with increasing LWC is due to increase in the imaginary part of permittivity and extinction coefficients, mainly absorption as shown in Figs.3-15 (b) and (c).

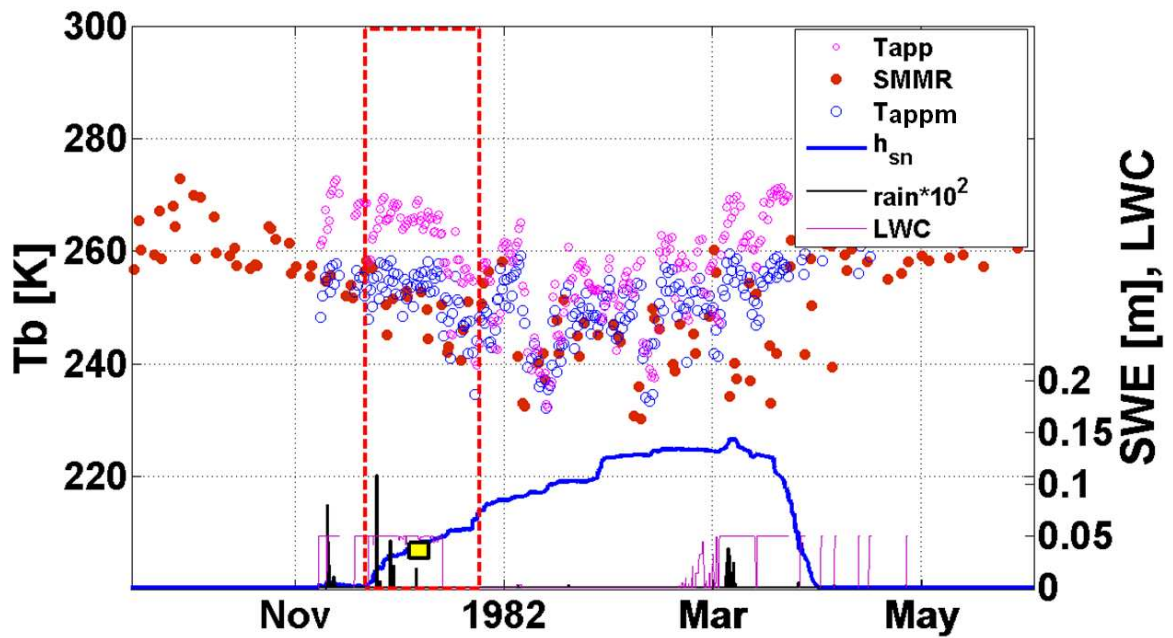


Figure 3-14 Radiation properties and corresponding physical properties of snowpack during 1982 to 1983 snow year (red dot square: Domain for liquid water assessment, Yellow square, triangle, and circle: accumulation, peak and melting, respectively, green parallelogram and diamond: wet and dry snow case for diurnal cycle study). Note: the dotted horizontal line in LWC is the maximum LWC specified for the Valdai simulation.

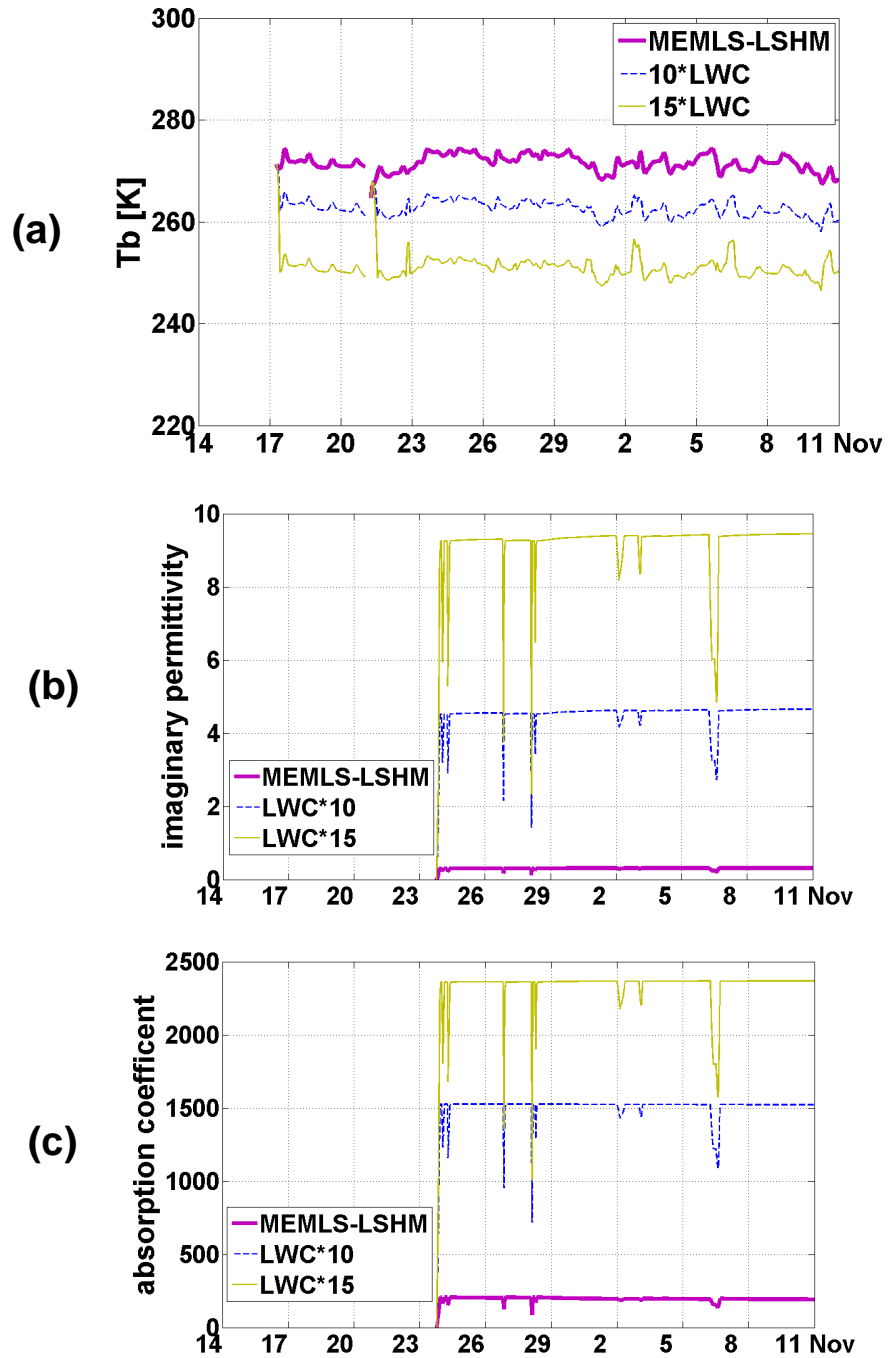


Figure 3-15 (a): Sensitivity of permittivity to LWC within the red square from Fig. 3-14, (b): imaginary part of permittivity and (c): absorption coefficient during the same time.

3.4.3. Seasonal Responses of Snowpack Radiation

The square, triangle and circle markers in Figure 3-14 identify times corresponding to different phases of snowpack evolution, respectively accumulation, peak and melting at 18:00 LST on the selected day in Valdai. Table 3-6 shows and compares the physical state and radiation parameters at each of the three snow evolution points. The snow water equivalent, SWE (h_{sn}) decreases over time as the density ρ_s monotonically increases up to the onset of the melting phase proper. Considering e_{back} the emissivity calculated by dividing T_b by the surface temperature T_s , the outgoing radiation to the atmosphere from the internal snowpack D_i decreases with increasing snow surface transmissivity ($1-s_i$). The decrease in the interface reflectivity s_i is due to the increasing real part of refractive index of snowpack proportional to real part of permittivity. Because melting processes involve both mass and energy transfer, the evolution of an internal property such as density ρ_s represents the integrated internal energy and structure of the snowpack better than state variables such as T_s and SWE at any given time. This is consistent with early research regarding snow permittivity and density [Wiesmann and Mätzler1998].

Although the temporal evolution of brightness temperatures follows closely the evolution of snowpack temperature, T_s , discrepancies are expected as snow density changes. The most important attenuation factor in the wet snow regime is the absorption of radiation per unit length of the line of wave propagation. Consequently,

the absorption and scattering coefficients, respectively γ_a and γ_b , also decrease. Although both γ_a and γ_b in the internal snowpack decrease, the outgoing radiation from the snowpack, i.e. the brightness temperature also decreases due to decreasing interface reflectivity of the snowpack s_n at the peak of the snow accumulation season. As a result, the transmitted radiation from the snowpack expressed by $(1-s_n)D_1$ increases with D_1 . This discrepancy between increase of brightness temperature and that of actual snow temperature, T_s can be explained by the internal extinction coefficients of γ_a, γ_b , and s_n , and how in turn they affect the snowpack emissivity.

Table 3-6 Seasonal cycle of snowpack evolution with respect to physical and radiation properties.

		Accumulation	Peak	Melt
Physical Properties	T_s [K]	270.80	274.20	275.60
	ρ_s [kg/m ³]	150.71	348.32	354.60
	$h_{sn}(SWE)$ [m]	0.11	0.31	0.15
	LWC	0.05	0.05	0.05
Radiation Properties	ϵ'	1.50	1.90	1.92
	ϵ''	0.31	0.32	0.32
	γ_a [1/m]	195.82	181.33	180.90
	γ_s [1/m]	0.44	0.42	0.41
	r	2.4E-04	1.8E-04	1.8E-04
	T	2.4E-12	1.7E-30	2.8E-15
	E	1	0.9998	0.9998
	s_n	7.45E-06	8.85E-04	9.49E-04
	$1-s_n$	0.999993	0.999115	0.999051
	D_n	270.7	274.1	275.5
	e_{back}	0.999756	0.998932	0.998875
	T_b	270.7	273.9	275.3

3.4.4. Diurnal Cycle of Snowpack Radiation

To assess the diurnal cycle of the snowpack emission, two cases are examined for dry and wet snow snowpack regimes and for 37-V GHz, which is sensitive to scattering as a function of snow grain size, and is the most frequently used frequency for the retrieval of snow physical properties from remote sensing data (Chang et al. 1987 and many others after).

The dry snow case is from February 3rd to 4th in 1982 corresponding to the time marked by the green rhombus in Figure 3-14. Note that the overall *LWC* values are zero or negligible during the 48 hours of simulation from midnight on February 2nd to midnight on February 4th. Figures 3-16a to 3-16d show time-series of radiation parameters such as real and imaginary permittivity, and absorption and scattering coefficients compared with snow density. The real part of permittivity shows strong linear relationship with the snow density, whereas the imaginary part shows no dependence on snow density in this dry snow case. Although the absorption coefficient strongly varies with the imaginary part of the permittivity in Fig. 3-16 (d), it is comparably small vis-à-vis the wet snow case which will be discussed later. During the two-day simulation, the absorption coefficient peaks at 16:00 and 40:00 hours in the simulation corresponding to 4 PM LST, reflecting the fact that the absorption of microwave propagation reaches a maximum when the daytime heating and melting are at a peak. Finally, the scattering coefficient plays a main role of extinction behavior of microwave propagation in the dry snow regime.

The wet snow case is from midnight on December 5th to midnight on December 7th in 1981, and corresponds to the time marked by the green parallelogram in Figure 3-14. The *LWC* is always above 4 % during this period. Figures 3-17a to 3-17d depict radiation properties such as real and imaginary permittivity, and scattering and absorption coefficients compared with snow density. As in the dry snow case, the real part of the permittivity also shows distinct linear relationship with the snow density. Despite the strong relationship between the real part of permittivity and snow density, absorption and scattering coefficients are inversely related with respect to the snow density. By comparing Figure 3-17-(d) with 17-(b), note how the absorption coefficient somewhat decreases with the increasing snow density. In *MEMLS*, the absorption coefficient, γ_a is a function of the refractive index n'' ($\gamma_a = \frac{4\pi n''}{\lambda}$), and n'' is a function of the real and imaginary permittivity:

$$n'' = \frac{\text{sgn}(\epsilon'')}{\sqrt{2}} \sqrt{\sqrt{\epsilon'^2 + \epsilon''^2} - \epsilon'} \quad (3-42)$$

As ϵ' increases with the snow density, the refraction index of snow n'' decreases. The inverse relationship (dampening) of the scattering coefficient γ_b with snow density is illustrated in Figure 3-17 (c). However, the imaginary part of permittivity can significantly increase with increasing *LWC* because the imaginary part of liquid water is about 20 times larger than that of ice (Fig. 3-17d). When *LWC* is greater than 0.5, the 20 fold increase factor leads to increasing both the real and imaginary permittivity of the

snowpack. This explains why γ_a has above 190 1/m in the wet snow case. Therefore, the absorption coefficient, γ_a is a primary factor in the extinction of radiation propagating through the wet snowpack due to large values of the imaginary part of permittivity. This illustrates the importance of how to characterize the snowpack's water retention capacity (e.g. effective porosity) in order to relate the microwave behavior to the physical properties of wet snow. In the case of dry snow, the snow structure (porosity, layering, metamorphosis, etc), which can strongly impact snow density, is essential.

In summary, the real part of permittivity ϵ' is sufficient to estimate snow density in dry snow. The imaginary part of permittivity ϵ'' on the other hand is key in the case of wet snow. Quantifying how much liquid water including water percolation and snowpack surface water ponding can be retained in wet snow is key to parameterize its radiative behavior. One interesting implication of this behavior is that instead of using physical properties to describe snowpack condition, radiative properties such as permittivity and absorption and scattering coefficients can provide an alternative assessment of snowpack conditions.

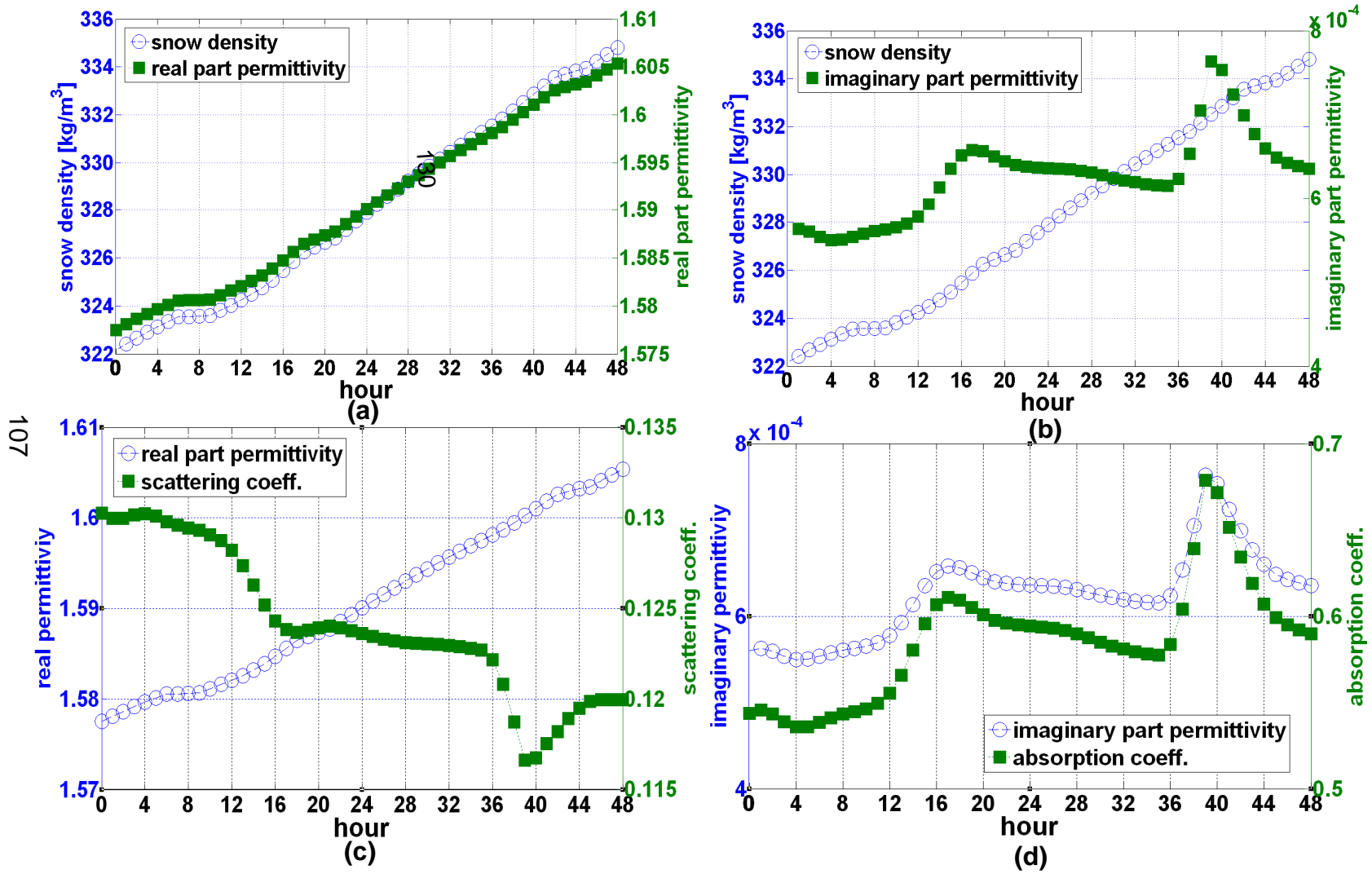


Figure 3-16 Temporal evolution of radiation properties with snow density in the *dry snow* regime on February 3rd to 4th in 1982.

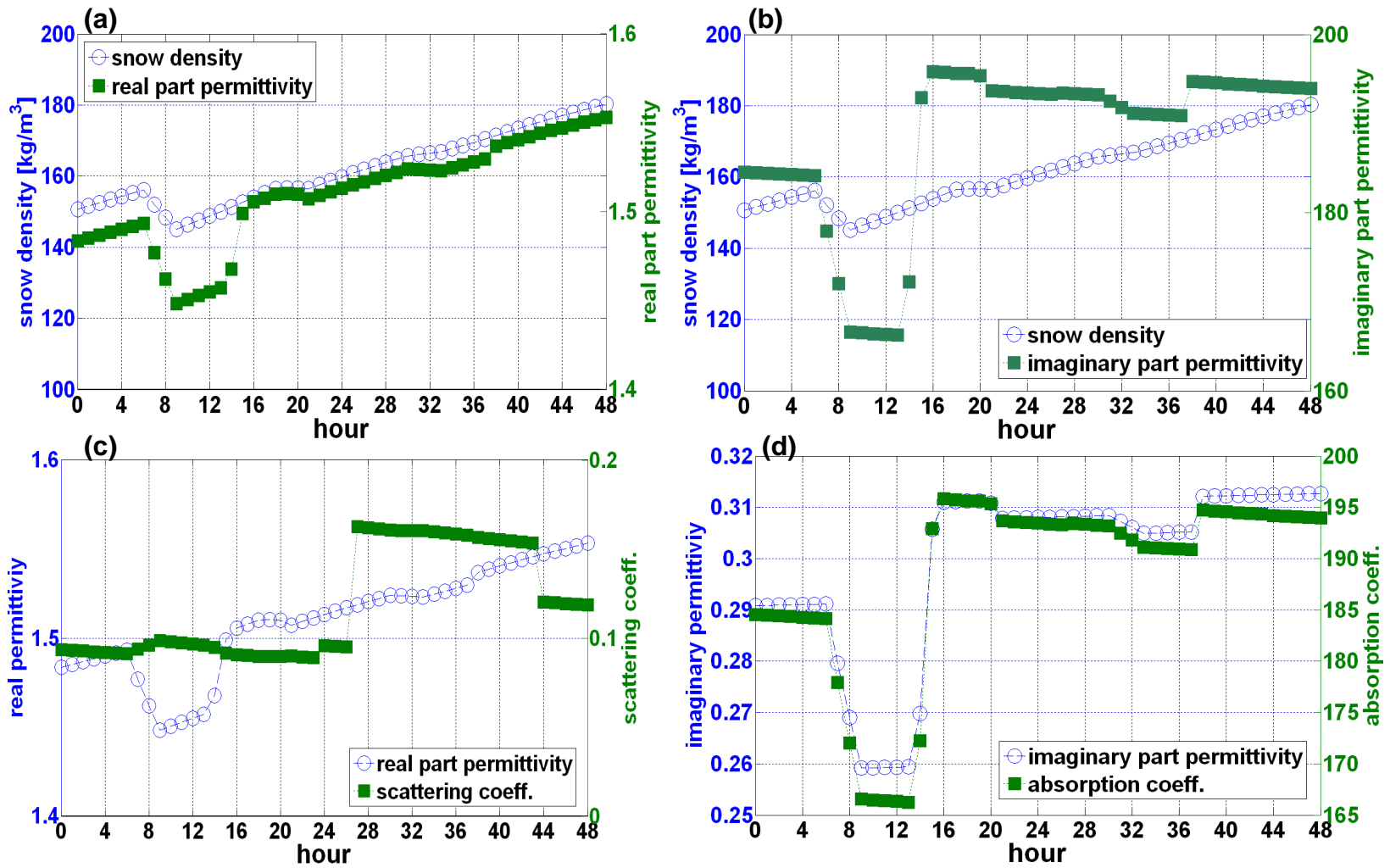


Figure 3-17 Comparison of radiation properties with snow density in the *wet snow* regime on December 5th to 7th in 1981.

3.5. Comprehensive Simulation of CLPX Conclusion

The focus here is on the application of LSHM-MEMLS to the Fraser MSA during CLPX (Fig. 3-2). Results of the LSHM snow hydrology forced by RUC40 (40 km resolution) were discussed in Section 3-3 (see also Figure 3-7). Figure 3-18a and 3-18b show the simulated snowpack physical temperature, T_s compared with the snow pit profile observations during February and March, 2003 within the Fraser, MSA. Multiple points at each date reflect measurements at various sampling depths. The LSHM snowpack temperature, T_s is relatively well located around the mean value of the observed snow temperatures from snow pit data. Figures 3-19 and 3-20 show the simulated brightness temperatures T_b compared against *SSM/I* and *AMSR-E* observations at their respective frequencies, H and V polarizations from October 2002 to June 2003. In Figures 3-19 and 3-20, the simulations show that LSHM-MEMLS T_b s match generally well the observations especially during the melting phase. During the accumulation phase in winter there is some bias, but more importantly the model is not capturing the concave shape that is implied by the increasingly colder brightness temperatures observed by *SSM/I* and *AMSR-E* consistent with increasing snow density. A review of Fig. 3-7 indicates that the model underestimates snow density which can explain this behavior at least in part. This effect should be especially critical for the vertical polarization (Rees et al. 2010). Note that the presence of trees, which is considered an important microwave signal in CLPX (Tedesco et al. 2005), is not explicitly accounted in MEMLS, and in the LSHM the effect is only accounted for in

terms of fractional vegetation cover. Nevertheless, the lowest snow temperature in March is well simulated and snowpack warming till the initiation of the snowmelt in May is well described by the increase of the simulated brightness temperatures even at 37GHZ.

Error statistics for the entire period of simulation from October 2002 through June 2003 are summarized in Table 3-7 using the same measures as described in Section 4.1. Previously, [Andreadis et al. (2008)] and [Durand et al. 2008] focused on modeling a dry snow regime period in February 2003 at small spatial scales. [Andreadis et al. 2008] used the AMSR-E (25 km spatial scale) for the entire month of February. The Variable Infiltration Capacity (VIC) hydrology model was coupled with DMRT to simulate the bulk layer snowpack including snow density, snow temperature, snow depth, and snow grain size. They also compared their model results against one week (February 18-26, 2003) of observations at GBMR-7 under dry snow conditions. [Durand et al. 2008] used point data from GBMR-7 for six days (February 19-24) also in the dry snow regime. They imported observed snow pit stratigraphy and measured snow properties directly into MEMLS, and [Tedesco et al. 2005] conducted a similar study at GBMR-7, but using DMRT instead of MEMLS. [Wójcik et al. (2008)] used a version of the HUT model as well as DMRT and MEMLS coupled to VIC for simulations at two sites within the Fraser MSA February-May 2003, thus including both dry and wet snow regimes over a four month period. Because it encompasses a longer period of time, and thus more robust statistics, Table 3-7 also includes error statistics reported by [Wójcik et al. 2008] for the

comparison statistics with AMSR-E. Despite the spatial scale disparities and the differences in ancillary data availability, and duration of simulations (days versus snow season in this study), and different snow regimes (both wet and dry, accumulation and melting phases in this study), the error statistics of end-to-end LSHM-MEMLS brightness temperature estimates are in line with previous studies, and even consistently better for the vertical polarization, especially at 18 and 37 GHz. Also, note that the error statistics against AMSR-E are better than against SSM/I.

Dramatic changes in emissivity behavior between wet and dry snow regimes are illustrated in Figures 3-21 and 3-22 that illustrate the effect of the snow liquid water content on the increase of the brightness temperature. First, Figure 3-21 (a) shows the volume scattering effects on the decrease of the emissivity as the snow accumulates during early winter. Abrupt increases of snow emissivity at 37 GHz V are consistent with the increases of the brightness temperature at that point of time. Based on Eq. (3-22) of the outgoing radiation, D , the brightness temperature of the snowpack increases due to increased snow wetness. In mid-February, around February 14th, there is no significant increase in snow wetness (Fig. 3-21b) at the scale of the Fraser MSA (or RUC cell). However, a simulation using LSHM-MEMLS for GBMR-7 using the forcing from the local tower, shows that rainfall was observed locally, which caused a short-duration increase in simulated brightness temperatures (Fig. 3-22) due to the transient increase of LWC in the snowpack from rainfall, as well as subsequent warming due to latent heating release as the rainwater freezes.

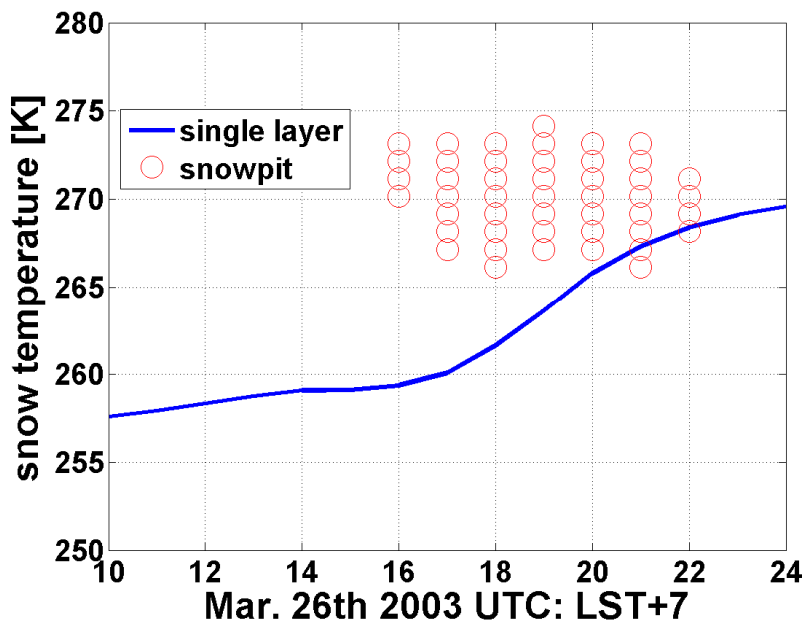
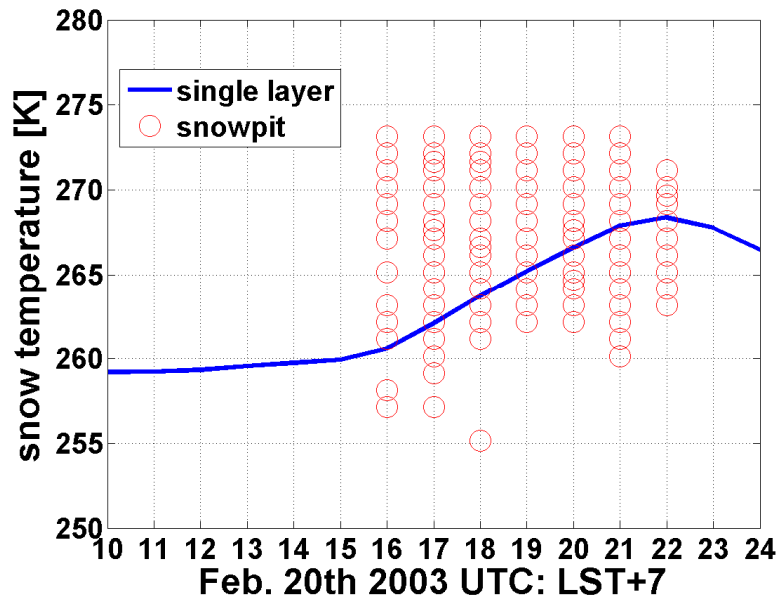


Figure 3-18 Snow temperature simulation compared with snow pit measurement in Feb and Mar. 2003 during CLPX located only in Fraser, MSA

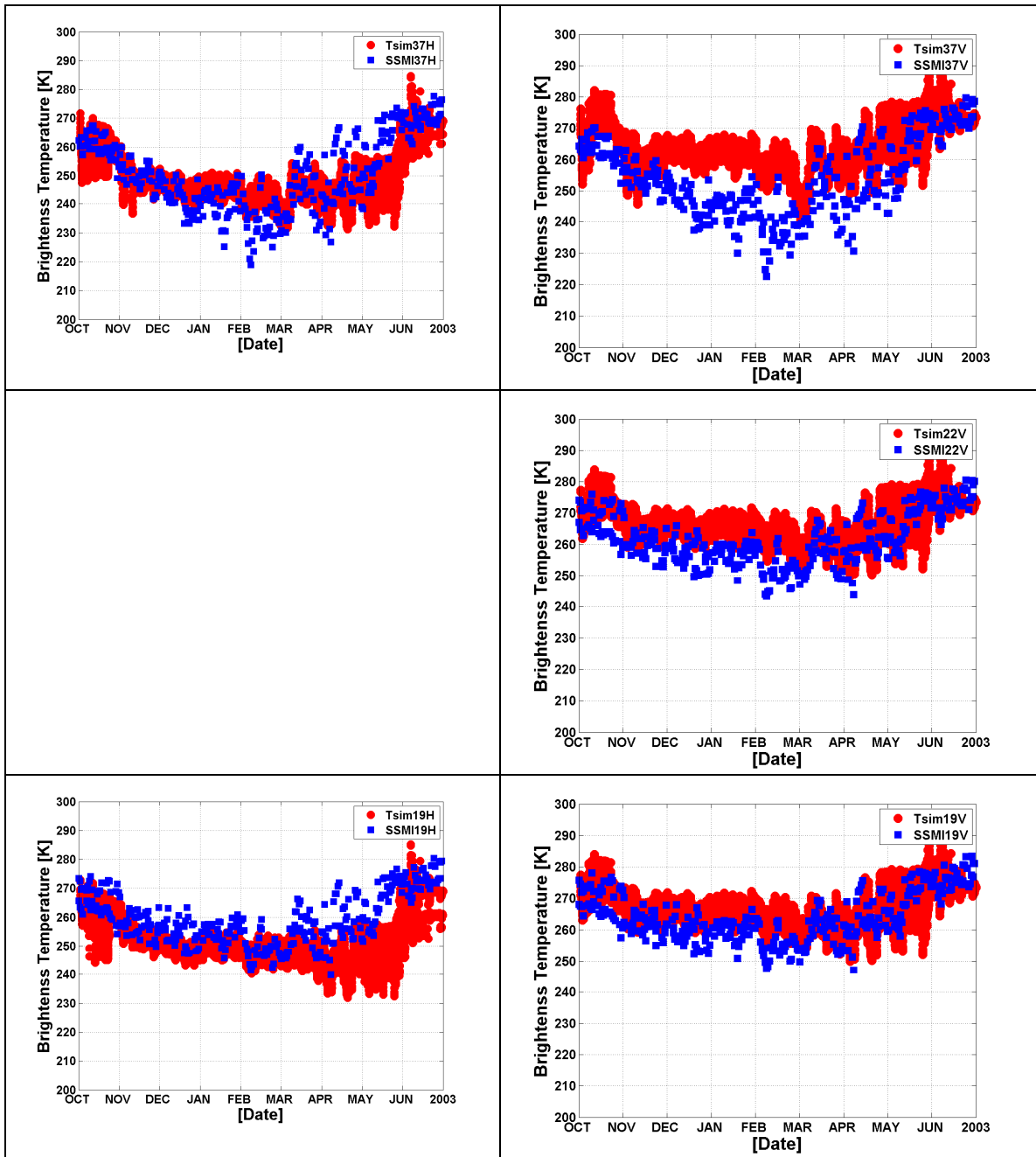


Figure 3-19 Inter-Comparison among SSM/I (blue filled circle), MEMLS-LSHM (red star) at 37.0, 22.2, and 19.35 GHz H/V (22.2 H is not available).

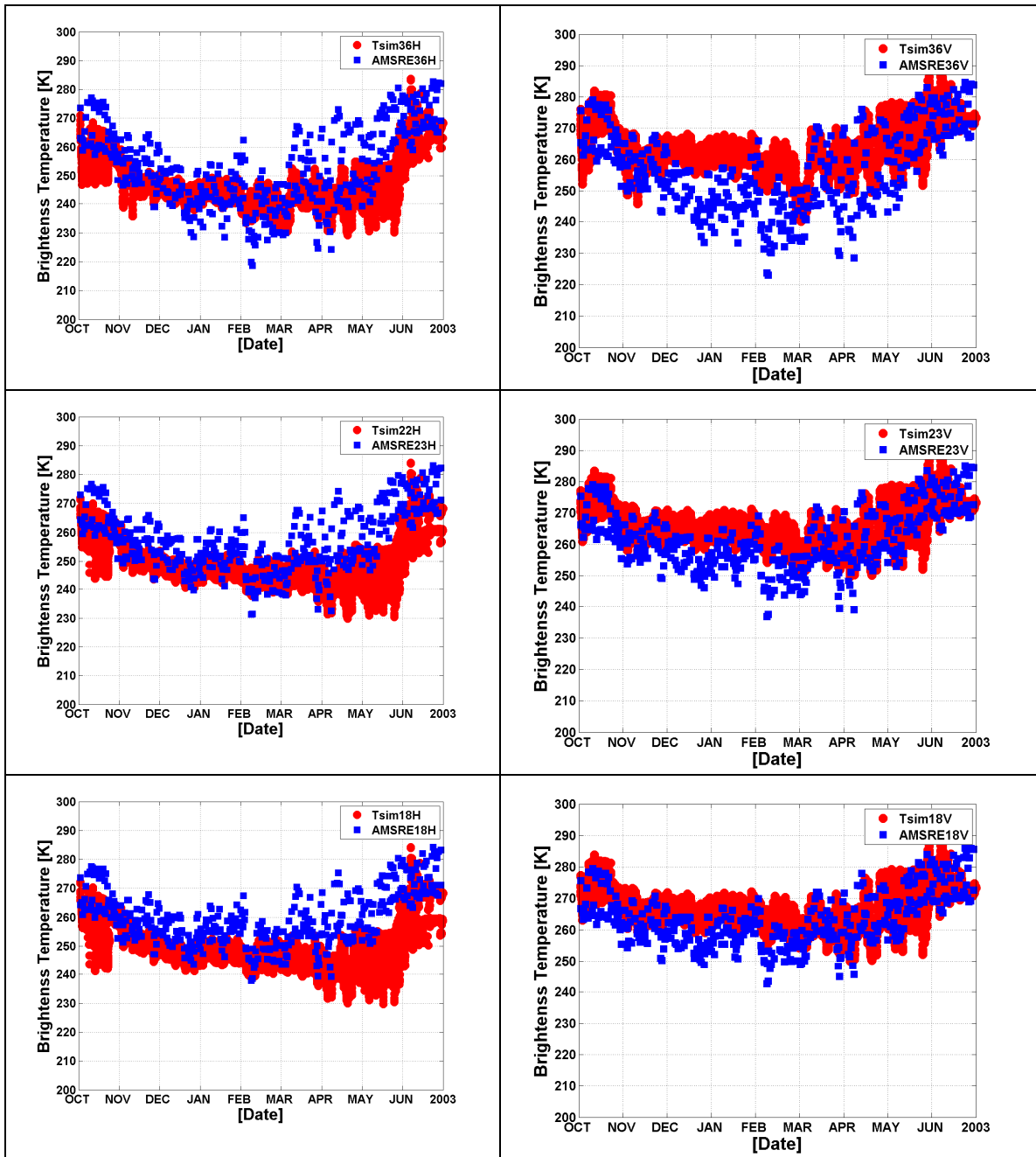
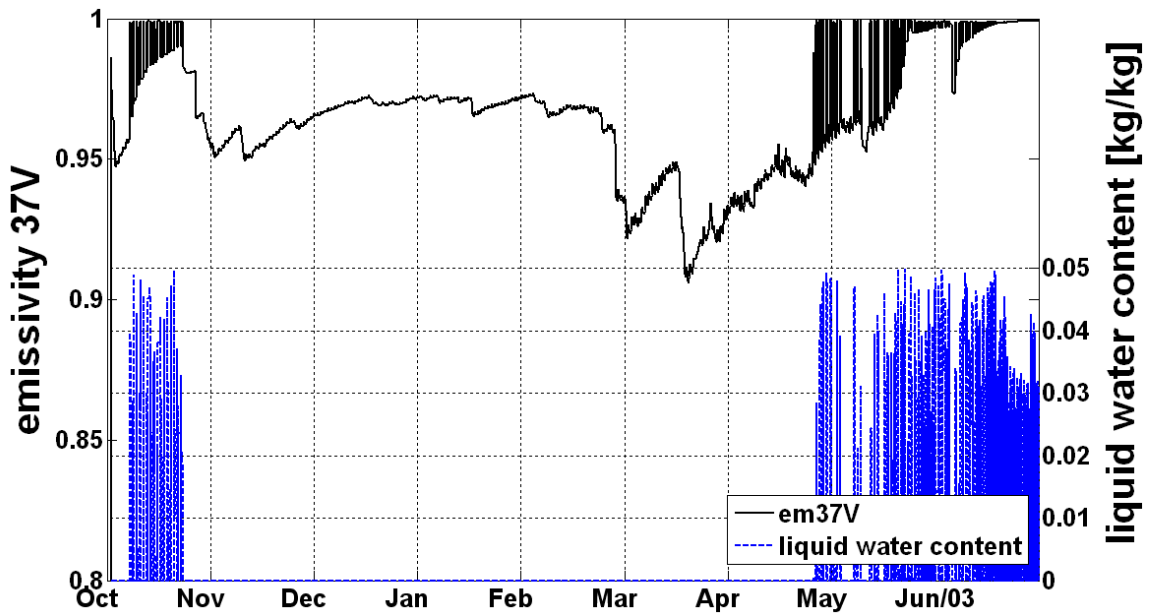
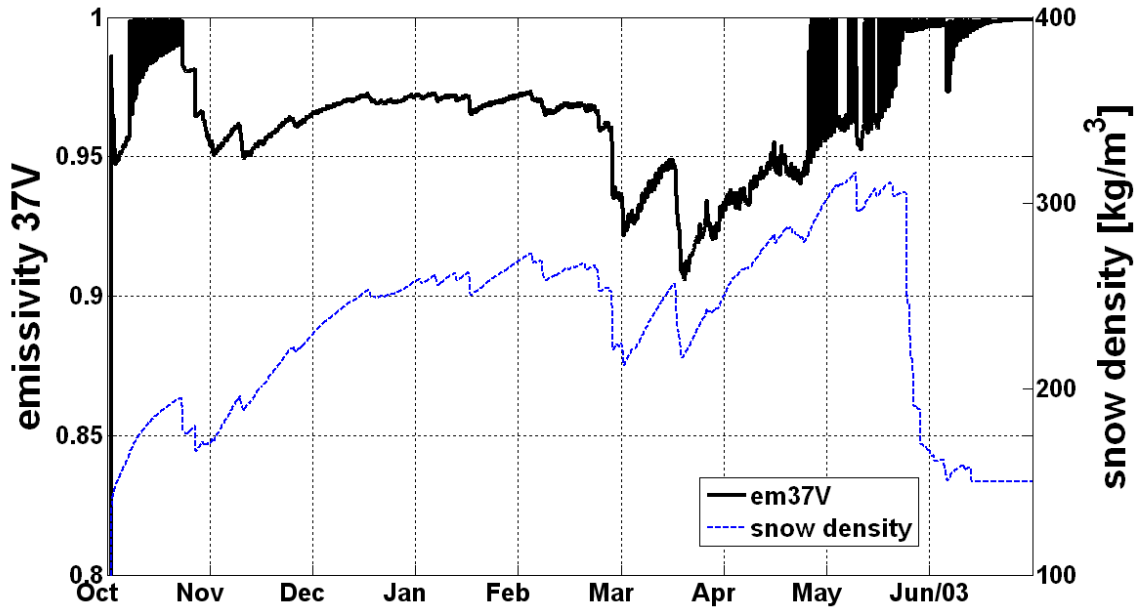


Figure 3-20 Inter-Comparison among AMSR-E (blue filled circle), MEMLS-LSHM (red star) at 36.5, 23.8, and 18.7 GHz H/V.

Table 3-7 - Intercomparison of error statistics using the correlation length, p_{ec} based on the classification by Mätzler (1996), for the Val dai and CLPX case-studies reported here and results from the literature: Wójcik et al. 2008 [W08] Note: 22 GHz H-polarization from SSM/I is not available.

		H			V		
		<i>Valdai</i>	<i>CLPX (SSM/I/AMSR-E)</i>	<i>[W08]</i>	<i>Valdai</i>	<i>CLPX (SSM/I/AMSR-E)</i>	<i>[W08]</i>
18~19GHz	<i>Bias</i>	15.23 (T_{appm})	-10.58/-8.83	---	-2.06 (T_{appm})	6.89/4.99	---
	<i>ME</i>	15.40 (T_{appm})	10.78/9.83	8.46	5.30 (T_{appm})	9.51/6.89	8.1
	<i>RMSE</i>	17.18 (T_{appm})	13.54/12.26	10.21	6.90 (T_{appm})	11.55/8.29	9.7
22-23GHz	<i>Bias</i>	10.27 (T_{appm})	--- /-6.85	---	1.97 (T_{appm})	2.02/6.12	---
	<i>ME</i>	10.96 (T_{appm})	--- / 8.65	---	5.49 (T_{appm})	5.69/7.85	---
	<i>RMSE</i>	13.17 (T_{appm})	--- /11.10	---	6.94 (T_{appm})	6.87/9.39	---
36~37GHz	<i>Bias</i>	17.90 (T_{app})	-3.99/-4.36	---	4.53 (T_{appm})	6.89/8.82	---
	<i>ME</i>	18.81 (T_{app})	7.71/8.52	12.47	7.98 (T_{appm})	9.51/10.81	12.02
	<i>RMSE</i>	21.44 (T_{app})	10.56/10.92	14.39	10.28 (T_{appm})	11.55/13.08	14.37



(b)

Figure 3-21 Snow emissivity at 37 GHz V versus snow density (a), and versus snow wetness, LWC (b) [kg/kg].

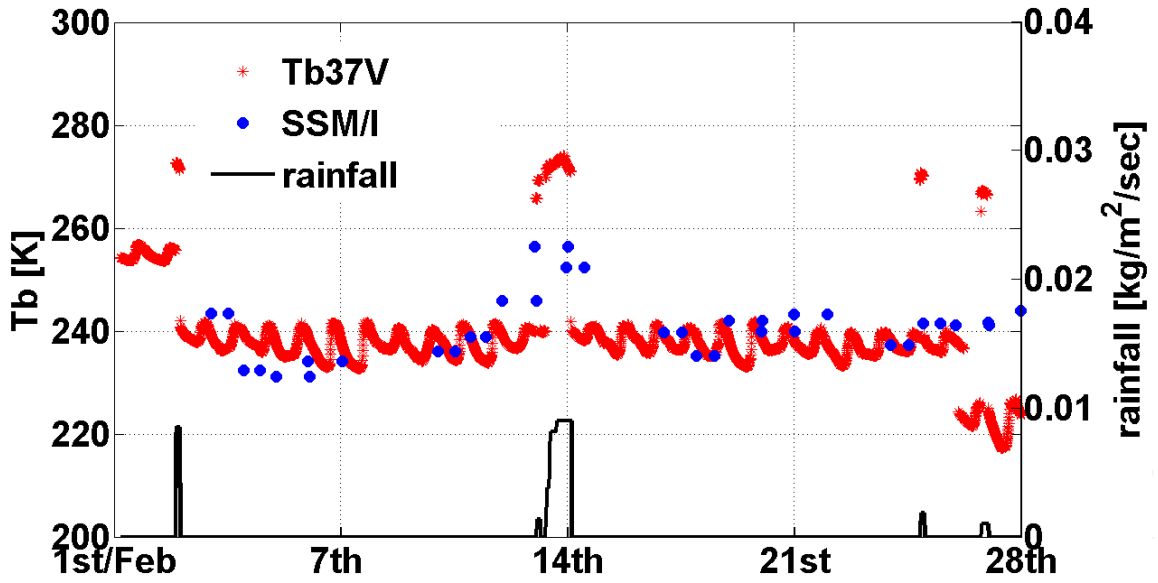


Figure 3-22 Increase of brightness temperature induced by snow wetness at 37-V GHz SSM/I (blue filled circle), T_b (red star), and rainfall (solid line) during February, 2003

3.6. Conclusion

A coupled snow hydrology-emission model LSHM-MEMLS [Devonec and Barros 2002, Wiesmann and Mätzler 1999, and Mätzler and Wiesmann 1999] was tested independently for two very different climatic and physiographic regions (Valdai and CLPX) for both wet and dry snow regimes over multiple years with good results. These applications demonstrate transferability of the modeling system, and its potential utility in large-scale retrieval over large areas with limited if any ground-based observations to constrain the model or for data-assimilation. Despite overall good skill as demonstrated by relatively low errors, one weakness was identified with respect to the simulation of the radiative behavior of the snowpack, especially for horizontal polarization, when ice layers (ice lenses) form due to freezing of liquid water either due to daytime melting or due to rain-on-snow events. Another likely source of error is the presence of vegetation, which is not explicitly represented in the model. Furthermore, it was established that a more accurate estimation of snow density especially in the case of wet snow regimes would be important to improve skill for vertical polarization. One approach to address these weaknesses would be to develop a multi-layer snow hydrology model to capture heterogeneities in the vertical structure of the snowpack due to rain-on-snow and melting events, and to capture snowpack gradients in water content that change its radiative behavior. In addition, a multilayer representation of the snowpack allows taking advantage of the multi-layer structure in MEMLS to describe the extinction

behavior of radiation transfer inside the snowpack. Also, research toward evaluating the parameterization of the snow grain size, here inferred from the correlation length p_{ec} , is necessary because it is a governing parameter in the estimation of the scattering coefficient γ_b and of the surface roughness of the snowpack [Roy and Mätzler 2004]. Significant improvements with locally calibrated atmospheric correction parameters in Valdai suggest there is an opportunity to further investigate the effectiveness of atmospheric correction algorithms currently used in operational retrievals, toward developing location specific optimal parameterization making use of global datasets such ERA40 for example.

CHAPTER 4:
**Characterization of microwave signatures of snowpack using Multi-layer
Snow Hydrology Model**

4.1. Introduction

After the launch of LandSat and several NOAA satellites equipped with sensors operating over a wide range of frequencies including visible and infrared imagers and microwave radiometers, remote sensing of the cryosphere experienced a big surge in research toward development of retrieval algorithms [Rango et al. 1985]. Generally, the ultimate goal of such research is to map ice sheets, glaciers, and snowpack properties including snow covered area, snow depth, snow wetness and snow water equivalent especially in regions of remote access or inhospitable climate and terrain where ground-based measurements are not feasible and aircraft based measurements are impractical. Recently, the potential impacts of climate variability and change, and especially warming of the lower troposphere and the Earth surface have brought issues such as the long-term sustainability of glaciers and ice-sheets as well as the extent of snow cover and snow water equivalent to the forefront of climate research [NRC Decadal Survey, 2007]. Indeed, snow cover extent and composition are critical elements of the surface radiative properties, and thus a key governing factor in the surface energy budget of the planet. Furthermore, because it stores precipitation temporarily during the cold season for release during the warm season, snow accumulation plays also a critical role in the water balance of vast regions of the world, such as the western U.S. which depend on it for water resources [Mote et al. 2005].

Satellite-based remote sensing of snow originally relied on physically-based empirical relationships between the radiative behavior at 37GHz (V or H

polarizations), the most sensitive frequency to changes in snow microstructure (e.g. grain size distribution), the radiative behavior at a lower frequency such as 18-19 GHz with the same polarization, and snowpack properties namely snow depth and snow water equivalent [Chang et al. 1987, Singh and Gan 2000]. Relevant sensors in this context include passive microwave radiometers such as SMMR (Madrid 1978), SSM/I (Rivers 1982), and AMSR-E (Imaoca et al. 2000) respectively on board of Nimbus-7 (Horan 1978), DMSP (Eather 1979), and AQUA (Nosek 2004) satellites. Prompted by the necessity to estimate snowpack properties at locations around the world with different terrain, soils, vegetation cover, air pollution, and overall climate, it became clear that empirical models requiring place-based calibration based on local observations could not be used reliable for operational retrievals. To address this challenge, physically-based forward models that simulate the microwave emission of the snowpack as a function of its physical properties have been developed. Among these, the Helsinki University of Technology (HUT) [Hallikainen et al. 1997, Lemmetyinen et al. 2010], the Dense Media Radiative Transfer (DMRT) model [Tsang et al. 2000], and the Microwave Emission Model of Layered Snowpack (MEMLS)[Weismann and Mätzler 1999, Mätzler and Wiesmann 1999] are the most widely used. MEMLS has been widely applied to various studies of snow hydrology and forward microwave radiation modeling [Kang and Barros 2010^b, Durand et al. 2008, Andreadis et. al. 2008, and Tedesco and Kim 2006, among others]. The multi-layer formulation in MEMLS requires input regarding the vertical structure of snow density, snow wetness, snow temperature, and the snow grain

size distribution (via a parameterization that depends on correlation length, and snowpack density and temperature). To provide this input, multi-layer snow hydrology models such as SNTHERM [Jordan 1991], CROCUS [Brun et al. 1992], and SNOWPACK [Lehning et al. 2001] have been coupled to MEMLS in various ways with success [Mätzler 2009]. Previously, Kang and Barros [2010^b] coupled a single-layer snow hydrology model with an analytical description of compaction processes and parameterization of snow microphysics from SNTHERM to a one-layer adaptation of MEMLS with good results for simulations of SMMR, SSMI and AMSR-E over several seasons. Although error statistics presented by Kang and Barros [2010^b] were better or similar to previous studies using multi-layer formulations, the forward simulations of snowpack emissivity were significantly better for the vertical polarization than for horizontal polarization at all frequencies. In addition, an evaluation of the snowpack physical properties indicated that melting was taking place faster than observed, and density (snow depth) tended to be lower (larger) during the late accumulation and ripening phases than those from snowpit observations where available. Although some of these disparities may be the result of spatial scaling discrepancies between model and observations, as well as land-cover effects (e.g. fractional vegetation cover), it is expected that a multi-layer formulation of snow hydrology should have a positive impact on the representation of vertical gradients of temperature, compaction rates and thus density, which in turn will also have an impact on microwave emission as it is possible to fully use the original multilayer formulation of MEMLS.

In this chapter, a new multi-layer snow hydrology model coupled to MEMLS (MLSHM-MEMLS) is presented which is based on a multilayer implementation of the previous single-layer snow hydrology model [LSHM, Devonec and Barros 2002]. The multi-layer model is applied to two case-studies also used by Kang and Barros [2010^b]) a multi-year simulation in Valdai, Russia to be compared against SMMR observations; and 2) a cold season (October-May) in 2002-2003 encompassing accumulation, ripening and melting phases during the Cold Land Processes Experiment (CLPX) in Colorado to be compared against SSM/I and AMSR-E brightness temperatures. In both cases a suite of ground-based observations including snow water equivalent and snow depth are available, which permit evaluation of the evolution of the snowpack physics concurrently. Because it allows us to link the microwave behavior of the snowpack at various frequencies to specific snow processes and states, these studies also provide an opportunity to better understand the utility and sensitivity of satellite-based observations.

Section 4-2 introduces a new multi-layer snow evolution model (LSHM-MEMLS) and describes the mass and energy balance algorithms. Data used to force the coupled LSHM-MEMLS and to evaluate the model simulations are described in Section 4-3. Section 4-4 presents analysis of the results and discussion for Valdai, whereas the CLPX case-study is presented in Section 4-5. Synthesis and conclusion are presented in Section 4-6.

4.2. Model Description

The basic structure of the snow hydrology model is the same as the bulk layer approach [Kang and Barros 2010^b] except for the introduction of a snow layering algorithm that treats the mass and energy balance and snow compaction equations on a layer by layer basis using 1st order finite-difference approximations to describe vertical gradients. The model is coupled to the original multi-layer formulation of MEMLS. The purpose of the coupled MLSHM-MEMLS model is to characterize the microwave behaviors of the snowpack throughout the entire water year from accumulation, through ripening and melting phases. When needed, the same atmospheric correction scheme described by Kang and Barros [2010^b] is applied here to the brightness temperatures at the top of the snowpack.

4.2.1. LSHM-MEMLS

The multi-layer snow hydrology model follows the governing equations of mass and energy balance of the land surface hydrology model (LSHM) [Devonec and Barros 2002]. The difference is that the layers are divided and compacted as the snow depth increases with precipitation or decreases due to snowmelt. Also, liquid water percolation between the snow layers and between the bottom snow layer and the upper soil layer is explicitly resolved. A schematic view of the stacked snowpack is shown in Figure 4-1. Each snow layer is characterized by state variables such as layer thickness, snow temperature, snow water equivalent, bulk density, and liquid water. Snow layers begin to accumulate from the bottom (layer 1) up to the top layer (layer n). The mass

flow exchange between layers below the top layer is governed by liquid water flow when melting occurs, and during rain-on-snow events. The integrated effect of diffusion in the vapor phase, which is actually an important process at short time-scales determining the evolution of snowflake morphology after snowfall, is assumed here as negligible, though this is a crude approximation at short time-scales (~ few hours) which may have important implications when metamorphic processes are important such as during the formation of depth hoar. The mass balance equation of each layer is expressed by:

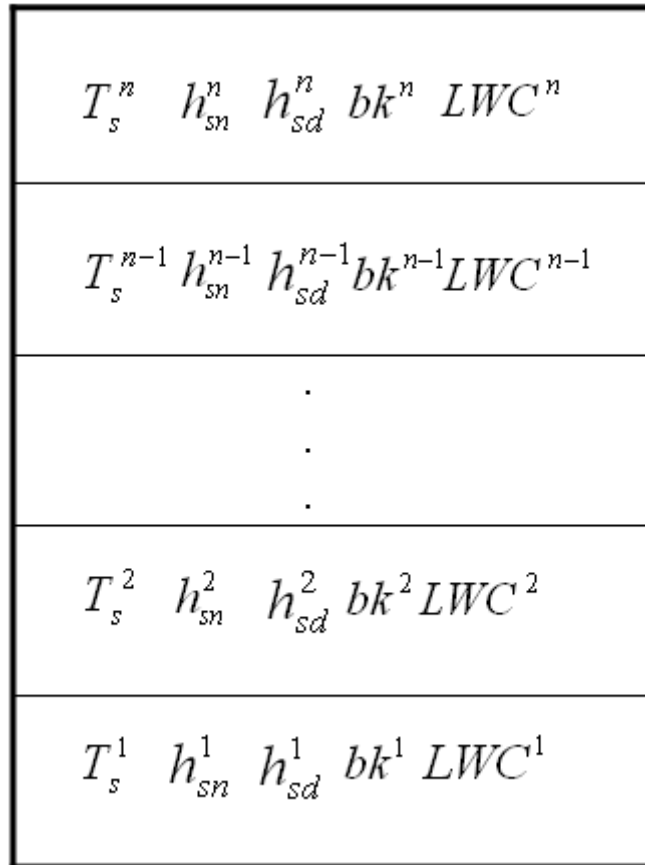


Figure 4-1 Schematic view of snow layers containing snow temperature, snow water equivalent, snow depth, snow density, and liquid water content at each snow layer.

$$\frac{dh_{sd}^j}{dt} = \frac{1}{\rho_w} \left(P_{sn}^j + xP_r^j + E_{sk}^{snow,j} \right) - \Phi_{sn}^j \quad j=1 \text{ to } n \quad (4-1)$$

Where ρ_w is the density of water, E_{sk}^{snow} is the snow skin evaporation, P_{sn} is precipitation in the form of snow [m/s], xP_r is the accumulated precipitation from rain-on-snow events [m/s]. P_{sn}^j and xP_r^j are zero when j is not equal to n . And Φ_{sn}^n is the snowmelt flux toward the lower layer:

$$\Phi_{sn}^j = \rho_w \frac{dh_{sm}^j}{dt} \quad j = 1 \text{ to } n \quad (4-2)$$

Where h_{sm}^j is net the amount of liquid water from snowmelt or rainfall in layer, j .

This is obtained from the energy balance equation.

When the snow depth at layer j layer, h_{sd}^j is less than a specified maximum criterion, h_{sd}^* , all related mass terms such as h_{sd}^j and h_{sn}^j are combined whereas T_s^j , h_{sd}^j , and the layer density bk^j are depth-averaged using as weights the snow layer thickness at the previous and current time-steps similar to [Jordan 1991]:

$$T_{s\ comb} = \frac{h_{sn}^m \cdot T_s^m + h_{sn}^{m-1} \cdot T_s^{m-1}}{h_{sn}^m + h_{sn}^{m-1}} \quad (4-3)$$

$$h_{sd\ comb} = \frac{h_{sn}^m \cdot h_{sd}^m + h_{sn}^{m-1} \cdot h_{sd}^{m-1}}{h_{sn}^m + h_{sn}^{m-1}} \quad (4-4)$$

$$bk_{comb} = \frac{h_{sn}^m \cdot bk^m + h_{sn}^{m-1} \cdot bk^{m-1}}{h_{sn}^m + h_{sn}^{m-1}} \quad (4-5)$$

The multi layer simplified energy balance equation for the top layer n of the multi-layered snowpack at the snow-atmosphere interface is expressed as follows:

$$c_{sn}^* h_o \frac{\partial T_o}{\partial t} = FR + S_h + L_h + k_{sn} \frac{\partial T_o}{\partial z} \quad (4-6)$$

where c_{sn}^* is the heat capacity of snow [J/kg K], $h_o = h_{sn}^n$ is the snow water equivalent [m], $T_o = T_s^n$ is the snow temperature of the top layer, FR is the net (shortwave plus longwave) radiation flux [W/m²], S_h is the sensible heat transfer [W/m²], L_h is the latent heat transfer [W/m²]. The value of T_o at the initial time step is set to $(T_{air} - 2.0 \text{ [K]})$ if surface observations are not available. The specific heat capacity reflects the fractional snow covered area over the spatial scale at which the model is implemented as described in Chapter 3:

$$c_{sn}^* = c_i C_{sn} + c_s (1 - C_{sn}) \quad (4-7)$$

Where C_{sn} is the fraction of snow covered area, c_i is the heat capacity of ice and c_s is the heat capacity of the soil. The heat transfer equation between adjacent internal layers is expressed by:

$$c_{sn}^* h_{sd}^k \frac{\partial T_s^k}{\partial t} = k_{sn} \frac{\partial T_s^k}{\partial z} + k_{sn} \frac{\partial T_s^{k-1}}{\partial z} \quad k=2, \text{ to } n \quad (4-8)$$

$$c_{sn}^* h_{sd}^1 \frac{\partial T_s^1}{\partial t} = -G_h = k_s \frac{\partial T_d}{\partial z} \quad k = 1 \quad (4-9)$$

Where h_{sd}^k is the k^{th} snow depth [m], T_s^k is the k^{th} snow temperature, T_d is the soil temperature [K], G_h is the heat flux at the interface between the bottom layer of the snowpack the top soil layer, k_{sn} is the heat conductivity of snow mixture [W/(m K)] and k_s is the heat conductivity of soil [W/(m K)]. The heat conductivity of soil is expressed as per [Jordan 1991]:

$$k_{sn} = \left(k_a + 7.75 \times 10^{-5} b k^k + 1.105 \times 10^{-6} b k^{k^2} \right) \cdot (k_i - k_a) \quad (4-10)$$

where k_a and k_i are the heat conductivities of air and ice, 0.023 and 2.29 W/(m K), respectively.

The net radiation flux is composed of the net solar radiation, F_s , the incoming long wave radiation, F_{li} from cloud and aerosols, and the outgoing long wave radiation, F_{lo} from the ground surface. The sign convention is positive for incoming solar radiation and negative for the outgoing radiation.

$$FR = F_s + F_{li} + F_{lo} \quad (4-11)$$

F_s is determined by the sum of incoming short wave radiation, F_{si} subtracted by outgoing short wave radiation reflected from the ground surface by albedo, a_g .

$$F_s = F_{si} - a_g F_{si} \quad (4-12)$$

The albedo, a_g is a composite of bare soil, snow, and vegetated fractions.

$$a_g = C_{sn} a_{sn} + (1 - C_{sn} - C_v) a_0 + C_v a_v \quad (4-13)$$

Where C_v is the fraction of vegetation cover. The net long wave radiation is calculated by Stefan-Boltzmann's law:

$$F_l = F_{li} - F_{lo} = \sigma(\varepsilon_{am}T_a^4 - \varepsilon_sT_0^4) \quad (4-14)$$

Where ε_s and ε_{am} are emissivity of snowpack/ground surface and ambient atmosphere, respectively. σ is the Stefan-Boltzmann's constant, ($5.67 \times 10^{-8} W / m^2 K^4$).

The sensible heat flux, S_h , and the latent heat flux, L_h are parameterized by:

$$S_h = C_p \rho_a K_H |U_1| (T_1 - T_0) \quad (4-15)$$

$$L_h = L_v^* \rho_a K_L |U_1| (q_1 - q_{sat}) \quad (4-16)$$

Where subscript 1 indicates variables measured at the reference height. C_p is the heat capacity of air at the constant pressure, L_v^* is the latent heat of vaporization from liquid water to vapor, ρ_a is the air pressure, U_1 is the horizontal wind speed, T_1 is the temperature measured in the reference height, and K_H and K_L are the aerodynamic transfer coefficients for heat and vapor, respectively.

Within each layer, melting is initiated when T_s^k exceeds the melting temperature, T_i ($T_i = 273.15$ K), and the heat flux, $Q_{sn} = C_{sn} c_i h_{sn} (T_s^k - T_i)$ is used to melt the snowpack layer. As in Devonec and Barros [2002] and Kang and Barros [2010^b], the melting processes in each layer are divided into two phases: superficial and deep melting. The criterion is set based on the equilibrium temperature, T_e .

$$T_e = T_s^k + C_{sn}^* \left[(T_s^{k-1} - T_s^k) + \frac{c_i}{c} (T_s^k - T_i) \right] \quad (4-17)$$

$$C_{sn}^* = C_{sn} \cdot \min \left\{ 1, \frac{h_{sn}^k}{h_0} \right\} \quad (4-18)$$

Where C_{sn}^* is the snow depth coefficient. Light melting occurs when $T_e < T_i$, and in this case only the upper part of the layer melts to subsequently refreeze. Deep snowmelt occurs when $T_e > T_i$ and, affects the entire layer leading to a change in snow depth:

$$\Delta h_{sm}^k = \min \left\{ h_{sn}^k, \frac{c_i h_{sn}^k (T_s^k - T_i)}{L_m \rho_w} \right\} \quad (4-19)$$

Where L_m is the specific heat for fusion for ice, and ρ_w is the density of water.

The liquid water content, lw^k is the amount of liquid water that is retained in the snowpack. The maximum of lw^k at k^{th} layer is the liquid water retention capacity. Above the retention capacity, additional water is released from the snowpack as infiltration or runoff. The snow depth, h_{sn} is calculated based on the snow density which is initially set at 50.0 kg/m³ for fresh snow. After changing the snow water equivalent, h_{sn} due to the snowmelt, sublimation, rain on snow, and snowfall, the snow depth is decreased by the compaction ratio, CR [1/sec]. CR is parameterized with metamorphosis and overburden effects following [Jordan 1991]. CR controls snow depth and consequently density: CR over $k=1$ to n

$$CR = \left. \frac{1}{\Delta h_{sd}^k} \frac{d\Delta h_{sd}^k}{dt} \right|_{metamorphosis} + \left. \frac{1}{\Delta h_{sd}^k} \frac{d\Delta h_{sd}^k}{dt} \right|_{overburden} \quad (4-20)$$

$$\left. \frac{1}{\Delta h_{sd}^k} \frac{d\Delta h_{sd}^k}{dt} \right|_{metamorphosis} = -2.778 \times 10^{-6} \times C3 \times C4 \times e^{-0.04(273.15 - T_s^k)} \quad (4-21)$$

Where $C3 = C4 = 1$ if $\gamma_l = 0$ and $\gamma_i \leq 150.0 \text{ kg/m}^3$

$$C3 = \exp^{[-0.046(\gamma_i - 150)]} \quad \text{if } \gamma_i > 150.0 \text{ kg kg/m}^3$$

$$C4 = 2.0 \quad \text{if } \gamma_i > 0.0$$

$$\left. \frac{1}{\Delta h_{sd}^k} \frac{d\Delta h_{sd}^k}{dt} \right|_{\text{overburden}} = \frac{-P_s}{\eta_0} e^{-c5 \cdot 0.04(273.15 - T_s^k)} \cdot e^{-c6 \rho_s} \quad (4-22)$$

Where η_0 = the viscosity coefficient at $T = 273.15 \text{ K}$ [N s/m^2]

$$C5 = 0.08 \text{K}^{-1}$$

$$C6 = 0.21 \text{m}^3/\text{kg}$$

P_s = Pressure due to snowpack weight [N/m^2]

Where γ_i is the ice bulk density, γ_l is the liquid bulk density in the snowpack layer. The condition 'C3=C4=1' is designated for dry snow which implies the compaction due to metamorphosis is slower than for wet snow. However, if γ_l is larger than 150.0 kg/m³ when the melting occurs, snowpack metamorphosis slows down further. The overburden compaction rate is based on the pressure of the layer due to weight for unit area [P_s]. By multiplying this compaction rate with current snowpack depth layer, a new snowpack depth layer is determined. Only overburden effects were taken into consideration for the CLPX 2002 simulations.

4.2.2. Microwave Emission Model of Layered Snowpack (MEMLS)

While the bulk layer approach only considers the one layer simulation of the emissions of the snowpack, the multi-layer model has n horizontal stacks, which interact

with the radiation fluxes inside the snowpack. The description of *MEMLS* presented next follows [Wiesmann and Mätzler 1999] and [Mätzler and Wiesmann 1999] closely.

Considering planar boundaries between air-snow and snow-soil, the bulk snow layer is characterized at frequency, f , polarization, p , and incidence angle, θ by the snowpack brightness temperature T_b , the ground-snow interface reflectivity s_0 , the ground temperature T_o , the interface reflectivity s_j on top of each layer j , the thickness d_j , temperature T_j , internal reflectivity r_j , emissivity e_j , and transmissivity t_j , of each layer, the sky downwelling radiation, represented by the brightness temperature T_{sky} .

Considering one layer within the multi-layers, the outgoing radiation from the snowpack to the atmosphere above and the soil beneath can be described as follows (Figure 4-2):

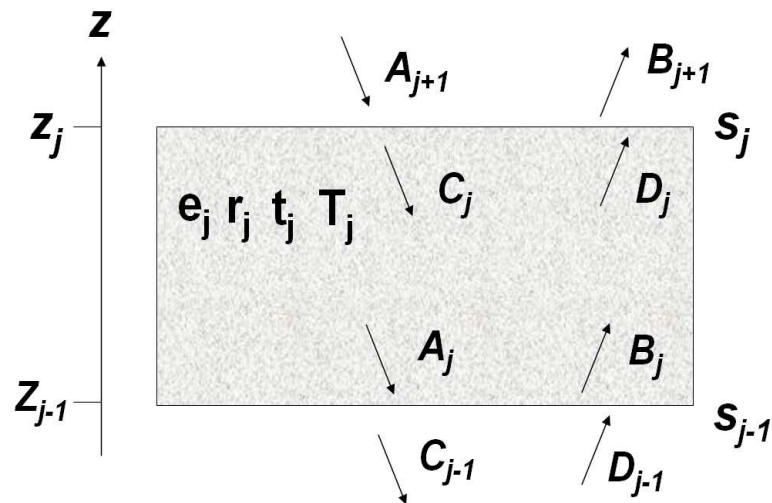


Figure 4-2 Schematic view of the incoming and outgoing microwave propagation variables of snow layers in *MEMLS*

$$A_j = r_j B_j + t_j + e_j T_j \quad (4-23)$$

$$D_j = t_j B_j + r_j C_j + e_j T_j \quad (4-24)$$

With incoming radiation from soil and atmosphere to the snowpack, respectively:

$$B_j = s_{j-1} A_j + (1 - s_{j-1}) D_{j-1} \quad (4-25)$$

$$C_j = (1 - s_j) A_{j+1} + s_j D_j \quad (4-26)$$

Adapting the MEMLS multi-layer simulation, the brightness temperature, T_b of the bulk layer is B_{j+1} ($B_{j+1} = s_j A_{j+1} + (1 - s_j) D_j$), A_{j+1} is the T_{sky} and s_j is the interface reflectivity between snow surface and atmosphere.

Equation (4-25) and (4-26) can be sorted out to the coupled system of linear equations for the temperatures A_j and D_j

$$A_j = r_j [s_{j-1} A_j + (1 - s_{j-1}) D_{j-1}] + t_j [(1 - s_j) A_{j+1} + s_j D_j] + e_j T_j \quad (4-27)$$

$$D_j = t_j [s_{j-1} A_j + (1 - s_{j-1}) D_{j-1}] + r_j [(1 - s_j) A_{j+1} + s_j D_j] + e_j T_j \quad (4-28)$$

With the matrix formation, the equations above can be rewritten:

$$A = M_1 \cdot A + M_2 \cdot D + E \quad (4-29)$$

$$D = M_3 \cdot A + M_4 \cdot D + E \quad (4-30)$$

Where A and D contains the brightness temperatures of n layers, M_1 to M_4 are n by n matrices containing r, t and e, and E and F are the n vectors with brightness temperatures at the boundaries including T_{sky} and T_{soil} . The linear algebra solution yields:

$$D = (I - M_5)^{-1} \cdot (M_3 \cdot (I - M_1)^{-1} \cdot E + F) \quad (4-31)$$

where

$$M_5 = M_3 \cdot \{(I - M_1)^{-1} \cdot M_2\} + M_4 \quad (4-32)$$

After determining D_n , the outgoing brightness temperature from the snow surface is given by B_2 which is T_b :

$$T_b = B_2 = s_n T_{sky} + (1 - s_n) D_n \quad (4-33)$$

When n is equal to 1, D_n becomes,

$$D_1 = \frac{\left[t_1 s_0 \frac{r_1 (1 - s_0) T_0 + t_1 (1 - s_1) T_{sky} + e_1 T_1}{1 - r_1 s_0} + t_1 (1 - s_0) T_0 + r_1 (1 - s_1) T_{sky} + e_1 T_1 \right]}{\left[1 - r_1 s_1 - \frac{s_0 s_1 t_1^2}{1 - r_1 s_0} \right]} \quad (4-34)$$

4.2.3. Coupled MLSHM-MEMLS Modeling

A flow chart showing the LSHM-MEMLS structure is shown in Figure 4-3. The meteorological forcing data such as air temperature, precipitation, wind and radiation drive the coupled MLSHM-MEMLS. The vertical structure of the multi-layer snowpack is described by the layer-by-layer distribution of liquid water content lw^k (kg/kg), snow depth h_{sd}^k (m), snow density bk^k (kg/m³), snow temperature T_s^k (K), and the correlation length, p_{cc}^k (m), which are used by MEMLS coupled to MLSHM-MEMLS as a function of frequency to simulate brightness temperatures and emissivity. To estimate apparent brightness temperatures at the sensor antenna when necessary using atmospheric correction, local atmospheric effects are accounted for in the calculation of the

atmospheric optical depth τ of the atmosphere based on atmospheric moisture profiles both of water vapor and liquid water obtained from operational numerical weather prediction models or reanalysis.

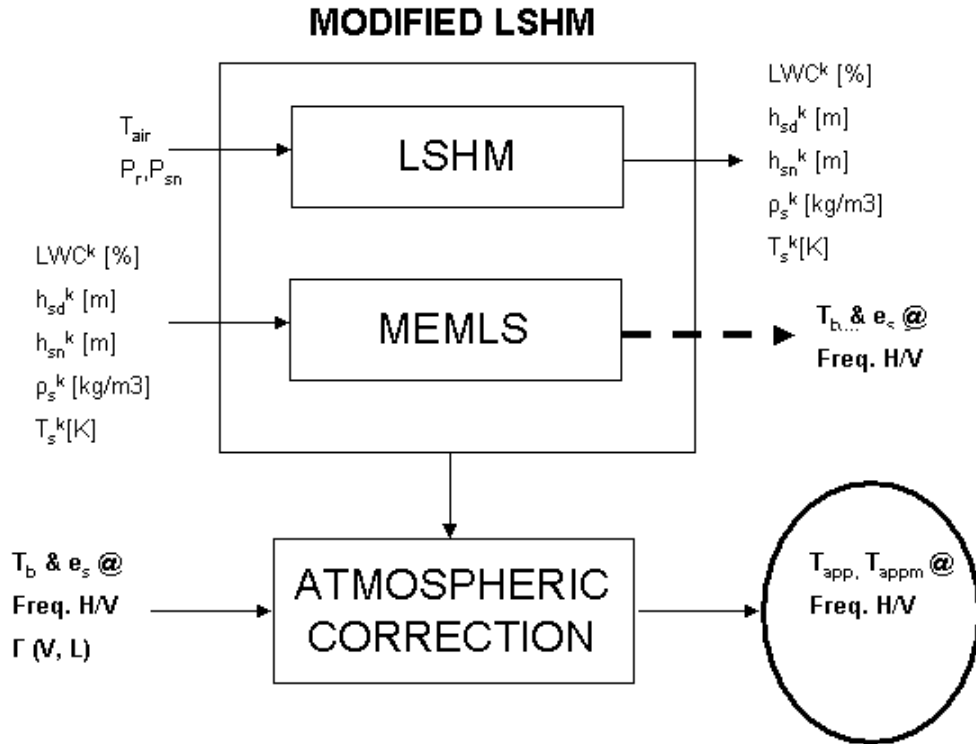


Figure 4-3 Schematic view of model flow chart for simulated and apparent brightness temperature at radiometer, T_{sim} , T_{app} , and T_{appm} using the simulation of multi-layer snowpack

4.3. Data

4.3.1. Satellite Data

For the intercomparison between simulated and observed microwave signatures of the snowpack, SMMR is used for the Valdai case-study and SSM/I and AMSR-E are utilized for the CLPX case. Basic descriptions of the satellite data presented here follow closely [Kang and Barros 2010^b] as the data are the same.

The *SMMR* was operational aboard NASA's Nimbus-7 satellites from 26 October 1978 to 20 August 1987 [Gloersen 1977]. This polar orbit passive microwave radiometer has a fixed incidence angle of 50.2° . The *SMMR* data are transmitted twice a day corresponding to ascending (mid-day) and descending (mid-night) paths. *SMMR* is a multi-channel radiometer with 10 channels and 5 frequencies of both vertical and horizontal polarizations (6.6, 10.69, 18, 21, and 37 GHz). Previous research on retrieving physical properties of snow using *SMMR* data, relied on the difference between 37 GHz and 21 or 18 GHz brightness temperatures to better capture the sensitivity of microwave behavior at 37 GHz to the snow grain size [Foster 1997]. The geographic context of Valdai, Russia is presented in Figure 4-4. Also marked are the spatial resolution of *SMMR* and the European Center Reanalysis Dataset (*ERA-40*). As illustrated, the resolution of *SMMR* is 0.25° while *ERA-40*'s grid is 2.5° . Within the coarser domain of *ERA-40*, Valdai is located in 33.25° E and 57.90° N in the lower left corner.

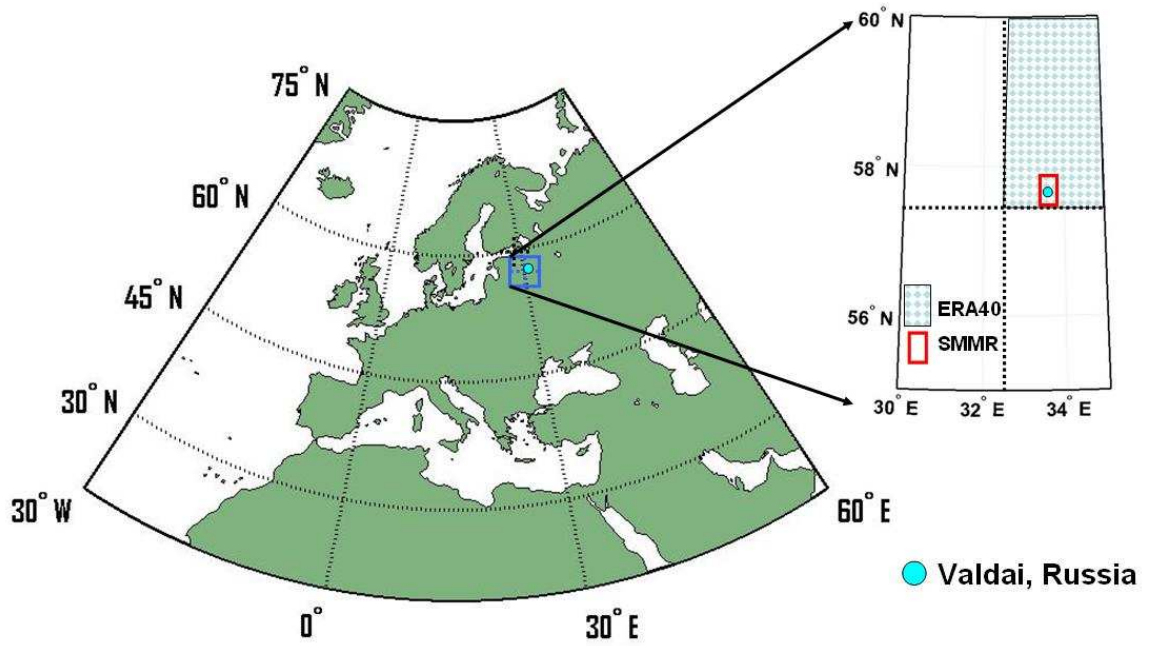


Figure 4-4 Schematic view of grid resolutions of *ERA40* (2.5 °) and *SMMR* (0.25 °) located in Valdai, Russia

The Special Sensor Microwave Imager (*SSM/I*) is carried by Defense Meteorological Satellite Program (DMSP) satellites. This passive microwave radiometer operates with seven channels, four frequencies, and orthogonal polarizations at 19.35, 22.2, 37.7, and 85.5 GHz. Within the Large Regional Study Area (LRSA) of CLPX, *SSM/I* brightness temperature data can be obtained from the National Snow and Ice Data Center (NSIDC). Figure 4-5 shows the Large Regional Study Area (LRSA) including the Fraser Meso-Cell Area (Fraser MSA) that is used in this study for detailed simulations analysis. For this study, observed brightness temperatures at 19.35, 22.2, and 37.7 GHz H/V were selected to be close to 18, 21, and 37 GHz V/H in the case of SMMR. *SSM/I* data resources and detailed description are publicly available at (<http://nsidc.org/data/nsidc-0144.html>).

The Advanced Microwave Scanning Radar-EOS (*AMSR-E*) is carried by NASA's Earth Observing System (EOS) Aqua satellite since May 4th, 2002. *AMSR-E* is a passive microwave radiometer operating with 6.9, 10.65, 18.7, 23.8, 36.5, and 89.0 GHz H/V. *AMSR-E* data designated for CLPX from February 1st to May 30th 2003 were obtained from the CLPX web site. The UTM grid size of 25 km is selected for the comparison study. Given the grid resolution, the cell for Fraser Meso-Cell Study Area (MSA) was used to extract *AMSR-E* brightness temperatures at 18.7, 23.8, and 36.5 GHz H/V. Data and metadata are available at (<http://nsidc.org/data/nsidc-0145.html>).

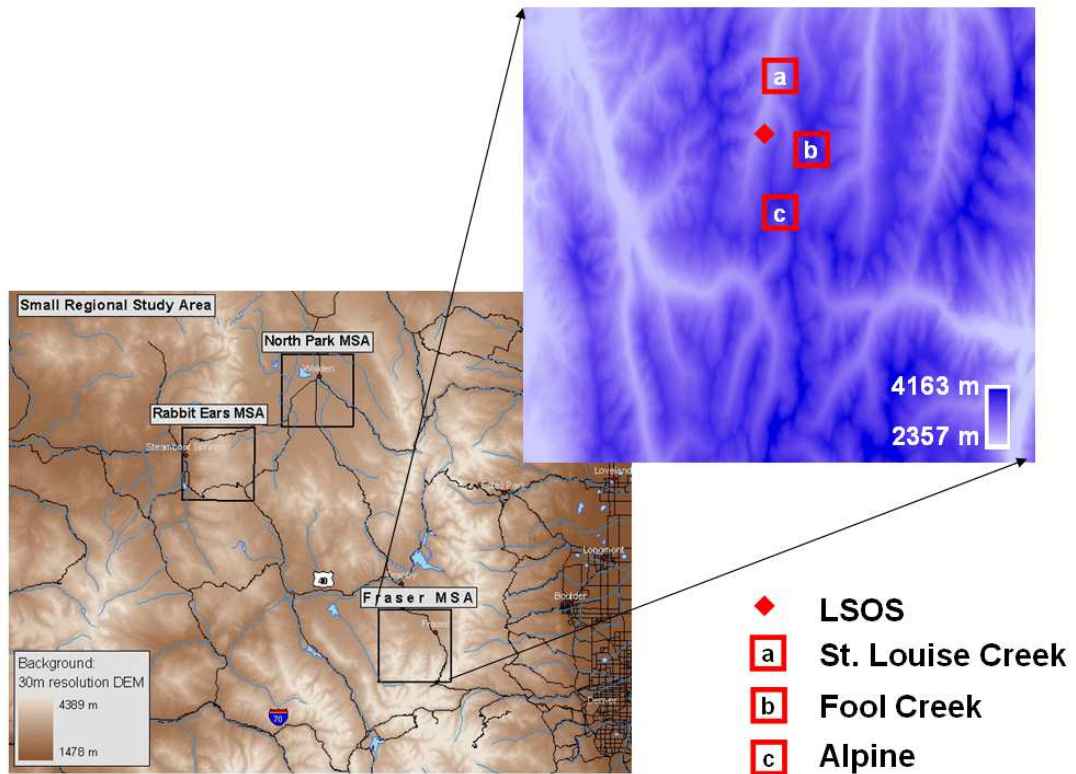


Figure 4-5 Small Regional Study Area for CLPX 2002 including our application site, Fraser MSA, also corresponding to GBMR-7 site and Local Scale Observation Site (LSOS), in the lower right corner. (L:LSOS, S: St. Louis Creek, F: Fool Creek, A: Alpine) Sources: [http://nsidc.org/data/docs/daac/nsidc0173_clpx_ISA_corner_met/ and http://nsidc.org/data/clpx/clpx_pits.html]. GBMR-7 is located in the Local Scale Observation Station, LSOS, in Fraser, MSA.

4.3.2. Reanalysis Data

In order to account for atmospheric attenuation due to the absorption and scattering of radiation between the snowpack and the satellite borne radiometer, vertical profiles of liquid water content (L), and precipitable water (V) were extracted from ERA-40 ECMWF (European Centre for Medium-Range Weather Forecasts) Reanalysis data set at 00:00 and 12:00 UTC were interpolated to the times of SMMR overpasses at Valdai. Note that besides the time difference between overpass time and ERA-40 moisture profiles, there is a substantial difference among the spatial scale of the Valdai case-study (effectively one location), the spatial resolution of SMMR ($0.25^\circ \times 0.25^\circ$) brightness temperature fields, and the spatial resolution of ERA-40 products ($2.5^\circ \times 2.5^\circ$), which adds uncertainty to the estimation of atmospheric correction effects due to the large spatial and temporal variability of atmospheric moisture. Nevertheless, this is the best available data for this purpose at the specific time and location of interest. A detailed description of ECMWF ERA-40 is provided by [Uppala 2005]. The vertical liquid water (L) and the precipitable water (V) for the grid element that contains Valdai, Russia peak during the summer season (June, July and August) and decrease during the winter time in this region (see Fig. 3-8 in Chapter 3). Therefore, atmospheric attenuation effects can be significant In Valdai during fall and spring seasons.

4.3.3. Forcing Data for Valdai and CLPX 2002

Motivated by the Project for the Intercomparison of Land Surface Process

Schemes [PILPS, Henderson-Sellers et al. 1993 and 1995], the PILPS phase2d data for Valdai, Russia was used by [Devonec and Barros 2002] to evaluate the representation of snow hydrology in the LSHM. The Valdai research station is located within a grassland watershed in a forested region south of St. Petersburg (57.68N, 33.18E). PILPS provides 18 years (1966-1983) of hourly hydrological and meteorological data aggregated to the catchment scale including rain, snowfall, wind, incoming solar radiation, soil moisture, streamflow, snow water equivalent, and evaporation in the region. The Valdai datasets allow us to simulate brightness temperatures using *LSHM-MEMLS* which can be compared with *SMMR* data from 1978 to 1983. The Rapid Update Cycle (RUC-40) for the CLPX case study is a subset of the Mesoscale Analysis and Prediction System forecasts (MAPS). (Benjamin et al. 1997 http://nsidc.org/data/docs/daac/nsidc0211_clpx_ruc40/). RUC-40 data are available at 40 km resolution on an hourly basis, and the output variables for the grid-cell containing the Fraser, MSA were selected as forcing for the LSHM-MEMLS.

4.3.4. Ground Truth Data from CLPX 2002

A detailed description of CLPX is provided by the National Snow and Ice Data Center (NSIDC) CLPX website (<http://nsidc.org/data/clpx/>). Interdisciplinary research on cold region hydrology from modeling to field measurements was conducted from 2002 to 2003 spring season [Cline 2003]. In order to characterize a variety of topographical and ecological responses induced by snow hydrological processes, eastern parts of the

Rocky Mountains of the western United States were selected for the CLPX during two seasons during which intense ground, airborne and space-borne observations were collected: mid-winter, when conditions are generally frozen and dry, in 2002, and in the early spring of 2003 to capture the transitional period when both frozen and thawed, and dry and wet snow regimes are widespread. The spatial scales covered by CLPX ranged from 1 ha to 160,000 km² from west of Denver to south-western Wyoming. Also, snowpit observations were obtained at various locations, including the location where the Ground Based Passive Microwave Radiometer N° 7 (GBMR-7) was installed, and which will use here for detailed analysis of MLSHM-MEMLS results. Further details on all available data sets from CLPX area available at (<http://nsidc.org/data/docs/daac>).

4.4. Results and Discussion: Valdai

4.4.1. Snow Physics

Figures 4-6a to 4-6c show the interannual variability of SWE, snow depth and snow density simulated by the LSHM-MEMLS using both single and multi-layer formulations (MLSHM-MEMLS). The multi-layer and the single-layer simulations yield very similar SWE results, which is consistent with the mass balance imposed in both formulations. Slight differences from one year to another reflect different types of precipitation in terms of snow hydrology. For example percolation of liquid water deep into the snowpack during rain-on-snow events is described differently in single and multi-layer models. In addition, surface melting takes place at a faster rate in the multi-

layer simulation because the uppermost layer interacting with the atmospheric boundary is shallower than the single layer model, and therefore, it warms faster for the same energy forcing (radiation, turbulent heat fluxes).

Snow depth (snow density) in the multi-layer simulation is significantly larger (smaller) than in the single-layer case. This difference is because the bulk snow density in the multi-layer snowpack increases more slowly than the density of the single layer. Compaction rate (Equation 4-22) is strongly influenced by the thickness of the layers considered to account for overburden effects. Consequently, each individual layer in the multi-layer formulation (Figure 4-7) is much thinner and exhibits less overburden effects than the single-layer, leading to lower density.

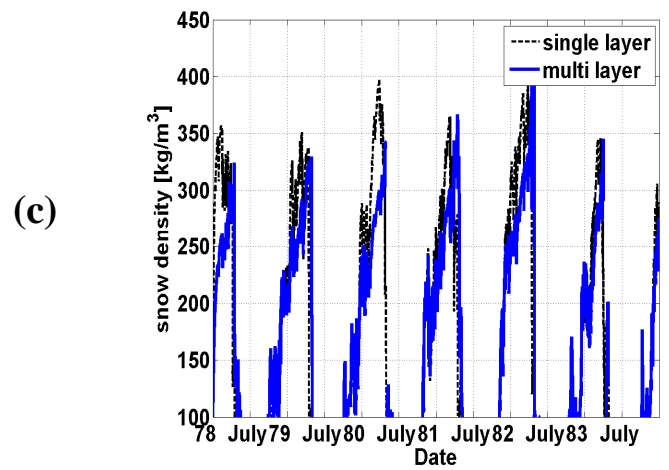
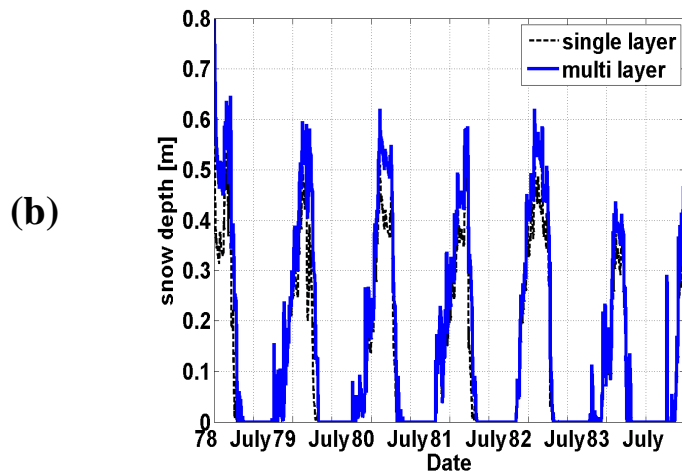
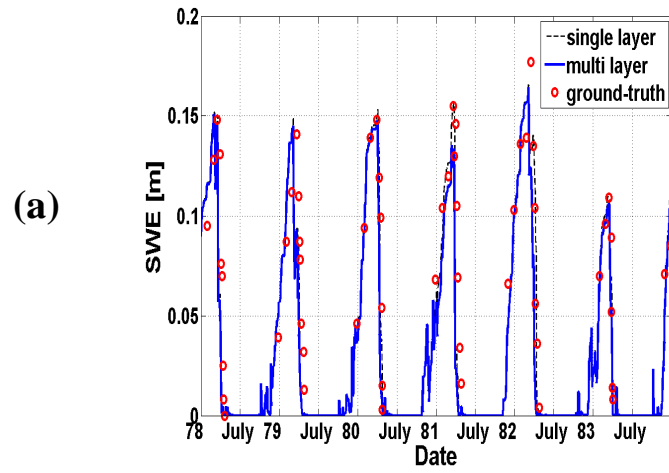


Figure 4-6 *LSHM-MEMLS* simulations in Valdai, Russia using PILPS of snow physical properties compared with ground assimilated observation only in SWE: a) SWE, b) snow depth, and c) snow density.

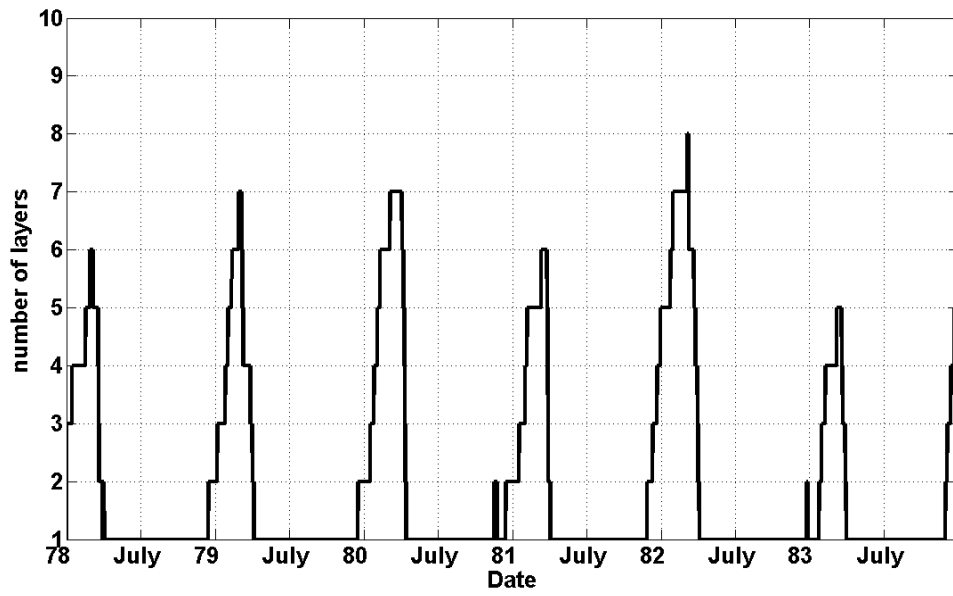


Figure 4-7 Number of snow layers in LSHM-MEMLS corresponding to with SWE simulation in Valdai, Russia.

4.4.2. Microwave Behavior

Figures 4-8, 4-9 and 4-10 show the time series of MLSHM-MEMLS simulations after applying local atmospheric correction (T_{appm}) compared with SMMR observation from 1978 to 1983 at 37, 21 and 18 GHz, H and V polarizations. The same atmospheric correction scheme and parameters described by [Kang and Barros 2010b] were used here without further calibration. There is a significant improvement in the multi-layer simulation of brightness temperatures for horizontal polarizations at all frequencies as hypothesized earlier. However, there is excessive cooling of brightness temperatures for vertical polarization especially at the peak of the accumulation and ripening phases. Tables 4-1 and 4-2 provide local estimates for atmospheric correction parameters as described in Chapter 3. Tables 4-3 and 4-4 show the error statistics between SMMR and multi-layer and single-layer simulations after atmospheric correction (T_{appm}) for ascending (11:00 AM LST) and descending (11:00 PM LST) paths. For ascending paths (daytime), the results for vertical polarization are somewhat worse for multi-layer than for single-layer simulations. The errors for horizontal polarization (H-pol) are generally better for all frequencies, with more improvement at 37GHz. For descending paths (nighttime), there is improvement for horizontal polarization and comparable performance for vertical polarization. There is also significant improvement in the case of multi-layer simulations for vertical polarization at 37 GHz. In the case of V-pol (vertical polarization), volume scattering effects dominate, and this why there are not significant changes between the single-layer and multi-layer formulations. In empirical

retrieval algorithms (e.g. Chang et al. 1987), H-polarization tends to be used to estimate SWE, whereas V-polarization is an indicator of snow mass.

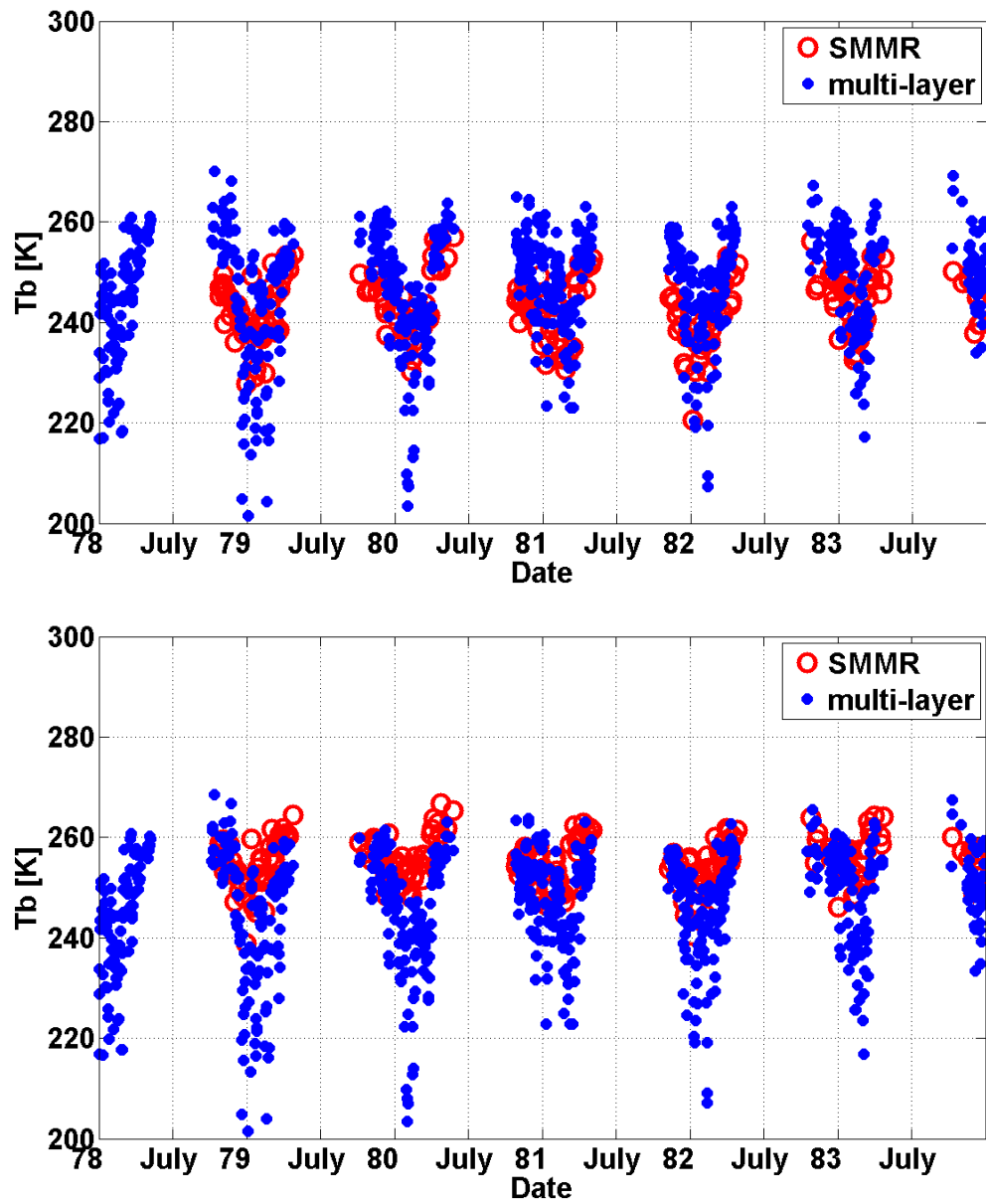


Figure 4-8 SMMR (red circle), compared with *multi-layer* (blue dot) at 37 GHz (H and V polarizations, upper and lower panels, respectively).

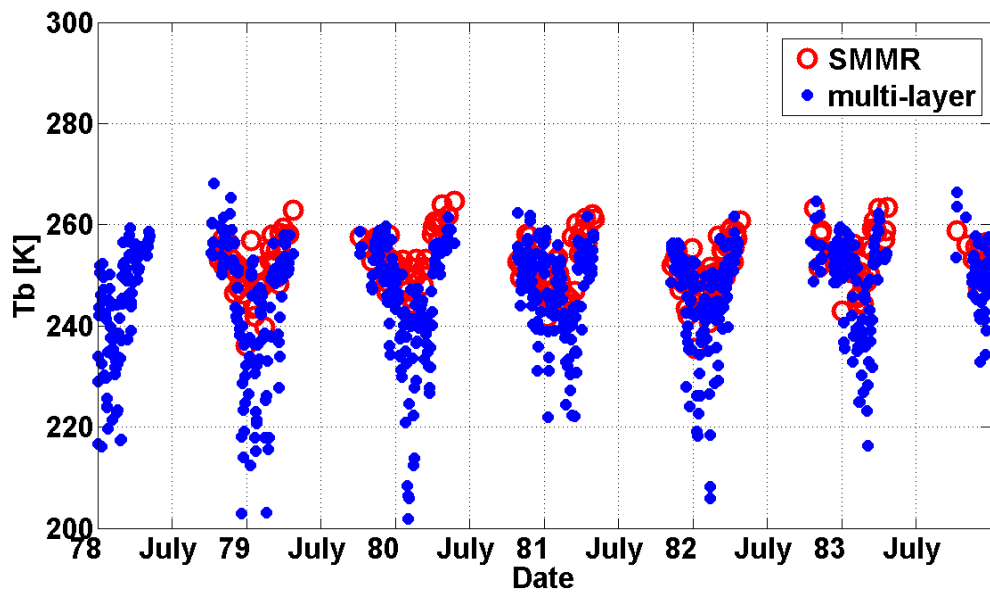
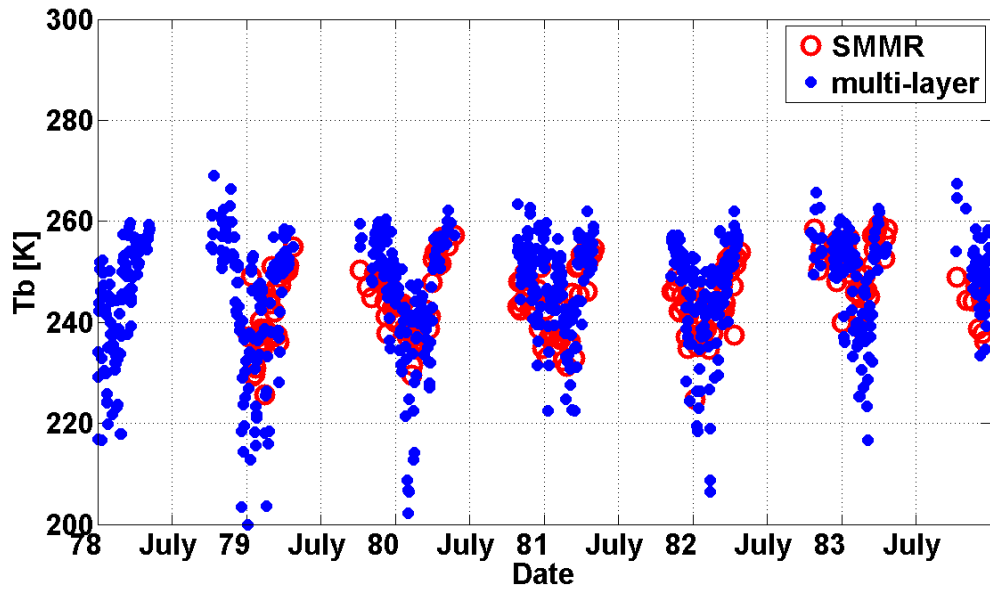


Figure 4-9 SMMR (red circle), compared with *multi-layer* (blue dot) at 21 GHz (H and V polarizations, upper and lower panels, respectively).

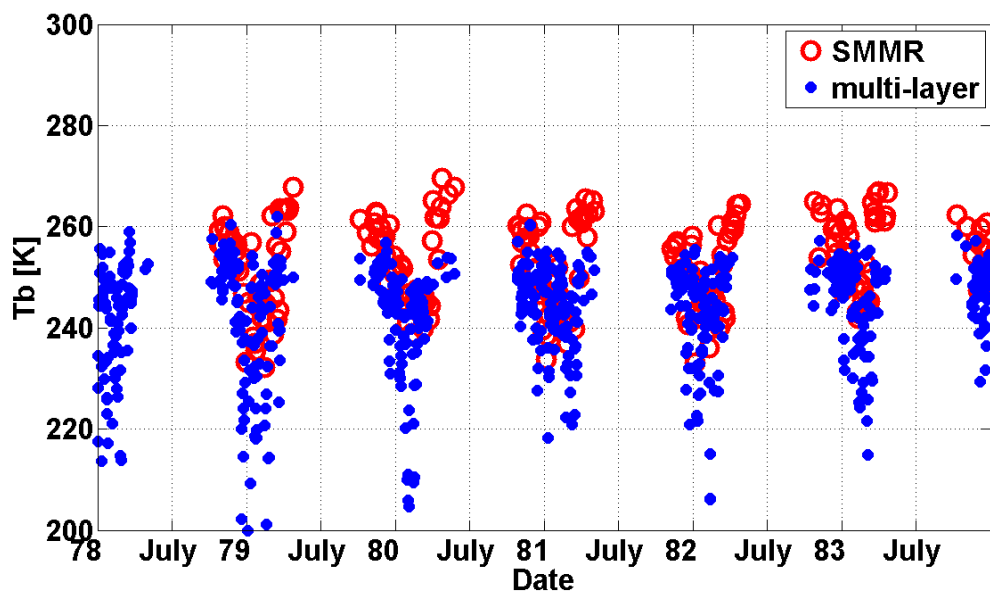
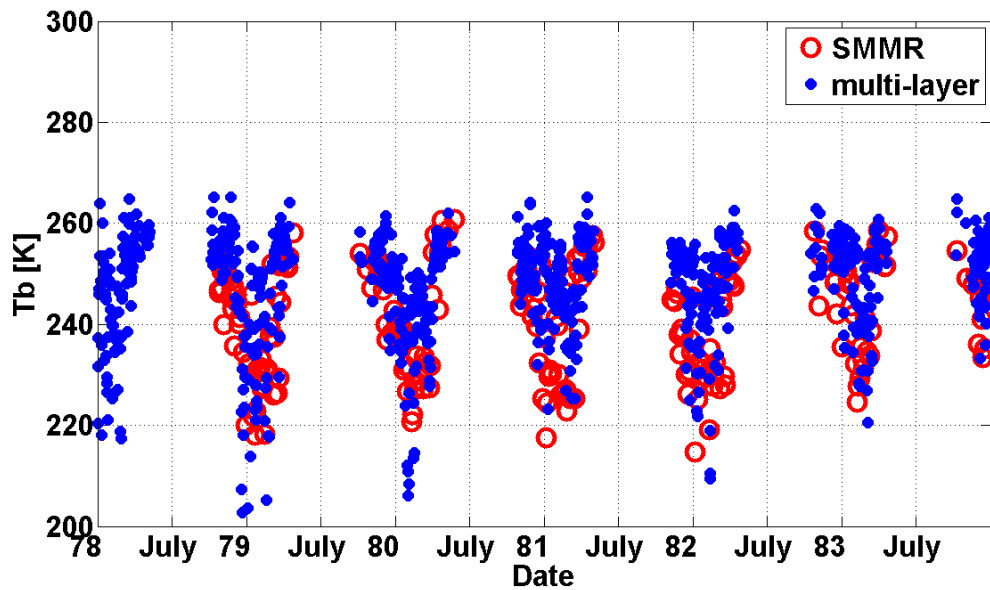


Figure 4-10 SMMR (red circle), compared with *multi-layer* (blue dot) at 18 GHz (H and V polarizations, upper and lower panels, respectively).

Table 4-1 Locally estimated parameters β_f and ϕ_f ($\tau_{f,i} - \zeta_f L_i = \beta_f + \phi_f V_i$), using two years of SMMR and LSHM-MEMLS data at Valdai while ζ_f was maintained as per [Mätzler 1996] for ascending paths.

Frequency	Parameters
18.0 GHz H	$\beta=0.9465$ neper, $\phi= 0.009$ neper/mm, $\zeta = 0.0819$ neper/mm
18.0 GHz V	$\beta=1.3255$ neper, $\phi= 0.0083$ neper/mm, $\zeta= 0.0819$ neper/mm
21.0 GHz H	$\beta=0.8017$ neper, $\phi= 0.0152$ neper/mm, $\zeta= 0.0819$ neper/mm
21.0 GHz V	$\beta= 1.0194$ neper, $\phi= 0.0259$ neper/mm, $\zeta= 0.0819$ neper/mm
37.0 GHz H	$\beta= 0.6345$ neper, $\phi= 0.0295$ neper/mm, $\zeta= 0.1867$ neper/mm
37.0 GHz V	$\beta= 0.4957$ neper, $\phi= 0.0062$ neper/mm, $\zeta= 0.1867$ neper/mm

Table 4-2- Locally estimated parameters β_f and ϕ_f ($\tau_{f,i} - \zeta_f L_i = \beta_f + \phi_f V_i$), using two years of SMMR and LSHM-MEMLS data at Valdai while ζ_f was maintained as per [Mätzler 1996] for descending paths.

Frequency	Parameters
18.0 GHz H	$\beta=0.9245$ neper, $\phi= 0.0062$ neper/mm, $\zeta = 0.0819$ neper/mm
18.0 GHz V	$\beta=1.1915$ neper, $\phi= 0.00274$ neper/mm, $\zeta= 0.0819$ neper/mm
21.0 GHz H	$\beta=0.8399$ neper, $\phi= 0.0119$ neper/mm, $\zeta= 0.0819$ neper/mm
21.0 GHz V	$\beta= 1.0792$ neper, $\phi= 0.0149$ neper/mm, $\zeta= 0.0819$ neper/mm
37.0 GHz H	$\beta= 0.4677$ neper, $\phi= 0.0367$ neper/mm, $\zeta= 0.1867$ neper/mm
37.0 GHz V	$\beta= 0.5143$ neper, $\phi= 0.062$ neper/mm, $\zeta= 0.1867$ neper/mm

Table 4-3 Differences in error statistics between T_{appm} and SMMR observations for ascending paths (11:00 AM LST).

		H		V	
		single	multi	single	multi
18 GHz	<i>Bias</i>	10.83	9.72	-1.13	-4.66
	<i>ME</i>	11.2	10.06	4.86	5.94
	<i>RMSE</i>	12.5	11.49	6.27	7.36
21 GHz	<i>Bias</i>	7.56	8.24	-0.29	-2.11
	<i>ME</i>	8.73	9.10	4.74	5.04
	<i>RMSE</i>	10.28	10.86	6.1	6.41
37 GHz	<i>Bias</i>	13.59	10.49	-1.4	-3.43
	<i>ME</i>	14.07	11.57	6.73	7.46
	<i>RMSE</i>	16.4	14.23	8.45	9.23

Table 4-4 Differences in error statistics between T_{appm} and SMMR observations for descending paths (11:00 PM LST).

		H		V	
		single	multi	single	multi
18 GHz	<i>Bias</i>	15.23	14.32	-2.06	-2.39
	<i>ME</i>	15.40	14.37	5.30	5.35
	<i>RMSE</i>	17.18	15.90	6.90	6.86
21 GHz	<i>Bias</i>	10.27	10.24	1.97	1.87
	<i>ME</i>	10.96	10.83	5.49	5.07
	<i>RMSE</i>	13.17	12.93	6.94	6.43
37 GHz	<i>Bias</i>	19.25	15.72	4.53	1.29
	<i>ME</i>	19.44	16.04	7.98	7.20
	<i>RMSE</i>	21.79	18.61	10.28	9.19

Figure 4-11 shows the temporal evolution of SWE and LWC (liquid water content) in the snowpack as well as simulated and observed SMMR brightness temperatures at 37 GHz, H-polarization during the 1982-1983 snow season. Note that the brightness temperature reaches a minimum before the maximum SWE accumulation, and thus there is an increase in internal energy before melting starts, the so-called “ripening” phase of the snowpack during which temperatures increase until they reach 273.15 K. The density and temperature profiles at three times corresponding to accumulation A¹, ripening A² and melting A³ phases (Figure 4-11) are shown in Figure 4-12. Consistent with the compaction model described in Section 4-2, snow density increases from the top to the bottom layer. However, the temperature profiles at A¹ and A² are very different from A³. A³ exhibits a strong inversion with the upper layers much warmer than the lower layers, an indication that the melting phase is underway. A comparison of A¹ and A² illustrates the persistent cooling trend during the wintertime. The yellow circle in Figure 4-11 marks March 21st 1983 during the melt season initiated. On this particular date of March 21st, 1983 there was significant daytime superficial melt resulting in high LWC both in the multi and single layer simulations.

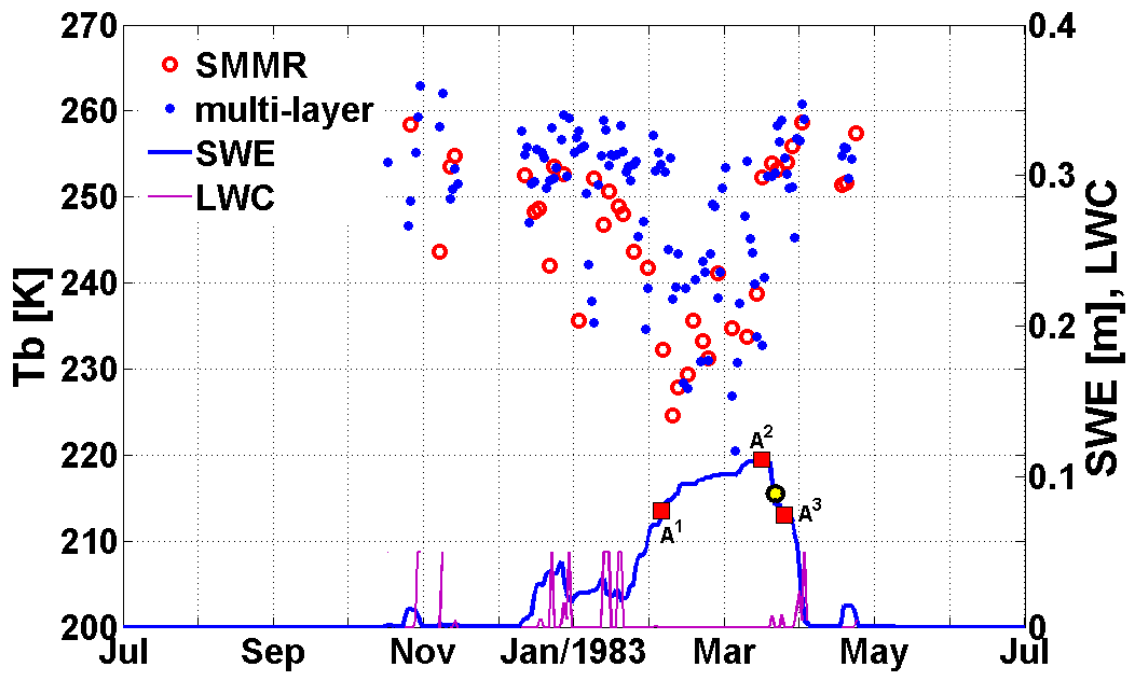


Figure 4-11 - Radiation properties and corresponding physical properties of snowpack during 1982 to 1983 snow year, and the Circle: melting point, A¹ to A³: Accumulation to peak, respectively. Note: LWC has the maximum LWC of 0.05 [kg/kg] assigned in this Valdai case. A¹: Feb. 5th, A²: Mar. 15th, A³: Mar. 23rd, and Yellow Ellipse: March 21st.

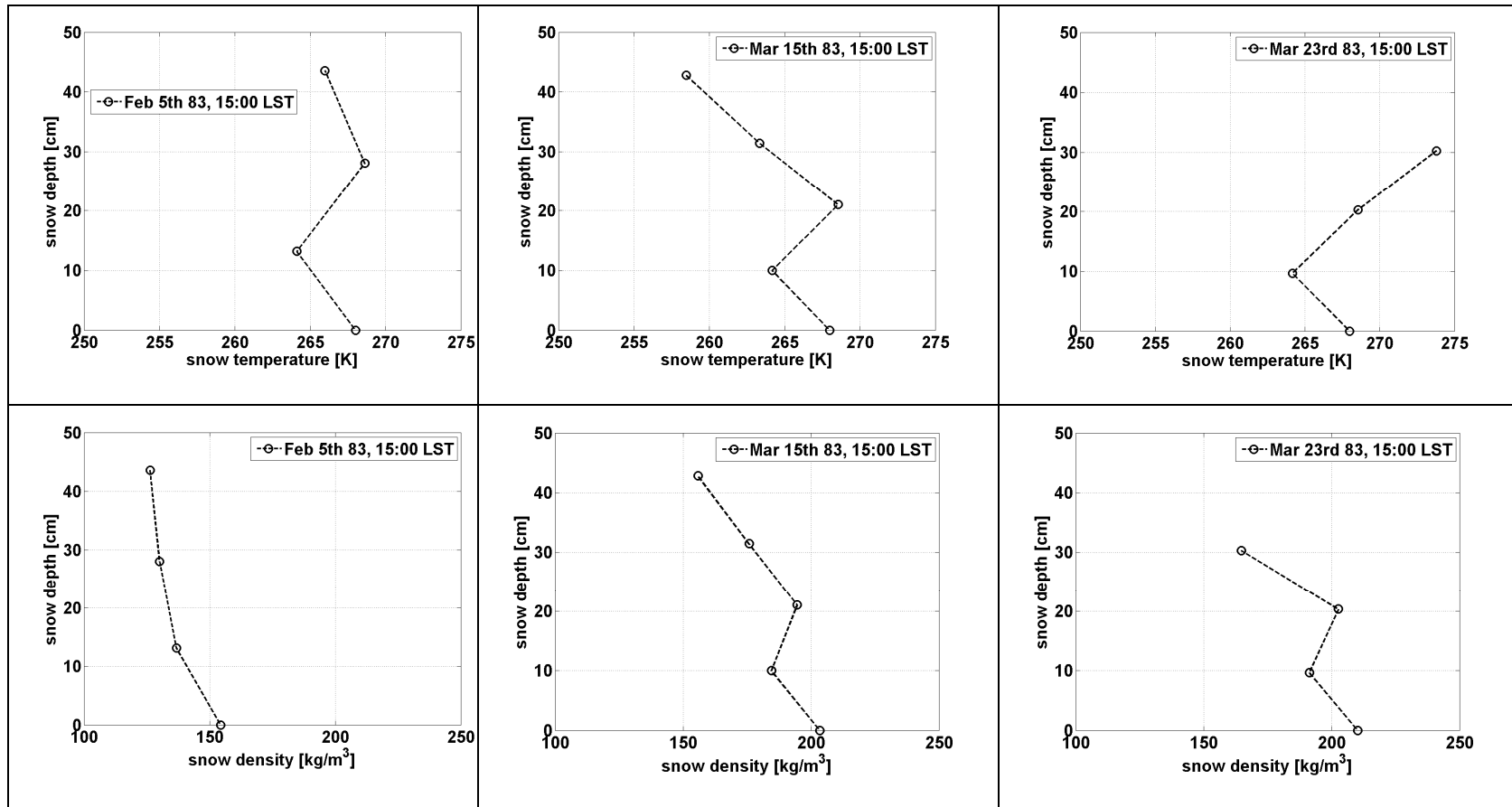


Figure 4-12 Snow temperature and density with the vertical snow depth with respect to A¹, A², and A³ from Figure 4-11

However, Figure 4-13 shows that the brightness temperature from the multi-layer model increases during the afternoon while that from single layer is relatively constant. The brightness temperature reflects two contributions both of which are displayed in Figure 4-14: 1) outgoing radiation, D_n , and 2) interface reflectivity s_{n+1} (see Equation 4-33). Compared with D_n , the change of $1.0-s_n$ between multi and single layer is negligible. The outgoing radiation is influenced by the surface emissivity which is the complementary of the summation of reflectivity and transmissivity. Figure 4-15 shows that $(r + t)$ sharply decreases after 16:00 LST which results in significantly higher brightness temperatures in the multi-layer snow simulation. This increase is explained by the increase in liquid water content inside the snowpack during the afternoon (Figure 4-16). First, superficial melting around noon increased the LWC of the multi-layer, leading to lower internal reflectivity and transmissivity and fast increase of the outgoing radiation, D_n Figure 4-14 (a). Second, rainfall at the end of the day further increases the LWC. As previously pointed out by [Kang and Barros 2010^b] using the single-layer formulation, small increases in LWC “warm” the snowpack and lead to an increase in outgoing radiation, D_n .

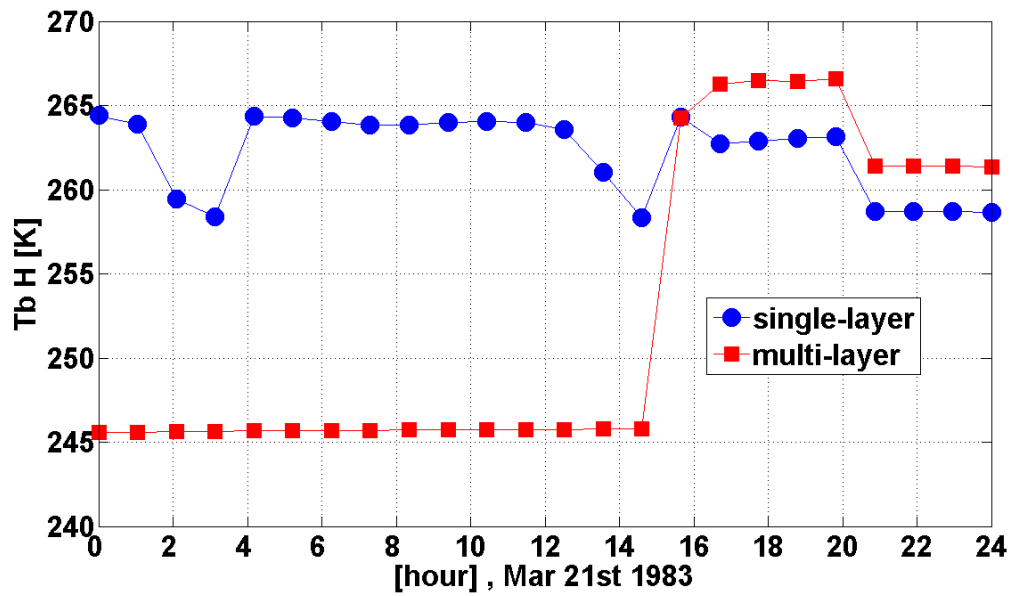


Figure 4-13 Horizontal brightness temperatures at 37 GHz H on March 21st 1983 corresponding to the yellow circle from Figure 4-11

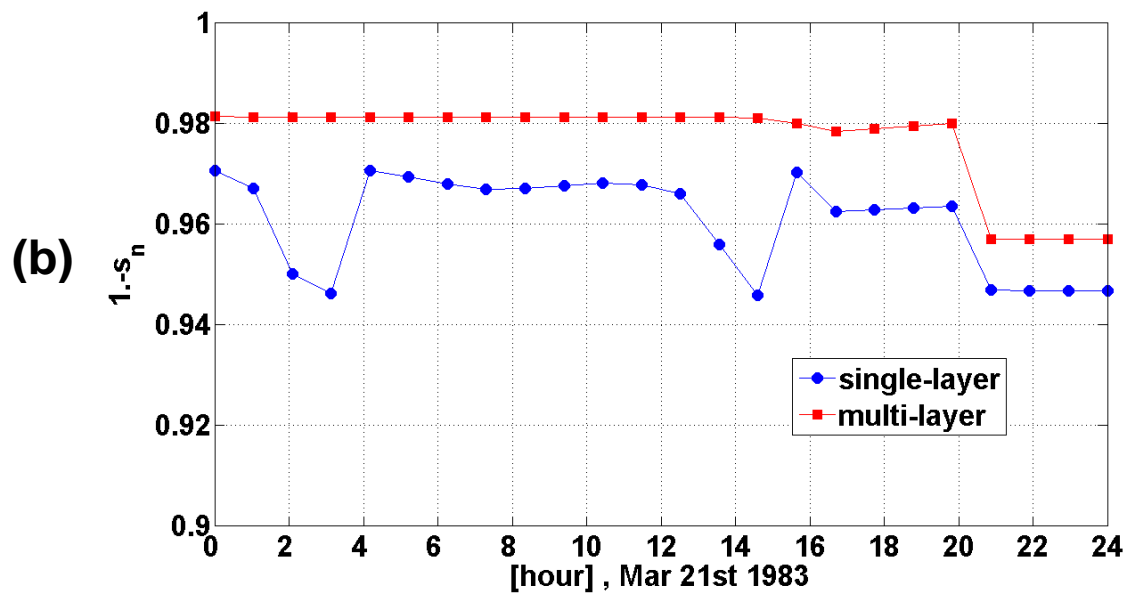
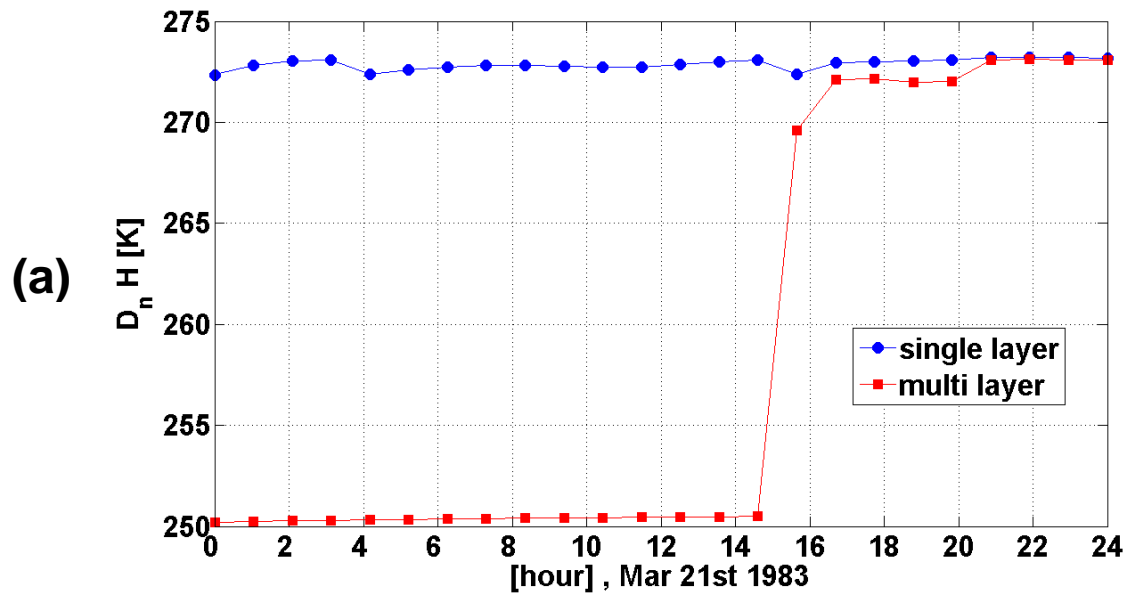


Figure 4-14 D_n and $1-s_n$ on March 21st 1983 by decomposing T_b at 37-H GHz.

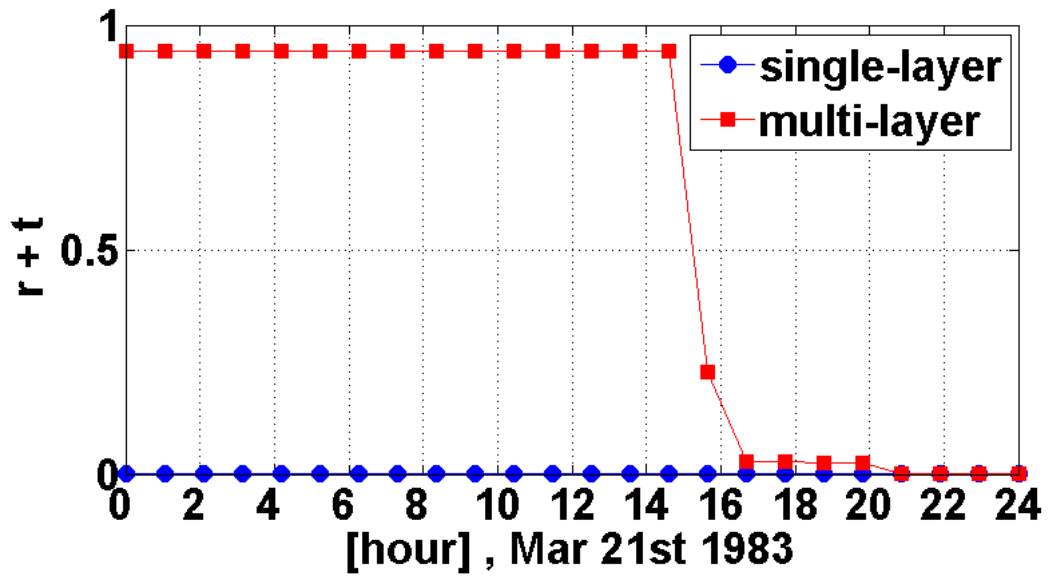


Figure 4-15 Summation of internal reflectivity and transmissivity on March 21st, 1983

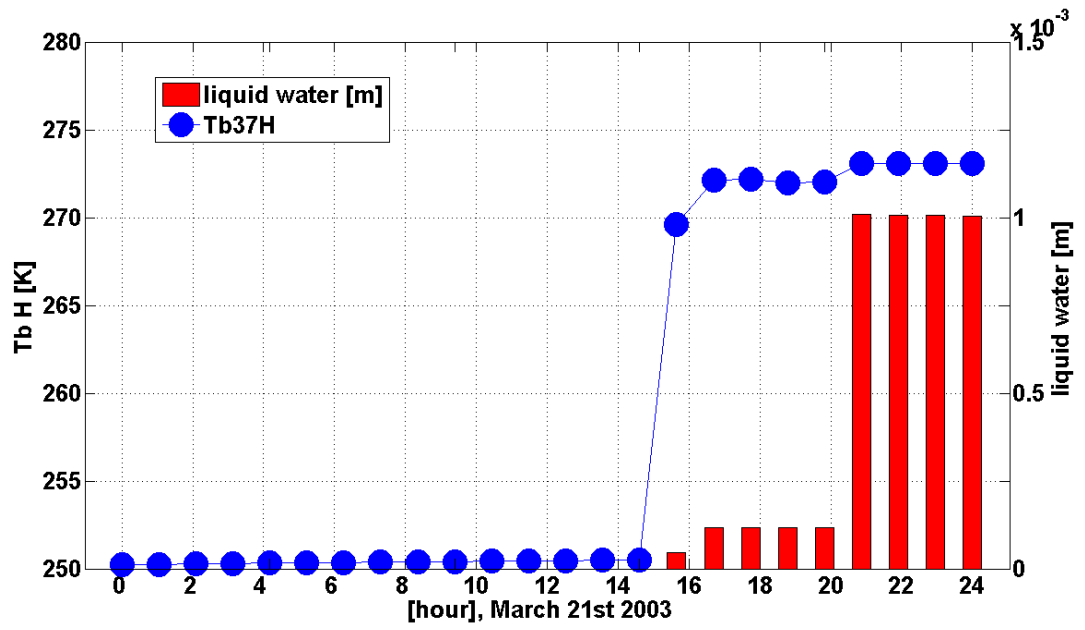


Figure 4-16 Horizontal brightness temperature of multi-layer simulation at 37 GHz H superposed with the rainfall occurred during the entire day on March 21st, 1983

4.5. Results and Discussion: CLPX 2002-2003

4.5.1. Snow Physics

Figure 4-17 shows the SWE, snow density, and snow depth evolution comparing the multi-layer and the single layer simulations against snowpit observations at the GBMR-7 location (see Figure 4-5 for map). The simulations show that during accumulation and beginning of ripening phases the two formulations lead to similar results, whereas there are significant differences during late ripening and melting phases. Melting is faster in the single-layer case and, based on snowpit observations, melting is faster in both formulations than in the observations. The model snowpack never reaches the high density values observed in mid-May, and presumably the densification of the snowpack in March-May is underestimated by the model though there are no observations in that period. Note that the model results correspond to the grid cell that contains the entire Fraser MSA using RUC40 forcing; the GBMR-7 data are presented for reference purposes and therefore some variability is expected around the observed values. One important result for modeling microwave signatures is that in both formulations, and better so in the case of multi-layer, the changes in density during the accumulation season are well captured by the model. Figure 4-18 shows the evolution of the number of snow layers in the model which goes up to 25 during the peak accumulation season.

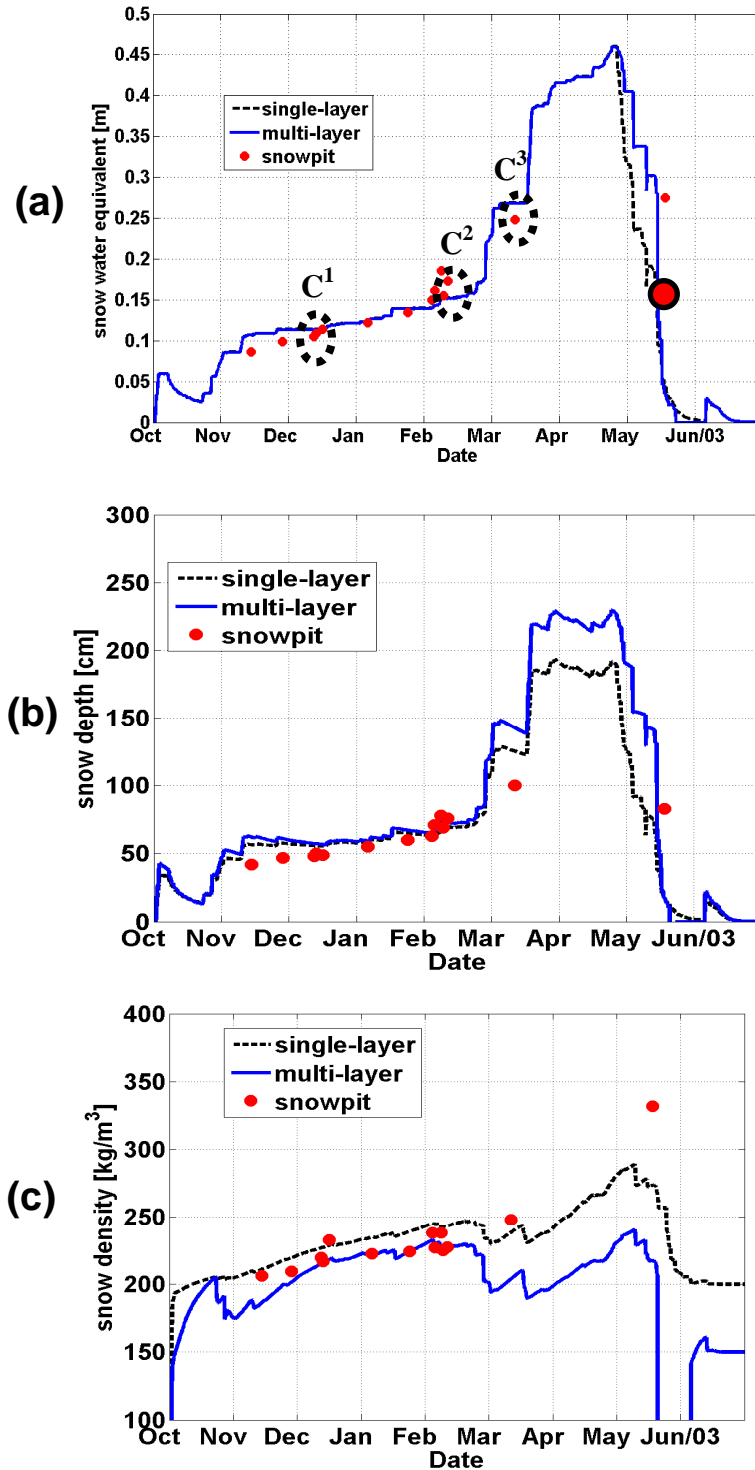


Figure 4-17 LSHM-MEMLS simulations of CLPX conditions using RUC40 forcing compared with GBMR snowpit observations: a) SWE, b) snow depth, and c) snow density (C¹, C² and C³ are 12/19/2002, 2/21/2003, and 3/16/2003, respectively, the red circle in (a) is on April 9th to 10th 2003).

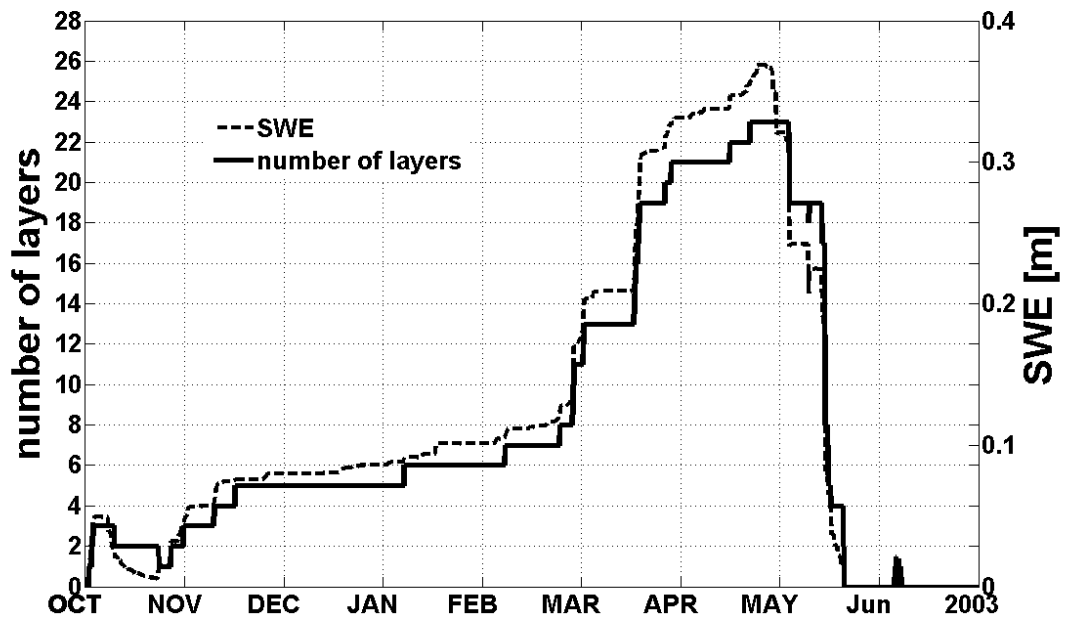


Figure 4-18 Number of snow layers in LSHM-MEMLS corresponding to with SWE simulation in CLPX.

Figure 4-19 shows the snow temperature and snow density profiles at three different times corresponding to the points marked with C¹ (12/19/2002), C² (2/21/2003), and C³ (3/26/2003) located in Figure 4-17 (a) from left to right, respectively. The number of layers varies with time as per Figure 4-18. At C¹, the temperature of top layer is at 257 K while the internal layers except for the top layer have increasing temperatures up to the melting point both in the observations and in the simulations. This is the typical situation of heat insulating effect within the snowpack against solar radiation and sensible heat flux [Cohen 1994]. Even though the ambient temperature is cold, the internal layers adjacent to the soil keep the snowpack temperature higher at the bottom. At C², there is an increase of snow density from the top to bottom layers due to overburden effects while some density profiles have lower density in the bottom layers which can be caused by depth hoar from the soil moisture flux. Despite differences in snowpack density at C², the temperature profiles agree well especially considering that the different profiles were obtained at a wide range of locations (Figure 4-5) with very different surface characteristics. The increase in density in the uppermost layers of the snowpit observations at C³ indicates the presence of liquid water from surface layer melting in the top layer, whereas top layer temperatures in the model are still below freezing. Subsequent refreezing of this liquid water at nighttime may lead to the formation of ice lenses and heterogeneities that should have an impact on microwave emissivity. Indeed larger differences in density in the upper layers of the snowpack

should have an impact also on the parameterization of the snow size distribution [Mätzler 2002].

Figure 4-20 also shows the temperature and density profiles on February 3rd, 9th, and 21st, 2003 corresponding to markers D¹, D², and D³. The ambient air temperature used for the model forcing and snowfall are shown in the lower graph. Overall Figure 4-20 shows that in the dry snow regime, during the accumulation phase, the model and the observations come closer to agreement below the top layer before the end of the month. Note that snowfall rarely occurs during this period and the air temperature does not exceed the melting point of 273.15 K, which implies that the microwave behavior in February is controlled by radiative forcing at the snowpack surface and internal processes within the snowpack, specifically metamorphosis, which in turn strongly affects the snow microstructure. Depth hoar, characterized by coarse ice crystals formed by sublimation and deposition in dry snow layers, is patent at the bottom of the snowpack in the observations by mid-February and extends to the intermediate layers at D³, but cannot be captured by the model because its effect is not parameterized.

Figures 4-21a to 4-21c show the simulated diurnal cycle of temperature at various depths compared against snowpit observations at three distinct locations within the large CLPX domain: Alpine, Fool Creek, and St. Louise Creek (see Figure 4-5 for map location). The bottom layers of the snowpack in the model and in the observations agree well and both show the expect insulation effect away from the atmosphere-snow

interface, whereas there is strong diurnal cycle in the top layers with a good agreement between the model forced by RUC40 at 40 km resolution and the snowpit observations, especially at St. Louis Creek. St. Louis Creek is located in the valley below 3000 m a.s.l., while the other two locations are above 3000 m on the slopes, and thus topographic effects may be important in terms of exposure for example as well as snow redistribution by boundary layer winds, which cannot be captured by the model.

Figure 4-22 shows profiles of snow temperature and density profiles from three different snowpits within the Fraser, MSA at 9:00, 12:00 and 15:00 on Feb. 20th. The approximate area of each MSA is about 250 km². Note the increase in top layer temperature during the day and the effect of spatio-temporal variability in the propagation of the heat flux from the top to the bottom snow layer, whereas the density profiles do not change significantly. The snowpit data at the Alpine site at 12 PM show densification at mid-levels in the snowpack, which is explained by the presence of some structural heterogeneity or the presence of the liquid water. On the other hand, in the afternoon at 3:00 PM, the temperature profiles both in the measurements and in the simulation show a linear increase of temperature at the top layer and they are in good agreement, though the model is colder on average by about 3 K.

Overall, the snowpit profiles show large variations within the Fraser, MSA. This is a good example of the heterogeneous distribution of the snowpack and snowpack profiles at small spatial scale. Snowpit measurements are destructive, and once excavated, it is not possible to track the diurnal cycle at the same location. This

illustrates the need for non-destructive monitoring such as the RF snow sensor described in Chapter 2.

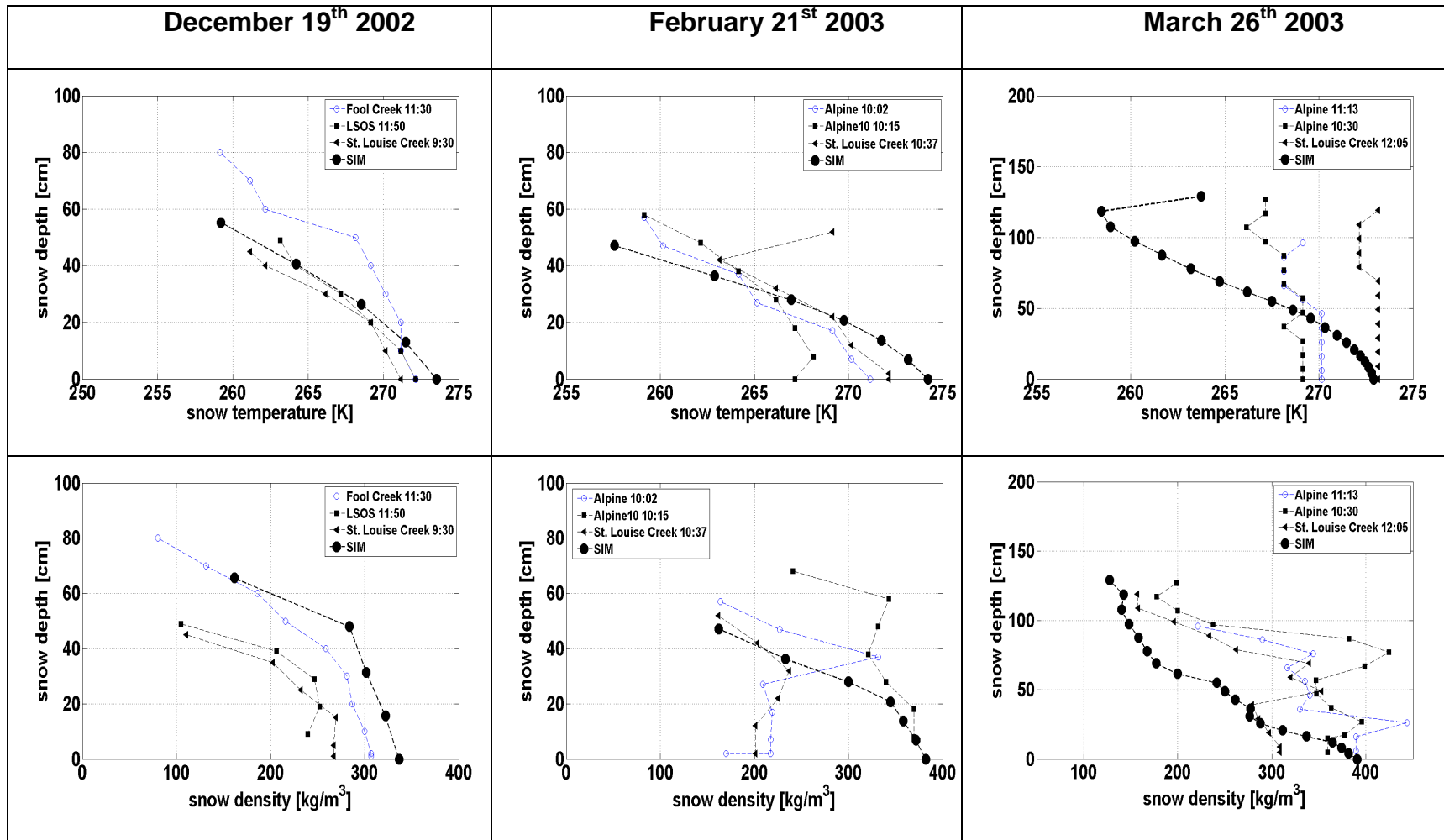


Figure 4-19 Snow temperature and density with the vertical snow depth with respect to GBMR C¹, C², and C³ in Figure 4-17. Dates are 12/19/2002, 2/21/2003, and 3/16/2003, respectively

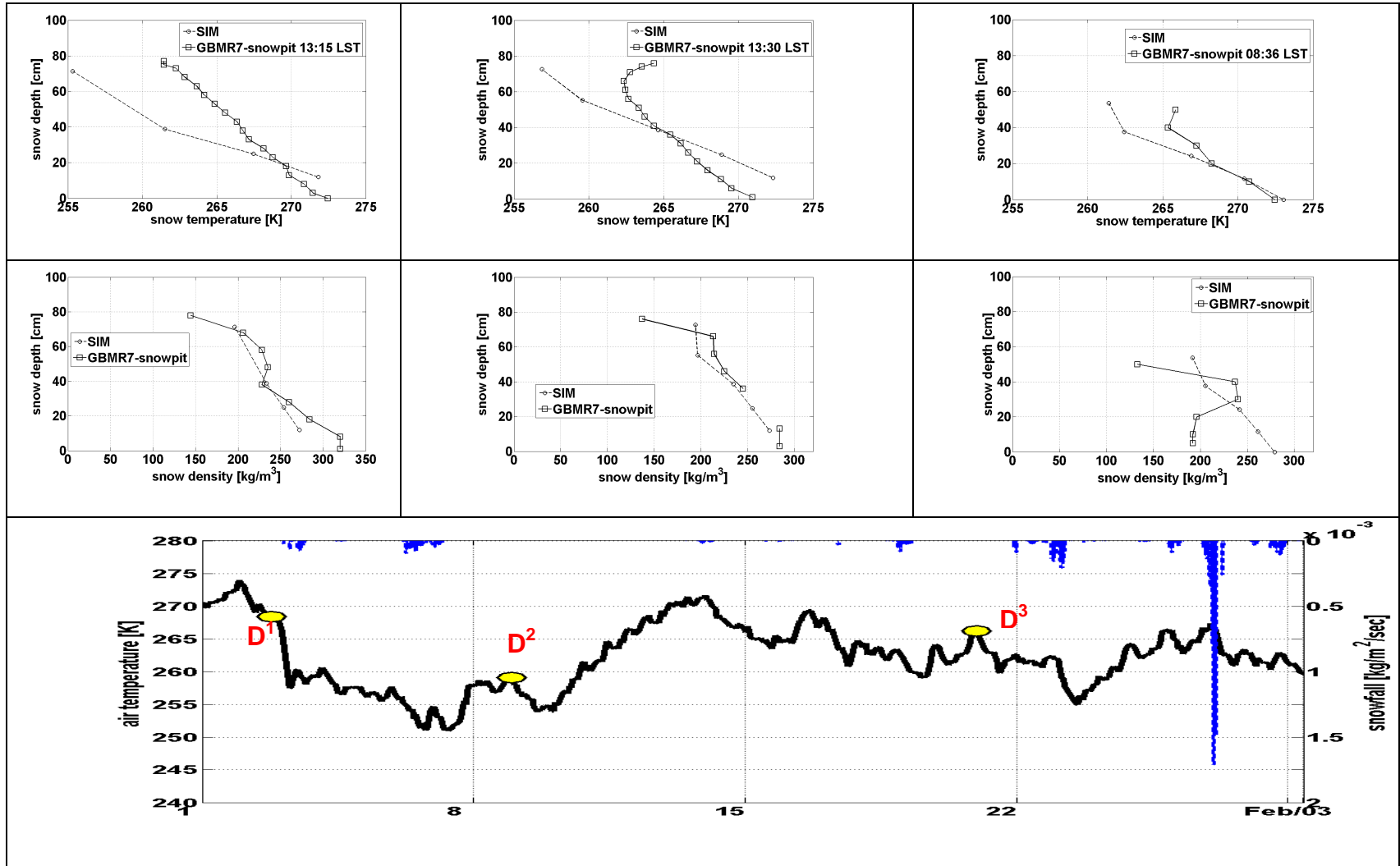


Figure 4-20 Snow temperature and density with the vertical snow depth with respect to GBMR D¹, D², and D³ only in Feb/2003 in Figure 4-17.

Dates are 3rd, 9th, and 21st of February 2003, respectively

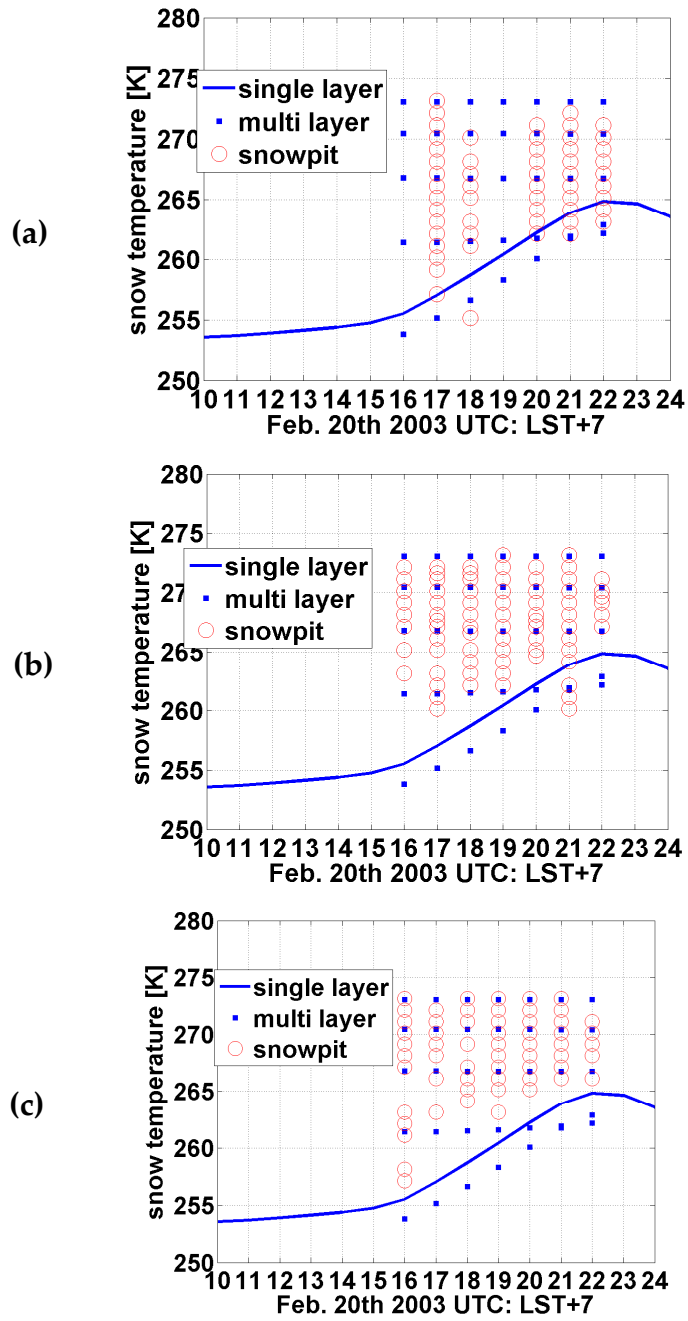


Figure 4-21 Snow temperature distribution compared with the snow pit data in Fraser, (a): Alpine (b): Fool Creek, (c): St. Louis Creek

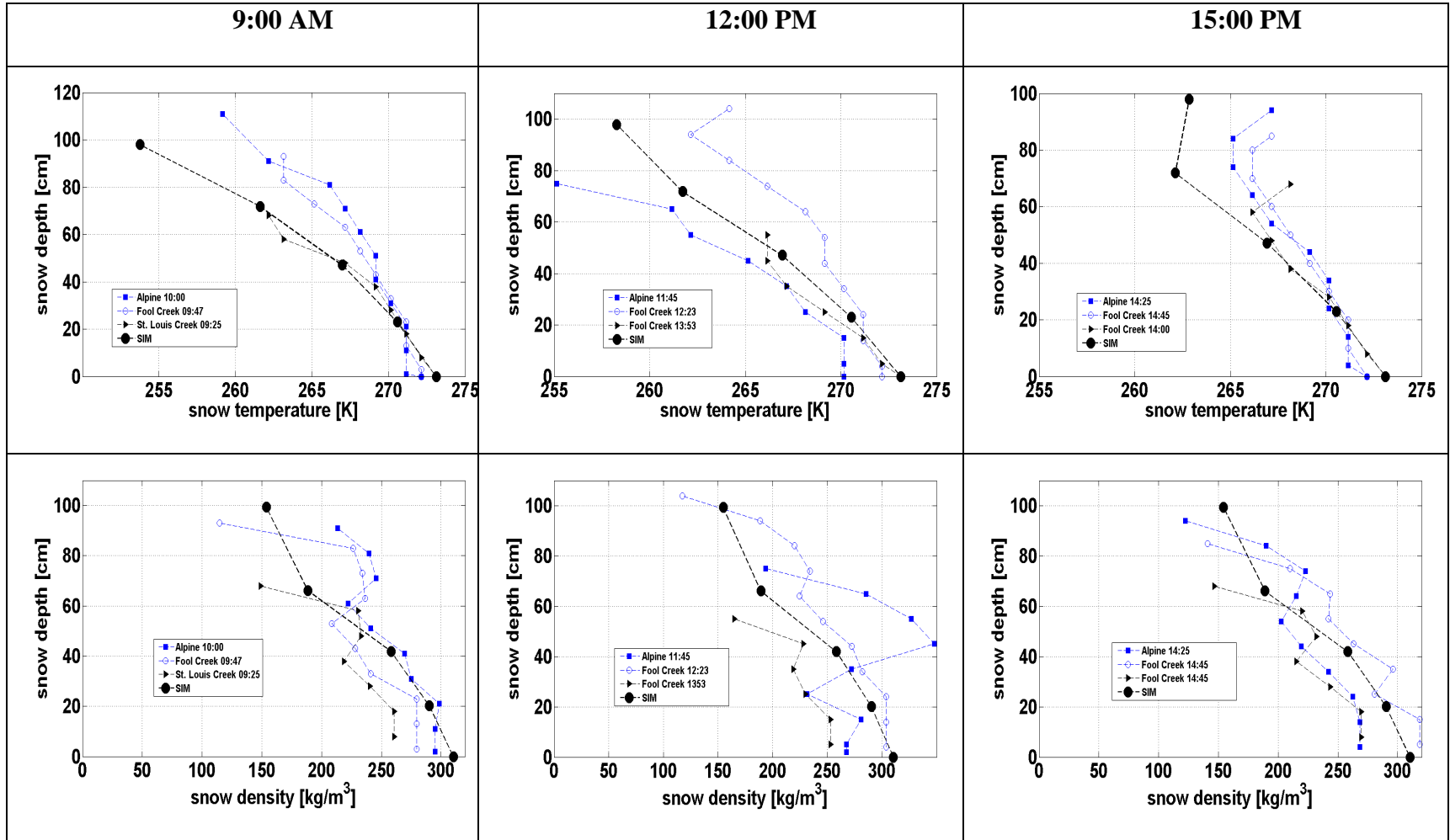


Figure 4-22 Vertical profiles of snow temperature and density in diurnal cycles 9:00, 12:00 and 15:00 on Feb. 20th 2003 in Fraser MSA.

4.5.2. Microwave Signature

Figure 4-23 shows the temporal evolution difference of the brightness temperatures between 37-H and 19-H GHz for multi-layer and single layer simulations against the snow water equivalent similar to empirical retrieval algorithms (Chang et al. 1987). As the snow accumulates, volume scattering effects in the ripening phase in late April and early May are quite different in the multi-layer and single-layer simulations. When melting initiates in mid-May, the multi-layer results exhibit more sensitivity than the single layer where the difference between 19-H and 37-H brightness temperatures abruptly decreases as the snowmelt leaves the snowpack. On the other hand, Figure 4-24 shows the same plot as Figure 4-23 but now for SSM/I and AMSR-E observations. Note that the lower frequency for the SMM/I is 19.35 GHz and for AMSR-E is 18.7 GHz; both are represented by 19 GHz in the Figures. The higher frequencies are 37 GHz for SSM/I and 36.5 GHz for AMSR-E; both are represented by 37 GHz in the Figures. The difference between 19-H and 37-H Tbs increases during the snow accumulation phase, though the magnitude is 10 K less than in the simulation case. Furthermore, the convex shape of the observations is not captured by the model, SWE peaks in May whereas brightness temperatures reach a maximum in March. This is tentatively attributed to the poor performance of the compaction rate model and the lack of parameterization of depth hoar effects which have a strong impact not only on density profiles, but also on grain size distribution for the bottom layers, and therefore internal scattering. The profound

effect of increased density as well as depth hoar on brightness temperatures at 37 GHz was addressed by Hall (1987) who pointed out differences on the order of 20 to 40 K at 37-H GHz depending on layer thickness for dry snowpacks, and by Toure et al. (2008) for very dense snow samples.

Figure 4-25 shows the scatter plots for, AMSR-E and SSM/I observation and multi-layer model simulation of the difference between 19-H and 37-H GHz brightness temperatures. There is very large ambiguity in the relationship between SWE and brightness temperature differences, which illustrates well the challenges in using empirical models that depend on microwave signatures alone. First, there is a clear sensor to sensor difference, but more importantly, and in contrast with the model simulations, there is no unique retrieval for most of the simulation period, especially during the melting (inside the hexagon in Figure 4-25) and peak accumulation phases (inside the circle in Fig. 4-25). This suggests that the scattering properties during the melting phase are not linearly related to snow mass alone, but indeed they are strongly affected by changes in the internal snowpack structure, grain size distribution, and liquid water content. Singh and Gan (2000) explored various empirical retrieval models and found that incorporating dependencies on elevation, land-cover categories, and atmospheric conditions decreased ambiguity and improved performance. An alternative approach to address the retrieval problem is to develop an algorithm that optimally derives the snow physical properties from the observations using a model such as

LSHM-MEMLS and a Bayesian approach(Stephens et al. 2007).

The relationship between the difference in brightness temperatures and snow depth is more sensitive at higher frequencies because of the significant attenuation effects within the snowpack. The imaginary part of permittivity at 37-H GHz is larger than at 19-H GHz. Also, the top layer's reflectivity, r , increases while the transmissivity, t decreases. At 19 GHz, if t increases, there is a strong increase in the outgoing radiation within the snowpack. The increase of the transmissivity, t is due to the decrease of the absorption coefficient, γ_a . The decrease of ϵ'' at 37-H GHz explains the decrease of the absorption coefficient, γ_a . This brightness temperature anomaly between high and low frequencies is also confirmed in Equation (4-34) of D_1 in the bulk layer calculation of D because the increased transmissivity significantly decreases the denominator of D in Equation (4-31) [Wiesmann and Mätzler 1999].

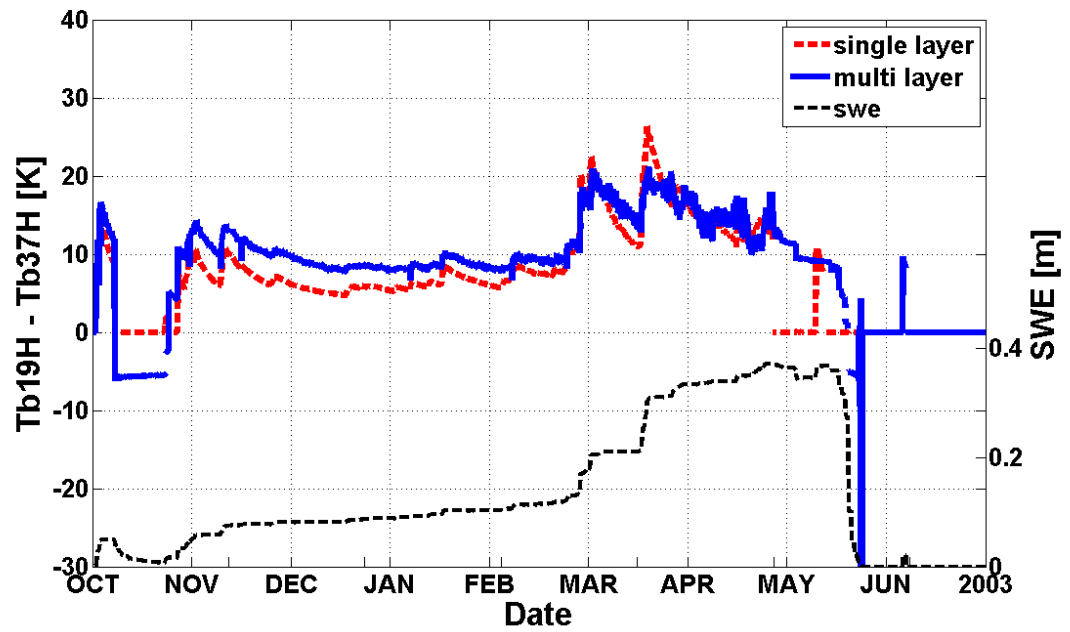


Figure 4-23 Temporal evolution of the difference in Brightness temperature between 37-H and 18-H GHz from single and multi-layer simulations and simulated Snow Water Equivalent.

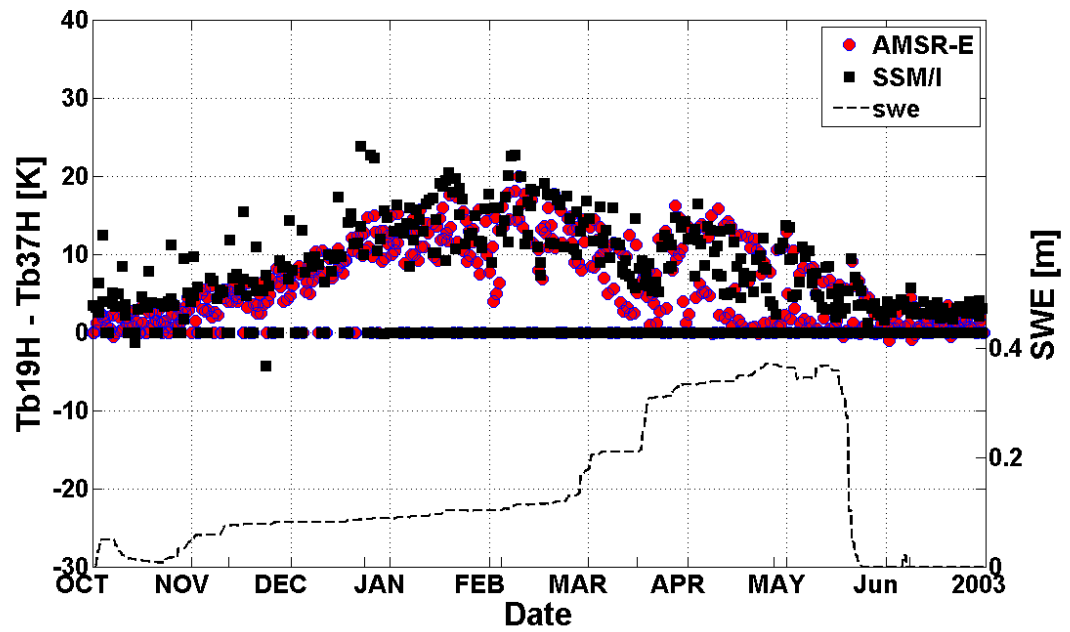


Figure 4-24 Temporal evolution of the difference in brightness temperature between 18-H and 37-H GHz for AMSRE-E and SSM/I and simulated Snow Water Equivalent.

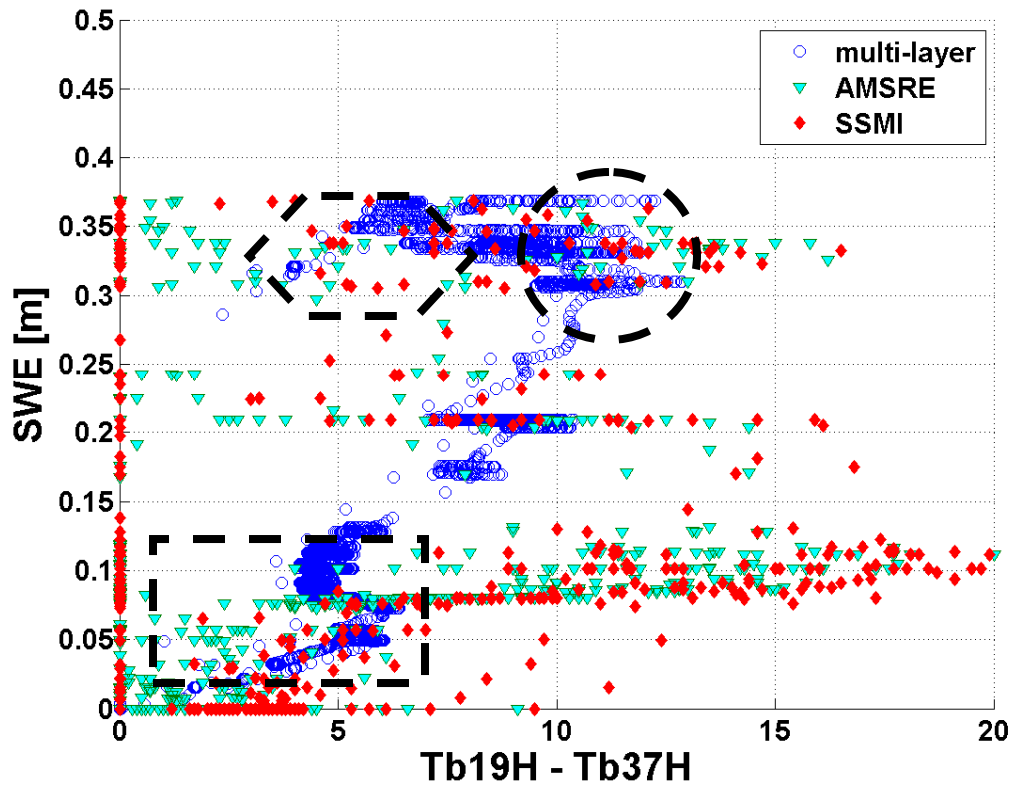


Figure 4-25 Scatter plot of AMSR-E, SSM/I, and multi-layer simulations of brightness temperature differences at 37-H GHz versus SWE. (rectangle: accumulation, circle: peak, and hexagon: melting phases)

Finally, Figures 4-26 and 4-27 show the brightness temperature responses at 19, 23, and 37 GHz V/H against SSM/I and AMSR-E observations respectively for the entire period of simulation. The results capture well the seasonal cycle especially in the melting season, and at 37-H GHz, but there is a large bias in the accumulation season between December and early March, during which the model is consistently warmer than the observations and the typical concave shape corresponding to increasingly lower temperatures before the onset of melt is not captured by the model especially at 37-V GHz. As noted previously, this is explained by the fact that the model predicts lower density than observed on the one hand, and by the lack of a depth hoar parameterization in the model during dry periods in the cold season during the accumulation phase on the other hand [Hall 1987]. Table 4-6 shows a summary of error statistics including results from Wójcik et al. [2008]. Wójcik et al. (2008) used a version of the HUT model as well as DMRT and MEMLS coupled to VIC for simulations at two sites within the Fraser MSA, February-May 2003, thus including both dry and wet snow regimes over the four month period. There are very small differences in error statistics between the single and the multilayer simulations using the correlation length classification from Mätzler (1996), with results getting worse in most cases except for the case of 37-H GHz for SSM/I. This is in contrast with the results obtained for Valdai, and suggests that snow physics are more complex in CLPX where the weather is more variable and orographic effects are important than in the northern latitudes and flatter

topography of Valdai. As in the case of single layer simulations, the overall performance for V polarization in CLPX is better than for H-polarization.

Because these results are somewhat unexpected, two additional simulations using a constant grain size correlation length ($p_{ec}=0.06$ mm) independently of the density and age of snow were conducted for both single and multilayer formulations (Figures 4-28 and 4-29). In this case, the multilayer formulation produces significantly better error statistics for most vertical polarization results especially for the intercomparison between LSHM-MEMLS and AMSR-E for V-polarization at 37 GHz. A survey of Table 4-7 shows that simulation results using a constant grain size correlation length corresponding to values typical of low density snow are better than those following Mätzler's (1996) parameterization independently of single or multilayer model formulation. Given the substantial differences associated with grain size correlation length, and density, and the fact that even for multilayer simulations the results in the case of CLPX do not significantly improve for horizontal polarization, further analysis is required with regard to: 1) improvement of the representation of snow densification processes, especially the effect of metamorphosis on compaction rate; b) explicit parameterization of depth hoar effects; and c) sensitivity analysis of the horizontal and vertical scattering coefficients to grain size correlation length and density on a layer by layer basis. Another important aspect that must be accounted for is the role of subgrid scale variability of the terrain as well as land-cover.

Table 4-5 Comparison of simulated radiation properties between 36.5-V and 23.8-V GHz. Time is 20:00 UTC, 13:00 LST, 3/20/2003.

		36.5 GHz V	23.8 GHz V
Physical Properties	T_s [K]	256.35 (top)	
	ρ_s [kg/m ³]	170.24 (bulk)	
	$h_{sn}(SWE)$ [m]	0.3505 (bulk)	
	h_{sd} [m]	2.06	
	LWC	0.0 (top)	
	Tgnd	270.0	
Radiation Properties	ϵ'	1.23 (top)	1.23
	ϵ''	0.0001825 (top)	0.0001193
	γ_a [1/m]	0.1259 (top)	0.0536
	γ_s [1/m]	0.0396	0.0136
	r	0.0145	0.0056
	t	0.7893	0.9073
	e	0.1962	0.0871
	s_n	0.0003941	0.0003941
	$1-s_n$	0.9996	0.996
	D_n	258.87	265.01
	e_{back}	0.9803	0.9916
	T_b	258.77	264.91

Table 4-6 Model error statistics [Multilayer(single layer)] intercomparison using the correlation length, p_{ec} based on the classification by Mätzler (1996) for the Fraser MSA during CLPX: SSM/I, AMSR-E and Wójcik et al. [2008, W08]. Single-layer simulation results are from Chapter 3 (Kang and Barros 2010^b).

		H [K]			V [K]		
		<i>SSM/I</i>	<i>AMSR-E</i>	[W08]	<i>SSM/I</i>	<i>AMSR-E</i>	[W08]
18~19GHz	<i>Bias</i>	-10.76(-10.58)	-10.83 (-8.83)	---	7.60 (6.89)	3.82 (4.88)	---
	<i>ME</i>	10.96 (10.78)	11.57 (9.83)	8.46	9.03 (9.51)	6.59 (6.89)	8.1
	<i>RMSE</i>	12.93 (13.54)	16.90 (12.26)	10.21	11.18 (11.55)	10.29 (8.29)	9.7
22-23GHz	<i>Bias</i>	---	-8.79 (-6.85)	---	2.95 (2.02)	4.94 (6.12)	---
	<i>ME</i>	---	9.91 (8.65)	---	5.27 (5.69)	7.41 (7.85)	---
	<i>RMSE</i>	---	15.40 (11.10)	---	6.44 (6.87)	10.74 (9.39)	---
36~37GHz	<i>Bias</i>	-3.97 (-3.99)	-6.53 (-4.36)		7.60 (6.89)	7.15 (8.82)	---
	<i>ME</i>	6.71 (7.71)	9.05 (8.52)	12.47	9.03 (9.51)	10.04 (10.81)	12.02
	<i>RMSE</i>	8.54 (10.56)	14.41 (10.92)	14.39	11.18 (11.55)	13.30 (13.08)	14.37

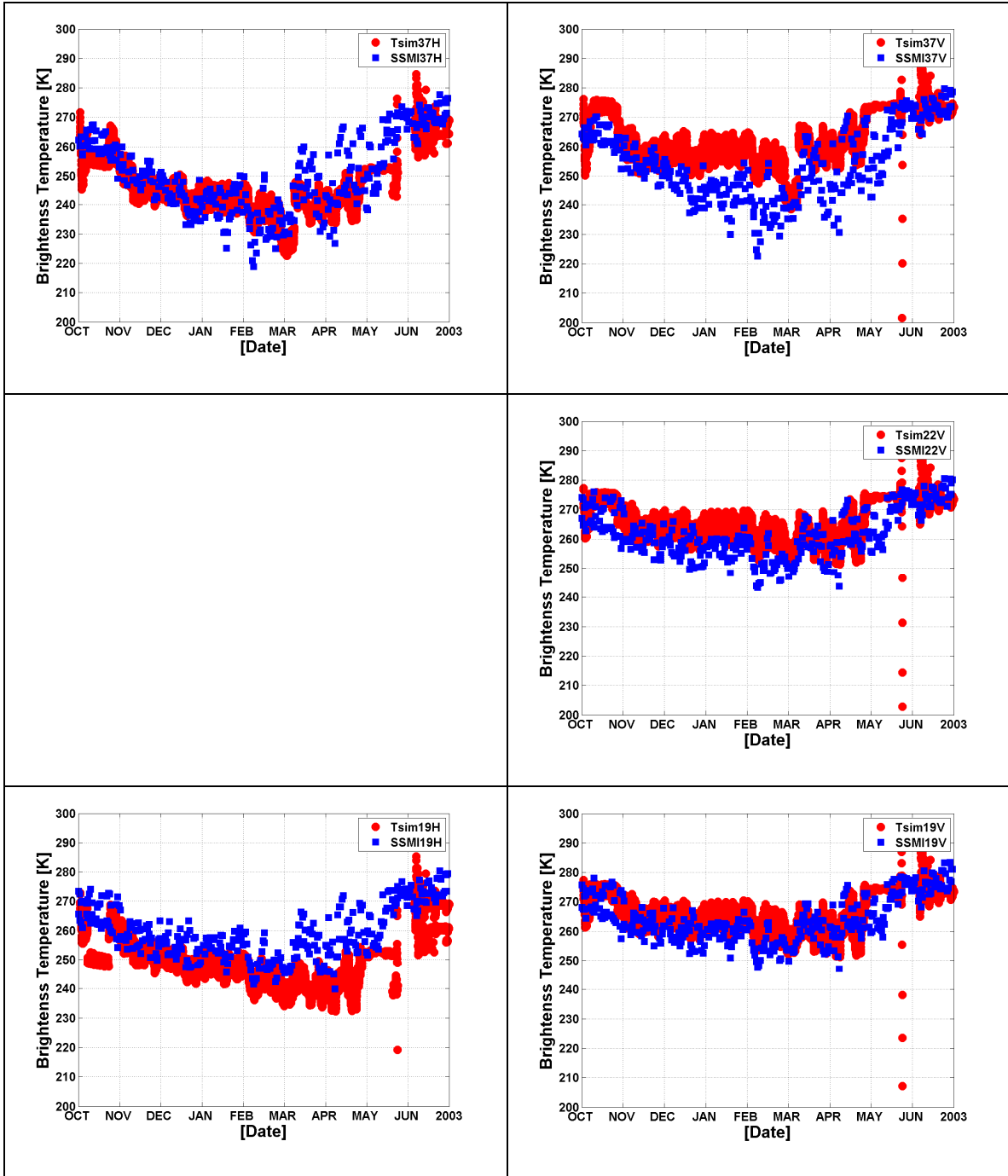


Figure 4-26 Comparison of brightness temperatures between multi-layer model and SSM/I at 19.35, 22.2, and 37.0GHz H/V.

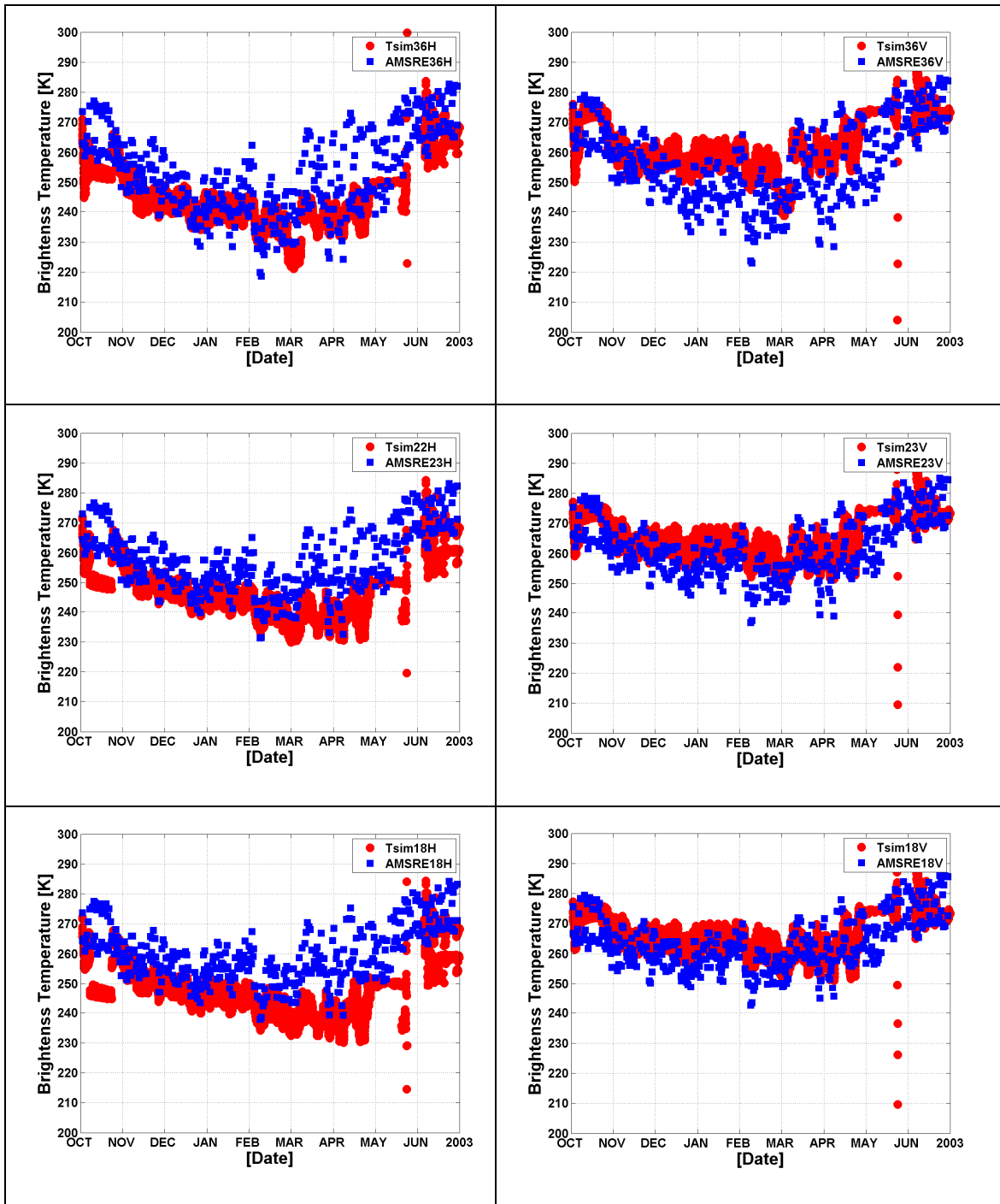


Figure 4-27 Comparison of brightness temperatures between multi-layer model and AMSR-E at 18.7, 23.8, and 36.5 GHz H/V.

Table 4-7 Model error statistics [Multilayer(single layer)] intercomparison using the correlation length, p_{ec} =constant=0.06mm, for the Fraser MSA during CLPX: SSM/I, AMSR-E and Wójcik et al. [2008, W08]. Single-layer simulation results are from Chapter 3 (Kang and Barros 2010^b).

		H [K]			V[K]		
		<i>SSM/I</i>	<i>AMSR-E</i>	[W08]	<i>SSM/I</i>	<i>AMSR-E</i>	[W08]
18~19GHz	<i>Bias</i>	-3.78 (1.68)	-6.27 (-1.87)	---	4.53 (5.23)	4.66 (5.35)	---
	<i>ME</i>	6.26 (5.17)	7.82 (6.00)	8.46	7.15 (7.11)	7.95 (7.81)	8.1
	<i>RMSE</i>	8.73 (6.50)	10.70 (8.33)	10.21	8.53 (8.58)	9.35 (9.28)	9.7
22-23GHz	<i>Bias</i>	---	-4.41 (0.06)	---	4.31 (7.23)	2.39 (4.81)	---
	<i>ME</i>	---	7.41 (6.63)	---	6.57 (8.25)	6.45 (8.11)	---
	<i>RMSE</i>	---	10.16 (8.98)	---	7.76 (9.40)	9.87 (9.74)	---
36~37GHz	<i>Bias</i>	1.92 (7.90)	-2.90 (1.79)		8.53 (12.26)	3.80 (7.12)	---
	<i>ME</i>	8.32 (10.84)	8.94 (9.58)	12.47	11.08 (13.85)	9.47 (11.98)	12.02
	<i>RMSE</i>	10.44 (12.51)	11.90 (12.28)	14.39	13.04 (15.75)	11.76 (14.00)	14.37

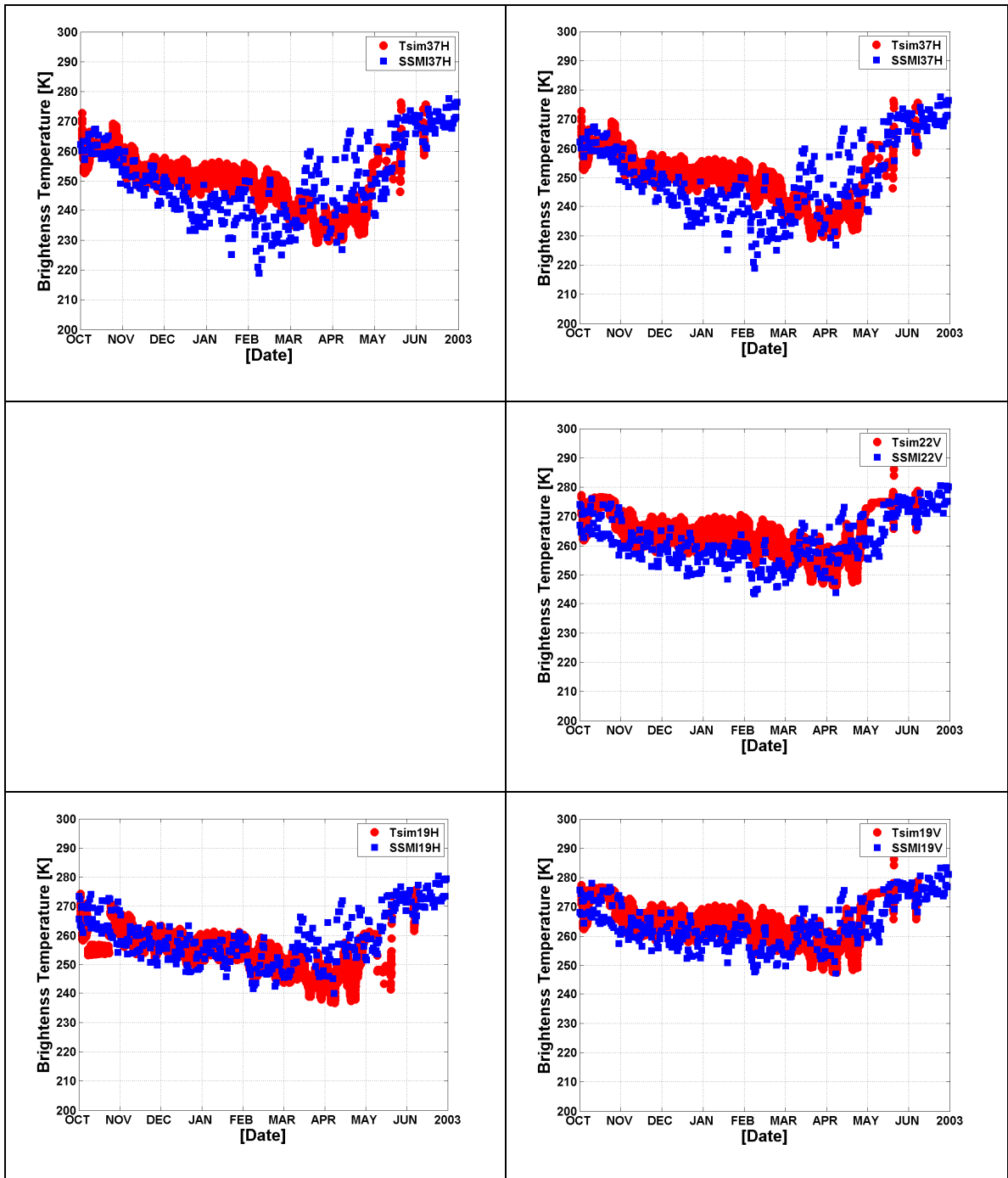


Figure 4-28 Comparison of brightness temperatures between multi-layer model and SSM/I at 19.35, 22.2, and 37.0GHz H/V.

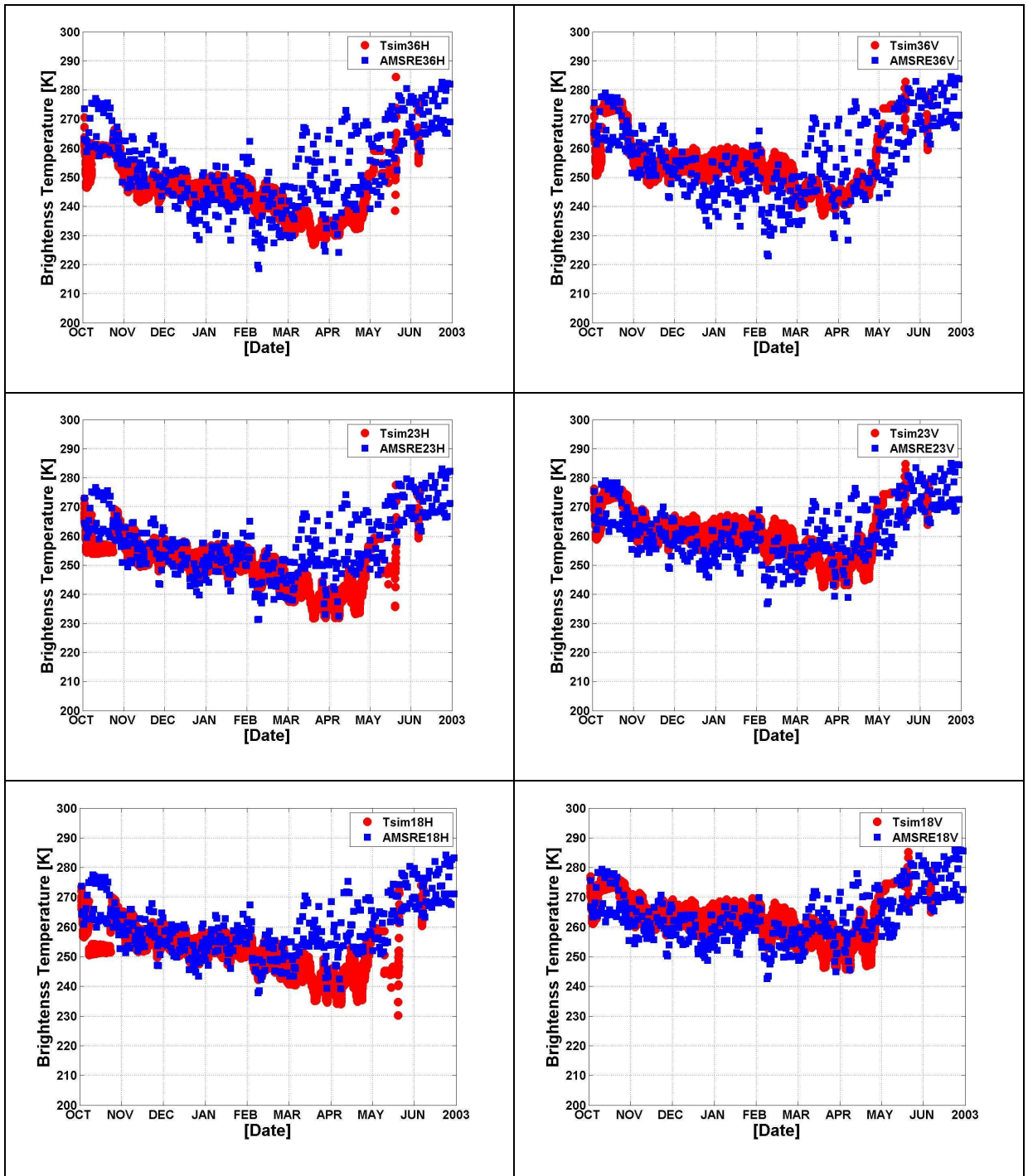


Figure 4-29 Comparison of brightness temperatures between multi-layer model and AMSR-E at 18.7, 23.8, and 36.5 GHz H/V.

4.6. Conclusion

Compared with the single-layer approach [Kang and Barros 2010^b], the multilayer approach lead to significantly improved results, especially for the case of horizontal polarization, for the Valdai Observing System Simulation (OSS) of SMMR observations, but the CLPX OSS was somewhat inconclusive with improvements in the multilayer formulation only when the grain size correlation length in MEMLS was held constant throughout the season and for vertical polarization mainly. Nevertheless, the results obtained with the coupled multilayer MLSHM-MEMLS for CLPX without calibration are competitive with results obtained from emissivity models supplied by direct observations of snowpack characteristics [e.g. Tedesco et al. 2008, Wójcick e al. 2008, Lemmtyienen et al. 2010]. The multi-layer formulation further facilitates physically-based inquiry into the processes that govern the coupled snow hydrology and emissivity behaviors by focusing on vertical structure. There are two groups of processes that require improved model parameterizations: (1) densification and the representation of snow metamorphic processes, and especially the formation of depth hoar in dry cold climates during the winter season, which has implications for both snow density and snow grain size distribution; and 2) the simulation of the snowpack energy balance, and specifically the diurnal cycle of snowpack top temperature. Furthermore, water percolation processes associated with the effect of abrupt and intermittent melting in early spring need to be better described [Martinec 1987]. During the fast melting snow season, as the melting water percolates though the layered

snowpack, multidirectional routing of liquid water within the snowpack over complex terrain should also be accounted for, including outflow through intermediate layers as well as lateral redistribution of liquid water interflow.

CHAPTER 5: Concluding Remarks

5.1. Overview

Whereas point-based measurements such as those obtained from man-held snow-core samples and snow sounding probes can provide highly accurate estimates of snow-pack properties one location at a time, the man-power required and technical challenges posed by the need to obtain such measurements at very high-resolution on a continuous basis prevent the establishment of high-density snow measurement networks that can support operational hydrological forecasting activities, let alone field-based process studies in support of remote –sensing activities (Cold Land Processes Mission Science Plan, <http://www.nohrsc.nws.gov>). This state of affairs is particularly critical in the context of the large *spatial heterogeneity and strong diurnal and seasonal cycles of snowpack processes* in temperate latitudes (Roger and Harrington, 1995; Cagnati *et al.* 2004, among others) which cannot be captured by remote-sensing estimates at coarse scale (e.g. 25 km from AMSR, Kelly *et al.* 2003). The objective of the research conducted in the context of this Ph.D. dissertation was to characterize the space-time variability of physical properties of the snowpack at high spatial and temporal resolution for downscaling of remote-sensing products of snow cover, snow depth and snow water equivalent using both improved ground-based measurements

and models. To meet this goal, a new RF sensor for systematic, ground-based, nondestructive monitoring of snowpack physical properties was presented, and two passive microwave observing system implementations using a coupled emission-snow hydrology with both single and multi-layer representations of snowpack processes were developed and two multi-year OSS (Observing System Simulations) studies were conducted and evaluated against SMMR, SSMI and AMSR-E satellite-based observations. Next, we summarize the findings and contributions of the research by focusing separately on measurement and modeling.

5.2. Summary of Findings and Contributions

5.2.1 – Measurement

A new L-band TX-RX wireless sensor to monitor snow accumulation and snow wetness was tested under laboratory conditions. The sensor was designed to operate at 39 discrete frequencies (39 channels) in the 1.00-1.76 GHz frequency range (0.02 GHz increments). Full system testing of the first generation system was conducted using commercial attenuators up to 20.0 dB to test the prototypes against design specifications. It was determined that performance was nearly optimal in the 1-1.2 GHz range. Next, snow layers of varying snow wetness were physically modeled under controlled laboratory conditions. This was achieved by adding varying amounts of

water to a layer of fixed porosity foam inside a rectangular tank placed above the transmitter. The attenuation and relative phase-shift of the RF signal propagating through the experimental “snowpack” and through the laboratory “atmosphere” were subsequently analyzed as a function of volumetric water content equivalent to snow wetness. Under the space and geometry limitations of the laboratory set-up, the data show that the single-frequency measurements exhibit high sensitivity for wetness values up to 24%, whereas multi-frequency retrieval is necessary for higher liquid water contents. Measurements from a field deployment during snowfall in January 2009 are also presented. The results suggest that there is potential for using the RF sensor to measure cumulative snowfall for short-duration events. This is the first such system that can provide reliable estimates of snow wetness for very wet snow conditions (> 20%) whereas previous instrumentation was limited to ~5% wetness. Major specific accomplishments that establish the utility of the new sensor for wet snow conditions include: 1) demonstration of instrumental sensitivity up to 72% snow wetness in the 1-1.1 GHz, which can be used in a time-dependent algorithm to retrieve very wet snow conditions from cyclic signal amplitude attenuation.; and 2) demonstration of potential utility of relative phase for constraining snow wetness retrieval at 1.08 and 1.10 GHz. Finally, the design and operating principle of this sensor permits autonomous

systematic noninvasive/ nondestructive monitoring of snow over long periods of time.

5.2.2 Modeling

A coupled snow hydrology-emission model LSHM-MEMLS [Devonec and Barros 2002, Wiesmann and Mätzler 1999, and Mätzler and Wiesmann 1999] was tested independently for two very different climatic and physiographic regions (Valdai, Russia and Colorado, USA) for both wet and dry snow regimes over multiple years with good results using both single -layer and multi-layer snowpack representations. These applications demonstrate transferability of the modeling system, and its potential utility in large-scale retrieval over large areas with limited if any ground-based observations to constrain the model or for data-assimilation. No calibration of the snow hydrology or the emission model was conducted, and the LSHM-MEMLS OSS error statistics both single and multi-layer parameterizations are at par, or yield better results than either the MEMLS and HUT models when supplied with snow properties from snowpit observations (Wójcik et al. 2008, Lemmetyinen et al. 2010). This suggests there is therefore great potential in using the LSHM-MEMLS coupled model for hemispheric scale operational retrievals of snow properties.

In the case of the single-layer OSS, and despite overall good skill as demonstrated by relatively low errors compared with previous work, one weakness was

identified with respect to the simulation of the radiative behavior of the snowpack, especially for horizontal polarization, when ice layers (ice lenses) form due to freezing of liquid water either due to daytime melting, or due to rain-on-snow events, and the development of depth hoar as the snowpack ages before the melting starts. Furthermore, it was established that a more accurate estimation of snow density especially in the case of wet snow regimes would be important to improve skill for vertical polarization.

These weaknesses were addressed by developing a multi-layer snow hydrology model that can capture liquid water flow within the snowpack due to melting and rain-on-snow events, as well as snowpack gradients in water content and structure that change its emission behavior. In addition, a multilayer representation of the snowpack should allow to take advantage of the multi-layer radiate transfer in MEMLS to better describe the extinction behavior of radiation transfer inside the snowpack.

Indeed, there is an improvement in the simulation of SWE, snow depth and snow density in the multi-layer presentation of snow physics. However, the OSS for CLPX shows that the compaction model is not adequate to capture the strong densification that takes place in the transition from early spring to late spring (mid April-mid May) when the model severely underestimates the snow density. This has

implications for the microwave emission model, and one can see that as opposed to what was expected the overall (October-June) error statistics of the multi-layer simulation for CLPX are not as good as the single layer simulations. Besides the effect of densification and deep metamorphism leading to the formation of depth hoar, which are not captured by the model, the parameterization of volume scattering in MEMLS utilized for these simulations is the same for vertical and horizontal polarization. As shown by Toure et al. (2008), there is significant ambiguity in the relationship between density, grain size correlation length and volume scattering when the snow is very dense, which is the case in CLPX from early winter through mid-spring. This warrants the consideration of different parameters in the relationship between scattering coefficients γ_b , snow density and grain size correlation length p_{ec} for vertical and horizontal polarization [Toure et al. 2008] and the relationship with snow surface roughness [Roy and Mätzler 2004]. Finally, OSS comparisons against SSM/I and AMSR-E after the peak accumulation phase show that the model can capture the cold temperatures, but underestimates the higher (daytime) values during the ripening and intermittent melting phases for CLPX. One possible explanation for this discrepancy is the effect of vegetation cover, specifically trees, which should start playing an important role in the spring as canopies loose all intercept snowfall. Currently the presence of

vegetation is parameterized in terms of fractional vegetation cover and leaf-area index (LAI) in the LSHM, but this parameterization is not shared with MEMLS, where it is assumed that the surface is fully covered by snow alone. Besides the effect of fractional snow cover and albedo, the presence of vegetation will also have an impact on the characterization of surface roughness. These effects must be incorporated next in the coupled LSHM-MEMLS.

One potential use of the coupled LSHM-MEMLS OSS in inverse mode was demonstrated by tracking the decomposition of the attenuation coefficient in MEMLS between scattering and absorption effects coefficients which can be used to detect snowpack regime, specifically the presence of liquid water which may be very useful for hazard monitoring (snow avalanches, rapid melt or large areas).

Finally, it is important to recall that the LSHM-MEMLS OSS was implemented at very coarse resolutions as compared to the subgrid scale variability of snow heterogeneities. Although, the downscaling challenge has not been addressed, the fact that the coupled snow-hydrology and radiative-transfer models, despite the various assumptions, captures well the average behavior at the satellite-based sensor resolution is very promising operationally as it opens the possibility for physically-based downscaling by nesting of one or multiple grids in order to better capture terrain and

land-cover effects.

5.3. Recommendations for Further Research

Measurement – Further research must to proceed in three fronts: 1) Field testing of the L-band microwave sensor to complement the preliminary testing done by Kang and Barros (2010^a). This includes experimentation to determine how to optimize sensor performance in complex and remote terrain. 2) Development and validation of a retrieval algorithm for long-term monitoring. 3) Research and development toward the next generation of sensors that may be completely autonomous and deployable in remote regions.

Modeling – Further research must focus on improving both the snow hydrology and the radiative transfer models. In the case, of snow hydrology the representation of snow metamorphosis processes is very limited, and both densification by overburden and depth decreases in density due to the formation of depth hoar must be reexamined and parameterized, including the representation of vapor phase transport that is currently neglected. The representation of transient melt and freeze processes must be represented beyond simple mass and energy fluxes to incorporate some statistical representation of porosity and ice lens and ice layer formation from layer-to-layer in the snowpack, which should have implications for the parameterization of grain size

correlation length that is critical for estimating scattering effects. In the case of the radiative transfer model, it is critical to improve the representation of horizontal and vertical scattering effects as well as the time dependence of the relationship between density and grain size correlation length, which should also include snow layer age, and weather conditions (time-of-the-year). The presence of vegetation and its impact on the microwave signature of the landscape in the ripening and melting phases must be incorporated explicitly in the radiative transfer model.

Scaling Analysis -The need for downscaling in Earth Sciences applications of remote-sensing arises from the discrepancy between the spatial resolution of existing products and the need for high resolution estimates for hydrological and water resources applications. Taking advantage of their work to characterize the subgrid-scale variability of soil moisture (Kim and Barros 2002a), Kim and Barros (2002b) developed and tested a downscaling algorithm that consists of an adaptive fractal interpolation method with contraction mapping that captures higher order moments and the spatial statistical structure of soil moisture fields at high spatial resolution. The fractal interpolation functions are derived from the application of Iterated Function Systems (Barnsley, 1986) using time and space varying functional parameters that can be obtained adaptively in real-time or via calibration against high-resolution data when

high-resolution ground-based observations are available. The advantage of this approach as compared to other fractal interpolation approaches is that the interpolated (downscaled surfaces) are unique spatial distributions of the original data at higher resolutions. Likewise, we propose here to use the results from OSS modeling experiments to formulate such adaptive fractal interpolation functions that express the co-evolution of snowpack physical properties at different scales. This approach could be tested using MODIS, AMSR-E, SSM/I and AMSU snow products at various resolutions.

Appendix A: Uncertainties of Phase Measurements

1.08 GHz

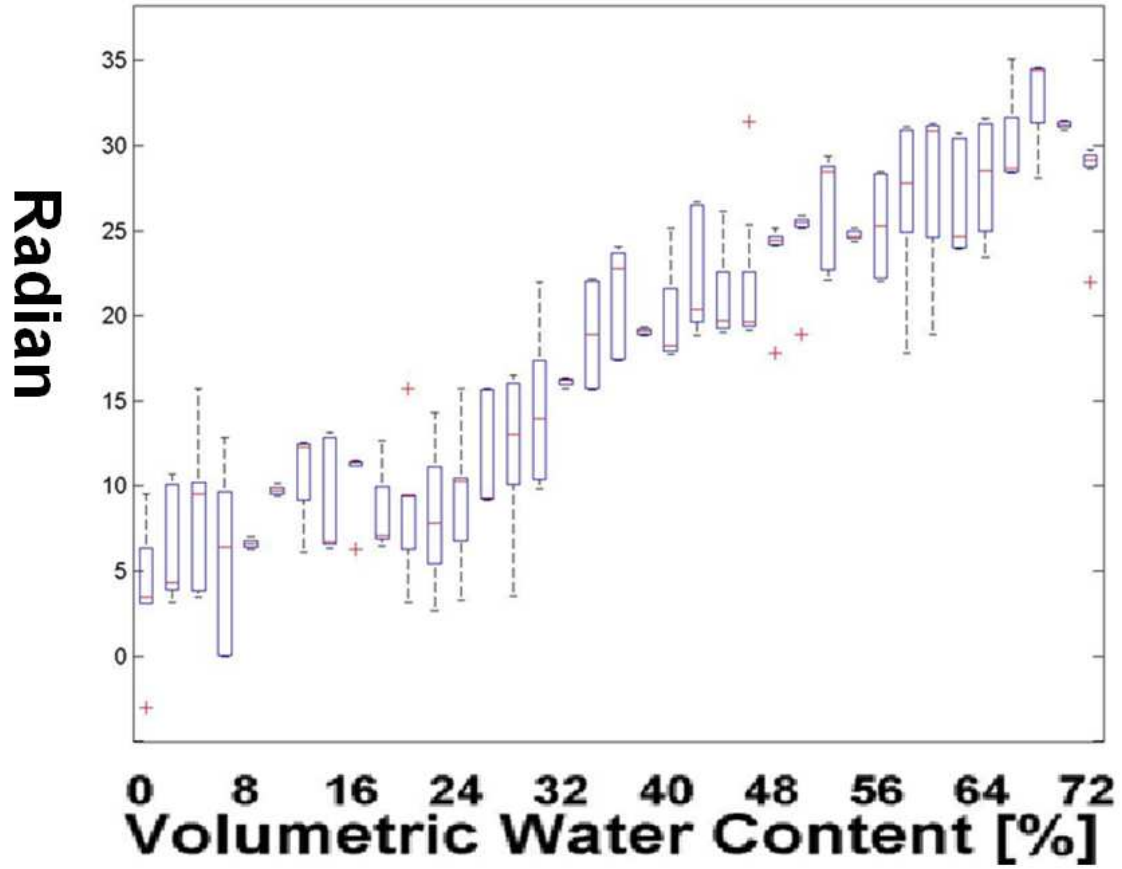


Figure A-1 Box-plot for phase extraction from RF signals with respect to water content at 1.08 GHz

Appendix B: Lobe Diagram of RF sensor

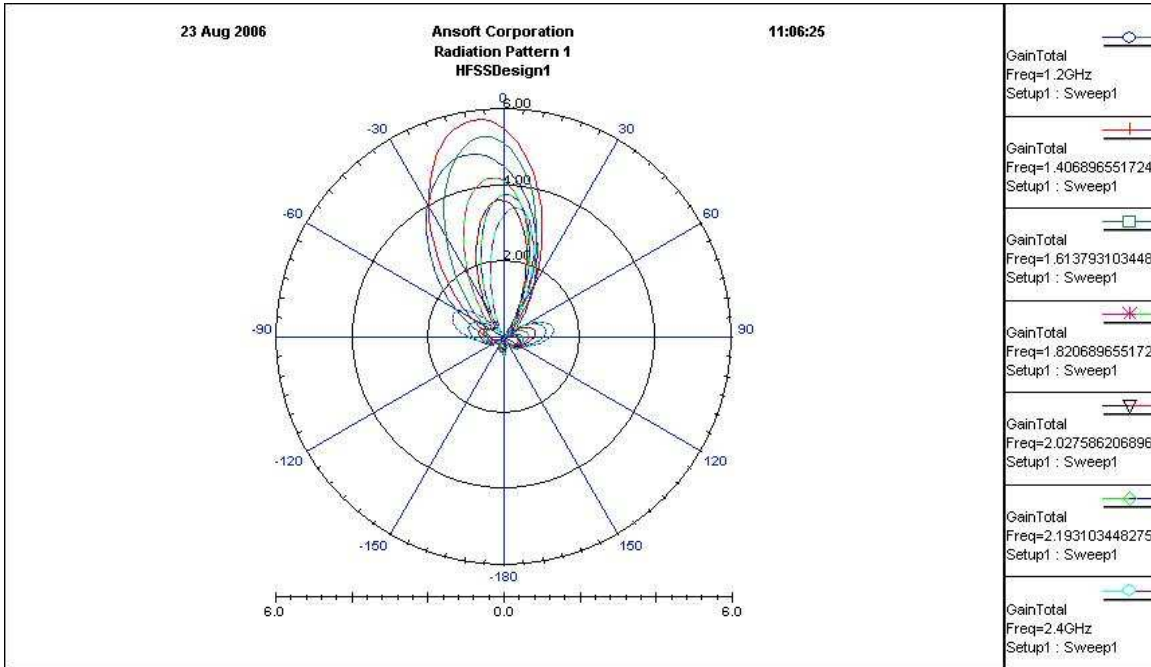


Figure B-1 Simulated Antenna Pattern provided by Vadum, Inc.

References

- Achammer, T., and Denoth, A. (1994). Snow dielectric properties: from DC to microwave X-band. *Annals of Glaciology*, 19, 92-96.
- Ambach, W., and Denoth, A. (1980). The dielectric behavior of snow: a study versus liquid water content, *NASA Workshop on the Microwave Remote Sensing of Snowpack Properties*. Fort. Collins, USA, May 20-22, NASA CP-2153.
- Anderson, E.A (1976) *A point energy and mass balance model of a snow cover*. NOAA Technical Report NWS 19, U.S. Department of Commerce, 1976.
- Anderson, E.A. (1973) *National Weather Service River Forecast System-Snow Accumulation and Ablation Model*. NOAA Technical Memorandum NWS HYDRO-17, U.S. Department of Commerce, 1973.
- Anderson, E.A., and Crawford, N.H. (1964) *The synthesis of continuous snowmelt hydrographs on a digital computer*. Technical Report, no. 36, Stanford University, Dept. of Civil Engineering.
- Andreadis, K.M., Liang, D., Tsang, L., and Letenmaier, D.P. (2008). Characterization of errors in a coupled snow hydrology-microwave emission model. *Journal of Hydrometeorology*. 9(1), 149-164.
- Armstrong, R. L., Knowles, K. W., Brodzik, M. J. and Hardman, M. A. (1994). Updated current year. DMSP SSM/I Pathfinder Daily EASE-Grid Brightness Temperatures, [2002-2003]. Boulder, Colorado USA: National Snow and Ice Data Center. Digital media.
- Armstrong, R.L. and Brodzik, M.J. (2001). Recent northern hemisphere snow extent: A comparison of data derived from visible and microwave satellite sensors. *Geophysical Research Letters*. 28(19), 3673-3676.
- Arsenault, K. (2003). CLPX-Model: Rapid Update Cycle 40km (RUC-40) Model Output Reduced Data Set. Boulder, CO: National Snow and Ice Data Center. Digital Media.
- Aschbacher, J. (1990) Parameterization of atmospheric influence for microwave land surface radiometry. *International Geoscience and Remote Sensing Symposium*, 2, 1551-1554.

- Benjamin, S.G., Brown, J.M., Brundage, K.J., Devenyi, D., Kim, D., Schwartz, B.E., Smirnova, T.G., Smith, T.L., and Marroquin, A. (1997). Improvements in aviation forecasts from the 40-km RUC. Preprints, *7th Conference on Aviation, Range, and Aerospace Meteorology*, Long Beach, February, 411-416.
- Brun, E., David, P., Sudul, M., and Brunot, G. (1992). A numerical model to simulate snow cover stratigraphy for operational avalanche forecasting. *Journal of Glaciology*. 38, 13-22.
- Chang, A.T. C., Foster, J.L., and Hall, D.K. (1987) Nimbus-7 derived global snow cover parameters. *Annals of Glaciology*. 9, 39-44.
- Chelidze, T., Derevyanko, A.I., and Kurilenko, O.D. (1977). Electrical spectroscopy of heterogeneous systems. *Naukova Dumka, Kiev*. 21-25.
- Choudhury, B.J. (1992). Atmospheric effects on SMMR and SSM/I 37 GHz polarization difference over the sahel. *International journal of remote sensing*, 13(18), 3443-3463.
- Cline, D., Armstrong, R., Davis, R., Elder, K., and Liston, G. (2002). Updated July 2004. CLPX GBMR Snow Pit Measurements. Edited by M. Parsons and M.J. Brodzik. In CLPX-Ground: Ground Based Passive Microwave Radiometer (GBMR-7) Data, T. Graf, T. Koike, H. Fujii, M. Brodzik, and R. Armstrong. 2003. Boulder, CO: National Snow and Ice Data Center. Digital Media.
- Cline, D., Elder, K., Davis, B., Hardy, J., Liston, G.E., Imel, D., Yueh, S.H., Gasiewski, A.J., Koh, G., Armstrong, R.L., and Parsons, M. (2003). Overview of the NASA cold land processes field experiment. *Proceedings of the SPIE- The International Society for Optical Engineering*. 4894, 361-72.
- Cumming, W. A. (1952). The dielectric properties of ice and snow at 3.2 centimeters. *Journal of Applied Physics*, 23(7), 768-73.
- Denoth, A. (1994). An electronic device for long-term snow wetness recording. *Annals of Glaciology*, 19, 104-106, 1994.
- Derksen, C. and Walker, A.E. (2003) Identification of systematic bias in the cross-platform (SMMR and SSM/I) EASE-grid brightness temperature time series *IEEE Transactions on Geoscience and Remote Sensing*. 41(4), 910-915.
- Devonec, E. and Barros, A.P. (2002). Exploring the transferability of a land-

- surface hydrology model. *Journal of Hydrology*, 265(1-4), 258-282.
- Durand, M., Kim, E.J., and Margulis, S.A. (2008). Quantifying uncertainty in modeling snow microwave radiance for a mountain snowpack at the point-scale, including stratigraphic effects. *IEEE Geoscience and Remote Sensing*. 46(6), 1753-1767.
- Eather, R.H. (1979). DMSR calibration. *Journal of Geophysical Research*. 84(A8), 4134-44.
- Foster, J.L., Sun, C., Walker, J.P., Kelly, R., Chang, A.T.C., and Dong, J. (2005) Quantifying the uncertainty in passive microwave snow water equivalent observations. *Remote sensing of Environment*. 94, 187-203.
- Foster, J.L., Chang, A.T.C., and Hall, D.K. (1997) Comparison of snow mass estimates from a prototype passive microwave algorithm and a snow depth climatology. *Remote Sensing of the Environment*. 62, 132-142.
- Frolov, A.D., and Macheret, Y.Y. (1999). On dielectric properties of dry and wet snow. *Hydrological Processes*. 13, 1755-1760.
- Gloersen, P. and Barath, F.T. (1977). A scanning multichannel microwave radiometer for Nimbus-G and SeaSat-A. *IEEE Journal of Oceanic Engineering*. 2, 172-178.
- Goodison, B., Rott, H., and Armstrong, R. (1993). Snow group workshop report in *Proceedings of ESA/NASA international workshop on passive microwave sensing research related to land atmosphere interaction*, St. Lary, France.
- Graf, T., Koike, T., Fujii, H., Brodzik, M., and Armstrong, R. (2003). CLPX-Ground: Ground Based Passive Microwave Radiometer (GBMR-7) Data. Boulder, CO: National Snow and Ice Data Center. Digital Media.
- Granlund, N., Lundbert, A., Feiccabrino, J., and Gustafsson, D. (2009). Laboratory test of snow wetness influence on electrical conductivity measured with ground penetrating radar. *Hydrology Research*. 40(1), 33-44.
- Grody, N.C. and Bassist, A.N. (1996). Global identification of snow cover using SSM/I measurements. *IEEE Transaction on Geoscience and Remote Sensing*. 34, 237-249.
- Hall, D.K. (1987). Influence of depth hoar on microwave emission from snow in

- northern Alaska. *Cold Regions Science and Technology*. 13, 225-231.
- Hallikainen, M. and Jolma, P. (1992). Comparison of algorithms for retrieval of snow water equivalent from Nimbus-7 SMMR data in Finland. *IEEE Trans. Geosci. Remote Sensing*. 30, 124–131.
- Hallikainen, M., Pulliainen, J., Kurvonen, L., and Grandell, J. (1997). The HUT brightness temperature model for snow-covered terrain. *International Geoscience and Remote Sensing Symposium*, 2, 622-624.
- Hallikainen, M., Ulaby, F.T., and Abderazik, M. (1982) Measurements of the dielectric properties of snow in the 4-18 GHz. *European Microwave Conference*. Helsinki Finland, 151-156.
- Henderson-Seller, A., Yang, Z.L., and Dickinson, R.E. (1993). The project for intercomparison of land-surface parameterization schemes: Phase 2 and 3 *Bulletin of American Meteorological Society*, 74(7), 1335-1349.
- Henderson-Sellers, A., Pitman, A. J., Love, P. K., Irannejad, P., and Chen, P. (1995). The Project for Intercomparison of Land Surface Parameterization Schemes (PILPS): Phases 2 and 3. *Bulletin of American Meteorological Society*, 76, 489–503.
- Herzfeld, U.C., Maslanik, J.A. and Sturm, M.(2006). Geostatistical Characterization of Snow-Depth Structures on Sea Ice Near Barrow, Alaska – A Contribution to the AMSR-Ice03 Field Validation Campaign, *IEEE Transactions on Geoscience and Remote Sensing*, 44(11), 3038-3056.
- Horan, J.J. (1978). Nimbus: the vanguard of remote sensing. *IEEE Spectrum*, 15(11), 36-43.
- Imaoka, K., Shibata, A., Nakagawa, N., Nakajima, Y., Haijima, H., Tanaka, H., and Imatani, T. (2000). Airborne microwave radiometer for AMSR and AMSR-E project. *SPIE: Microwave remote sensing of the atmosphere and environment II*, 4152, 303-309.
- Intergovernmental Panel on Climate Change, *Climate change 2007: The physical science basis, summary for policymakers*, IPCC Secretary, Geneva, Switzerland.
- Jordan, R. (1991). A one-dimensional temperature model for a snow cover. U.S.

- Army Corps of Engineers, *Special Report* 91-16.
- Kang, D., and Barros, A.P. (2010^a) Introducing an L-band snow sensor system for in situ monitoring of changes in water content-full system testing. in press to *IEEE Transaction on Geoscience and Remote Sensing*.
- Kang, D., and Barros, A.P. (2010^b). An evaluation of a coupled snow hydrology and microwave emission model for data-sparse regions. In preparation.
- Kelly, R., Chang, A., Tsang, L., and Foster, J. (2003). A prototype AMSR-E global snow area and snow depth algorithm. *IEEE Transactions on Geoscience and Remote Sensing*. 41(2), 230-242.
- Knowles, K.W., Njoku, E. G., Armstrong, R. L., and Brodzik, M. J. (2002). Nimbus-7 SMMR Pathfinder Daily EASE-Grid Brightness Temperatures. Boulder, Colorado USA: National Snow and Ice Data Center. Digital media.
- Kondo, J., and Yamazaki, T. (1990) A prediction model for snowmelt, snow surface temperature and freezing depth using a heat balance method. *Journal of Applied Meteorology*. 29, 375-384.
- Kovacs, A., Grow, A, Moray, R.M. (1993) *A reassessment of the in situ dielectric constant of the polar film*. U.S. Army Corps Cold Regions Research and Engineering Laboratory *Special Report*, Hanover, M.A. 93-26.
- Kummerow, C., Hong, Y., Olson, W.S., Yang, S., Adler, R.F., McCollum, J., Ferraro, R., Petty, G., Shin, D-B., and Wilheit, T.T. (2001) The evolution of the Goddard profiling algorithm (GPROF) for rainfall estimation from passive microwave sensors. *Journal of Applied Meteorology*. 40(11), 1801-1820.
- Lehning, M., Fierz, C., and Lundy, C. (2001). An objective snow profile comparison method and its application to SNOWPACK. *Cold Regions Science and Technology*, 33 253-261.
- Lemmetyinen, J., Pulliainen, J.I. Rees, J., Kontu, A., and Qiu, Y. (2010) Multiple-Layer Adaptation of HUT Snow Emission Model: comparison With Experimental Data. *IEEE Transactions on Geoscience and Remote Sensing*, 48(7), 2781-94.
- Linlor, W.I. (1980). Permittivity and attenuation of wet snow between 4 and 12

- GHz, *Journal of Applied Physics*, 51, 2811-2816.
- Looyenga, H. (1965) Dielectric constant of heterogeneous mixture. *Physica*, 31, 401-406.
- Lundberg, A. (1977). Laboratory calibration of TDR-probes for snow wetness measurements. *Cold Regions Science and Technology*, 25, 197-205.
- Lundberg, A., and Thunehed, H. (2000). Snow Wetness Influence on Impulse Radar Snow Surveys Theoretical and Laboratory Study. *Nordic Hydrology*, 31, 2, 89-106.
- Lundberg, A., Thunehed, H., and Bergström, J. (2000). Impulse Radar Snow Surveys – Influence of Snow Density. *Nordic Hydrology*, 31(1), 1-14.
- Lundberg, H., Thunehed, H., and Bergström, J. (2000) Impulse Radar Snow Surveys – Influence of Snow Density. *Nordic Hydrology*. 31(1), 1-14.
- Madrid, C.R., (Ed.) (1978). The Numbus-7 User's Guide. Greenbelt, MD: NASA Goddard Space Flight Center.
- Magono, C. and Lee, C. W. (1996). Meteorological Classification of Natural Snow Crystals. *Journal of the Faculty of Science*. Hokkaido University.
- Markus, T., Cavalieri, D. J., Gasiewski, A. J., Klein, M., Maslanik, J.A., Powell, D. C., Stankov, B. B., Stroeve, J. C. and Sturm, J. C. (2006). Microwave Signatures of Snow on Sea Ice: Observations, *IEEE Transactions on Geoscience and Remote Sensing*, 44(11), 3081-3090.
- Martinec, J., (1987). Meltwater percolation through an alpine snowpack. *Avalanche Formation, Movement and Effects* (Proceedings of the Davos Symposium, September 1986), IAHS Publ. no. 162, 1987.
- Mätzler, C. and Wiesmann, A. (1999). Extension of the microwave emission model of layered snowpacks to coarse grained snow. *Remote Sensing of Environment*, 70(3), 317-325.
- Mätzler, C. (1992). Ground-based observations of atmospheric radiation at 5, 10, 21, 35, and 94 GHz. *Radio Science*. 27(3), 403-415.
- Mätzler, C. (1996). Microwave permittivity of dry snow. *IEEE Transactions on*

- Geoscience and Remote Sensing*, 34, 573-581.
- Mätzler, C. (2002). Relation between grain-size and correlation length of snow. *Journal of Glaciology*, 48(162), 461-466.
- Mätzler, C. (2009¹). Advances in Microwave Emission Models for Snow and Ice. Second Workshop on Remote Sensing and Modeling of Surface Properties, Meteo France, Toulouse, 9-11.
- Morris, E.M. *Sensitivity of the European Hydrological System snow models*. in Hydrological Aspects of Alpine and High Mountain Areas, Proceedings of the Exeter Symposium, IAHS Publication no. 138, pp. 221-231, 1982.
- Mote, P.W., Hamlet, A.F., Martyn, P.C., and Lettenmaier, D.P. (2005). Declining mountain snowpack in western north America. *Bulletins of American Meteorological Society*. 86, 39-49.
- National Research Council (NRC). (2007). Earth Science and Applications from Space: National Imperatives for the Next Decade and Beyond (Executive Summary), <http://www.nap.edu/catalog/11820.html>. National Academy of Sciences, National Academies Press, Washington DC, 35pp.
- Nosek, T.P., and Thomas, P. (2004). The EOS aqua/aura experience: Lessons learned on design, integration, and test of earth-observing satellites," AIAA Space 2004 Conference and Exposition, 3, 1916-1923, *A Collection of Technical Papers - AIAA Space 2004 Conference and Exposition*.
- Nyfors, E. (1983). On the dielectric properties of dry snow in the 800 MHz to 13 GHz region. *Report 5135*, Helsinki University of Technology, Radio Laboratory, Otaniemi, Finland.
- Polder, D. and Van Santen, J.H. (1946). The effective permeability of mixtures of solids. *Physica.*, 12, 257-271.
- Pomeroy, J.W. (2007) Cold regions hydrology, snow and PUB. *Predictions in Ungauged Basins: PUB Kick-off*. IAHS Publication, No. 309. IAHS Press. Wallingford, UK, 85-91.
- Pulliainen, J., Karna, J.P., and Hallikainen, M.(1993). Developing of geophysical retrieval algorithms for MIMR. *IEEE Transactions on Geosciences and Remote Sensing*. 3, 268-277.

- Rango, A. (1986). Progress in snow hydrology research. *IEEE Transactions on Geoscience and Remote Sensing*. GE-24(1), 47-53.
- Rees, A., Lemmetyinen, J., Derksen, C., Pulliainen, J., and English, M. (2010) Observed and modelled effects of ice lens formation on passive microwave brightness temperatures over snow covered tundra. *Remote Sensing and Environment*. 114, 116-126.
- Rivers, Jr., J.W. (1982). Defense meteorological satellite program (DMSP). *IEEE International Conference on Communications*, 1G61/5, 1, 13-17. Philadelphia, PA, USA.
- Roy, V., Goita, K., Royer, A., Walker, A.E., and Goodison, B.E. (2004). Snow water equivalent retrieval in a Canadian boreal environment. *IEEE Geoscience and Remote Sensing*, 42(9), 1850-1859.
- Schanda, E. and Mätzler, C. (1981). Optimum characteristics for snow pack evaluation by microwave radiometry. *Advanced Space Research*. 1, 151-162.
- Schneebeli, M., and Johnson, J.B. (1998). A constant speed penetrometer for high-resolution snow stratigraphy. *Annals of Glaciology*, 26, 107-111.
- Schneebeli, M., Coleuo, C., Touvier, F., and Lesaffre, B. (1998). Measurement of density and wetness using time domain Reflectometry. *Annals of Glaciology*, 26, 69-72.
- Sihvola, H., and Kong, J. (1988) "Effective permittivity of dielectric mixtures," *IEEE Transactions on Geoscience and Remote Sensing*. 26(4), 420-429.
- Stephens, G. L., and Kummerow, C. D. (2007) The Remote Sensing of Clouds and Precipitation from Space: A Review. *Journal of the Atmospheric Sciences*. 64(1), 3742-3765.
- Sweneey, B.D., and Colbeck, S.C. (1974) Measurements of the dielectric properties of wet snow using a microwave technique. U.S. Army Corps of Engineers Cold Region Research and Engineering Laboratory *Special Report*, Hanover, Massachusete. 25, 34.
- Tedesco, M. and Kim, E.J. (2006). Intercomparison of electromagnetic models for passive microwave remote sensing of snow. *IEEE Transactions on Geoscience and Remote Sensing*. 44(10), 2654-66.

- Tedesco, M., Kim, E. J., Gasiewski, A., Klein, M., and Stankov, B., (2005): Analysis of multiscale radiometric data collected during the Cold Land Processes Experiment-1 (CLPX-1). *Geophysical Research Letter*, 32, L18501, doi:10.1029/2005GL023006.
- Tiuri, M., Sihvola, A.H., Nyfors, E.G., and Hallikainen, M. (1984). Complex dielectric constant of snow at microwave frequencies. *IEEE Journal of Oceanic Engineering*. 9(5), 377-382.
- Tsang, L., Chen, C., Chang, A.T.C., Guo, J., and Ding, K. (2000). Dense media radiative transfer theory based on quasicrystalline approximation with applications to passive microwave remote sensing of snow. *Radio Science*, 35(3), 731-749.
- U.S. Army Corps of Engineers. (1956). Snow Hydrology, Summary report of the Snow Investigations, U.S. Army Corps of Engineers *Special Report*, North Pacific Division, Portland, Oregon.
- Uppala, S. M., et al. (2005), The ERA-40 Re-analysis, *Quaternary Journal of Royal Society*, 131, 2961–3012.
- Von Hippel, A.R., (Ed.) (1954) *Dielectric materials and applications*. 301, MIT Press, Cambridge, Massachusetts, U.S.A.
- Westwater, E.R., Snider, J.B., and Falls, M.J. (1990). Ground-based radiometric observations of atmospheric emission and attenuation at 20.3, 31.65, and 90.0 GHz: A comparison of measurements and theory. *IEEE Transaction on Antennas and Propagation*, 38, 1569-1579.
- Wiesmann, A. and Mätzler, C. (1998) *Documentation for MEMLS 98.2, Microwave emission model of layered snowpacks*. Research Report No. 98-2, Microwave Department, Institute of Applied Physics, University of Bern, Switzerland.
- Wiesmann, A. and Mätzler, C. (1999) Microwave emission model of layered snowpacks. *Remote Sensing of Environment*. 70(3), 307-316.
- Wiesmann, A., and Mätzler, C. (1998). Radiometric and structural measurements of snow samples. *Radio Science*, 33(2), 273-289.
- Wójcik, R., Andreadis, K., Tedesco, M., Wood, E., Troy, T., and Lettenmeier, D. (2008). Multimodel estimation of snow microwave emission during CLPX 2003 using operational parameterization of microphysical snow

characteristics. *Journal of Hydrometeorology*. 9(6), 1491-1505.

Yoshida, Z., Oura, H., Kuroiwa, D., Huzioka, T., Kojima, K. and Kinoshita, S.
(1959). Physical studies on deposited snow. In: *Report 14*, Low Temp. Sci.
Inst., Hokkaido University, Sapporo, Japan.

Biography

Do Hyuk Kang was born in Jinjoo, South Korea. He attended the Seoul National University in Seoul, Korea and majored in Geography. He also pursued a Master of Science in Civil Engineering at Colorado State University, Fort Collins, Colorado. He is a Ph.D. Candidate in Civil and Environmental Engineering at Duke University. He received an Earth System Science Fellowship from NASA for three years. He is a member of the American Geophysical Union and the American Association of Geographers.